TOM KUPPENS

development of methodology to assign absolute configurations using vibrational circular dichroism

promotor: Prof. Dr. P. Bultinck, Ghent University

co-promotor: Prof. Dr. W. Herrebout, University of Antwerp

Dissertation for the degree of Doctor in Sciences: Chemistry – December 2006
Ghent University, Faculty of Sciences
Department of Inorganic and Physical Chemistry

And now for something completely different.
– Monty Python's Flying Circus

table of contents

list of publications

The following papers have been published as a direct consequence of the work undertaken for this thesis:

Determination of the stereochemistry of 3-hydroxymethyl-2,3-dihydro-[1,4]dioxino[2,3-b]pyridine by vibrational circular dichroism and the effect of DFT integration grids
Kuppens, T.; Langenaeker, W.; Tollenaere, J. P.; Bultinck, P.
Journal of Physical Chemistry A **2003**, *107*, 542-553

Determination of absolute configuration via vibrational circular dichroism
Kuppens, T.; Bultinck, P.; Langenaeker, W.
Drug Discovery Today: Technologies **2004**, *1*, 269-275

Determination of the absolute configuration of three *as*-hydrindacene compounds by vibrational circular dichroism
Kuppens, T.; Vandyck, K.; Van der Eycken, J.; Herrebout, W.; van der Veken, B. J.; Bultinck, P.
Journal of Organic Chemistry **2005**, *70*, 9103-9114

Elucidation of the absolute configuration of JNJ-27553292, a CCR2 receptor antagonist, by vibrational circular dichroism analysis of two precursors
Kuppens, T.; Herrebout, W.; van der Veken, B. J.; Corens, D.; De Groot, A.; Doyon, A.; Van Lommen, G.; Bultinck, P.
Chirality **2006**, *18*, 609-620

Intermolecular association of tetrahydrofuran-2-carboxylic acid in solution: A vibrational circular dichroism study
Kuppens, T.; Herrebout, W.; van der Veken, B. J.; Bultinck, P.
Journal of Physical Chemistry A **2006**, *100*, 10191-10200

A DFT conformational analysis and VCD study on methyl tetrahydrofuran-2-carboxylate
Kuppens, T.; Vandyck, K.; Van der Eycken, J.; Herrebout, W.; van der Veken, B. J.; Bultinck, P. Spectrochimica Acta Part A-Molecular and Biomolecular Spectroscopy **2006**, Published online.

Structure elucidation of polychloroterpenes obtained from optically active pinenes: 2-endo,5,5,8,8,9,9,10,10,10-decachlorofenchane by NMR and (1*R*,3*S*,4*S*,5*S*,6*S*,7*R*)-2,2,3-exo,5-endo,6-exo,8,9,9,10,10-decachlorobornane by VCD
Kruchkov, F. A.; **Kuppens, T.**; Kolehmainen, E.; Nikiforov, V. A.
Organohalogen Compounds **2006**, *68* In press
I was responsible for the VCD measurements/calculations and the absolute configuration assignment

Vibrational circular dichroism DFT study on bicyclo[3.3.0]octane products
Debie, E.; **Kuppens, T.**; Vandyck, K.; Van der Eycken, J.; van der Veken, B. J.; Herrebout, W.; Bultinck, P.
Submitted to Tetrahedron-Asymmetry **2006**
I was responsible for the conformational analysis, measurements and calculation of the spectra for all four compounds

The following papers have been published outside the scope of this thesis:

Quantum similarity superposition algorithm (QSSA): A consistent scheme for molecular alignment and molecular similarity based on quantum chemistry
Bultinck, P.; **Kuppens, T.**; Girone, X.; Carbo-Dorca, R.
Journal of Chemical Information and Computer Sciences **2003**, *43*, 1143-1150
I was responsible for the Fortran code testing

A selected ion flow tube study of the reactions of H_3O^+, NO^+ and $O_2^{\cdot +}$ with some oxygenated biogenic volatile organic compounds
Amelynck, C.; Schoon, N.; **Kuppens, T.**; Bultinck, P.; Arijs, E.
International Journal of Mass Spectrometry **2005**, *247*, 1-9
I was responsible for the conformational analysis and property calculations for all eight compounds

abbreviations

AAT	atomic axial tensor
AC	absolute configuration
APT	atomic polar tensor
BO	Born-Oppenheimer
CPHF	coupled perturbed Hartree-Fock
DFT	density functional theory
ECD	electronic circular dichroism
EMEA	European agency for the evaluation of medicinal products
ESI	enantiomeric similarity index
FDA	food and drug administration (US)
FTIR	Fourier transformed IR
GGA	generalized gradient approximation
GIAO	gauge including/invariant atomic orbitals
HF	Hartree-Fock
IR	infrared
KS	Kohn-Sham
LDA	local density approximation
LIA	lock-in amplifier
LOA	London atomic orbitals
LP	linearly polarized
MCT	mercury cadmium telluride (detector)
MFP	magnetic field perturbation
MO	molecular orbital
MP2	second-order Møller-Plesset perturbation theory
NDA	new drug application
NMR	nuclear magnetic resonance
NS	neighborhood similarity

OR	optical rotation
PEM	photoelastic modulator
PES	potential energy surface
RCP/LCP	right/left circularly polarized
S/N	signal-to-noise ratio
SCF	self consistent field
THF	tetrahydrofuran
VCD	vibrational circular dichroism
VCT	vibronic coupling theory
XRD	X-ray diffraction
ZPD	zero path difference

1

introduction

1.1 Absolute configuration

In recent years, a considerable interest in the biological activity of the enantiomers of chiral drugs has emerged.[1] This interest in drug stereochemistry has resulted from the considerable advances in the synthesis, analysis and separation of chiral molecules.[2] There are numerous examples in literature that show that enantiomers of chiral drugs, differ substantially in their biological properties.[3] In chiral drugs, one enantiomer is often responsible for a given pharmacological activity, whereas the other may be less active, inactive, toxic, or may give rise to an entirely different pharmacological response.[4]

As a result of these advances in technology and the benefits of single enantiomer drugs, drug stereochemistry became an issue for the pharmaceutical industry and the regulatory authorities. In 1992, the Food and Drug Administration (FDA) in the USA published a policy statement[5] for the development of new stereoisomeric drugs, which was closely followed by guidelines from the European Agency for the Evaluation of Medicinal Products (EMEA) in 1993.

At present, there is no absolute requirement from any of the regulatory authorities for the development of single enantiomer drugs, and the decision of the stereoisomeric form to be developed (racemic or single enantiomer) is left to the applicant. The applicant however, must recognize the occurrence of chirality in new drugs; attempt to separate the stereoisomers, assess the contribution of the various stereoisomers to the activity of interest and make a rational selection of the stereoisomer that is proposed for marketing.[6]

An illustration of a drug for which a single active enantiomer was developed from a previously marketed racemate, is ibuprofen. The main analgesic activity of ibuprofen resides predominantly in the *S* enantiomer.[7] Administration of the racemate, (*R*)-ibuprofen results in a biologically fortuitous metabolic chiral inversion to the active *S* enantiomer.[8]

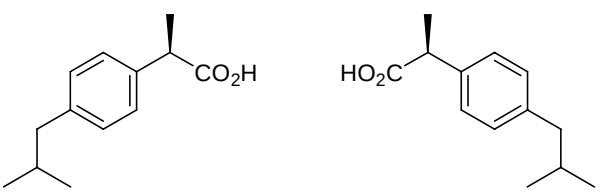

(*R*)-(–)-ibuprofen (*S*)-(+)-ibuprofen

Figure 1.1 Enantiomers of ibuprofen.

Regulatory bodies such as the FDA and EMEA are responsible for approving whether a drug can proceed to clinical trials and whether it should be allowed to be marketed. In order to get the new drug on the market in the US, a pharmaceutical company has to submit a New Drug Application (NDA) to the FDA. The applicant has to file an exhaustive report which details on the drug compound.[9] Evidently, structural information on the drug compound is also an important issue. For chiral drugs, the structural information provided needs to describe the absolute configuration (AC)[10] of the active molecule.

Not only the regulatory bodies demand such information on chiral drugs. If a pharmaceutical company wants to secure their intellectual properties for a potent compound in the early stages of the drugs discovery process, absolute configurations of the key compounds need to be known.[11,12] Research scientists are also interested

in the stereochemical structure of their enantiomers. The absolute configuration of chiral compounds is critical in understanding structure-activity relationships[13] or in the development for appropriate chiral separations[14], resolutions, or syntheses. Also, in a synthesis process, chemists always want to know the absolute configuration of their precursors and synthesized compounds as early as possible.

Given the combination of the rapidly growing market for chiral drugs and the general need to determine absolute configurations of the chiral molecules, there is evidently a need for tools that allow accessible absolute configuration determining.

The primary tool for determining absolute configurations is single-crystal X-ray diffraction (XRD) measurements using anomalous scattering.[10,15,16] This requires high-quality single crystals and additionally, the crystal should be subject to anomalous scattering which, for standard XRD experiments, can be obtained by introducing heavy atoms in the crystal. These conditions are not always met. Other methods are nuclear magnetic resonance (NMR),[17,18] optical rotation,[19-23] stereospecific synthesis and electronic circular dichroism (ECD).[23-26] The latter technique is a form of UV/VIS spectroscopy that relies on the differential absorption of a chiral molecule towards left and right circularly polarized light.[27] In order to be applicable, the compound needs specific functional groups, that is, chromophores that can absorb UV/VIS radiation.
A relative new technique in this context is vibrational circular dichroism (VCD), which combines the structural specificity of IR spectroscopy with the stereochemical sensitivity of circular dichroism.

In Table 1.1 an overview is given in which the most applied techniques are given with their advantages and disadvantages.[28]

Table 1.1 Comparison of different techniques that can be applied for absolute configuration determination

	advantage	disadvantage
vibrational circular dichroism (VCD)	- applicable in solution on a wide range of molecules	- measurements are not straightforward
X-ray diffraction (XRD)	- reliable - regulatory standard	- need for good quality single crystals and dispersive scatters
nuclear magnetic resonance (NMR)	- well known	- need for chiral shift reagents, chiral additives or derivatization
optical rotation (OR)	- relatively easy to measure	- higher level calculations needed compared to VCD - only one property can be compared in contrast to VCD (comparison of spectra) - sign depends on solvent used
electronic circular dichroism (ECD)	- applicable on molecules in solution	- only a few bands are available

1.2 Vibrational circular dichroism

Chiral molecules interact differently with left and right circularly polarized radiation (Figure 1.2). The measurement of differential absorption of the incident radiation in the infrared region is known as vibrational circular dichroism (VCD).[29] The significance of VCD lies in the fact that it provides a wealth of information on the structure and the stereochemistry of the chiral molecule as VCD intensities arise from vibrational transitions in a chiral molecule. In ordinary IR absorption spectra no stereochemical information is embedded. Because VCD is a differential

spectroscopy form, VCD intensities can be negative with the bands centered at the vibrational frequencies. Mirror image molecules have identical unpolarized IR absorption intensities, but have opposite VCD intensities. The latter is a reflection of the chiral nature of the compound that was measured. However, it does not provide any direct information on the actual absolute configuration.[30]

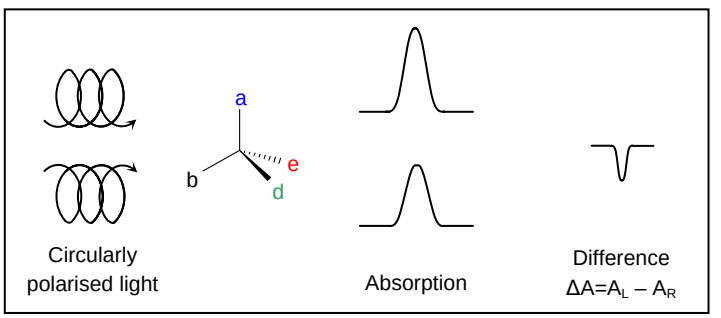

Figure 1.2 Differential absorption of RCP and LCP radiation by a chiral molecule.

Before VCD was experimentally observed, theoretical studies and predictions of VCD were performed in the early 1970s, using empirical models.[31-35] These theoretical predictions indicated that VCD intensities should be strong enough in order to be observed. This greatly encouraged and guided experimental observations of VCD. The earliest measurements of VCD were reported in 1973 by Holzwarth et al.[36,37] In the next few years, more VCD measurements were reported in literature.[38,39] The implementation of FTIR VCD by Nafie et al.[40-43] in 1979 and further development in the instrumentation (see Chapter 3) nowadays allows the measurement high quality VCD spectra for most chiral compounds in solution.

The interpretation and evaluation, that is, the process of extracting configurational and conformational information from experimental VCD spectra is not straightforward. For a reliable evaluation one needs calculated VCD spectra. Because a good theory was missing, a variety of empirical models emerged during the 1970s and 1980s that were applied to the analysis of the VCD spectra, with more or less success.[44] Theoretical modeling of spectra, however, has been hampered by the complexities involved in the calculation of VCD intensities. VCD originates from interaction between radiation and charged particles taking into account the magnetic dipole interaction. The rotational strength (which is proportional to the VCD intensity) is a scalar product of the electric and magnetic dipole transition

moments (see Chapter 2). The traditional approach based on the Born-Oppenheimer approximation yields good values for the electric dipole transition moments (IR absorption intensities). However, evaluation of the magnetic dipole transition moment yields no electronic contribution when associated to vibrational transitions, which is physically unacceptable.[45]

In the mid 1980s a theory that permitted a priori prediction of VCD spectra was developed.[46,47] This theory was implemented using ab initio computational methods.[48,49] The first calculations[48,50] were based on Hartree-Fock methods, which rendered insufficiently accurate spectra to permit comparison with experiment.[51] Introduction of post-HF methods such as Møller-Plesset second order perturbation (MP2) provided general improvements in the simulated spectra, however, due the computational cost, this approximation was practically not feasible.[52-54]

The development of density functional theory (DFT) and the introduction of hybrid functionals[55,56] in the early 1990s, meant a breakthrough for the calculation of VCD intensities. DFT methods provide a good accuracy, i.e. spectra comparable with experiment, and even more important, at a moderate computational cost.[57]

1.3 Aim

The scope of this thesis is the development of a methodology at the application level that allows the transparent calculation and measurement of VCD spectra, and ultimately the assignment of the AC.
The implementation of VCD intensities at the DFT level of theory in Gaussian[58], and the advent of the commercialization of VCD spectrometers meant that both theoretical calculations and the experimental methods were not longer restricted to the few specialist in the field. However, for VCD to become a practical technique for interested scientists, development is still needed. For some non-theoretical chemist, the barrier for using quantum chemical techniques is often rather high, and therefore the VCD technique needs to be made more accessible.

The main objectives of this study can be summarized as follows:

- Optimization of the calculation of VCD spectra and performance testing of different computational parameters for medium-sized/large molecules,
- gain insight in the measurement and interpretation of the VCD for organic synthesis and typical pharmaceutical drug compounds,
- introduce a method that allows a thorough, yet transparent and quick comparison of experimental and theoretical spectra.

The structure of this dissertation is organized in two major sections. The first part consists of Chapters 1 through 4. In Chapter 2 and 3 a general review is given of the fundamental principles of VCD as this research area was completely new to our group. In Chapter 2, the theory for the calculation of VCD intensities is outlined, whereas in Chapter 3 an overview of the experimental VCD measurements is given. Both the application of the experiment and theory are an essential part of this thesis. In Chapter 4 the simulation of the VCD spectra is explained. The principles of spectral comparison are introduced and spectral similarity measures are proposed.
In the second part, the experimental results are given in chronological order. Chapter 5 describes the earliest study that was performed in cooperation with Johnson & Johnson Pharmaceutical Research and Development (JNJPRD). Here, the AC of a pharmaceutical compound was validated using VCD. The performance of various basis sets and density functional grids was studied.
In Chapter 6, the ACs of three *as*-hydrindacene compounds were determined, in cooperation with the Department of Organic Chemistry of Ghent University.
Chapter 7 describes an extensive study that was performed on two precursor molecules of a potent CCR2 receptor antagonist (JNJPRD), in order to determine the AC of the latter.
In Chapter 8, the self-association of carboxylic acids is investigated using IR and VCD spectroscopy. Two position isomers of a tetrahydrofuroic acid and a corresponding methyl ester are studied.
In Chapter 9, the enantiomeric similarity index is proposed, which gives information about the similarity of experimental and theoretical spectra.

Throughout Chapter 5–8, different similarity measures are used. As the studies are presented chronologically, an evolution in the similarity measure (which was developed throughout the studies performed in this thesis) can be observed.

In the Appendix, unpublished VCD assignments are presented, which were mostly performed for JNJPRD.

Additionally, due to the extensive amount of comprehensive tables, spectra and other material, a Supplementary Material section is provided which is downloadable from the internet in PDF format:

http://www.quantum.UGent.be/tksup.pdf

1.4 Reference list

1. Caner, H.; Groner, E.; Levy, L.; Agranat, I. *Drug Discovery Today* **2004**, *9*, 105-110.
2. Rouhi, A. M. *Chem. Eng. News* **2004**, *82*, 47-62.
3. Szelenyi, I.; Geisslinger, G.; Polymeropoulos, E.; Paul, W.; Herbst, M.; Brune, K. *Drug. News. Perspect.* **1998**, *11*, 139-160.
4. Ariens, E. J. *Med. Res. Rev.* **1986**, *6*, 451-466.
5. *Chirality* **1992**, *4*, 338-340.
6. Branch, S. K. International Regulation of Chiral Drugs. In *Chiral Separation Techniques*, 2nd ed.; Subramanian, G., Ed.; Wiley-VCH: Weinheim, **2006**; pp 319-342.
7. Adams, S. S.; Bresloff, P.; Mason, C. G. *J. Pharm. Pharmacol.* **1976**, *28*, 256-257.
8. Caldwell, J.; Hutt, A. J.; Fournel-Gigleux, S. *Biochem. Pharmacol.* **1988**, *37*, 105-114.
9. Patrick, G. *Medicinal Chemistry;* 1st ed.; BIOS Scientific Publishers Limited: Oxford, **2001**.
10. Flack, H. D.; Bernardinelli, G. *Acta. Crystallogr. A* **1999**, *55*, 908-915.
11. Rouhi, A. M. *Chem. Eng. News* **2005**, *83*, 32-33.
12. Agranat, I.; Caner, H. *Drug Discovery Today* **1999**, *4*, 313-321.
13. Serilevy, A.; West, S.; Richards, W. G. *J. Med. Chem.* **1994**, *37*, 1727-1732.
14. Agrawal, Y. K.; Patel, R. *Rev. Anal. Chem.* **2002**, *21*, 285-316.
15. Bijvoet, J. M. *Koninkl. Ned. Akad. Wetenschap.* **1949**, *B52*, 313-314.
16. Flack, H. D.; Bernardinelli, G. *J. Appl. Crystallogr.* **2000**, *33*, 1143-1148.
17. Hoye, T. R.; Hamad, A. S. S.; Koltund, O.; Tennakoon, M. A. *Tetrahedron Lett.* **2000**, *41*, 2289-2293.

18. Hoye, T. R.; Koltun, D. O. *J. Am. Chem. Soc.* **1998**, *120*, 4638-4643.

19. Stephens, P. J.; McCann, D. M.; Cheeseman, J. R.; Frisch, M. J. *Chirality* **2005**, *17*, S52-S64.

20. Stephens, P. J.; Devlin, F. J.; Cheeseman, J. R.; Frisch, M. J. *J. Phys. Chem. A* **2001**, *105*, 5356-5371.

21. Polavarapu, P. L.; Petrovic, A.; Wang, F. *Chirality* **2003**, *15*, S143-S149.

22. Stephens, P. J.; Devlin, F. J.; Cheeseman, J. R.; Frisch, M. J.; Rosini, C. *Org. Lett.* **2002**, *4*, 4595-4598.

23. Specht, K. M.; Nam, J.; Ho, D. M.; Berova, N.; Kondru, R. K.; Beratan, D. N.; Wipf, P.; Pascal, R. A.; Kahne, D. *J. Am. Chem. Soc.* **2001**, *123*, 8961-8966.

24. Uray, G.; Verdino, P.; Belaj, F.; Kappe, C. O.; Fabian, W. M. F. *J. Org. Chem.* **2001**, *66*, 6685-6694.

25. Pescitelli, G.; Gabriel, S.; Wang, Y. K.; Fleischhauer, J.; Woody, R. W.; Berova, N. *J. Am. Chem. Soc.* **2003**, *125*, 7613-7628.

26. Vandyck, K.; Matthys, B.; Van der Eycken, J. *Tetrahedron Lett.* **2005**, *46*, 75-78.

27. Berova, N.; Nakanishi, K.; Woody, R. W. *Circular Dichroism: Principles and Applications;* 2nd ed.; Wiley-VCH: New York, **2000**.

28. Kuppens, T.; Bultinck, P.; Langenaeker, W. *Drug Discovery Today: Techn.* **2004**, *1*, 269-275.

29. Nafie, L. A. *Appl. Spectrosc.* **1996**, *50*, A14-A26.

30. Polavarapu, P. L. *Spectroscopy* **1994**, *9*, 48-55.

31. Deutsche, C. W.; Moscowitz, A. *J. Chem. Phys.* **1968**, *49*, 3257-3272.

32. Deutsche, C. W.; Moscowitz, A. *J. Chem. Phys.* **1970**, *53*, 2630-2644.

33. Schellman, J. A. *J. Chem. Phys.* **1973**, *58*, 2882-2886.

34. Schellman, J. A. *J. Chem. Phys.* **1974**, *60*, 343.

35. Holzwart, G.; Chabay, I. *J. Chem. Phys.* **1972**, *57*, 1632-1635.

36. Holzwart, G.; Hsu, E. C.; Mosher, H. S.; Faulkner, T. R.; Moscowit, A. *J. Am. Chem. Soc.* **1974**, *96*, 251-252.

37. Hsu, E. C.; Holzwart, G. *J. Chem. Phys.* **1973**, *59*, 4678-4685.

38. Nafie, L. A.; Keiderling, T. A.; Stephens, P. J. *J. Am. Chem. Soc.* **1976**, *98*, 2715-2723.

39. Nafie, L. A.; Cheng, J. C.; Stephens, P. J. *J. Am. Chem. Soc.* **1975**, *97*, 3842-3843.

40. Lipp, E. D.; Nafie, L. A. *Appl. Spectrosc.* **1984**, *38*, 20-26.

41. Lipp, E. D.; Zimba, C. G.; Nafie, L. A. *Chem. Phys. Lett.* **1982**, *90*, 1-5.

42. Nafie, L. A.; Diem, M. *Appl. Spectrosc.* **1979**, *33*, 130-135.

43. Nafie, L. A.; Diem, M.; Vidrine, D. W. *J. Am. Chem. Soc.* **1979**, *101*, 496-498.

44. Stephens, P. J.; Lowe, M. A. *Annu. Rev. Phys. Chem.* **1985**, *36*, 213-241.

45. Faulkner, T. R.; Marcott, C.; Moscowitz, A.; Overend, J. *J. Am. Chem. Soc.* **1977**, *99*, 8160-8168.

46. Stephens, P. J. *J. Phys. Chem.-US* **1985**, *89*, 748-752.

47. Stephens, P. J. *J. Phys. Chem.-US* **1987**, *91*, 1712-1715.

48. Lowe, M. A.; Stephens, P. J.; Segal, G. A. *Chem. Phys. Lett.* **1986**, *123*, 108-116.

49. Jalkanen, K. J.; Stephens, P. J.; Amos, R. D.; Handy, N. C. *Chem. Phys. Lett.* **1987**, *142*, 153-158.

50. Lowe, M. A.; Segal, G. A.; Stephens, P. J. *J. Am. Chem. Soc.* **1986**, *108*, 248-256.

51. Cheeseman, J. R.; Frisch, M. J.; Devlin, F. J.; Stephens, P. J. *Chem. Phys. Lett.* **1996**, *252*, 211-220.

52. Stephens, P. J.; Jalkanen, K. J.; Devlin, F. J.; Chabalowski, C. F. *J. Phys. Chem.-US* **1993**, *97*, 6107-6110.

53. Devlin, F. J.; Stephens, P. J. *J. Am. Chem. Soc.* **1994**, *116*, 5003-5004.

54. Yang, D. Y.; Rauk, A. *J. Chem. Phys.* **1994**, *100*, 7995-8002.

55. Becke, A. D. *J. Chem. Phys.* **1993**, *98*, 5648-5652.

56. Stephens, P. J.; Devlin, F. J.; Chabalowski, C. F.; Frisch, M. J. *J. Phys. Chem.-US* **1994**, *98*, 11623-11627.

57. Stephens, P. J.; Devlin, F. J. *Chirality* **2000**, *12*, 172-179.

58. Frisch, M. J.; Trucks, G. W.; Schlegel, H. B.; Scuseria, G. E.; Robb, M. A.; Cheeseman, J. R.; Montgomery Jr, J. A.; Vreven, T.; Kudin, K. N.; Burant, J. C.; Millam, J. M.; Iyengar, S. S.; Tomasi, J.; Barone, V.; Mennucci, B.; Cossi, M.; Scalmani, G.; Rega, N.; Petersson, G. A.; Nakatsuji, H.; Hada, M.; Ehara, M.; Toyota, K.; Fukuda, R.; Hasegawa, J.; Ishida, M.; Nakajima, T.; Honda, Y.; Kitao, O.; Nakai, H.; Klene, M.; Li, X.; Knox, J. E.; Hratchian, H. P.; Cross, J. B.; Bakken, V.; Adamo, C.; Jaramillo, J.; Gomperts, R.; Stratmann, R. E.; Yazyev, O.; Austin, A. J.; Cammi, R.; Pomelli, C.; Ochterski, J. W.; Ayala, P. Y.; Morokuma, K.; Voth, G. A.; Salvador, P.; Dannenberg, J. J.; Zakrzewski, V. G.; Dapprich, S.; Daniels, A. D.; Strain, M. C.; Farkas, O.; Malick, D. K.; Rabuck, A. D.; Raghavachari, K.; Foresman, J. B.; Ortiz, J. V.; Cui, Q.; Baboul, A. G.; Clifford, S.; Cioslowski, J.; Stefanov, B. B.; Liu, G.; Liashenko, A.; Piskorz, P.; Komaromi, I.; Martin, R. L.; Fox, D. J.; Keith, T.; Al-Laham, M. A.; Peng, C. Y.; Nanayakkara, A.; Challacombe, M.; Gill, P. M. W.; Johnson, B.; Chen, W.; Wong, M. W.; Gonzalez, C.; Pople, J. A. *Gaussian03*, Revision B5; Gaussian, Inc.: Wallingford CT, **2004**.

2

vibrational circular dichroism intensities

2.1 Introduction

In this chapter, an overview of the theory for the calculation of VCD intensities is given. The main emphasis is given to the derivation of a usable wave function that produces a non-zero electronic contribution to the magnetic dipole transition moment. The vibronic coupling theory of Nafie and Freedman and subsequently, the magnetic field perturbation theory of Stephens are introduced. The implementation and evaluation of the VCD expressions is discussed.

2.2 VCD theory

2.2.1 Problem outline[1,2]

When a molecule is exposed to IR radiation with a frequency $\omega=2\pi\upsilon$, the molecule may undergo a vibrational transition if the energy difference between two vibrational states, say Ψ_i and Ψ_f, is $\hbar\omega$ and the transition dipole moment is non-zero. The transition dipole moment (or electric dipole transition moment) between states Ψ_i and Ψ_f is given as the integral

$$\boldsymbol{\mu}_{\mathrm{elec},if} = \langle \Psi_i \,|\, \boldsymbol{\mu}_{\mathrm{elec}} \,|\, \Psi_f \rangle \tag{2.1}$$

$\boldsymbol{\mu}_{\mathrm{elec}}$ is the electric dipole moment operator and Ψ_i and Ψ_f are the total molecular wave functions representing respectively the vibrational states *i* and *f*. The electric dipole moment operator is the sum of the electron (E) and nuclear (N) operators,

$$\boldsymbol{\mu}_{\mathrm{elec}}=\boldsymbol{\mu}_{\mathrm{elec}}^{\mathrm{E}} + \boldsymbol{\mu}_{\mathrm{elec}}^{\mathrm{N}} \tag{2.2}$$

with

$$\boldsymbol{\mu}_{\mathrm{elec}}^{\mathrm{E}} = -\sum_{d=1}^{n} \boldsymbol{r}_d \tag{2.3}$$

and

$$\boldsymbol{\mu}_{\mathrm{elec}}^{\mathrm{N}} = \sum_{\alpha=1}^{N} Z_\alpha \boldsymbol{R}_\alpha \tag{2.4}$$

Working in atomic units, $\boldsymbol{r}_d$ is the position of the d^{th} electron, and Z_α and $\boldsymbol{R}_\alpha$ are the charge and position of the α^{th} nucleus. *n* and *N* are respectively the number of electrons and nuclei.

The integrated intensity of an IR band is directly proportional to the dipole strength *D*, which is obtained from the square of the electric dipole transition moment

$$D_{if} = \left|\langle \Psi_i \left| \boldsymbol{\mu}_{\text{elec}} \right| \Psi_f \rangle\right|^2 \tag{2.5}$$

The dipole strength is related to the intensity of an IR absorption band[3] through the extinction coefficient ε according to

$$D_{if} = 9.184 \cdot 10^{-39} \int_{band} \varepsilon \frac{d\nu}{\nu} \tag{2.6}$$

where ν is the fundamental transition frequency in wave numbers. The units of D_{if} are esu^2cm^2. The extinction coefficient in molar absorptivity units is related to the absorbance *A* through Beer's Law

$$A = \varepsilon l c \tag{2.7}$$

with *l* the path length (in cm) and *c* the molar concentration.

Vibrational circular dichroism is formally defined as the difference in absorption by a chiral sample of left versus right circularly polarized IR radiation.

$$\Delta A = A_L - A_R \tag{2.8}$$

Where A_L and A_R are the corresponding absorbances.
The intensity of a VCD band is directly proportional to the vibrational rotational strength. For a transition between two vibrational states *i* and *f* of a chiral molecule in its ground electronic state, the rotational strength R_{if} is given by the imaginary part of the scalar product of the electric dipole and magnetic dipole transition moments

$$R_{if} = -\mathrm{i} \langle \Psi_i \left| \boldsymbol{\mu}_{\text{elec}} \right| \Psi_f \rangle \langle \Psi_f \left| \boldsymbol{\mu}_{\text{mag}} \right| \Psi_i \rangle \tag{2.9}$$

The imaginary part has to be taken because $\boldsymbol{\mu}_{\text{mag}}$ is a purely imaginary operator. The magnetic dipole moment operator is the sum of the electron and nuclear operators

$$\boldsymbol{\mu}_{\text{mag}} = \boldsymbol{\mu}_{\text{mag}}^{\text{E}} + \boldsymbol{\mu}_{\text{mag}}^{\text{N}} \tag{2.10}$$

with

$$\boldsymbol{\mu}_{\mathrm{mag}}^{\mathrm{E}} = -\sum_{d=1}^{n} \frac{1}{2c} \boldsymbol{r}_d \times \boldsymbol{p}_d \tag{2.11}$$

and

$$\boldsymbol{\mu}_{\mathrm{mag}}^{\mathrm{N}} = \sum_{\alpha=1}^{N} \frac{Z_\alpha}{2M_\alpha c} \boldsymbol{R}_\alpha \times \boldsymbol{P}_\alpha \tag{2.12}$$

$\boldsymbol{p}_d$ is the momentum of the d^{th} electron, and M_α and $\boldsymbol{P}_\alpha$ are the mass and momentum of the α^{th} nucleus. c in Equations (2.11) and (2.12) is the speed of light.
According to Equation (2.9) the rotational strength is positive or negative depending on the angles between the two transition vectors, i.e., it is positive if the angle between the vectors is less than $\frac{\pi}{2}$, negative if the angle is greater than $\frac{\pi}{2}$ and zero if the angle is equal to $\frac{\pi}{2}$ (or when $\boldsymbol{\mu}_{\mathrm{elec},if}$ or $\boldsymbol{\mu}_{\mathrm{mag},if}$ is zero).
The rotational strength is proportional to the integrated intensity of the VCD absorption band[3] according to

$$R_{if} = 2.296 \cdot 10^{-39} \int_{band} \Delta\varepsilon \frac{d\nu}{\nu} \tag{2.13}$$

The units of R_{if} are esu^{2}cm^2. $\Delta\varepsilon$ is the differential molar absorptivity.

Computation of IR and VCD intensities requires the evaluation of electric and magnetic transition moments. The total vibronic wave function can be approximated as the product of the vibrational (χ_{gv}) and electronic (ψ_g) wave functions using adiabatic Born-Oppenheimer[4,5] (BO) functions

$$\Psi_{gv}(\boldsymbol{r}, \boldsymbol{R}) = \psi_g(\boldsymbol{r}; \boldsymbol{R}) \cdot \chi_{gv}(\boldsymbol{R}) \tag{2.14}$$

with sub indexes g for the electronic state and v for the vibrational state. The electronic wave function depends on the electronic coordinate $\boldsymbol{r}$ and has a parametric dependence on the nuclear coordinate $\boldsymbol{R}$, i.e., ψ_g is a function of $\boldsymbol{r}$ defined for fixed values of $\boldsymbol{R}$. The nuclear motion wave function χ_{gv} is a function of $\boldsymbol{R}$.

For a vibrational transition in the electronic and vibrational ground state (00) to the vibrationally excited state (01), the transition moments can be written as

$$\langle \Psi_{00} \,|\, \boldsymbol{\mu}_{\mathrm{elec}} \,|\, \Psi_{01} \rangle = \big\langle \chi_{00}(\boldsymbol{R}) \big| \big\langle \psi_0(\boldsymbol{r};\boldsymbol{R}) \big| \boldsymbol{\mu}^{\mathrm{E}}_{\mathrm{elec}}(\boldsymbol{r}) \big| \psi_0(\boldsymbol{r};\boldsymbol{R}) \big\rangle + \boldsymbol{\mu}^{\mathrm{N}}_{\mathrm{elec}}(\boldsymbol{R}) \big| \chi_{01}(\boldsymbol{R}) \big\rangle \tag{2.15}$$

$$\begin{aligned} \big\langle \Psi_{00} \big| \boldsymbol{\mu}_{\mathrm{mag}} \big| \Psi_{01} \big\rangle &= \big\langle \chi_{00}(\boldsymbol{R}) \big| \big\langle \psi_0(\boldsymbol{r};\boldsymbol{R}) \big| \boldsymbol{\mu}^{\mathrm{E}}_{\mathrm{mag}}(\boldsymbol{r}) \big| \psi_0(\boldsymbol{r};\boldsymbol{R}) \big\rangle + \boldsymbol{\mu}^{\mathrm{N}}_{\mathrm{mag}}(\boldsymbol{R}) \big| \chi_{01}(\boldsymbol{R}) \big\rangle \\ &= \big\langle \chi_{00}(\boldsymbol{R}) \big| \boldsymbol{\mu}^{\mathrm{N}}_{\mathrm{mag}}(\boldsymbol{R}) \big| \chi_{01}(\boldsymbol{R}) \big\rangle \end{aligned} \tag{2.16}$$

Because of the hermitian and imaginary nature of $\boldsymbol{\mu}^{\mathrm{E}}_{\mathrm{mag}}$ together with the fact that the singlet non-degenerate electronic ground state ψ_0 can be chosen to be real, the electronic contribution to the magnetic dipole transition moment is cancelled,[6] that is

$$\big\langle \psi_0 \big| \boldsymbol{\mu}^{\mathrm{E}}_{\mathrm{mag}} \big| \psi_0 \big\rangle = 0 \tag{2.17}$$

In order to include the important contributions from the electrons to the magnetic dipole transition moment, one has to choose either to make further approximations to the magnetic dipole operator yielding effective non-vanishing magnetic transition moments, or to go beyond the BO approximation. Various approximations[7] are results of the former approach, which will not be discussed here. In the latter approach, more accurate wave functions are obtained by adding some corrections to the BO wave functions.

2.2.2 Born-Oppenheimer approximation and beyond[2,8,9]

The total molecular Hamiltonian *H* (2.18) is defined as the sum of the nuclear and electronic kinetic energy operator and the potential energy denoted respectively as T_{N}, T_{E} and $U(\boldsymbol{r},\boldsymbol{Q})$.

$$H(\boldsymbol{r},\boldsymbol{Q}) = T_{\mathrm{E}}(\boldsymbol{r}) + U(\boldsymbol{r},\boldsymbol{Q}) + T_{\mathrm{N}}(\boldsymbol{Q}) \tag{2.18}$$

with

$$T_{\mathrm{N}} = -\frac{\hbar^2}{2}\sum_{\alpha=1}^{N}\frac{1}{M_\alpha}\nabla_\alpha^2 = \frac{1}{2}\sum_{\alpha=1}^{N}\frac{\boldsymbol{P}_\alpha^2}{M_\alpha} \tag{2.19}$$

or in mass-weighted coordinates (see further)

$$T_{\mathrm{N}} = -\frac{\hbar^2}{2}\sum_{k=1}^{3N-6}\nabla_k^2 = -\frac{\hbar^2}{2}\sum_{k=1}^{3N-6}\frac{\partial^2}{\partial \boldsymbol{Q}_k^2} \tag{2.20}$$

and

$$T_{\mathrm{E}} = -\frac{\hbar^2}{2}\sum_{d}\nabla_d^2 = \frac{1}{2}\sum_{d}\boldsymbol{p}_d^2 \tag{2.21}$$

The potential energy term $U(\boldsymbol{r},\boldsymbol{Q})$ incorporates the nuclear-nuclear repulsion V_{NN}, the nuclear-electron attraction V_{NE} and the electron-electron interaction V_{EE}.

$$U(\boldsymbol{r},\boldsymbol{Q}) = V_{\mathrm{NN}} + V_{\mathrm{NE}} + V_{\mathrm{EE}} \tag{2.22}$$

The electronic Hamiltonian can be defined as the sum of the electronic kinetic energy operator and the potential energy term,

$$H_{\mathrm{E}}(\boldsymbol{r};\boldsymbol{Q}) = T_{\mathrm{E}}(\boldsymbol{r}) + U(\boldsymbol{r},\boldsymbol{Q}) \tag{2.23}$$

The complete Schrödinger equation can be written as:

$$H\Psi(\boldsymbol{r},\boldsymbol{Q}) = \varepsilon\Psi(\boldsymbol{r},\boldsymbol{Q}) \tag{2.24}$$

The nuclear coordinates are given in terms of mass-weighted normal coordinates[5] $\boldsymbol{Q_k} = \{\boldsymbol{Q}_1,\boldsymbol{Q}_2,\ldots,\boldsymbol{Q}_{3N\text{-}6}\}$ which can be related to the displacement coordinates $\sqrt{M_\alpha}\left(\boldsymbol{R}_\alpha - \boldsymbol{R}_\alpha^0\right)$ via the linear transformation

$$\boldsymbol{R}_\alpha = \boldsymbol{R}_\alpha^0 + \sum_{k=1}^{3N-6}\boldsymbol{S}_{\alpha,k}\boldsymbol{Q}_k \tag{2.25}$$

$\boldsymbol{R}_\alpha$ is the position vector of nucleus α (α=1,N) and $\boldsymbol{R}_\alpha^0$ is its equilibrium position. $\boldsymbol{S}_{\alpha,k}$ is the displacement vector of the α^{th} atom, incorporating the factor $\frac{1}{\sqrt{M_\alpha}}$.

If it is assumed that the solutions of the electronic Schrödinger equation

$$H_{\mathrm{E}}\psi_g(\boldsymbol{r};\boldsymbol{Q}) = E_g(\boldsymbol{Q})\psi_g(\boldsymbol{r};\boldsymbol{Q}) \tag{2.26}$$

are known for sets of fixed values of $\boldsymbol{Q}$, each set specifying a molecular configuration, the total wave function can be written as a linear combination of complete set of wave functions $\{\psi_g(\boldsymbol{r};\boldsymbol{Q})\}$.[11]

$$\Psi_g(\boldsymbol{r},\boldsymbol{Q}) = \sum_g \chi_g(\boldsymbol{Q})\psi_g(\boldsymbol{r};\boldsymbol{Q}) \tag{2.27}$$

The total Schrödinger equation can then be written as

$$(H_{\mathrm{E}} + T_{\mathrm{N}})\sum_g \chi_g(\boldsymbol{Q})\psi_g(\boldsymbol{r};\boldsymbol{Q}) = \varepsilon\sum_g \chi_g(\boldsymbol{Q})\psi_g(\boldsymbol{r};\boldsymbol{Q}) \tag{2.28}$$

and simplifying the expression

$$\sum_g (H_{\mathrm{E}} + T_{\mathrm{N}} - \varepsilon)\chi_g(\boldsymbol{Q})\psi_g(\boldsymbol{r};\boldsymbol{Q}) = 0 \tag{2.29}$$

The nuclear kinetic operator gives rise to the three following terms

$$\begin{aligned} T_{\mathrm{N}}\psi(\boldsymbol{r};\boldsymbol{Q})\chi(\boldsymbol{Q}) = (T_{\mathrm{N}}\psi(\boldsymbol{r};\boldsymbol{Q}))\chi(\boldsymbol{Q}) + \psi(\boldsymbol{r};\boldsymbol{Q})(T_{\mathrm{N}}\chi(\boldsymbol{Q})) \\ -\hbar^2\sum_k \nabla_k\psi(\boldsymbol{r};\boldsymbol{Q})\nabla_k\chi(\boldsymbol{Q}) \end{aligned} \tag{2.30}$$

The introduction of Equation (2.30) in (2.29) yields

$$\sum_g \left(\psi_g(\boldsymbol{r};\boldsymbol{Q})\left(E_g + T_{\mathrm{N}} - \varepsilon\right) + T_{\mathrm{N}}\psi_g(\boldsymbol{r};\boldsymbol{Q}) - \hbar^2\sum_k \nabla_k\psi_g(\boldsymbol{r};\boldsymbol{Q})\nabla_k \right)\chi_g(\boldsymbol{Q}) = 0 \tag{2.31}$$

If this expression is multiplied with $\psi_e^*(\boldsymbol{r};\boldsymbol{Q})$ and integrating over the electronic coordinates, based on the orthonormality of the electronic eigenfunctions it can be written that

$$\sum_g \begin{pmatrix} \delta_{eg}\left(E_g + T_{\mathrm{N}} - \varepsilon\right) + \langle\psi_e(\boldsymbol{r};\boldsymbol{Q})|T_{\mathrm{N}}\left|\psi_g(\boldsymbol{r};\boldsymbol{Q})\right\rangle - \\ \hbar^2\sum_k \langle\psi_e(\boldsymbol{r};\boldsymbol{Q})|\nabla_k\left|\psi_g(\boldsymbol{r};\boldsymbol{Q})\right\rangle\nabla_k \end{pmatrix}\chi_g(\boldsymbol{Q}) = 0 \tag{2.32}$$

Separation of diagonal and non-diagonal terms gives

$$\begin{aligned} &((E_e + T_{\mathrm{N}} - \varepsilon) + \langle\psi_e(\boldsymbol{r};\boldsymbol{Q})|T_{\mathrm{N}}\left|\psi_e(\boldsymbol{r};\boldsymbol{Q})\right\rangle)\chi_e(\boldsymbol{Q}) = \\ &-\sum_{g\neq e}\left(\langle\psi_e(\boldsymbol{r};\boldsymbol{Q})|T_{\mathrm{N}}\left|\psi_g(\boldsymbol{r};\boldsymbol{Q})\right\rangle - \hbar^2\sum_k \langle\psi_e(\boldsymbol{r};\boldsymbol{Q})|\nabla_k\left|\psi_g(\boldsymbol{r};\boldsymbol{Q})\right\rangle\nabla_k\right)\chi_g(\boldsymbol{Q}) \end{aligned} \tag{2.33}$$

The right-hand side of Equation (2.33) represents the coupling between electronic functions through nuclear motion. These terms are neglected in the adiabatic approximation. In adiabatic motion, electrons do not make transition from one electronic state to the other. Only the diagonal terms remain, i.e.,

$$((E_e(\boldsymbol{Q}) + T_{\mathrm{N}} - \varepsilon) + \langle\psi_e(\boldsymbol{r};\boldsymbol{Q})|T_{\mathrm{N}}\left|\psi_e(\boldsymbol{r};\boldsymbol{Q})\right\rangle)\chi_e(\boldsymbol{Q}) = 0 \tag{2.34}$$

Which can also be written as

$$(T_{\mathrm{N}} + [E_e(\boldsymbol{Q}) + \langle\psi_e(\boldsymbol{r};\boldsymbol{Q})|T_{\mathrm{N}}\left|\psi_e(\boldsymbol{r};\boldsymbol{Q})\right\rangle])\chi_{ei}(\boldsymbol{Q}) = \varepsilon_{ei}\chi_{ei}(\boldsymbol{Q}) \tag{2.35}$$

where

$$E_e(\boldsymbol{Q}) + \langle\psi_e(\boldsymbol{r};\boldsymbol{Q})|T_{\mathrm{N}}\left|\psi_e(\boldsymbol{r};\boldsymbol{Q})\right\rangle \tag{2.36}$$

represents the potential for nuclear motion.

In Equation (2.35) a sub index *i* is introduced to distinguish the different eigenvalues and eigenfunctions for a given *e*.

Neglecting the non-diagonal terms in Equation (2.33) corresponds to expressing the total wave function as an adiabatic product,

$$\Psi_{ei}(\boldsymbol{r},\boldsymbol{Q}) = \psi_e(\boldsymbol{r};\boldsymbol{Q})\chi_{ei}(\boldsymbol{Q}) \tag{2.37}$$

In what is usually called the Born-Oppenheimer (BO) approximation, the expectation value of the nuclear kinetic energy over the electronic wave function given as the second term in Equation (2.36) is neglected. This is usually a good approximation because of the small electron to nuclear mass ratio. Within the BO approximation one can write the Schrödinger equation for the nuclear movement as

$$\left(T_{\mathrm{N}} + E_g(\boldsymbol{Q})\right)\chi_{gi}(\boldsymbol{Q}) = \varepsilon_{gi}\chi_{gi}(\boldsymbol{Q}) \tag{2.38}$$

The vibrational wave functions are eigenfunctions of $\left(T_{\mathrm{N}} + E_g(\boldsymbol{Q})\right)$ with energy ε_{gi}. The electronic energy $E_g(\boldsymbol{Q})$ serves as the potential for nuclear motion. The vibrational wave function $\chi_{gi}(\boldsymbol{Q})$ applies to the i^{th} level of a vibration, for the g^{th} electronic state. It is supposed that this vibration corresponds to normal mode $\boldsymbol{Q}_j$ and all other normal vibrations are unaltered in the vibrational transition.

The BO wave functions can be refined by retrieving the neglected terms from the nuclear kinetic energy

$$T'_{\mathrm{N}} = -\hbar^2 \sum_k \left(\frac{\partial}{\partial \boldsymbol{Q}_k}\right)_{\mathrm{E}} \left(\frac{\partial}{\partial \boldsymbol{Q}_k}\right)_{\mathrm{N}} - \frac{\hbar^2}{2}\sum_k \left(\frac{\partial^2}{\partial \boldsymbol{Q}_k^2}\right)_{\mathrm{E}} \tag{2.39}$$

The differentiation subscripts E and N in Equation (2.39) indicate on which wave function the differential operator will operate.

One can use T'_{N} in Equation (2.39) as a perturbation operator to refine the BO wave functions,

$$\Psi_{gi}(\boldsymbol{r},\boldsymbol{Q}) = \psi_g(\boldsymbol{r};\boldsymbol{Q})\chi_{gi}(\boldsymbol{Q}) + \sum_{ev\neq gi} a_{ev,gi}(\boldsymbol{Q})\psi_e(\boldsymbol{r};\boldsymbol{Q})\chi_{ev}(\boldsymbol{Q}) \tag{2.40}$$

where the coefficients are defined, on the basis of Rayleigh-Schrödinger perturbation theory, as

$$a_{ev,gi}(\boldsymbol{Q}) = \frac{\langle \psi_e(\boldsymbol{r};\boldsymbol{Q})\chi_{ev}(\boldsymbol{Q}) | T_N' | \psi_g(\boldsymbol{r};\boldsymbol{Q})\chi_{gi}(\boldsymbol{Q})\rangle}{E_{gi}(\boldsymbol{Q}) - E_{ev}(\boldsymbol{Q})} \tag{2.41}$$

This approach is the non-adiabatic or BO vibronic coupling mechanism.

The adiabatic electronic wave function ψ_g can be expanded as a function of its nuclear dependence using as a starting point the crude adiabatic approximation.[5,10] Here, the crude adiabatic wave functions are written as

$$\Psi_{gi}(\boldsymbol{r},\boldsymbol{Q}) = \psi_g(\boldsymbol{r};\boldsymbol{Q}_0)\chi_{gi}(\boldsymbol{Q}) \tag{2.42}$$

The only nuclear dependence is now contained in the vibrational wave function $\chi_{gi}(\boldsymbol{Q})$ which is subtly different compared to its adiabatic counterpart because ψ_g is defined here as nuclear independent.
Using perturbation theory the nuclear dependence is reintroduced in the electronic wave function,

$$\psi_g(\boldsymbol{r};\boldsymbol{Q}) = \psi_g(\boldsymbol{r};\boldsymbol{Q}_0) + \sum_{e\neq g}\sum_k \frac{\left\langle \psi_e(\boldsymbol{r};\boldsymbol{Q}_0)\left|\frac{\partial U(\boldsymbol{r},\boldsymbol{Q})}{\partial \boldsymbol{Q}_k}\right|_{\boldsymbol{Q}=\boldsymbol{Q}_0}\left|\psi_g(\boldsymbol{r};\boldsymbol{Q}_0)\right\rangle}{E_g(\boldsymbol{Q}_0) - E_e(\boldsymbol{Q}_0)} \cdot \boldsymbol{Q}_k\psi_e(\boldsymbol{r};\boldsymbol{Q}_0) \tag{2.43}$$

The notation $\left.\frac{\partial}{\partial \boldsymbol{Q}_k}\right|_{\boldsymbol{Q}=\boldsymbol{Q}_0}$ indicates that the derivatives are evaluated at equilibrium geometry.

Equation (2.43) can be written more elegantly as

$$\psi_g(\boldsymbol{r};\boldsymbol{Q}) = \psi_g(\boldsymbol{r};\boldsymbol{Q}_0) + \sum_k \left.\frac{\partial\psi_g(\boldsymbol{r};\boldsymbol{Q})}{\partial \boldsymbol{Q}_k}\right|_{\boldsymbol{Q}=\boldsymbol{Q}_0} \cdot \boldsymbol{Q}_k \tag{2.44}$$

This expression can be interpreted as a Taylor expansion about the equilibrium geometrie of the electronic wave function, truncated to the linear term. This equation is also known as the Herzberg-Teller coupling[12] or adiabatic coupling as electron and nuclear wave functions can still be separated,

$$\Psi_{gi}(\boldsymbol{r},\boldsymbol{Q}) = \left(\psi_g(\boldsymbol{r};\boldsymbol{Q}_0) + \sum_k \frac{\partial \psi_g(\boldsymbol{r};\boldsymbol{Q})}{\partial \boldsymbol{Q}_k}\bigg|_{\boldsymbol{Q}=\boldsymbol{Q}_0} \cdot \boldsymbol{Q}_k \right) \chi_{gi}(\boldsymbol{Q}) \tag{2.45}$$

Using Equations (2.44), (2.40) and (2.41) and neglecting higher order terms one obtains following expression for the wave function of interest for VCD,

$$\begin{aligned} \Psi_{gi} = {} & \psi_g(\boldsymbol{r};\boldsymbol{Q}_0)\chi_{gi}(\boldsymbol{Q}) + \sum_k \frac{\partial \psi_g(\boldsymbol{r};\boldsymbol{Q})}{\partial \boldsymbol{Q}_k}\bigg|_{\boldsymbol{Q}=\boldsymbol{Q}_0} \cdot \boldsymbol{Q}_k \chi_{gi}(\boldsymbol{Q}) \\ & + \hbar^2 \sum_k \sum_{ev \neq gi} \frac{\left\langle \psi_e(\boldsymbol{r};\boldsymbol{Q}_0) \middle| \frac{\partial \psi_g(\boldsymbol{r};\boldsymbol{Q})}{\partial \boldsymbol{Q}_k}\Big|_{\boldsymbol{Q}=\boldsymbol{Q}_0} \right\rangle \left\langle \chi_{ev}(\boldsymbol{Q}) \middle| \frac{\partial \chi_{gi}(\boldsymbol{Q})}{\partial \boldsymbol{Q}_k} \right\rangle}{E_{ev}(\boldsymbol{Q}) - E_{gi}(\boldsymbol{Q})} \psi_e(\boldsymbol{r};\boldsymbol{Q}_0)\chi_{ev}(\boldsymbol{Q}) \end{aligned} \tag{2.46}$$

2.2.3 Vibronic coupling transition moments[2,8]

In the previous paragraph a BO corrected wave function was derived using adiabatic and non-adiabatic coupling. If we introduce a general operator θ, which represents a radiation field interaction operator, the transition moment between vibronic states *gi* →*gf* can be written as $\langle \Psi_{gi} | \theta | \Psi_{gf} \rangle$. θ can be written as the sum of an electronic and a nuclear part

$$\theta = \theta^{\mathrm{N}} + \theta^{\mathrm{E}} \tag{2.47}$$

The nuclear terms of the transition moment, i.e., $\langle \Psi_{gi} | \theta^{\mathrm{N}} | \Psi_{gf} \rangle$ can be written as

$$\langle \Psi_{gi} | \theta^{\mathrm{N}} | \Psi_{gf} \rangle = \langle \chi_{gi}(\boldsymbol{Q}) | \theta^{\mathrm{N}} | \chi_{gf}(\boldsymbol{Q}) \rangle \tag{2.48}$$

An electronic contribution to the transition moment can be introduced using the wave functions as given in (2.46). Retaining only first order terms, the electronic transition moment $\langle \Psi_{gi} | \theta^{\mathrm{E}} | \Psi_{gf} \rangle$ can be written as

$$
\begin{aligned}
&\langle \Psi_{gi} | \theta^{\mathrm{E}} | \Psi_{gf} \rangle = \langle \psi_g(\boldsymbol{r};\boldsymbol{Q}_0)\chi_{gi}(\boldsymbol{Q}) | \theta^{\mathrm{E}} | \psi_g(\boldsymbol{r};\boldsymbol{Q}_0)\chi_{gf}(\boldsymbol{Q}) \rangle \\
&+\left\langle \psi_g(\boldsymbol{r};\boldsymbol{Q}_0)\chi_{gi}(\boldsymbol{Q}) \middle| \theta^{\mathrm{E}} \middle| \sum_k \frac{\partial \psi_g(\boldsymbol{r};\boldsymbol{Q})}{\partial \boldsymbol{Q}_k}\bigg|_{\boldsymbol{Q}=\boldsymbol{Q}_0} \cdot \boldsymbol{Q}_k \cdot \chi_{gf}(\boldsymbol{Q}) \right\rangle \\
&+\left\langle \sum_k \frac{\partial \psi_g(\boldsymbol{r};\boldsymbol{Q}_0)}{\partial \boldsymbol{Q}_k}\bigg|_{\boldsymbol{Q}=\boldsymbol{Q}_0} \cdot \boldsymbol{Q}_k \cdot \chi_{gi}(\boldsymbol{Q}) \middle| \theta^{\mathrm{E}} \middle| \psi_g(\boldsymbol{r};\boldsymbol{Q}_0)\chi_{gf}(\boldsymbol{Q}) \right\rangle \\
&+\hbar^2 \sum_k \sum_{ev \neq gf} \frac{\left\langle \psi_e(\boldsymbol{r};\boldsymbol{Q}_0) \middle| \frac{\partial \psi_g(\boldsymbol{r};\boldsymbol{Q})}{\partial \boldsymbol{Q}_k}\Big|_{\boldsymbol{Q}=\boldsymbol{Q}_0} \right\rangle \left\langle \chi_{ev}(\boldsymbol{Q}) \middle| \frac{\partial \chi_{gf}(\boldsymbol{Q})}{\partial \boldsymbol{Q}_k} \right\rangle}{E_{ev}(\boldsymbol{Q}) - E_{gf}(\boldsymbol{Q})} \langle \psi_g(\boldsymbol{r};\boldsymbol{Q}_0)\chi_{gi}(\boldsymbol{Q}) | \theta^{\mathrm{E}} | \psi_e(\boldsymbol{r};\boldsymbol{Q}_0)\chi_{ev}(\boldsymbol{Q}) \rangle \\
&+\hbar^2 \sum_k \sum_{ev \neq gi} \frac{\left\langle \psi_e(\boldsymbol{r};\boldsymbol{Q}_0) \middle| \frac{\partial \psi_g(\boldsymbol{r};\boldsymbol{Q})}{\partial \boldsymbol{Q}_k}\Big|_{\boldsymbol{Q}=\boldsymbol{Q}_0} \right\rangle \left\langle \chi_{ev}(\boldsymbol{Q}) \middle| \frac{\partial \chi_{gi}(\boldsymbol{Q})}{\partial \boldsymbol{Q}_k} \right\rangle}{E_{ev}(\boldsymbol{Q}) - E_{gi}(\boldsymbol{Q})} \langle \psi_e(\boldsymbol{r};\boldsymbol{Q}_0)\chi_{ev}(\boldsymbol{Q}) | \theta^{\mathrm{E}} | \psi_g(\boldsymbol{r};\boldsymbol{Q}_0)\chi_{gf}(\boldsymbol{Q}) \rangle
\end{aligned}
\tag{2.49}
$$

The first term of Equation (2.49) is not expected to contribute to the vibrational transition moment as no overlap is possible between the vibrational levels of the same electronic state. As a consequence this term vanishes. The remaining terms contribute nuclear dependence to the vibrational integrals through $\boldsymbol{Q}$ and $\frac{\partial}{\partial \boldsymbol{Q}}$. If the assumption is made that the energy difference between electronic-vibronic levels are approximately equal to the separation between electronic levels regardless of the vibrational excitations, it can be written that

$$
E_{ev}(\boldsymbol{Q}) - E_{gf}(\boldsymbol{Q}) = E_e(\boldsymbol{Q}_0) - E_g(\boldsymbol{Q}_0) \tag{2.50}
$$

This approximation is based on the fact that energy differences between vibrational states are much smaller than between electronic states. Under such an approximation one is able to formally close the sum over the vibronic wave functions in the fourth and fifth terms in (2.49) and it can be written as

$$
\begin{aligned}
&\langle \Psi_{gi} | \theta^{\mathrm{E}} | \Psi_{gf} \rangle = \\
&\left(\left\langle \psi_g(\boldsymbol{r};\boldsymbol{Q}_0) \middle| \theta^{\mathrm{E}} \middle| \sum_k \frac{\partial \psi_g(\boldsymbol{r};\boldsymbol{Q})}{\partial \boldsymbol{Q}_k}\bigg|_{\boldsymbol{Q}=\boldsymbol{Q}_0} \right\rangle + \left\langle \sum_k \frac{\partial \psi_g(\boldsymbol{r};\boldsymbol{Q})}{\partial \boldsymbol{Q}_k}\bigg|_{\boldsymbol{Q}=\boldsymbol{Q}_0} \middle| \theta^{\mathrm{E}} \middle| \psi_g(\boldsymbol{r};\boldsymbol{Q}_0) \right\rangle \right) \langle \chi_{gi}(\boldsymbol{Q}) | \boldsymbol{Q} | \chi_{gf}(\boldsymbol{Q}) \rangle \\
&+\hbar^2 \sum_k \sum_{e \neq g} \frac{\left\langle \psi_e(\boldsymbol{r};\boldsymbol{Q}_0) \middle| \frac{\partial \psi_g(\boldsymbol{r};\boldsymbol{Q})}{\partial \boldsymbol{Q}_k}\Big|_{\boldsymbol{Q}=\boldsymbol{Q}_0} \right\rangle \left\langle \chi_{gi}(\boldsymbol{Q}) \middle| \frac{\partial \chi_{gf}(\boldsymbol{Q})}{\partial \boldsymbol{Q}_k} \right\rangle}{E_e(\boldsymbol{Q}_0) - E_g(\boldsymbol{Q}_0)} \langle \psi_g(\boldsymbol{r};\boldsymbol{Q}_0) | \theta^{\mathrm{E}} | \psi_e(\boldsymbol{r};\boldsymbol{Q}_0) \rangle \\
&+\hbar^2 \sum_k \sum_{e \neq g} \frac{\left\langle \psi_g(\boldsymbol{r};\boldsymbol{Q}_0) \middle| \frac{\partial \psi_e(\boldsymbol{r};\boldsymbol{Q})}{\partial \boldsymbol{Q}_k}\Big|_{\boldsymbol{Q}=\boldsymbol{Q}_0} \right\rangle \left\langle \chi_{gf}(\boldsymbol{Q}) \middle| \frac{\partial \chi_{gi}(\boldsymbol{Q})}{\partial \boldsymbol{Q}_k} \right\rangle}{E_e(\boldsymbol{Q}_0) - E_g(\boldsymbol{Q}_0)} \langle \psi_e(\boldsymbol{r};\boldsymbol{Q}_0) | \theta^{\mathrm{E}} | \psi_g(\boldsymbol{r};\boldsymbol{Q}_0) \rangle
\end{aligned}
\tag{2.51}
$$

Equation (2.51) represents the principal sources of vibronic coupling in molecules, i.e., the first term is traditionally[8] regarded as adiabatic whereas the last two terms are considered non-adiabatic and beyond the BO approximation.

At this stage, the interaction operator introduced in Equation (2.47) can be specified so that for both the electric and magnetic dipole transition moment equations can be put forward.
If Equation (2.51) is evaluated using the electric dipole operator, that is, if $\theta^{\mathrm{E}} = \boldsymbol{\mu}_{\mathrm{elec}}^{\mathrm{E}}$ the non-adiabatic terms will cancel. This is due to the anti-symmetric property of the $\frac{\partial}{\partial \boldsymbol{Q}}$ operator with respect to the interchange of wave functions

$$\left\langle \chi_{gi} \left| \frac{\partial}{\partial \boldsymbol{Q}} \right| \chi_{gf} \right\rangle = -\left\langle \chi_{gf} \left| \frac{\partial}{\partial \boldsymbol{Q}} \right| \chi_{gi} \right\rangle \tag{2.52}$$

Also, because $\boldsymbol{\mu}_{\mathrm{elec}}^{\mathrm{E}}$ is hermitian and it can be written that

$$\left\langle \psi_g \left| \boldsymbol{\mu}_{\mathrm{elec}}^{\mathrm{E}} \right| \psi_e \right\rangle = \left\langle \psi_e \left| \boldsymbol{\mu}_{\mathrm{elec}}^{\mathrm{E}} \right| \psi_g \right\rangle \tag{2.53}$$

For the same reason the adiabatic terms are equal. Combining Equations (2.48) and (2.51) the expression for the electric dipole transition moment becomes

$$\begin{aligned} \left\langle \Psi_{gi} \left| \boldsymbol{\mu}_{\mathrm{elec}} \right| \Psi_{gf} \right\rangle = {} & \left\langle \chi_{gi}(\boldsymbol{Q}) \left| \boldsymbol{\mu}_{\mathrm{elec}}^{\mathrm{N}} \right| \chi_{gf}(\boldsymbol{Q}) \right\rangle \\ & + 2 \left\langle \psi_g(\boldsymbol{r};\boldsymbol{Q}_0) \left| \boldsymbol{\mu}_{\mathrm{elec}}^{\mathrm{E}} \left| \sum_k \frac{\partial \psi_g(\boldsymbol{r};\boldsymbol{Q})}{\partial \boldsymbol{Q}_k} \right|_{\boldsymbol{Q}=\boldsymbol{Q}_0} \right\rangle \left\langle \chi_{gi}(\boldsymbol{Q}) \left| \boldsymbol{Q} \right| \chi_{gf}(\boldsymbol{Q}) \right\rangle \end{aligned} \tag{2.54}$$

As indicated before, the non-adiabatic terms cancel and Equation (2.54) is entirely attributable to Herzberg-Teller coupling. This means that the electronic contribution to the induced dipole moment, which is the result of charge distribution changes induced by vibrational transitions, can be properly described by introducing explicit nuclear position dependence to the ground electronic wave function.

For the magnetic dipole transition moment the first two terms will cancel because of the anti-symmetric property of the integrals by wave function interchange because $\boldsymbol{\mu}_{\mathrm{mag}}^{\mathrm{E}}$ is hermitian and imaginary

$$\left\langle \psi_g \left| \boldsymbol{\mu}_{\mathrm{mag}}^{\mathrm{E}} \right| \psi_e \right\rangle = -\left\langle \psi_e \left| \boldsymbol{\mu}_{\mathrm{mag}}^{\mathrm{E}} \right| \psi_g \right\rangle \tag{2.55}$$

The non-adiabatic terms are equal, so the expression of the magnetic dipole transitions becomes

$$\begin{aligned}\left\langle \Psi_{gi} \left| \boldsymbol{\mu}_{\mathrm{mag}} \right| \Psi_{gf} \right\rangle &= \left\langle \chi_{gi}(\boldsymbol{Q}) \right| \boldsymbol{\mu}_{\mathrm{mag}}^{\mathrm{N}} \left| \chi_{gf}(\boldsymbol{Q}) \right\rangle \\ &+ 2\hbar^2 \sum_k \sum_{e \neq g} \frac{\left\langle \psi_g(\boldsymbol{r};\boldsymbol{Q}_0) \right| \boldsymbol{\mu}_{\mathrm{mag}}^{\mathrm{E}} \left| \psi_e(\boldsymbol{r};\boldsymbol{Q}_0) \right\rangle \left\langle \psi_e(\boldsymbol{r};\boldsymbol{Q}_0) \left| \frac{\partial \psi_g(\boldsymbol{r};\boldsymbol{Q})}{\partial \boldsymbol{Q}_k} \right|_{\boldsymbol{Q}=\boldsymbol{Q}_0} \right\rangle}{E_e(\boldsymbol{Q}_0) - E_g(\boldsymbol{Q}_0)} \left\langle \chi_{gi}(\boldsymbol{Q}) \left| \frac{\partial \chi_{gf}(\boldsymbol{Q})}{\partial \boldsymbol{Q}_k} \right. \right\rangle\end{aligned} \tag{2.56}$$

In this expression a non-vanishing electronic contribution to the magnetic dipole moment is obtained which comes from BO coupling. In Equation (2.56) it can be seen that excited electronic states are involved ("sum over states"). The electronic part of the induced magnetic moment is caused by the changes of the motion state of the electrons which are a direct response to the changes in the nuclear momentum. The response to the ground electronic state is described by mixing excited electronic states into the unperturbed ground electronic state wave functions.[2]

Expressions (2.54) and (2.56) describe the electronic and magnetic dipole transitions moments within the vibronic coupling theory (VCT) of Nafie and Freedman.[8] Evaluation of the magnetic dipole transition moment as expressed in (2.56) has been implemented at ab initio level.[13] Results from this implementation, however, do not seem to converge with increasing basis set size.[14]

In this work, a different approach is used for the evaluation of the magnetic dipole transition moment, i.e., the magnetic field perturbation theory of Stephens[9] which is discussed further.

First, expressions for the evaluation of the electronic dipole transition moment are derived.

2.2.4 Atomic polar tensors[2,9]

For the electronic dipole transition moment a more classical approach can be used which yields an expression formally equal to Expression (2.54) for the electronic dipole transition moment within the vibronic coupling theory.

The quantity expressed in (2.15), i.e., $\left\langle \psi_g \left| \boldsymbol{\mu}_{\mathrm{elec}}^{\mathrm{E}} \right| \psi_g \right\rangle + \boldsymbol{\mu}_{\mathrm{elec}}^{\mathrm{N}} \equiv \boldsymbol{\mu}_{\mathrm{elec}}^{g}$, is the adiabatic electric dipole moment of the ground state. Its nuclear coordinate dependence, in terms of a particular vibrational normal mode, may be expressed as a Taylor expansion about the equilibrium geometry, to the first order:

$$\boldsymbol{\mu}_{\mathrm{elec}}^{g} = \boldsymbol{\mu}_{\mathrm{elec}}^{g}\big|_{\boldsymbol{Q}=\boldsymbol{Q}_0} + \left.\frac{\partial \boldsymbol{\mu}_{\mathrm{elec}}^{g}}{\partial \boldsymbol{Q}}\right|_{\boldsymbol{Q}=\boldsymbol{Q}_0} \cdot \boldsymbol{Q} \tag{2.57}$$

$$\begin{aligned} \left\langle \Psi_{gi} \left| \boldsymbol{\mu}_{\mathrm{elec}} \right| \Psi_{gf} \right\rangle &= \left.\frac{\partial \boldsymbol{\mu}_{\mathrm{elec}}^{g}}{\partial \boldsymbol{Q}}\right|_{\boldsymbol{Q}=\boldsymbol{Q}_0} \left\langle \chi_{gi}(\boldsymbol{Q}) \middle| \boldsymbol{Q}_j \middle| \chi_{gf}(\boldsymbol{Q}) \right\rangle \\ &= \sqrt{\frac{\hbar}{2\omega_j}} \sum_{\alpha} \left.\frac{\partial \boldsymbol{\mu}_{\mathrm{elec}}^{g}}{\partial \boldsymbol{R}_{\alpha}}\right|_{\boldsymbol{R}=\boldsymbol{R}_0} \boldsymbol{S}_{\alpha,j} \end{aligned} \tag{2.58}$$

Writing it in vector components, with β the Cartesian component of the electric field and λ the Cartesian component of the nuclear coordinates,

$$\begin{aligned} \left\langle \Psi_{gi} \left| \mu_{\mathrm{elec},\beta} \right| \Psi_{gf} \right\rangle &= \sqrt{\frac{\hbar}{2\omega_j}} \sum_{\alpha} \sum_{\lambda} \left.\frac{\partial \mu_{\mathrm{elec},\beta}^{g}}{\partial R_{\alpha\lambda}}\right|_{0} S_{\alpha\lambda,j} \\ &= \sqrt{\frac{\hbar}{2\omega_j}} \sum_{\alpha} \sum_{\lambda} \mathbf{P}_{\lambda\beta}^{\alpha} S_{\alpha\lambda,j} \end{aligned} \tag{2.59}$$

In the above expression, the atomic polar tensor (APT) of nucleus α is introduced and given by

$$\mathbf{P}_{\lambda\beta}^{\alpha} = \left.\frac{\partial \mu_{\mathrm{elec},\beta}^{g}}{\partial R_{\alpha\lambda}}\right|_{0} \tag{2.60}$$

The APT was first introduced by Morcillo et al.[15-18] Later, Person and Newton[19] reviewed the properties of APTs.

Because $\boldsymbol{\mu}^{g}_{\mathrm{elec}} = \langle \psi_g \,|\, \boldsymbol{\mu}_{\mathrm{elec}} \,|\, \psi_g \rangle$, $\mathbf{P}^{\alpha}_{\lambda\beta}$ can be separated in a nuclear and electronic part,

$$\mathbf{P}^{\alpha}_{\lambda\beta} = 2\left\langle \psi_g(\boldsymbol{r};\boldsymbol{R}_0) \middle| \mu^{\mathrm{E}}_{\mathrm{elec},\beta} \middle| \frac{\partial \psi_g(\boldsymbol{r};\boldsymbol{R})}{\partial R_{\alpha\lambda}} \middle|_0 \right\rangle + Z_\alpha \delta_{\lambda\beta} \tag{2.61}$$

2.2.5 Magnetic field perturbation[9,20]

The infinite sum over electronic wave functions can be circumvented by invoking the magnetic field dependence of the wave function in Stephens' magnetic field perturbation (MFP) approach for calculating rotational strengths.
The external uniform magnetic field dependence of the wave function may be treated in an explicit manner. The magnetic field dependence of the electronic ground state can be expressed as a Taylor expansion, truncated after the linear term,

$$\psi_g(\boldsymbol{Q}_0, \boldsymbol{B}) = \psi_g(\boldsymbol{Q}_0, \boldsymbol{B}_0) + \left.\frac{\partial \psi_g(\boldsymbol{Q}_0, \boldsymbol{B})}{\partial \boldsymbol{B}}\right|_{\boldsymbol{B}=0} \cdot \boldsymbol{B} \tag{2.62}$$

$\boldsymbol{B}$ is the magnetic induction vector associated to the external magnetic field represented by vector potential $\boldsymbol{A}$. The derivatives in the second term of Equation (2.62) are evaluated in absence of the magnetic field (zero magnetic field, $\boldsymbol{B}_0 = 0$). The perturbed electronic Hamiltonian in the presence of a magnetic field perturbation[21] can be written to the first order:

$$H_{\mathrm{E}}(\boldsymbol{B}) = H_{\mathrm{E}}(\boldsymbol{B}_0) - \boldsymbol{\mu}^{\mathrm{E}}_{\mathrm{mag}} \cdot \boldsymbol{B} \tag{2.63}$$

with $H_{\mathrm{E}}(\boldsymbol{B}_0)$ the unperturbed Hamiltonian in absence of a magnetic field and the first order perturbation Hamiltonian $H'_{\mathrm{E}}(\boldsymbol{B})$ given by

$$H'_{\mathrm{E}}(\boldsymbol{B}) = -\boldsymbol{\mu}^{\mathrm{E}}_{\mathrm{mag}} \cdot \boldsymbol{B} \tag{2.64}$$

One can write the electronic ground state wave function, using a perturbation series with the perturbation $H'_{\mathrm{E}}(\boldsymbol{B})$ as

$$\psi_g(\boldsymbol{Q}_0,\boldsymbol{B}) = \psi_g(\boldsymbol{Q}_0,\boldsymbol{B}_0) + \sum_{e\neq g}\frac{\langle\psi_e(\boldsymbol{Q}_0,\boldsymbol{B_0})|H'_{\mathrm{E}}|\psi_g(\boldsymbol{Q}_0,\boldsymbol{B_0})\rangle}{E_g(\boldsymbol{Q}_0)-E_e(\boldsymbol{Q}_0)}\cdot\psi_e(\boldsymbol{Q}_0,\boldsymbol{B}_0) \tag{2.65}$$

Combining (2.62) and (2.65), one may identify the relation

$$\left.\frac{\partial\psi_g(\boldsymbol{Q}_0,\boldsymbol{B})}{\partial\boldsymbol{B}}\right|_{\boldsymbol{B}=0} = -\sum_{e\neq g}\frac{\langle\psi_e(\boldsymbol{Q}_0,\boldsymbol{B})|\boldsymbol{\mu}^{\mathrm{E}}_{\mathrm{mag}}|\psi_g(\boldsymbol{Q}_0,\boldsymbol{B})\rangle}{E_g(\boldsymbol{Q}_0)-E_e(\boldsymbol{Q}_0)}\psi_e(\boldsymbol{Q}_0,\boldsymbol{B}_0) \tag{2.66}$$

Insertion of (2.66) in the electronic part of (2.56) yields

$$\langle\Psi_{gi}|\boldsymbol{\mu}^{\mathrm{E}}_{\mathrm{mag}}|\Psi_{gf}\rangle = -2\hbar^2\sum_k\left\langle\left.\frac{\partial\psi_g(\boldsymbol{Q}_0,\boldsymbol{B})}{\partial\boldsymbol{B}}\right|_{\boldsymbol{B}=0}\left|\left.\frac{\partial\psi_g(\boldsymbol{Q})}{\partial\boldsymbol{Q}_k}\right|_{\boldsymbol{Q}=\boldsymbol{Q}_0}\right\rangle\left\langle\chi_{gi}(\boldsymbol{Q})\left|\frac{\partial\chi_{gf}(\boldsymbol{Q})}{\partial\boldsymbol{Q}_k}\right\rangle\right. \tag{2.67}$$

Invoking the harmonic oscillator nuclear wave functions, a number of simplifications are possible. The potential energy of the ground state can be written as

$$E_g(\boldsymbol{Q}) = E_g(\boldsymbol{Q}_0) + \frac{1}{2}\sum_{k=1}^{3N-6}\kappa_k\boldsymbol{Q}_k^2 \tag{2.68}$$

κ_j is the eigenvalue of the Hessian in Expression (2.69) using the transformation in (2.25).

$$\left.\frac{\partial^2 E_g}{\partial\left(\boldsymbol{R}_\alpha-\boldsymbol{R}^0_\alpha\right)\partial\left(\boldsymbol{R}_{\alpha'}-\boldsymbol{R}^0_{\alpha'}\right)}\right|_{\boldsymbol{R}=\boldsymbol{R}_0} \tag{2.69}$$

Each normal coordinate $\boldsymbol{Q_j}$ is associated with a frequency $\omega_j=\sqrt{\kappa_j}$. For the $0\rightarrow 1$ excitation of the j^{th} vibrational normal mode, it is known that

$$\langle\chi_{gi}(\boldsymbol{Q})|\boldsymbol{Q}_j|\chi_{gf}(\boldsymbol{Q})\rangle = \sqrt{\frac{E_{gf}-E_{gi}}{2w_j^2}} = \sqrt{\frac{\hbar}{2\omega_j}} \tag{2.70}$$

with

$$E_{01} - E_{00} = \hbar\omega_j \tag{2.71}$$

Also, using the commutator relationship

$$[\boldsymbol{Q}_j, T_{\mathrm{N}}] = \hbar^2 \frac{\partial}{\partial \boldsymbol{Q}_j} \tag{2.72}$$

it can be written that

$$\langle \chi_{gi}(\boldsymbol{Q}) | \frac{\partial}{\partial \boldsymbol{Q}_j} | \chi_{gf}(\boldsymbol{Q}) \rangle = \sqrt{\frac{\omega_j}{2\hbar}} \tag{2.73}$$

If *k* is taken equal to *j*, Equation (2.67) can be written as[2]

$$\langle \Psi_{gi} | \boldsymbol{\mu}_{\mathrm{mag}}^{\mathrm{E}} | \Psi_{gf} \rangle = -2\hbar^2 \left\langle \frac{\partial \psi_g(\boldsymbol{Q}_0, \boldsymbol{B})}{\partial \boldsymbol{B}}\bigg|_{\boldsymbol{B}=0} \middle| \frac{\partial \psi_g(\boldsymbol{Q})}{\partial \boldsymbol{Q}_j}\bigg|_{\boldsymbol{Q}=\boldsymbol{Q}_0} \right\rangle \left\langle \chi_{gi}(\boldsymbol{Q}) \middle| \frac{\partial \chi_{gf}(\boldsymbol{Q})}{\partial \boldsymbol{Q}_j} \right\rangle \tag{2.74}$$

Taking into account Expression (2.73) and the transformation in Equation (2.25);

$$\begin{aligned} \langle \Psi_{gi} | \boldsymbol{\mu}_{\mathrm{mag}}^{\mathrm{E}} | \Psi_{gf} \rangle &= -2\hbar^2 \sum_{\alpha} \left\langle \frac{\partial \psi_g(\boldsymbol{R}_0, \boldsymbol{B})}{\partial \boldsymbol{B}}\bigg|_{\boldsymbol{B}=0} \middle| \frac{\partial \psi_g(\boldsymbol{R})}{\partial \boldsymbol{R}_\alpha}\bigg|_{\boldsymbol{R}=\boldsymbol{R}_0} \right\rangle \left\langle \chi_{gi}(\boldsymbol{Q}) \middle| \frac{\partial \chi_{gf}(\boldsymbol{Q})}{\partial \boldsymbol{Q}_j} \right\rangle \boldsymbol{S}_{\alpha,j} \\ &= -2\sqrt{\frac{\hbar^3 \omega_j}{2}} \sum_{\alpha} \left\langle \frac{\partial \psi_g(\boldsymbol{R}_0, \boldsymbol{B})}{\partial \boldsymbol{B}}\bigg|_{\boldsymbol{B}=0} \middle| \frac{\partial \psi_g(\boldsymbol{R})}{\partial \boldsymbol{R}_\alpha}\bigg|_{\boldsymbol{R}=\boldsymbol{R}_0} \right\rangle \boldsymbol{S}_{\alpha,j} \end{aligned} \tag{2.75}$$

$\boldsymbol{\mu}_{\mathrm{mag}}^{\mathrm{E}}$ can further be written in vector components, where β is the Cartesian component of the uniform magnetic field and λ is the Cartesian component of the nuclear coordinates.

$$\langle \Psi_{gi} | \boldsymbol{\mu}_{\mathrm{mag},\beta}^{\mathrm{E}} | \Psi_{gf} \rangle = -2\sqrt{\frac{\hbar^3 \omega_j}{2}} \sum_{\alpha} \left\langle \frac{\partial \psi_g(\boldsymbol{R}_0, \boldsymbol{B})}{\partial B_\beta}\bigg|_{\boldsymbol{B}=0} \middle| \frac{\partial \psi_g(\boldsymbol{R})}{\partial R_{\alpha\lambda}}\bigg|_{\boldsymbol{R}=\boldsymbol{R}_0} \right\rangle S_{\alpha\lambda,j} \tag{2.76}$$

The nuclear part of (2.56) can be rewritten using (2.12) and Expression (2.77). The latter can be derived in the same way as Expression (2.73).

$$\begin{aligned}\left\langle \chi_{gi}(\boldsymbol{Q})\right|\frac{\partial}{\partial \boldsymbol{R}_\alpha}\left|\chi_{gf}(\boldsymbol{Q})\right\rangle &= M_\alpha \frac{E_{gf}-E_{gi}}{\hbar^2}\left\langle \chi_{gi}(\boldsymbol{Q})\right|\boldsymbol{R}_\alpha - \boldsymbol{R}_\alpha^0\left|\chi_{gf}(\boldsymbol{Q})\right\rangle \\ &= \sqrt{\frac{\hbar}{2\omega_j}}\boldsymbol{S}_{\alpha,j}\end{aligned} \tag{2.77}$$

$$\begin{aligned}\left\langle \Psi_{gi}\left|\boldsymbol{\mu}_{\mathrm{mag}}^{\mathrm{N}}\right|\Psi_{gf}\right\rangle &= \left\langle \chi_{gi}(\boldsymbol{Q})\right|\sum_\alpha \frac{\hbar Z_\alpha}{2iM_\alpha c}\boldsymbol{R}_\alpha \times \frac{\partial}{\partial \boldsymbol{R}_\alpha}\left|\chi_{gf}(\boldsymbol{Q})\right\rangle \\ &= \sum_\alpha \frac{Z_\alpha}{2i\hbar c}\hbar\omega_j \left\langle \chi_{gi}(\boldsymbol{Q})\right|\boldsymbol{R}_\alpha^0 \times \left(\boldsymbol{R}_\alpha - \boldsymbol{R}_\alpha^0\right)\left|\chi_{gf}(\boldsymbol{Q})\right\rangle\end{aligned} \tag{2.78}$$

Introducing the Levi-Civita tensor $\varepsilon_{\lambda\beta\gamma}$ which is an isotropic unit tensor of rank 3, the cross-product in Expression (2.78) can be rewritten in terms of vector components,[22]

$$\begin{aligned}\left\langle \Psi_{gi}\left|\mu_{\mathrm{mag},\beta}^{\mathrm{N}}\right|\Psi_{gf}\right\rangle &= \sum_\alpha \frac{Z_\alpha \omega_j}{2ic}\sum_\gamma\sum_\lambda \left\langle \chi_{gi}(\boldsymbol{Q})\right|\varepsilon_{\lambda\beta\gamma}R_{\alpha\gamma}^0\left(R_\alpha - R_\alpha^0\right)_\lambda\left|\chi_{gf}(\boldsymbol{Q})\right\rangle \\ &= \sqrt{\frac{\hbar^3\omega_j}{2}}\sum_\alpha\sum_\gamma\sum_\lambda \frac{Z_\alpha}{2\hbar ic}\varepsilon_{\lambda\beta\gamma}R_{\alpha\gamma}^0 S_{\alpha\lambda,j}\end{aligned} \tag{2.79}$$

The total magnetic dipole transition moment can be written by summing Expressions (2.76) and (2.79) and

$$\begin{aligned}\left\langle \Psi_{gi}\left|\boldsymbol{\mu}_{\mathrm{mag},\beta}\right|\Psi_{gf}\right\rangle &= -\sqrt{\frac{\hbar^3\omega_j}{2}}\sum_\alpha\sum_\lambda\left(\sum_\gamma \frac{Z_\alpha \mathrm{i}}{2\hbar c}\varepsilon_{\lambda\beta\gamma}R_{\alpha\gamma}^0 + 2\left\langle \left.\frac{\partial\psi_g(\boldsymbol{R}_0,\boldsymbol{B})}{\partial B_\beta}\right|_{\boldsymbol{B}=0}\left|\left.\frac{\partial\psi_g(\boldsymbol{R})}{\partial R_{\alpha\lambda}}\right|_{\boldsymbol{R}=\boldsymbol{R}_0}\right\rangle\right)S_{\alpha\lambda,j} \\ &= -\sqrt{2\hbar^3\omega_j}\sum_\alpha\sum_\lambda \mathbf{M}_{\lambda\beta}^\alpha S_{\alpha\lambda,j}\end{aligned} \tag{2.80}$$

$\mathbf{M}_{\lambda\beta}^\alpha$ is referred to as the atomic axial tensor (AAT)[23] of nucleus α in analogy to the APT and is given by

$$\mathbf{M}_{\lambda\beta}^\alpha = \mathbf{I}_{\lambda\beta}^\alpha + \mathbf{J}_{\lambda\beta}^\alpha \tag{2.81}$$

where

$$\mathbf{I}^{\alpha}_{\lambda\beta} = \left\langle \left.\frac{\partial\psi_g(\boldsymbol{R}_0,\boldsymbol{B})}{\partial B_\beta}\right|_{\boldsymbol{B}=0} \left| \left.\frac{\partial\psi_g(\boldsymbol{R})}{\partial R_{\alpha\lambda}}\right|_{\boldsymbol{R}=\boldsymbol{R}_0} \right\rangle \tag{2.82}$$

$$\mathbf{J}^{\alpha}_{\lambda\beta} = \sum_{\gamma} \frac{Z_\alpha \mathrm{i}}{4\hbar c} \varepsilon_{\lambda\beta\gamma} R^0_{\alpha\gamma} \tag{2.83}$$

2.2.6 Dipole and rotational strengths

Expression for the dipole and rotational strengths for a 0→1 transition for the j^{th} normal mode, can be written substituting Expressions (2.59) and (2.80) in Expressions (2.5) and (2.9),

$$D_{j,ge} = \frac{\hbar}{2\omega_j}\left(\sum_{\beta}\sum_{\alpha}\sum_{\lambda} \mathbf{P}^{\alpha}_{\lambda\beta} S_{\alpha\lambda,j}\right)^2 \tag{2.84}$$

$$R_{j,ge} = \mathrm{i}\hbar^2 \sum_{\beta}\left(\sum_{\alpha}\sum_{\lambda} \mathbf{P}^{\alpha}_{\lambda\beta} S_{\alpha\lambda,j} \sum_{\alpha'}\sum_{\lambda'} \mathbf{M}^{\alpha}_{\lambda'\beta} S_{\alpha'\lambda',j}\right) \tag{2.85}$$

Equation (2.85) forms the basis for the calculation of vibrational rotational strengths. Their accuracy will depend on the accuracy on which $\mathbf{P}^{\alpha}_{\lambda\beta}$, $\mathbf{I}^{\alpha}_{\lambda\beta}$ and $\boldsymbol{S}_{\alpha,k}$ can be calculated. In the next paragraph a brief discussion will be given on the implementation of this equation using density functional theory.

2.3 Implementation

2.3.1 Approximation methods

To find a solution for the electronic Schrödinger equation, one has to apply approximate methods. Generally, using proper functionals, the accuracy of DFT is much higher than Hartree-Fock, with almost the same computational demand.[24] In this work, DFT is used. Because the practical implementation of DFT via the Kohn-Sham formalism is associated with HF theory, first HF method is briefly introduced.

2.3.1.1 Hartree-Fock[25]

In the Hartree-Fock (HF) approximation, one writes the electronic wave function ψ_g as a single Slater determinant Φ^{HF},

$$\Phi^{HF}(\boldsymbol{x}_1,\boldsymbol{x}_2,\ldots,\boldsymbol{x}_n)=\frac{1}{\sqrt{n!}}\begin{vmatrix}\Phi_1(\boldsymbol{x}_1) & \Phi_2(\boldsymbol{x}_1) & \ldots & \Phi_n(\boldsymbol{x}_1)\\ \Phi_1(\boldsymbol{x}_2) & \Phi_2(\boldsymbol{x}_2) & \cdots & \Phi_n(\boldsymbol{x}_2)\\ \vdots & \vdots & & \vdots\\ \Phi_1(\boldsymbol{x}_n) & \Phi_2(\boldsymbol{x}_n) & \cdots & \Phi_n(\boldsymbol{x}_n)\end{vmatrix} \tag{2.86}$$

where Φ_i are spin-orbitals. These describe the spatial distribution of a single electron and its spin through the spatial orbital $\phi(\mathbf{r})$ and the spin functions $\alpha(\omega)$ and $\beta(\omega)$,

$$\Phi(\boldsymbol{x})=\phi(\boldsymbol{r})\alpha(\omega) \tag{2.87}$$

x describes both the spatial coordinates ***r*** and spin coordinates ω. The spin (and spatial) orbitals are orthonormalized,

$$\left\langle \Phi_i(\boldsymbol{x})\middle|\Phi_j(\boldsymbol{x})\right\rangle = \delta_{ij} \tag{2.88}$$

The idea behind the HF method is to simplify the *n*-electron problem to a number of one-electron problems. The one-electron Fock-operator $\hat{f}_i$ (written with a caret, to avoid mistakes) is given by

$$\begin{aligned}\hat{f}_i &= -\frac{1}{2}\nabla_i^2 - \sum_{\alpha=1}^{N}\frac{Z_\alpha}{|\boldsymbol{R}_\alpha - \boldsymbol{r}_i|} + \sum_{b=1}^{n}(J_b(i)-K_b(i))\\ &= \hat{h} + V_{ext}\end{aligned} \tag{2.89}$$

where $\hat{h}$ is the one-electron part of the Hamiltonian and V_{ext} is the effective one-electron potential or Hartree-Fock potential that replaces the electron-electron repulsion term. V_{ext} is the average potential experienced by the i^{th} electron due to the presence of the other electrons.

$J_b(i)$ and $K_b(i)$ are respectively the coulomb and exchange operators.
The Hartree-Fock equations can be written as,

$$\hat{f}_i\Phi_j(\boldsymbol{x}_i)=\varepsilon_j\Phi_j(\boldsymbol{x}_i) \tag{2.90}$$

Using the variation principle, that states that the best wave function gives the lowest possible energy of the system, together with the restriction that the spinorbitals are orthonormal, one can derive the HF equations.

The Hartree-Fock equations most often are solved in the space spanned by a set of basis functions (Hartree-Fock Roothaan-Hall equations for closed shell systems) with an expansion coefficient c_{pj},

$$\phi_i = \sum_{p=1}^{m} \gamma_p c_{pi} \tag{2.91}$$

This approximation would be exact if the basis set $\{\gamma_p\}$ would be complete. This is not feasible however. Therefore, the basis sets are limited to *m* basis functions.

The Hartree-Fock-Roothaan equation can be written in matrix form as

$$\sum_q F_{pq}C_{qi} = \varepsilon_i \sum_q S_{pq}C_{qi} \tag{2.92}$$

with

$$S_{pq} = \langle \gamma_p(\boldsymbol{r}_1) | \gamma_q(\boldsymbol{r}_1) \rangle \tag{2.93}$$

$$F_{pq} = \langle \gamma_p(\boldsymbol{r}_1) | \hat{f}_1 | \gamma_q(\boldsymbol{r}_1) \rangle \tag{2.94}$$

Equation (2.92) can be written more compactly

$$FC = SCE \tag{2.95}$$

E is a diagonal matrix of the orbital energies ε_i

The solution of the equations depends on the orbitals, via the Coulomb and Exchange part. Hence, the need to guess some initial orbitals and refine these guesses iteratively. For this reason, Hartree-Fock is termed a self-consistent-field (SCF) approach.

2.3.1.2 Density functional theory[26]

Density functional theory is based on the theorems by Hohenberg and Kohn, published in 1964.[27] They proved that all aspects of the electronic structure of a system of interacting electrons, in the non-degenerate ground state, in an 'external' potential V_{ext}, are completely determined, within a constant, as a functional of the electron density $\rho(\boldsymbol{r}_1)$.

The electron density is defined as

$$\rho(\boldsymbol{r}_1) = n\int ...\int |\Psi(\boldsymbol{x}_1,\boldsymbol{x}_2,...,\boldsymbol{x}_n)|^2 \mathrm{d}\omega_1 \mathrm{d}\boldsymbol{x}_2 \ ...\mathrm{d}\boldsymbol{x}_n \tag{2.96}$$

and determines the probability of finding any of the n electrons within the volume element dr_1 with arbitrary spin. The others electrons are described by Ψ.

This means that only the electron density of the system has to be known to investigate the ground state properties. Thus, electron density is the central quantity that has to be found instead of the many electron wave function, which is the case in other solutions to the many body problem

Hohenberg and Kohn also proved that the ground state energy of the interacting electrons system is a unique functional of $\rho(\boldsymbol{r})$. The value of this functional is at a minimum when the charge density is correct for a given an external potential V_{ext}.

$$E_0 \leq E[\tilde{\rho}] = T[\tilde{\rho}] + E_{\mathrm{NE}}[\tilde{\rho}] + E_{\mathrm{EE}}[\tilde{\rho}] \tag{2.97}$$

$\tilde{\rho}$ is any trial density fulfilling $\tilde{\rho}(\boldsymbol{r}) \geq 0$ and $\int \tilde{\rho}(\boldsymbol{r})d\boldsymbol{r} = n$, the latter being the number of electrons in the system.

The theorem guarantees the existence of an energy functional $E[\rho]$ that reaches its minimum for the correct density, yet gives no explicit prescription for its construction.

One particular way of exploiting the Hohenberg-Kohn theorems is the well-known Kohn-Sham scheme, expressing the ground state density of the interacting particles of a molecular system in terms of the orbitals of auxiliary non-interacting particles moving in an effective external local potential V_{ext}.[28,29] In order to determine $E[\rho]$ it is useful to separate the various known contributions to the total energy,

$$E[\rho(\boldsymbol{r})] = T_S[\rho(\boldsymbol{r})] + E_{ext}[\rho(\boldsymbol{r})] + E_C[\rho(\boldsymbol{r})] + E_{XC}[\rho(\boldsymbol{r})] \tag{2.98}$$

$T_S[\rho(\boldsymbol{r})]$is the kinetic energy of the system of non-interacting electrons. $E_{ext}[\rho(\boldsymbol{r})]$ the classical Coulomb energy of the electrons moving in the external potential V_{ext}. $E_C[\rho(\boldsymbol{r})]$ the classical energy due to the mutual Coulomb interaction of the electrons. The last term $E_{XC}[\rho(\boldsymbol{r})]$ contains everything else which was not accounted for yet, that is, exchange energy, correlation energy and in principle, the difference between the true kinetic energy ($T[\tilde{\rho}]$) and the kinetic energy of the system of non-interaction electrons ($T_S[\rho(\boldsymbol{r})]$).

Due to the second part of the Hohenberg-Kohn theorem, namely that the total energy is minimized by the true ground-state density, the following set of equations can be derived:

$$\left(-\frac{1}{2}\nabla^2 + V_{eff}(\boldsymbol{r}_1)\right)\varphi_i = \varepsilon_i\varphi_i \tag{2.99}$$

$$\rho(\boldsymbol{r}) = \sum_{i}^{occ} |\varphi_i(\boldsymbol{r})|^2 \tag{2.100}$$

With the effective potential given by a functional of the electron density,

$$V_{eff}(\boldsymbol{r}_1) = V_{eff}[\rho(\boldsymbol{r})] = \int \frac{\rho(\boldsymbol{r}_2)}{\boldsymbol{r}_{12}} d\boldsymbol{r}_2 - \sum_{\alpha}^{N} \frac{Z_\alpha}{|\boldsymbol{R}_\alpha - \boldsymbol{r}_1|} + V_{XC}(\boldsymbol{r}_1) \tag{2.101}$$

The last term is the exchange-correlation potential, which also is a functional of the density, defined as the functional derivative of the exchange-correlation energy

$$V_{XC}[\rho(\boldsymbol{r})] \equiv \frac{\delta E_{XC}[\rho(\boldsymbol{r})]}{\delta \rho} \tag{2.102}$$

The set of Equations (2.99), (2.100) and (2.101) are known as the KS equations. They have to be solved iteratively, that is, starting from some initial density a potential $V_{eff}[\rho(\boldsymbol{r})]$ is obtained for which the Equations (2.99) are solved and a new electronic density is determined via (2.100). From the new density an updated effective potential can be calculated, until self-consistency is reached.

This exchange-correlation potential is a universal functional of the density, i.e., the functional form of its dependence on the density is the same, irrespective of the system that is studied.

Formally, the KS equations describe a system of non-interacting particles. This makes the KS equation easy to solve. However, because the KS electrons move in an effective potential which is set up by other electrons, many-body correlation effects are considered within the KS equation. In fact, the KS equations give an exact description of the many-electron system because up to this point no approximations have been made.
The approximations enter in the expression for the unknown exchange-correlation functional E_{XC}.
The simplest approximation that one can make is to imagine that at every point in space we can use the value of the density that the uniform electron gas would have at that point, and allow it to vary from point to point. This is called the local density approximation (LDA),

$$E_{XC}^{\mathrm{LDA}}[\rho] = \int \rho(\boldsymbol{r}) \varepsilon_{XC}(\rho(\boldsymbol{r})) d\boldsymbol{r} \tag{2.103}$$

Here, $\varepsilon_{XC}(\rho(\boldsymbol{r}))$ is the exchange-correlation energy per particle of a uniform electron gas of density $\rho(\boldsymbol{r})$. The $E_{XC}^{\mathrm{LDA}}[\rho]$ can formally be split into exchange and correlation contributions

$$E_{XC}^{\mathrm{LDA}} = E_{X}^{\mathrm{LDA}} + E_{C}^{\mathrm{LDA}} \tag{2.104}$$

The exchange part of the LDA functional[30] is given by

$$E_{X}^{\mathrm{LDA}} = -\frac{3}{4}\sqrt[3]{\frac{3}{\pi}}\int \rho^{4/3}(\boldsymbol{r})d\boldsymbol{r} \tag{2.105}$$

For the correlation part, E_{C}^{LDA} no explicit expression is known. However, various analytic expression were derived; the most widely used is from Vosko, Wilk and Nusair (VWN).[31]

The LDA by itself is not sufficiently accurate for chemical applications. It is necessary to include terms that explicitly take into account the spatial variation of the density. Within the generalized gradient approximation (GGA), E_{XC} is not only function of the local density $\rho(\boldsymbol{r})$ but also of the gradient of the charge density $\nabla\rho(\boldsymbol{r})$, which can formally be written as

$$E_{XC}^{\mathrm{GGA}}\left[\rho_{\alpha},\rho_{\beta}\right] = \int f(\rho_{\alpha},\rho_{\beta},\nabla\rho_{\alpha},\nabla\rho_{\beta})d\boldsymbol{r} \tag{2.106}$$

Here α and β refer to the spin state. In practice, E_{XC}^{GGA} is split up in an exchange and correlation contribution. Well-known exchange functionals are the B88 from Becke[32] and the PW86[33] from Perdew and Wang. The P86 functional from Perdew[34] is the correlation counterpart of the latter. Perdew and Wang also developed the PW91 exchange-correlation functional.[35] Nowadays, the most popular correlation functional is the LYP due to Lee, Yang and Parr.[36]

The so called hybrid functionals are exchange-correlation functionals including a mixture of HF exchange with DFT exchange and correlation,

$$E_{XC}^{\mathrm{hybrid}} = c^{\mathrm{HF}}E_{X}^{\mathrm{HF}} + c^{\mathrm{DFT}}E_{XC}^{\mathrm{DFT}} \tag{2.107}$$

Examples for such hybrid models are Becke's three parameter hybrid functional (B3)[37], and the popular B3PW91[35,37] and B3LYP[31,36-38]. The B3LYP functional is employed most often throughout this thesis. Other hybrid functionals are also employed, for which references can be found in the appropriate chapters.

2.3.2 Gauge invariance

It is well known that any physical quantity which describes molecular behavior should not depend on the choice of coordination system, that is, should be origin gauge invariant. The evaluation of the magnetic dipole moment derivatives suffers from origin gauge dependence.[23]

When applying an external uniform magnetic field represented by a constant magnetic induction vector $\boldsymbol{B}$, the associated vector potential $\boldsymbol{A}_O$ can be defined as

$$\boldsymbol{A}_O = \frac{1}{2}\boldsymbol{B} \times (\boldsymbol{r} - \boldsymbol{O}) \tag{2.108}$$

The vector potential vanishes at the location $\boldsymbol{O}$, which is the gauge origin. The magnetic induction is defined by the curl of the vector potential,

$$\boldsymbol{B} = \nabla \times \boldsymbol{A} \tag{2.109}$$

From this it follows that the gauge origin $\boldsymbol{O}$ can be arbitrarily chosen, which essentially redefines the vector potential, nevertheless, has no effect on the uniform field $\boldsymbol{B}$.[39]

The arbitrary nature of the vector potential or the choice of origin gauge has no effect in an exact calculation. It can be shown[23] that rotational strengths calculated via Equation (2.85), that is, via MPF theory, are independent of the gauge origin for exact wave functions and for approximate wave functions expanded in a complete basis set. However, it is practically impossible to carry out such calculations. Using finite basis sets, the calculated results are not necessarily gauge independent.

Accordingly, one needs a method that permits calculations that do not depend on the choice of origin. The common origin (CO) gauge is the first method that was implemented for the ab initio calculations of AATs.[20,40] In the CO gauge method, a single origin is chosen throughout the evaluation of the dipole transition moments. A distributed gauge origin (DO) method[23] was then introduced with origins distributed at the nuclei. This method was proven to be favorable for the calculation of AATs compared to calculations using a common origin.[41,42]

London introduced AOs (to investigate π-electron ring currents in aromatic molecules) which are gauge dependent orbitals.[43] London atomic orbitals (LOA) are formed by multiplying the AOs with a phase factor

$$\Gamma_p(\boldsymbol{R},\boldsymbol{B})=\exp\left(-\frac{1}{2}\mathrm{i}\boldsymbol{B}\times(\boldsymbol{R}_\alpha-\boldsymbol{O})\cdot\boldsymbol{r}\right)\gamma_p(\boldsymbol{R},\boldsymbol{B_0}) \tag{2.110}$$

$\boldsymbol{R}_\alpha$ is the center of the nucleus and $\boldsymbol{r}$ is the position of the electron. The AOs $\gamma_p(\boldsymbol{R},\boldsymbol{B_0})$ are the field-independent basis functions which are eigenvalues of $H(\boldsymbol{B}_0)$, the Hamiltonian in absence of a magnetic field (see Equation (2.63)).

It can be shown that the LAOs given in Equation (2.110) are eigenfunctions of the one electron Hamiltonian in the presence of an magnetic field (see Equation (2.63)) to first order in $\boldsymbol{B}$.[44,45] The properties calculated using LOAs therefore are independent of the choice of the gauge origin $\boldsymbol{O}$.[46]

These LAOs are also known as gauge-invariant atomic orbitals (GIAOs) for which the first reference in literature was found from Hameka.[47] Ditchfield developed the first ab intio theory using GIAOs.[48] The choice of the acronym GIAO is unfortunate, because these orbitals include a factor which depends on the gauge. A better description was proposed by Pople[49], i.e., ‘gauge-dependent atomic orbitals’. However, GIAO is the most common name which is most often read as gauge-invariant/including atomic orbitals.[50]
The first implementation for the calculation of GIAO-AATs at Hartree-Fock level of theory is from Bak et al.[45,51]
The current state-of-the-art in ab initio VCD rotational strength calculations was published by Cheeseman and Stephens[24] in 1996 with the development of the first GIAO-based DFT codes. Since the new approach was first made available in the Gaussian programs[52], the majority of VCD calculations in literature have made use of the GIAO-DFT methodology.[53,54] The calculations of the rotational strengths in this thesis are performed based on the GIAO-DFT method.

2.3.3 Analytical derivates

Evaluation of $\mathbf{P}^{\alpha}_{\lambda\beta}$ and $\mathbf{I}^{\alpha}_{\lambda\beta}$ requires derivatives of the ground state electronic wave function with respect to nuclear position or the magnetic field, i.e., $\frac{\partial\psi_g(\boldsymbol{R})}{\partial\boldsymbol{R}}$ and $\frac{\partial\psi_g(\boldsymbol{R}_0,\boldsymbol{B})}{\partial\boldsymbol{B}}$ as can be seen in Equations (2.61) and (2.82). In the early stages of MFP VCD theory development, these derivatives were obtained at the Hartree-Fock self-consistent field level using finite difference methods.[20] Soon afterwards, the coupled perturbed Hartree-Fock method[55,56] was introduced. This allowed that the evaluation of the wave functions derivatives could be performed analytically.[57,58] The latter was also implemented at DFT level[59,60] using the Coupled Perturbed KS[55,56,59] method.

If a closed shell system is assumed, Equation (2.82) can be written as

$$\mathbf{I}^{\alpha}_{\lambda\beta} = \sum_{i}^{occ} 2\left\langle \left.\frac{\partial\phi_i(\boldsymbol{R}_0,\boldsymbol{B})}{\partial B_\beta}\right|_{\boldsymbol{B}=0} \left| \left.\frac{\partial\phi_i(\boldsymbol{R})}{\partial R_{\alpha\lambda}}\right|_{\boldsymbol{R}=\boldsymbol{R}_0} \right\rangle \right. \tag{2.111}$$

In KS calculations, the KS orbitals φ_i can be expressed as linear combinations of a set of basis functions $\{\gamma_p(\boldsymbol{R})\}$. Here, non-degenerate KS orbitals $\varphi_i(\boldsymbol{R})$ will be expanded,

$$\varphi_i(\boldsymbol{R}) = \sum_{p=1}^{m} \gamma_p(\boldsymbol{R}) c_{pi}(\boldsymbol{R}) \tag{2.112}$$

The derivative of $\varphi_i(\boldsymbol{R})$ at $\boldsymbol{R} = \boldsymbol{R}_0$ with respect to the nuclear position is

$$\left.\frac{\partial\varphi_i(\boldsymbol{R})}{\partial\boldsymbol{R}}\right|_0 = \sum_{p=1}^{m}\left(c_{pi}(\boldsymbol{R}) \left.\frac{\partial\gamma_p(\boldsymbol{R})}{\partial\boldsymbol{R}}\right|_0 + \gamma_p(\boldsymbol{R}) \left.\frac{\partial c_{pi}(\boldsymbol{R})}{\partial\boldsymbol{R}}\right|_0 \right) \tag{2.113}$$

Thus in order to evaluate the derivative of KS orbitals with respect to the nuclear position, it is necessary to know the quantities $\left.\frac{\partial\gamma_p(\boldsymbol{R})}{\partial\boldsymbol{R}}\right|_0$ and $\left.\frac{\partial c_{pi}(\boldsymbol{R})}{\partial\boldsymbol{R}}\right|_0$. The first term involves the differentiation of the basis function and can thus be

straightforwardly evaluated by standard techniques[39]. The second term in (2.113) arises from the fact that the coefficients which define the KS orbitals in terms of the basis functions may also depend on $\boldsymbol{R}$. For the derivative taken with respect to the magnetic field, the first term in Equation (2.113) will be zero.[55,57]

This problem can generally be solved using the coupled perturbed Kohn-Sham (CPKS) method[59], which is briefly reviewed in this section. The CPKS is analogue to the CP Hartree-Fock equations which were derived by Gerrat and Mills[55] and generalized by Pople et al.[56]

In what follows the perturbation is taken to be the nuclear displacement. This perturbation can easily be transferred to magnetic field or an electric field.
We can write the SCF equation in the matrix form

$$F(\boldsymbol{R})\,C(\boldsymbol{R}) = S(\boldsymbol{R})\,C(\boldsymbol{R})E(\boldsymbol{R}) \tag{2.114}$$

F is the Fock matrix, *C* is the coefficient matrix built up from the column vectors $\boldsymbol{c}_i(\boldsymbol{R})$ and *E* is the diagonal matrix of the energies $\varepsilon_p(\boldsymbol{R})$. It is also required that the basis functions are orthonormal,

$$C^{\dagger}(\boldsymbol{R})S(\boldsymbol{R})\,C(\boldsymbol{R}) = \mathbf{1} \tag{2.115}$$

Another basis set $\{\varphi'_j(\boldsymbol{R})\}$ is constructed by a linear combination of the old basis set $\{\gamma_p(\boldsymbol{R})\}$,

$$\varphi'_j(\boldsymbol{R}) = \sum_{p=1}^{m} \gamma_p(\boldsymbol{R})\,c_{pj}\,(0) \tag{2.116}$$

$\{c_{pi}(0)\}$ are the KS coefficient in the unperturbed condition $\boldsymbol{R} = \boldsymbol{R}_0$. In the same way, the unperturbed KS orbitals can be written as $\varphi_j(0) = \varphi'_j(0)$. The perturbed KS orbital can be expanded in terms if $\varphi'_j(\boldsymbol{R})$,

$$\varphi_i(\boldsymbol{R}) = \sum_{j=1}^{n} \varphi'_j(\boldsymbol{R})\,u_{ji}(\boldsymbol{R}) \tag{2.117}$$

From Equation (2.112) and (2.117) it follows that

$$c_{pi}(\boldsymbol{R}) = \sum_{j=1}^{n} c_{pj}(0) u_{ji}(\boldsymbol{R}) \tag{2.118}$$

or in matrix notation

$$C(\boldsymbol{R}) = C(0)\, U(\boldsymbol{R}) \tag{2.119}$$

$U(0)$ is clearly a unit matrix. The computation of the derivatives of the KS orbitals is thus converted to the calculation of derivatives of $U(\boldsymbol{R})$.
If (2.119) is substituted in (2.114) and multiplying on the left with the Hermitian conjugate $C^{\dagger}(\boldsymbol{R})$, following expression is obtained;

$$C^{\dagger}(0) F(\boldsymbol{R}) C(0)\, U(\boldsymbol{R}) = C^{\dagger}(0) S(\boldsymbol{R}) C(0)\, U(\boldsymbol{R}) E(\boldsymbol{R}) \tag{2.120}$$

The Fock and overlap matrix, both transformed by $C(\boldsymbol{R})$ can be conveniently written

$$F'(\boldsymbol{R}) = C^{\dagger}(0) F(\boldsymbol{R}) C(0) \tag{2.121}$$

$$S'(\boldsymbol{R}) = C^{\dagger}(0) S(\boldsymbol{R}) C(0) \tag{2.122}$$

$F'(\boldsymbol{R})$ and $S'(\boldsymbol{R})$ are respectively the Fock and overlap matrices in the KS basis of $\{\varphi'_j(\boldsymbol{R})\}$.

The SCF equation can then be written

$$F'(\boldsymbol{R})\, U(\boldsymbol{R}) = S'(\boldsymbol{R})\, U(\boldsymbol{R}) E(\boldsymbol{R}) \tag{2.123}$$

With orthonormality condition

$$U^{\dagger}(\boldsymbol{R}) S'(\boldsymbol{R})\, U(\boldsymbol{R}) = \mathbf{1} \tag{2.124}$$

Because $S'(0)$ is the unit matrix (unperturbed KS orbitals are orthonormal), the unperturbed SCF equations are

$$F'(0)\,U(0) = U(0)E(0) \text{ and } U^{\dagger}(0)\,U(0) = \mathbf{1} \tag{2.125}$$

From (2.125) it also follows that $F'(0)$ is identical with $E(0)$ and is a diagonal matrix with diagonal elements equal to the unperturbed energies $\varepsilon_i(0)$.

Equations (2.123) and (2.124) have to be solved. The various matrices in these equations may be expanded as Maclaurin series expansion, that is at $R = R_0$, keeping only the linear terms,

$$F'(\boldsymbol{R}) = F'(0) + \left.\frac{\partial F'(\boldsymbol{R})}{\partial \boldsymbol{R}}\right|_0 \boldsymbol{R} = E(0) + \boldsymbol{R}F'^{(1)} \tag{2.126}$$

$$S'(\boldsymbol{R}) = S'(0) + \left.\frac{\partial S'(\boldsymbol{R})}{\partial \boldsymbol{R}}\right|_0 \boldsymbol{R} = \mathbf{1} + \boldsymbol{R}S'^{(1)} \tag{2.127}$$

$$U(\boldsymbol{R}) = U(0) + \left.\frac{\partial U(\boldsymbol{R})}{\partial \boldsymbol{R}}\right|_0 \boldsymbol{R} = \mathbf{1} + \boldsymbol{R}U^{(1)} \tag{2.128}$$

$$E(\boldsymbol{R}) = E(0) + \left.\frac{\partial E(\boldsymbol{R})}{\partial \boldsymbol{R}}\right|_0 \boldsymbol{R} = E(0) + \boldsymbol{R}E^{(1)} \tag{2.129}$$

It is noticeable that $E^{(1)}$ must be diagonal because $E(\boldsymbol{R})$ is diagonal for all values of $\boldsymbol{R}$.

Substitution of (2.126)–(2.129) in (2.123) and (2.124) and collecting together the corresponding orders in $\boldsymbol{R}$, the first order equations are

$$F'^{(1)} + E(0)\,U^{(1)} = S'^{(1)}E(0) + U^{(1)}E(0) + E^{(1)} \tag{2.130}$$

$$U^{\dagger(1)} + U^{(1)} + S'^{(1)} = 0 \tag{2.131}$$

The first order change $U^{(1)}$ can thus be obtained by solving Equations (2.130) and (2.131).

To describe the matrix elements of $U^{(1)}$ it is convenient to revert to a matrix element notation. The diagonal elements in Equation (2.131) give

$$u_{ii}^{(1)*} + s_{ii}'^{(1)} + u_{ii}^{(1)} = 0 \tag{2.132}$$

and if $u_{ii}^{(1)}$ is chosen to be real, then

$$u_{ii}^{(1)} = -\frac{s_{ii}'^{(1)}}{2} \tag{2.133}$$

The off-diagonal elements can be obtained by Equation (2.130),

$$u_{ij}^{(1)} = \frac{f_{ij}'^{(1)} - s_{ij}'^{(1)}\varepsilon_j(0)}{\varepsilon_j(0) - \varepsilon_i(0)} \tag{2.134}$$

The matrix elements of $U^{(1)}$ are thus expressed according to the first order changes of the transformed Fock and overlap matrices $F'^{(1)}$ and $S'^{(1)}$. The latter, that is, the derivative of the overlap matrix, can be handled easily because, from Equation (2.122), it can be written

$$s_{ii}'^{(1)} = \sum_{i,j}^{n} c_{ij}^{*}(0) \left.\frac{\partial s_{ij}(\boldsymbol{R})}{\partial \boldsymbol{R}}\right|_0 c_{ij}(0) \tag{2.135}$$

The derivative of the Fock matrix, $F'^{(1)}$, however depends on $U^{(1)}$. Thus Equation (2.134) must be solved by an iterative procedure.

2.4 Reference list

1. Stephens, P. J.; Lowe, M. A. *Annu. Rev. Phys. Chem.* **1985**, *36*, 213-241.

2. Rauk, A. Vibrational circular dichroism Intensities: Ab initio calculations. In *New developments in molecular chirality*, Mezey, P. G., Ed.; Kluwer academic publishers: **1991**; pp 57-92.

3. Schellman, J. A. *Chem. Rev.* **1975**, *75*, 323-331.

4. Born, M.; Oppenheimer, R. *Ann. Phys.* **1927**, *84*, 457-484.

5. Craig, D. P.; Thirunamachandran, T. *Mol. Phys.* **1978**, *35*, 825-840.

6. Faulkner, T. R.; Marcott, C.; Moscowitz, A.; Overend, J. *J. Am. Chem. Soc.* **1977**, *99*, 8160-8168.

7. Allinger, N. L.; Yuh, Y. H.; Lii, J. H. *J. Am. Chem. Soc.* **1989**, *111*, 8551-8566.

8. Nafie, L. A.; Freedman, T. B. *J. Chem. Phys.* **1983**, *78*, 7108-7116.

9. Stephens, P. J. *J. Phys. Chem.-US* **1985**, *89*, 748-752.

10. Buma, W. J. *High Resolution experimental ab initio spectroscopy;* Lecture Notes - The Post-doctoral Course on Theoretical Chemistry and Spectroscopy Han-sur-Lesse, Belgium, Dec 9-13th **2002**.

11. Craig, D. P.; Thirunamachandran, T. *Can. J. Chem.* **1985**, *63*, 1773-1779.

12. Orlandi, G.; Siebrand, W. *J. Chem. Phys.* **1973**, *58*, 4513-4523 and Orlandi, G.; Siebrand, W. *Chem. Phys. Lett.* **1972**, *15*, 465-468.

13. Dutler, R.; Rauk, A. *J. Am. Chem. Soc.* **1989**, *111*, 6957-6966.

14. Hansen, A. E.; Stephens, P. J.; Bouman, T. D. *J. Phys. Chem.-US* **1991**, *95*, 4255-4262.

15. Biarge, J. F.; Herranz, J.; Morcillo, J. *An. Soc. Esp. Fis. Quim.* **1961**, *57*, 81-92.

16. Morcillo, J.; Lastra, M.; Biarge, J. F. *An. Soc. Esp. Fis. Quim.* **1961**, *57*, 179-186.

17. Morcillo, J.; Zamorano, L. J.; Heredia, J. M. V. *Spectrochim. Acta* **1966**, *22*, 1969-1980.

18. Morcillo, J.; Biarge, J. F.; Heredia, J. M. V.; Medina, A. *J. Mol. Struct.* **1969**, *3*, 77-87.

19. Person, W. B.; Newton, J. H. *J. Chem. Phys.* **1974**, *61*, 1040-1049.

20. Lowe, M. A.; Segal, G. A.; Stephens, P. J. *J. Am. Chem. Soc.* **1986**, *108*, 248-256.

21. Atkins, P. W.; Friedman, R. S. *Molecular Quantum Mechanics;* 3rd ed.; Oxford University Press: Oxford, **1999**.

22. Chou, P. C.; Pagano, N. J. The Alternating Tensor §8.7. In *Elasticity: Tensor, Dyadic, and Engineering Approaches*, Dover: New York, **1992**; pp 182-186.

23. Stephens, P. J. *J. Phys. Chem.-US* **1987**, *91*, 1712-1715.

24. Cheeseman, J. R.; Frisch, M. J.; Devlin, F. J.; Stephens, P. J. *Chem. Phys. Lett.* **1996**, *252*, 211-220.

25. Szabo, A.; Ostlund, N. S. *Modern Quantum Chemistry;* Dover Publications, Inc.: New York, **1996**.

26. Koch, W.; Holthausen, M. C. *A Chemist's guide to density functional theory;* 2nd ed.; Wiley-VCH: Weinheim, **2002**.

27. Hohenberg, P.; Kohn, W. *Phys. Rev.* **1964**, *136*, B864-B871.

28. Kohn, W.; Sham, L. J. *Phys. Rev.* **1965**, *140*, A1133-A1138.

29. Sham, L. J.; Kohn, W. *Phys. Rev.* **1966**, *145*, 561-567.

30. Dirac, P. A. M. *Proc. Cambridge Phil. Soc.* **1930**, *26*, 376-385.

31. Vosko, S. H.; Wilk, L.; Nusair, M. *Can. J. Phys.* **1980**, *58*, 1200-1211.

32. Becke, A. D. *Phys. Rev. A* **1988**, *38*, 3098-3100.

33. Perdew, J. P.; Wang, Y. *Phys. Rev. B* **1986**, *33*, 8800-8802.

34. Perdew, J. P. *Phys. Rev. B* **1986**, *33*, 8822-8824.

35. Perdew, J. P.; Chevary, J. A.; Vosko, S. H.; Jackson, K. A.; Pederson, M. R.; Singh, D. J.; Fiolhais, C. *Phys. Rev. B* **1992**, *46*, 6671-6687.

36. Lee, C. T.; Yang, W. T.; Parr, R. G. *Phys. Rev. B-Condens. Matter* **1988**, *37*, 785-789.

37. Becke, A. D. *J. Chem. Phys.* **1993**, *98*, 5648-5652.

38. Stephens, P. J.; Devlin, F. J.; Chabalowski, C. F.; Frisch, M. J. *J. Phys. Chem.-US* **1994**, *98*, 11623-11627.

39. Gill, P. M. W.; Head-Gordon, M.; Pople, J. A. *J. Phys. Chem.-US* **1990**, *94*, 5564-5572.

40. Lowe, M. A.; Stephens, P. J.; Segal, G. A. *Chem. Phys. Lett.* **1986**, *123*, 108-116.

41. Jalkanen, K. J.; Kawiecki, R. W.; Stephens, P. J.; Amos, R. D. *J. Phys. Chem.-US* **1990**, *94*, 7040-7055.

42. Stephens, P. J.; Jalkanen, K. J.; Amos, R. D.; Lazzeretti, P.; Zanasi, R. *J. Phys. Chem.-US* **1990**, *94*, 1811-1830.

43. London, F. *J. Phys. Radium* **1937**, *8*, 397-408.

44. Helgaker, T.; Jorgensen, P. *J. Chem. Phys.* **1991**, *95*, 2595-2601.

45. Bak, K. L.; Jorgensen, P.; Helgaker, T.; Ruud, K.; Jensen, H. J. A. *J. Chem. Phys.* **1993**, *98*, 8873-8887.

46. Helgaker, T.; Jaszunski, M.; Ruud, K. *Chem. Rev.* **1999**, *99*, 293-352.

47. Hameka, H. F. Nuclear magnetic shielding in the hydrogen molecule. 1st ed.; **1958**; Taylor and Francis Ltd, pp 203-215.

48. Ditchfield, R. *Mol. Phys.* **1974**, *27*, 789-807.

49. Pople, J. A. *Discuss. Faraday Soc.* **1962**, *No. 34*, 7-14.

50. Hansen, A. E.; Bouman, T. D. *J. Chem. Phys.* **1985**, *82*, 5035-5047.

51. Bak, K. L.; Jorgensen, P.; Helgaker, T.; Ruud, K.; Jensen, H. J. A. *J. Chem. Phys.* **1994**, *100*, 6620-6627.

52. Frisch, M. J.; Trucks, G. W.; Schlegel, H. B.; Scuseria, G. E.; Robb, M. A.; Cheeseman, J. R.; Montgomery Jr, J. A.; Vreven, T.; Kudin, K. N.; Burant, J. C.; Millam, J. M.; Iyengar, S. S.; Tomasi, J.; Barone, V.; Mennucci, B.; Cossi, M.; Scalmani, G.; Rega, N.; Petersson, G. A.; Nakatsuji, H.; Hada, M.; Ehara, M.; Toyota, K.; Fukuda, R.; Hasegawa, J.; Ishida, M.; Nakajima, T.; Honda, Y.; Kitao, O.; Nakai, H.; Klene, M.; Li, X.; Knox, J. E.; Hratchian, H. P.; Cross, J. B.; Bakken, V.; Adamo, C.; Jaramillo, J.; Gomperts, R.; Stratmann, R. E.; Yazyev, O.; Austin, A. J.; Cammi, R.; Pomelli, C.; Ochterski, J. W.; Ayala, P. Y.; Morokuma, K.; Voth, G. A.; Salvador, P.; Dannenberg, J. J.; Zakrzewski, V. G.; Dapprich, S.; Daniels, A. D.; Strain, M. C.; Farkas, O.; Malick, D. K.; Rabuck, A. D.; Raghavachari, K.; Foresman, J. B.; Ortiz, J. V.; Cui, Q.; Baboul, A. G.; Clifford, S.; Cioslowski, J.; Stefanov, B. B.; Liu, G.; Liashenko, A.; Piskorz, P.; Komaromi, I.; Martin, R. L.; Fox, D. J.; Keith, T.; Al-Laham, M. A.; Peng, C. Y.; Nanayakkara, A.; Challacombe, M.; Gill, P. M. W.; Johnson, B.; Chen, W.; Wong, M. W.; Gonzalez, C.; Pople, J. A. *Gaussian03,* Revision B5; Gaussian, Inc.: Wallingford CT, **2004**.

53. Stephens, P. J.; Devlin, F. J. *Chirality* **2000**, *12*, 172-179.

54. Polavarapu, P. L.; Michalska, D. F.; Back, D. M. *Appl. Spectrosc.* **1984**, *38*, 438-442.

55. Gerratt, J.; Mills, I. M. *J. Chem. Phys.* **1968**, *49*, 1719-1729.

56. Pople, J. A.; Krishnan, R.; Schlegel, H. B.; Binkley, J. S. *Int. J. Quantum. Chem. Symp.* **1979**, *13*, 225-241.

57. Amos, R. D.; Handy, N. C.; Jalkanen, K. J.; Stephens, P. J. *Chem. Phys. Lett.* **1987**, *133*, 21-26.

58. Morokuma, K.; Sugeta, H. *Chem. Phys. Lett.* **1987**, *134*, 23-26.

59. Johnson, B. G.; Fisch, M. J. *J. Chem. Phys.* **1994**, *100*, 7429-7442.

60. Berces, A.; Dickson, R. M.; Fan, L. Y.; Jacobsen, H.; Swerhone, D.; Ziegler, T. *Comput. Phys. Commun.* **1997**, *100*, 247-262.

3

measurement of VCD

3.1 Introduction

In this chapter, the experimental part of this thesis related to the measurement of vibrational CD will be illuminated and the key elements of the instrumental setup are discussed.

The first molecular VCD spectra were reported more than 30 years ago, using a dispersive setup.[1-4] At that time, the technique appeared to be experimentally difficult and yielded weak, noisy spectra.[5] Over the years, the signal-to-noise ratio (S/N) problems have been addressed through the development of higher quality instrumentation[3,6,7] and through the implementation of FTIR VCD capability, as first proposed and demonstrated by Nafie and coworkers.[8-11]

The pioneer in commercial FTIR spectrometers is BioTools, the company of L. Nafie and R. Dukor, who developed the first commercially available VCD spectrometer in 1997, the Chiralir, built by ABB Bomem. Today, FTIR VCD spectrometers are available from various manufactures: Nicolet/Thermo (TOM), Jasco (FVC-4000)[12] and Bio-Rad (FTS-60A)[13,14]. Our VCD instrument is based on the PMA37 module from Bruker Optics.

In what follows, the VCD spectrometer is described in more detail. The different aspects and difficulties that come with the measurement of VCD will be outlined.

3.2 VCD spectrometer

Our VCD spectrometer is based on the Bruker PMA37 module and is coupled to a Bruker IFS 66v/S interferometer. The performance of a similar setup was tested by Urbanová et al.[15] In Figure 3.1 the VCD spectrometer arrangement is schematically given.

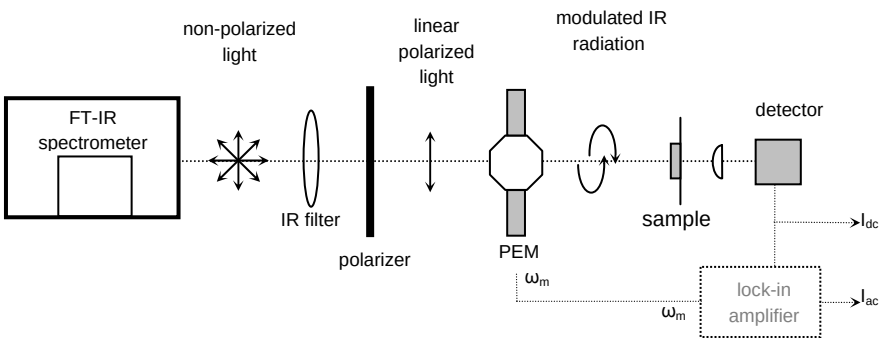

Figure 3.1 Schematic representation of our VCD instrument/setup

A parallel Fourier modulated beam exits the interferometer through a side-port window, passes through a wire grid linear polarizer and a ZnSe photoelastic modulator (PEM). The latter is a device which modulates the polarization of a beam of radiation at a specific frequency. The linear polarizer is placed immediately before the PEM and is set at 45° with respect to the modular axis of the crystal (see Figure 3.2). The circularly polarized radiation then passes through the chiral sample and the transmitted light is focused onto a liquid nitrogen cooled HgCdTe (MCT) detector with BaF_2 windows.

An optical filter is placed between the spectrometer and first polarizer to prevent detector saturation. Because of the double modulation, the signal obtained at the detector is a multiplexed signal. This signal is being processed separately to analyze the high frequency modulated *ac* signal and the *dc* signal. The *ac* signal is measured using a lock-in amplifier (LIA), the *dc* signal is processed as in a standard FTIR system.

3.2.1 Circularly polarized light creation

VCD is measured by modulating the polarization states of the incident beam between left circularly polarized (LCP) and right circularly polarized (RCP) states of infrared radiation. This modulation can be achieved using a device called a photoelastic modulator (PEM).[16]

The operating principle of a PEM is based on the photoelastic effect[17], in which a mechanically stressed sample exhibits birefringence proportional to the resulting strain. In a birefringent crystal, different linear polarizations of light have a slightly different speed when passing through the crystal. In Figure 3.2, a schematic representation of a PEM is given. A 50 kHz electric field is applied to a piezoelectric transducer that is attached to ZnSe crystal. The displacements of the piezoelectric crystal are along the *y* axis, virtually independent of *x* and *z* direction. The type, size and shape of the optical material for this PEM (PEM90II/ZS50 from Hinds instruments – Figure 3.2 is not representative) is chosen specifically for maximum performance in the IR region.[18]

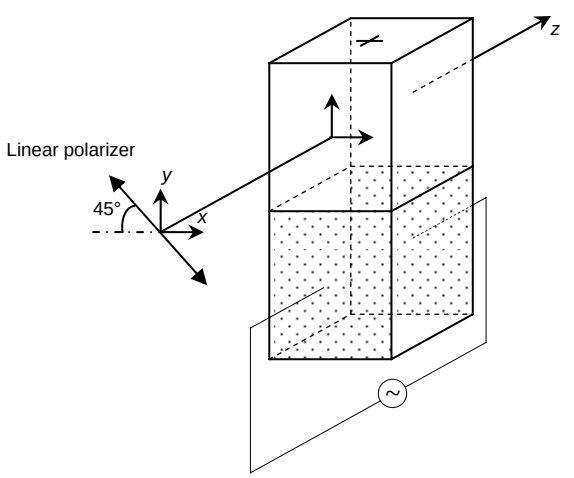

Figure 3.2 Schematic representation of a photoelastic modulator and the linear polarizer, set at 45° with respect to the modular axis (*y*) of the PEM. The *z* axis is the propagation direction of the beam.

The electric field applied to the piezoelectric transducer, causes a sinusoidal stress modulation with frequency ω_m = 50 kHz in the ZnSe crystal.[19] Compression of the ZnSe crystal will induce a phase-lead of the *y* component, stretching will induce a phase lag.[16] The maximal phase difference, and consequently, the maximum induced retardation δ^0 is chosen to be $\pi/2$ ($\lambda/4$) at the centre of the aperture of the crystal. This means that the radiation with a specific frequency υ_i will be modulated between left and right circularly polarized light. This is shown in Figure 3.2, in which the phase difference is given as a function of time. In one period, the light will modulate from linearly polarized (LP) to LCP and RCP radiation, with intermediate elliptical polarization. Figure 3.4 the condition at maximum (RCP and LCP) and minimum (LP) instant phase difference are given. Here, the electric field vectors in *x* and *y* direction are given, and the resultant **E** following the path coordinate *z* of the light.

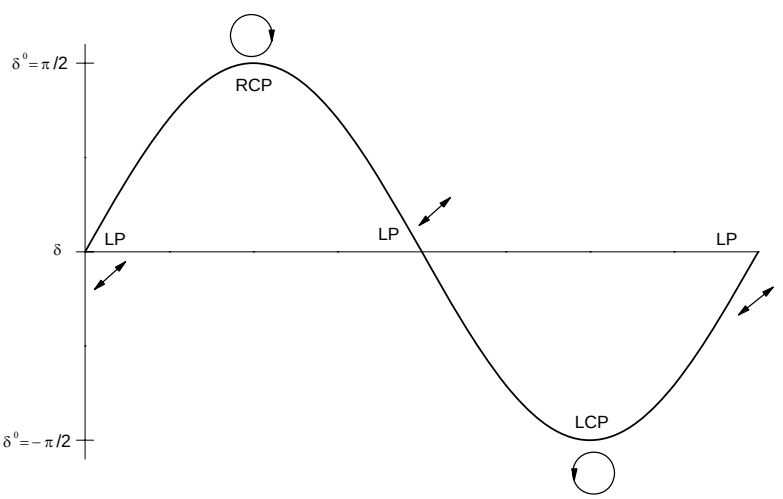

Figure 3.3 Phase difference δ versus time and the polarization states at several points in time with $\delta^0=\pi/2$. RCP = right circularly polarized, LCP = right circularly polarized and LP = linearly polarized

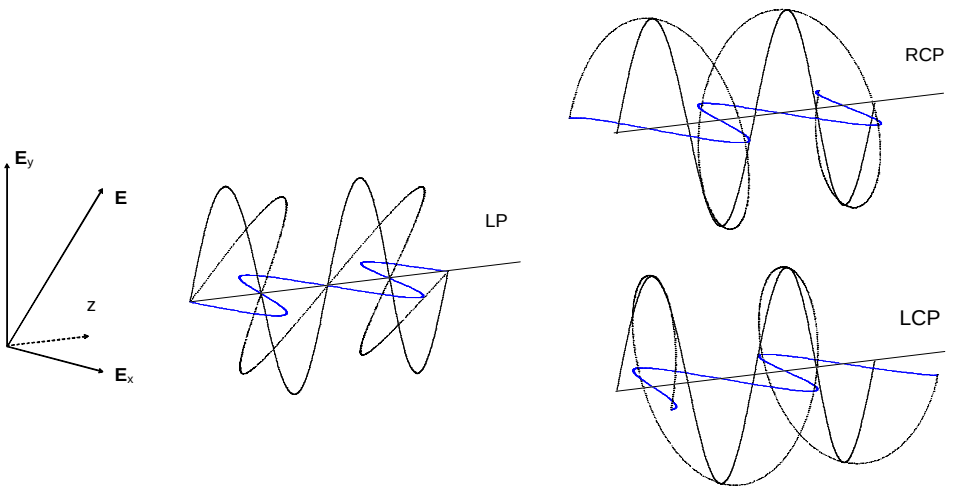

Figure 3.4 The condition of the *x* and *y* components of the electric field vectors at maximum (RCP and LCP) and minimum (LP) instant phase difference. *z* is the propagation direction of the radiation.

3.2.2 Signal detection

The beam that reaches the detector is doubly modulated. First, the light from the source is Fourier modulated. This low frequency modulated signal is then modulated between left and right circularly polarization states at a frequency of 50 kHz, which is significantly higher than the Fourier frequencies. The detector signal is pre-amplified and sent through a high- and low-pass filter. Passing the signal through a low-pass filter, as would be typically found in standard FTIR signal processing networks, yield a standard interferogram of the single beam transmission, often designated as the *dc* interferogram.[20] This part of the detector signal is constant with respect to the polarization modulation.

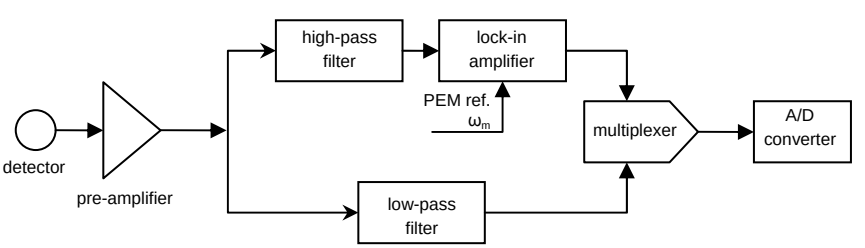

Figure 3.5 The electronic block diagram for the PMA37 featuring the high-pass and low-pass channel.[21]

A 25 kHZ high-pass filter attenuates the Fourier modulated signals (low frequencies) in the detector signal, and is subsequently supplied to a lock-in amplifier (LIA) referenced to the PEM frequency. The intensity modulated signal at a frequency ω_m generated by the VCD in the sample compartment, will be demodulated by the LIA. The output of the lock-in amplifier results in a signal from this VCD channel that is an interferogram corresponding to the polarization modulated signal alone,‡ often referenced to as the *ac* interferogram.[20] The signals from both channels, i.e., the *ac* and *dc* interferograms, are subsequently multiplexed into a single channel and are fed to an analog-to-digital converter.[21]

The multiplexed interferogram can be processed using the macro provided by Bruker.[21] When separated, the *ac* and *dc* interferograms are Fourier transformed, using the correct phase correction (see further), giving the *ac* and *dc* spectral intensities $I_{ac}(\nu)$ and $I_{dc}(\nu)$ at the detector.[23]

The absorbance spectrum can be calculated from these intensities using Equation (3.1) with $I_0(\nu)$ the intensity at the detector in the absence of a sample.[24]

$$A(\nu) = -\log \frac{I_{dc}(\nu)}{I_0(\nu)} \tag{3.1}$$

For the differential absorbance spectrum, the relation in Equation (3.2) was derived,[3] which is discussed extensively by Polavarapu.[19]

$$\Delta A(\nu) = \frac{0.8686}{2J_1(\delta^0_{v_i})} \frac{I_{ac}(\nu)}{I_{dc}(\nu)} \tag{3.2}$$

In the above equation $J_1(\delta^0_{v_i})$ is the first order Bessel function,[25] $\delta^0_{v_i}$ is the maximum retardation induced by the PEM at frequency ν_i. It should be realized that the gain factors introduced by the electronics of the LIA and filters are not explicitly given in Equation (3.2) and should also be taken into account.[19]

‡ In References 19 and 22 an additional *dc* signal at the output of the LIA is mentioned which is attenuated with an additional low-pass filter. Such a filter is not documented for the PMA37 module.

The quantity $\frac{0.8686}{2J_1(\delta_{v_i}^0)}$ can not be determined from a standard VCD experiment, however can be determined via a calibration arrangement.[3] This is discussed in the next section.

3.2.3 Calibration

In Fourier transform spectroscopy, interferograms are transformed in frequency spectra using FT algorithms.[26] In order to do so, the zero path difference (ZPD, no optical path difference between the parallel beams coming from the fixed and movable mirrors) needs to be determined to perform the phase correction. In standard FTIR experiments this is relatively straightforward, as these interferograms have a centre burst and the maximum of the interferogram in principle agrees with the ZPD.[26] For VCD experiments with chiral samples it is not possible to predict the location of the maximum intensity in the interferogram.[19] However, a calibration setup, using a birefringent plate (CdS multiple waveplate) and an extra polarizer (analyzer) can be used to determine the ZPD. The phase correction for this setup can then be transferred to the VCD measurement of a chiral sample using the same electronic and optical path as in the calibration.[27]
Calibration measurements, in our case, are performed with a CdS multiple waveplate (Cleveland Crystals) that is placed in the sample compartment. Its fast axis is parallel to the modular axis of the PEM. The direction of polarization of the analyzer placed after the birefringent plate, is parallel to that of the first polarizer.[21] The high-pass signal for this experiment is a typical two-signed interferogram with two intensity maxima as can be seen in Figure 3.6. The low-channel filtered transmission interferogram is a classic interferogram, also given in Figure 3.6.

The ZPD is determined by locating the position of the two highest values in the interferogram with the same sign. Resetting the ZPD to the mean value between those two positions[21] and using appropriate phase correction methods[15,28], the calibration interferogram can be successfully transformed. In Figure 3.7 the *ac* and *dc* calibration spectra are given. The calibration spectrum is obtained by taking the ratio of the *ac* and *dc* signals (see Equation (3.2)).

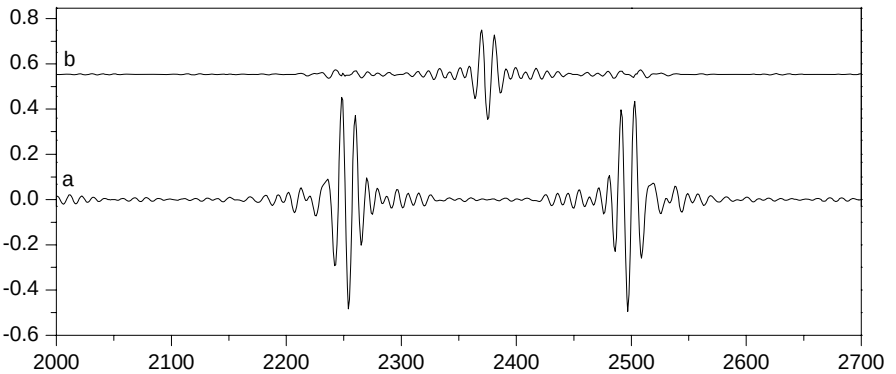

Figure 3.6 Interferograms obtained in a calibration experiment. The multiplexed signal is separated in (a) bi-signate *ac* interferogram (b) transmission *dc* interferogram.

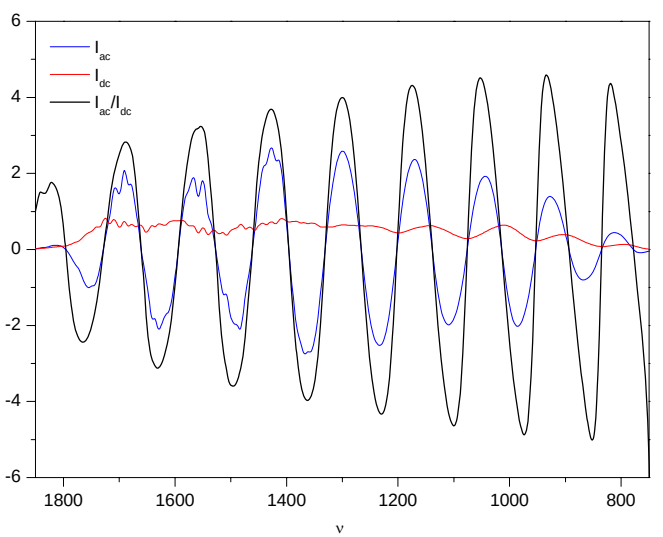

Figure 3.7 The calibration spectrum obtained by taking the ratio of the *ac* and the *dc* signal. The I_{ac} and I_{dc} spectra are measured with the CdS birefringent plate as described in the text.

The frequency dependent calibration factor used to correct VCD spectra as described before, can be determined from the absolute values of the calibration curve at the midpoint of zero-crossings[5], which is illustrated in Figure 3.8. These values can be interpolated for the desired frequency.

This calibration curve provides values for $J_1(\delta^0_{v_i})$ and the appropriate gain factors which are needed to convert the raw VCD spectrum in Equation (3.2). According to Nafie et al.[3] and Polavarapu[19] the calibration curve can be determined more

accurately by performing a second calibration experiment in which the polarization direction is perpendicular to that of the first polarizer, and the fast axis of the birefringent CdS plate is perpendicular to the modular axis of the PEM crystal.

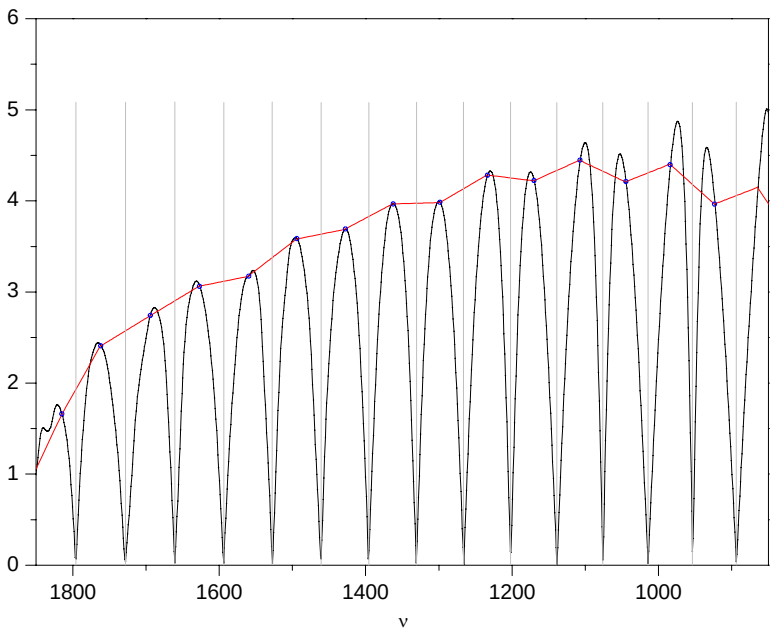

Figure 3.8 Calibration spectrum from Figure 3.6 in which all values are taken positive. The calibration curve is determined by taking the midpoint at in the interval of zero crossings.

3.3 Experimental procedure

Compared to the situation thirty years ago, the measurement of VCD has evolved, and high-quality VCD spectra can be obtained fairly easy these days. Measurements can still be complicated due to the various problems that can occur, i.e., the presence of baseline artifacts[29,30], weak VCD signal, low S/N ratios, etc.

Baseline artifacts typically arise from strain in the lenses and windows through which the beam passes. The strain manifests itself as linear birefringence, which in turn alters the polarization state of the radiation as it passes through the components of the spectrometer.[24] For our setup specifically, it was found that large baseline artifacts were induced at the detector. When the detector focus-lens was perfectly aligned giving a maximum signal at the detector, large artifacts were seen through a non-flat baseline. Reducing the signal at the detector by 10–15%, by moving the lens away from the detector, a much better baseline could be obtained. Cell windows

also introduce baseline deviations, mainly due to strain effects of the windows (CaF_2 and KBr). This was minimized by choosing the optimal orientation of the cell windows.
In addition, artifacts can be associated with the absorbance characteristics of the sample[24]; if the absorbance due to the chiral sample or the applied solvent is too high, a poor S/N ratio is achieved. An absorbance of the solution between 0.7–1.0 absorbance units, which agrees with a transmittance between approximately 10% and 30%, is found to give an optimal S/N ratio. If the largest part of this absorption is attributable to the solvent, then the effective amount of light absorbed by the chiral sample is less, which gives also a poor S/N ratio. The presence of intense solvent absorption in regions of interest is therefore unfavorable. Solvents that were found useful in the 1800–800 cm^{-1} region are $CDCl_3$, CD_2Cl_2, $Cl_2C{=}CCl_2$, and CS_2. Path lengths were most often chosen in the range of 100 and 200 µm, using demountable cells with KBr and CaF_2 windows.

The optical filter placed before the first polarizer is a long wave pass filter with an operational frequency window between 1830 and 800 cm^{-1}. This filter induces large artifacts near 1800 cm^{-1} which is unfavorable for investigations in this area, e.g. for the study of carbonyl stretch regions (see Chapter 8). In this frequency region a 1960 cm^{-1} limiting filter was therefore applied (Spectrogon, Sweden). The disadvantage of this filter is its relative small frequency window, as the long wave cutoff is at 1250 cm^{-1}. As a result, in order to measure the VCD of a sample in the region between 1850 and 800 cm^{-1} two different filters were used.

Various procedures can be found in the literature to facilitate the baseline (artifact) correction.[8,19,24] An overview of such methods is given in Polavarapu et al.[19,31] Recently, Nafie published[24] a paper in which it is stated that the linear birefringence can be eliminated by introducing a second PEM. This was also claimed in a patent filed by BioTools in 2001 describing a prototype of this spectrometer.[23]

In this work, the baseline correction is performed applying various methods. The general idea is to obtain a background VCD that could be used as a baseline. To acquire such a background, ideally, a racemic mixture can be used (a 1:1 mixture of both enantiomers). Such a mixture is not optically active and will therefore exhibit no VCD. In principle, the racemic VCD spectrum will give a good estimate for the baseline.

If the racemic mixture is not available, one can measure the VCD for both enantiomers. The sum of their VCD divided by two, in principle gives the same baseline as one would obtain when measuring the racemic mixture, because the VCD artifacts for both enantiomers are the equal, that is, if the same optical and electronic path is followed. In the same manner, a baseline corrected VCD spectrum can be obtained for a specific enantiomer, by subtracting the VCD of the other enantiomer and divide the resulting spectrum by two. These spectra are often called half-sum and half-difference spectra.[32]

When the racemate and both enantiomers are not readily available, the baseline can be estimated via the measurement of the solvent VCD in the same conditions as the chiral sample. Because the absorbance artifacts for the solvent and the chiral compound are different, this method only gives an approximate baseline. However, in many cases, the baselines obtained via this method yield high quality spectra (see Chapters 6 and 8).[33]

3.4 Reference list

1. Holzwart, G.; Hsu, E. C.; Mosher, H. S.; Faulkner, T. R.; Moscowit, A. *J. Am. Chem. Soc.* **1974**, *96*, 251-252.

2. Hsu, E. C.; Holzwart, G. *J. Chem. Phys.* **1973**, *59*, 4678-4685.

3. Nafie, L. A.; Keiderling, T. A.; Stephens, P. J. *J. Am. Chem. Soc.* **1976**, *98*, 2715-2723.

4. Nafie, L. A.; Cheng, J. C.; Stephens, P. J. *J. Am. Chem. Soc.* **1975**, *97*, 3842-3843.

5. Keiderling, T. A. Vibrational Circular Dichroism. Comparison of Techniques and Practical Considerations. In *Practical Fourier Transform Infrared Spectroscopy. Industrial and Laboratory Chemical Analysis.*, Ferraro, J. R., Krishnan, K., Eds.; Academic Press: San Diego, **1990**; pp 203-284.

6. Su, C. N.; Heintz, V. J.; Keiderling, T. A. *Chem. Phys. Lett.* **1980**, *73*, 157-159.

7. Setnicka, V.; Urbanova, M.; Bour, P.; Kral, V.; Volka, K. *J. Phys. Chem. A* **2001**, *105*, 8931-8938.

8. Lipp, E. D.; Nafie, L. A. *Appl. Spectrosc.* **1984**, *38*, 20-26.

9. Lipp, E. D.; Zimba, C. G.; Nafie, L. A. *Chem. Phys. Lett.* **1982**, *90*, 1-5.

10. Nafie, L. A.; Diem, M. *Appl. Spectrosc.* **1979**, *33*, 130-135.

11. Nafie, L. A.; Diem, M.; Vidrine, D. W. *J. Am. Chem. Soc.* **1979**, *101*, 496-498.

12. Miyazawa, M.; Inouye, K.; Hayakawa, T.; Kyogoku, Y.; Sugeta, H. *Appl. Spectrosc.* **1996**, *50*, 644-648.

13. Hilario, J.; Drapcho, D.; Curbelo, R.; Keiderling, T. A. *Appl. Spectrosc.* **2001**, *55*, 1435-1447.

14. Wang, B. L.; Keiderling, T. A. *Appl. Spectrosc.* **1995**, *49*, 1347-1355.

15. Urbanova, M.; Setnicka, V.; Volka, K. *Chirality* **2000**, *12*, 199-203.

16. Hipps, K. W.; Crosby, G. A. *J. Phys. Chem.-US* **1979**, *83*, 555-562.

17. Brewster, D. *Philos. Trans.* **1816**, *106*, 156.

18. Drake, A. F. *J. Phys.-E-Sci. Instrum.* **1986**, *19*, 170-181.

19. Polavarapu, P. L. Fourier transform infrared vibrational circular dichroism. In *Fourier Transform Infrared Spectroscopy, Vol 4*, Ferraro, J. R., Basile, L. J., Eds.; Academic Press, Inc.: Orlando, **1985**; pp 61-95.

20. Nafie, L. A. *Annu. Rev. Phys. Chem.* **1997**, *48*, 357-386.

21. *PMA 37 User's manual;* Bruker: **2001**.

22. Tsankov, D.; Eggimann, T.; Wieser, H. *Appl. Spectrosc.* **1995**, *49*, 132-138.

23. Nafie, L. A. US 6480277, 2002.

24. Nafie, L. A. *Appl. Spectrosc.* **2000**, *54*, 1634-1645.

25. Margenay, H.; Murphy, G. M. *The mathematics of physics and chemistry;* 2nd ed.; D. Van Nostrand Company, Inc.: New York, **1956**; Vol. 1.

26. Griffiths, P. R. *Chemical Infrared Fourier Transform Spectroscopy;* 1st ed.; John Wiley & Sons: New York, **1975**; Vol. 43.

27. Polavarapu, P. L. *Appl. Spectrosc.* **1984**, *38*, 26-28.

28. Mccoy, C. A.; Dehaseth, J. A. *Appl. Spectrosc.* **1988**, *42*, 336-341.

29. Cheng, J. C.; Nafie, L. A.; Stephens, P. J. *J. Opt. Soc. Am.* **1975**, *65*, 1031-1035.

30. Nafie, L. A.; Vidrine, D. W. Double Modulation Fourier Transform Spectroscopy. In *Fourier Transform Infrared Spectroscopy: Applications to Chemical Systems*, Ferraro, J. R., Krishnan, K., Eds.; Academic Press: New York, **1981**; pp 83-123.

31. Polavarapu, P. L.; Michalska, D. F.; Back, D. M. *Appl. Spectrosc.* **1984**, *38*, 438-442.

32. Aamouche, A.; Devlin, F. J.; Stephens, P. J.; Drabowicz, J.; Bujnicki, B.; Mikolajczyk, M. *Chem.-Eur. J.* **2000**, *6*, 4479-4486.

33. Kuppens, T.; Herrebout, W.; van der Veken, B. J.; Corens, D.; De Groot, A.; Doyon, A.; Van Lommen, G.; Bultinck, P. *Chirality* **2006**, *18*, 609-620.

4

comparison of spectra

4.1 Introduction

An important part in the process of determining absolute configurations (AC) or predominant conformations using vibrational circular dichroism (VCD), is the comparison of the experimental and calculated spectra. Based on their agreement, that is, the location, sign and intensity of the bands, the AC can be assigned.[1]
However, experiments are inherently different compared to results that come from standard DFT calculations. Experimental spectra are recorded for dilute solutions, preferably non-polar solvents, to minimize the solvent-solute interaction (not to mention solute-solute interaction). Theoretical spectra are most often based on a single molecule in vacuum. Computed vibrational frequencies are also overestimated because of the harmonic approximation and the finite basis sets applied.
Due to these differences in approach, “human eye” comparison is often a very subjective approach and can be biased by personal interpretation or as stated by W.C. Herndon and S.H. Bertz “Similarity, like beauty, lies in the eyes of the beholder”.[2] In order to avoid such a bias, numerical comparisons should be performed.
In this chapter, two different methods are discussed to compare and assess the agreement between experimental and calculated spectra; the classical, but labor

intensive approach, in which the experimental bands are assigned to the calculated fundamental frequencies, and a new method, that applies similarity measures for the comparison.

4.2 Simulation of spectra

The calculation of dipole and rotational strengths and their corresponding vibrational frequencies allows the simulation of vibrational spectra for specific chiral compounds with known stereochemistry. For each significant conformation, single conformational spectra can be obtained. Line broadening can be introduced by assuming a Lorentzian band shape[3],

$$f_i(\nu) = \frac{1}{\pi}\frac{\alpha}{(\nu - \nu_i)^2 + \alpha^2} \tag{4.1}$$

The band is centered at the frequency υ_i, and α is the Lorentzian half width at half max (hwhm). The full width at half max (fwhm) is defined as 2α. The area under the band is normalized due to the factor π^{-1}. In Figure 4.1 a Lorentzian band is depicted, centered at $\upsilon_i = 0$ cm^{-1} and $\alpha = 5$ cm^{-1}.

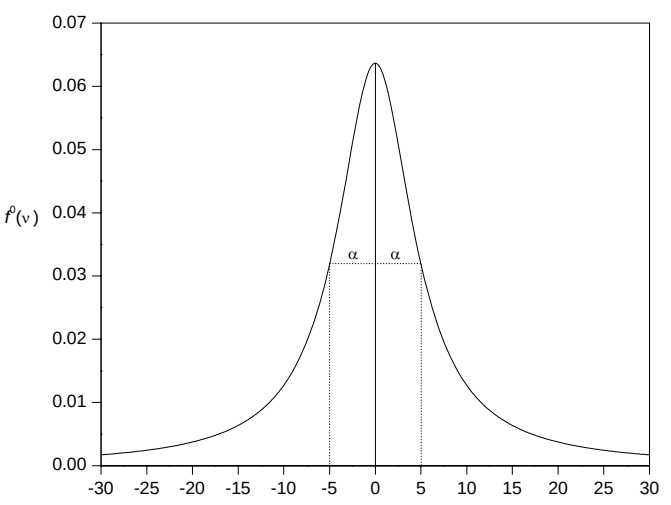

Figure 4.1 Lorentzian function $f^0(\upsilon)$ with a half width at half max (α) of 5 cm^{-1}, υ is in cm^{-1}.

The broadened single conformational spectra can be created and subsequently converted into molar absorptivity units based on Equations (2.6) and (2.13),

$$\varepsilon(\nu) = \frac{1}{9.184 \cdot 10^{-39}} \nu \sum_i D_i f_i(\nu) \tag{4.2}$$

$$\Delta\varepsilon(\nu) = \frac{1}{2.296 \cdot 10^{-39}} \nu \sum_i R_i f_i(\nu) \tag{4.3}$$

Each single conformational spectrum can be taken into account using Boltzmann statistics, creating the simulated IR and VCD spectrum for the studied compound.
These simulated spectra are actually produced to visualize the calculated data and to mimic the experimental spectra. This allows low-level comparison of experimental and theoretical spectra. Agreement between experimental and theoretical IR and VCD spectra allows the determination of the AC of the experimental sample. However, simple comparison, by superimposing both spectra, is not sufficient to determine ACs. A more thorough analysis of the available data has to be performed.

One can correlate the experimental and the simulated/calculated bands based on the available IR and VCD data. Deconvolution of the experimental spectra allows the assessment of the experimental dipole and rotational strengths. Based on the assignment of the experimental bands the experimental and the theoretical dipole and rotational strengths can be compared. This approach is discussed in more detail in §4.3.
Because this method is particularly labor-intensive, new tools were developed that allow the assessment of the similarity between experimental and theoretical spectra on the basis of a similarity measure. This measure quantifies the agreement between the two spectra giving fast and relatively accurate results. This is discussed in §4.4.

4.3 Assignment of fundamentals

To unambiguously assess the agreement between two spectra, a thorough analysis has to be performed. A reliable approach is the correlation of experimental and simulated bands. As VCD is a differential form of IR spectroscopy, IR and VCD transition frequencies are the same. Because of the differential intensities, VCD spectra have extra discriminating potential. As a result, assignment of unresolved IR

bands can be performed using the experimental VCD counterpart. Vice versa, assignment of unresolved VCD bands can sometimes be based on IR band locations. The actual assignments are performed using the calculated fundamentals. These can be performed very accurately and reliably. For example; a simulated IR band displays a good agreement with an experimental band, i.e., relative intensity and location of the band. Based on this agreement, the experimental band can be assigned. However, its corresponding simulated VCD band should also agree with the experimental VCD band which has exactly the same transition frequency as the IR band. The extra dimension of the VCD intensity makes that VCD is a very good tool to assign experimental IR spectra.

Experimental spectra can be deconvoluted using a Lorentzian band shape. In this procedure, Lorentzian functions are fitted against the experimental spectrum, enabling one to estimate the area under the experimental bands. The dipole and rotational strengths are related to the area under the bands via respectively Equations (4.4) and (4.5) which are approximations of Equations (4.2) and (4.3).

$$D_i = 9.184 \cdot 10^{-39} \frac{1}{\nu_{i,\max}} \int \varepsilon_i d\nu \tag{4.4}$$

$$R_i = 2.296 \cdot 10^{-39} \frac{1}{\nu_{i,\max}} \int \Delta\varepsilon_i d\nu \tag{4.5}$$

Accordingly, it is possible to obtain experimental dipole and rotational strengths and these can be correlated to the calculated values based on the experimental band assignments. Illustrations of these assignments and subsequent correlations can be ubiquitously found in literature, e.g., Devlin et al.[4,5] report the prediction of vibrational spectra for camphor, fenchone and α-pinene. Aamouche et al.[6] assigned the experimental bands of two naphtalenone derivatives, and correlated the experimental and theoretical *D* and *R*.

He et al.[7] demonstrated that for 3-chloro-butyne, a small and rigid molecule, the root-mean-square differences between B3LYP/aug-cc-pVTZ predicted and experimentally determined *D* and *R* values were rather large, respectively 29% and 22%. However, the correlation coefficients are respectively 88.7% and 99.5% and a very good resemblance is found between simulated and experimental spectra.

In this work, correlation between experimental/theoretical dipole and rotational strengths is performed for most studied compounds, i.e., in Chapters 5, 6, 7 and §8.4.

4.4 Spectral comparison

In this section, the concepts of correlation functions and similarity measures are proposed for the purpose of spectral comparison.

4.4.1 Correlation functions

The function that describes the overlap of two patterns as a function of a relative shift *r*, is called a correlation function. If we define two functions *f*(*x*) and *g*(*x*), the auto-correlation function can be written as,

$$c_{ff}(r) = \int f(x)f(x+r)dx \tag{4.6}$$

and the cross-correlation function,

$$c_{fg}(r) = \int f(x)g(x+r)dx \tag{4.7}$$

The integral of $c_{ff}(r)$, the auto-correlation integral, is given by

$$\int c_{ff}(r)dr = \left(\int f(x)dx\right)^2 \tag{4.8}$$

The cross-correlation integral is similarly written as

$$\int c_{fg}(r)dr = \int f(x)dx \int g(x)dx \tag{4.9}$$

From Equation (4.9) it can be seen that the area under the cross-correlation function is always equal to the product of the areas under the patterns *f*(*x*) and *g*(*x*). The cross-correlation function can therefore be normalized by dividing it by the root of

the product of the auto-correlation integrals which makes prescaling of $f(x)$ and $g(x)$ unnecessary.

$$c'_{fg}(r) = \frac{c_{fg}(r)}{\sqrt{\int f^2(x)dx \int g^2(x)dx}} \tag{4.10}$$

The integral of $c'_{fg}(r)$ will always be equal to 1. This means, however, that not the normalized cross-correlation integral itself is a measure for the similarity between $f(x)$ and $g(x)$. It is the shape of $c'_{fg}(r)$ that contains the information on the similarity between $f(x)$ and $g(x)$.

In Figure 4.2 the calculated and experimental IR spectra of hexahydro-*as*-indacene-1,8-diol are given. More information on these spectra can be found in Chapter 6. From now on, the simulated and experimental spectra in this chapter will be denoted respectively as *f* and *g*.

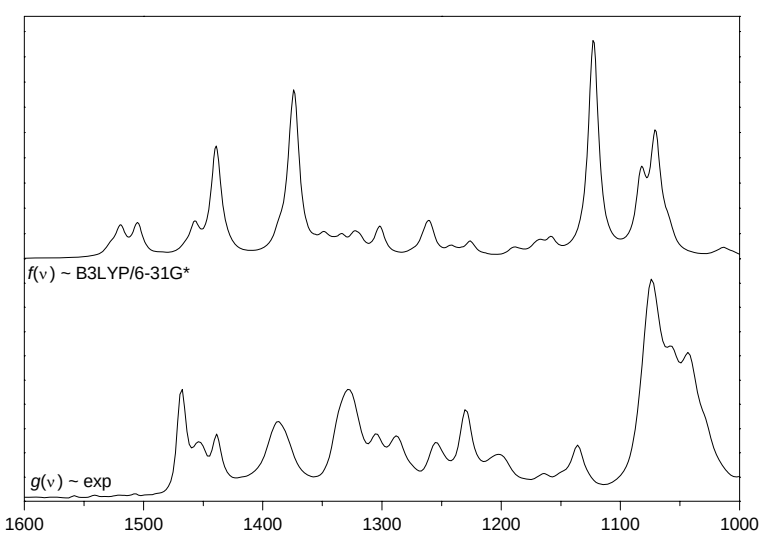

Figure 4.2 Example of two functions, i.e., $g(\upsilon)$ is an experimental IR spectrum and $f(\upsilon)$ is a B3LYP/6-31G* Boltzmann weighted broadened spectrum.[8] Frequency υ is in cm^{-1}.

The theoretically simulated spectrum $f(\upsilon)$ in Figure 4.2 is not frequency scaled. Accordingly, the predicted bands are shifted to higher frequencies, compared to the experimental spectrum. For both $f(\upsilon)$ and $g(\upsilon)$, the correlation functions are given in

Figure 4.3. The area under the correlation functions is normalized. The different shapes of the curves give information on the agreement between $f(\upsilon)$ and $g(\upsilon)$.

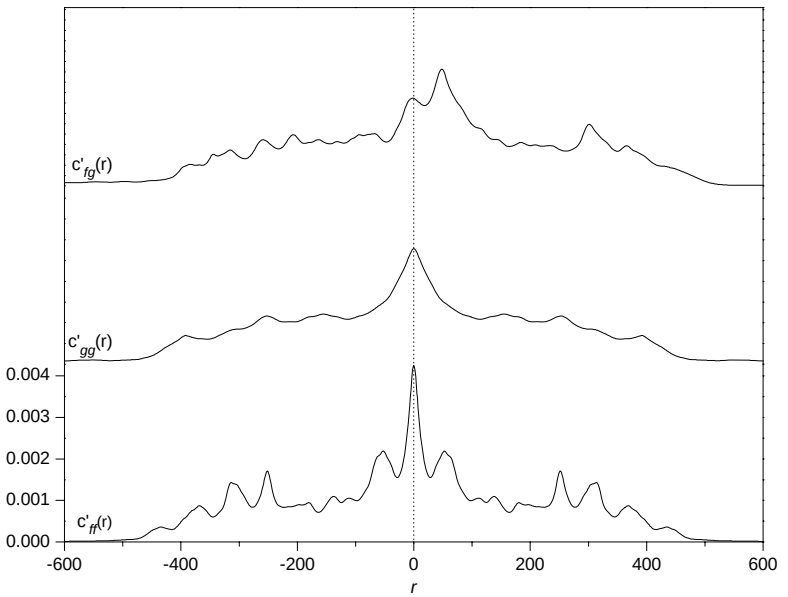

Figure 4.3 Normalized auto-correlation $c'_{ff}(r)$ and $c'_{gg}(r)$ and cross-correlation $c'_{fg}(r)$ functions for $f(\nu)$ and $g(\nu)$ as given in Figure 4.2. The relative shift r is given in cm^{-1}.

The maxima of the auto-correlation functions are situated at a relative shift $r = 0$. The cross-correlation function has a maximum at $r = 48$ cm^{-1}, which indicates that, if the frequencies of $g(\upsilon)$ are shifted over 48 cm^{-1}, the largest similarity can be found.

In contrast to IR spectra, a function that represents a VCD spectrum can have negative function values. Correlation functions of non-positive functions can not always be defined. For example, the normalized auto-correlation function of a sine function in the interval $[-\pi, \pi]$ is infinite because the normalization factor $\left[\int_{-\pi}^{-\pi} \sin x dx\right]^2$ is zero.

If, for a non-positive function, the positive and negative parts are dealt with separately, the evaluation of the correlation functions can be performed. The non-positive function is split-up into two functions, which then both can be evaluated as positive functions.

In Figure 4.4, the experimental and simulated VCD spectra are given, again for hexahydro-*as*-indacene-1,8-diol. Both spectra are partitioned, separating the negative and positive function values. $f^+(\upsilon)$ and $g^+(\upsilon)$ are formed by substituting all negative values with zero function values. $f^-(\upsilon)$ and $g^-(\upsilon)$ are formed similar for the negative part.

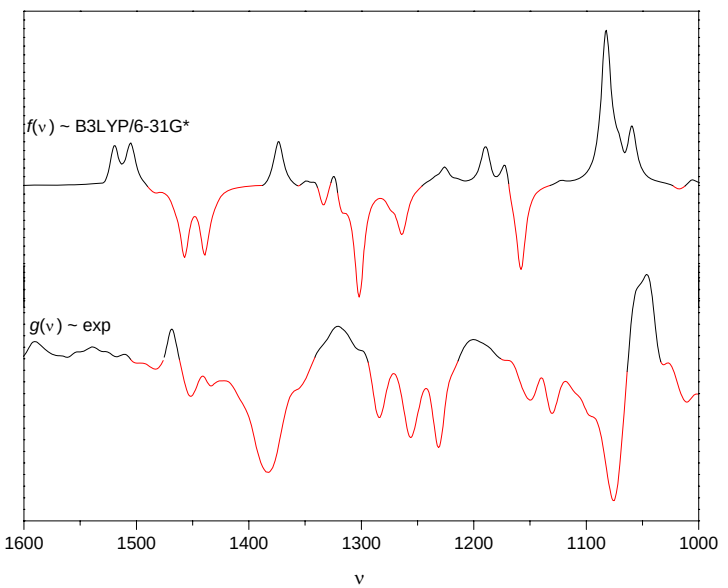

Figure 4.4 Example of two functions, i.e., $g(\upsilon)$ is an experimental VCD spectrum and $f(\upsilon)$ is a B3LYP/6-31G* Boltzmann weighted broadened spectrum.[8] Both spectra are partitioned, i.e., $f^+(\upsilon)$ and $g^+(\upsilon)$ (black) and $f^-(\upsilon)$ and $g^-(\upsilon)$ (red) separating positive and negative function values. υ is in cm^{-1}.

These positive and negative functions can separately be evaluated yielding positive and negative correlation function (c^+ and c^-) and are given in Figure 4.5.

In Figure 4.5 it can be seen that the maxima in the positive and negative cross-correlation functions are respectively shifted towards r values of approximately 32 and 70 cm^{-1}. The higher value for the negative cross-correlation function is due to the large deviation between the positive predicted rotational strength and the negative observed band for fundamental 37 and is discussed in more detail in Chapter 6.

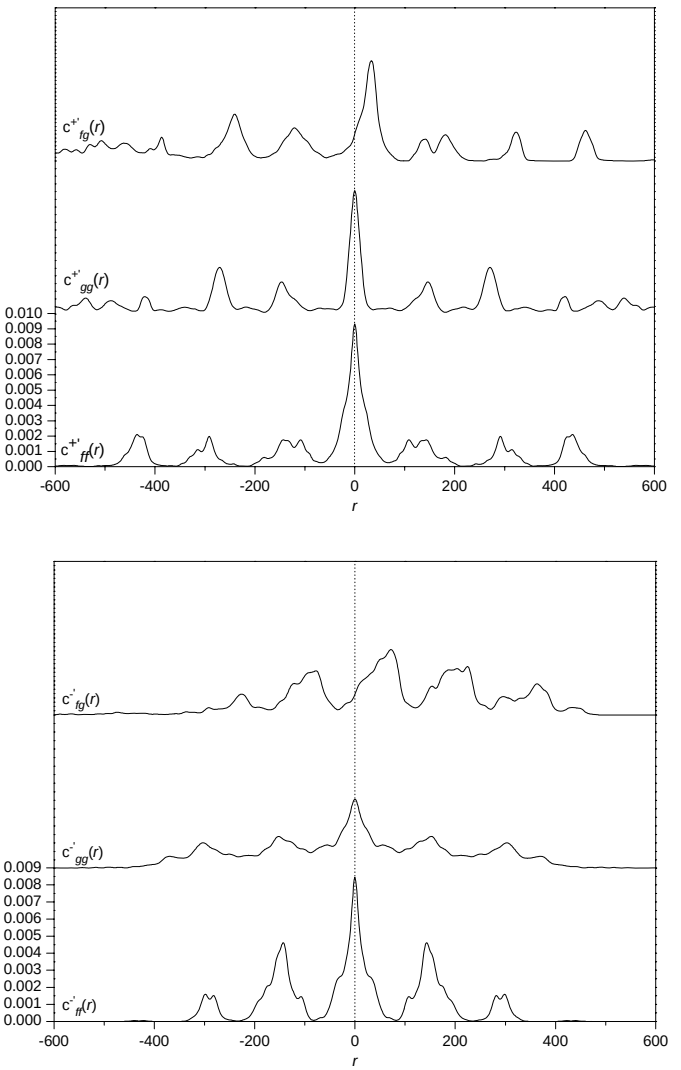

Figure 4.5 Top: Normalized auto-correlation $c^{+\prime}_{ff}(r)$ and $c^{+\prime}_{gg}(r)$ and cross-correlation $c^{+\prime}_{fg}(r)$ functions for $f^{+}(\upsilon)$ and $g^{+}(\upsilon)$ as given in Figure 4.4. Bottom: Normalized auto-correlation $c^{-\prime}_{ff}(r)$ and $c^{-\prime}_{gg}(r)$ and cross-correlation $c^{-\prime}_{fg}(r)$ functions for $f^{-}(\upsilon)$ and $g^{-}(\upsilon)$ as given in Figure 4.4. The relative shift r is given in cm^{-1}.

It is clear now that the similarity information for two spectra is embedded in the shape of the cross-correlation function. By using a special window function, this information can be extracted.

4.4.2 Generalized expression for similarity

In the previous section, it was described that the normalized cross-correlation integral does not contain any information on the similarity of two spectra. If one introduces a weighting function, the interval for the local shift can be chosen. Accordingly, a generalized expression[9] for the similarity *S* between *f*(x) and *g*(x), can be written,

$$S = \frac{\int w_{fg}(r)c_{fg}(r)dr}{\sqrt{\int w_{ff}(r)c_{ff}(r)dr \int w_{gg}(r)c_{gg}(r)dr}} \tag{4.11}$$

The weighting function $w_{fg}(r)$ determines in which manner the similarity information is extracted from the cross-correlation function. $w_{ff}(r)$ and $w_{gg}(r)$ determine the normalization of the weighted cross-correlation function via the auto-correlation functions. A normalized similarity measure is only obtained if the following conditions hold:

$$w_{ff}(r)=w_{fg}(r)=w_{gg}(r) \tag{4.12}$$

If the weighting function is chosen as

$$\begin{aligned} w(r) &= 1 \qquad && if\,|r| = 0 \\ w(r) &= 0 \qquad && if\,|r| \neq 0 \end{aligned} \tag{4.13}$$

the similarity measure in Equation (4.11) is reduced to the overlap integral of both functions, i.e., no relative shift is introduced.

To include the neighborhood in the comparison of the spectra, the weighting function should be defined for $r \neq 0$. Karfunkel et al.[10] proposed their fold criterion, using the function (4.14) which is depicted in Figure 4.6.

$$w(r) = \frac{1}{1 + \alpha\,|r|^{\beta}} \tag{4.14}$$

A triangular function[9] as presented in Equation (4.15) and in Figure 4.6 can also be used as a weighting function.

$$w(r) = 1 - \frac{|r|}{l} \qquad if\ |r| < l$$
$$w(r) = 0 \qquad if\ |r| \geq l \tag{4.15}$$

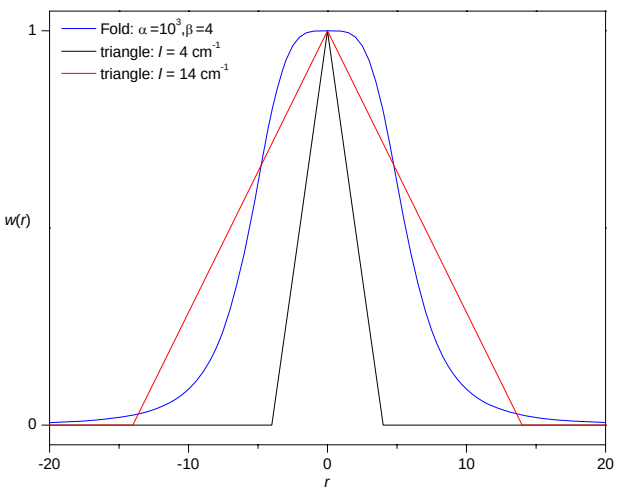

Figure 4.6 Representation of different weighting functions; fold criterion ($\alpha = 10^3$ and $\beta = 4$), and triangular functions (l = 4 and 14 cm^{-1}). The variable r is in cm^{-1}.

Next to the local shifting of function $g(x)$, one can also introduce a scaling factor σ into the function $f(x)$, which could be interesting for the comparison of vibrational spectra. The correlation function (4.7) is accordingly written,

$$c_{fg}^{\sigma}(r) = \int f(\sigma x) g(x + r) dx \tag{4.16}$$

The similarity expression in (4.11) can be rewritten using scaled correlation functions as defined in (4.16), which gives the scaled similarity S^{σ},

$$S^{\sigma} = \frac{\int w_{fg}(r) c_{fg}^{\sigma}(r) dr}{\sqrt{\int w_{ff}(r) c_{ff}^{\sigma}(r) dr \int w_{gg}(r) c_{gg}^{\sigma}(r) dr}} \tag{4.17}$$

When the weighting functions are chosen as defined in (4.13), i.e., only considering the correlation function at $r = 0$, the similarity measure in (4.17) reduces to a scaled overlap measure,

$$S^{\sigma} = \frac{\int f(\sigma x)g(x)dx}{\sqrt{\int f^2(\sigma x)dx \int g^2(x)dx}} \tag{4.18}$$

In Chapter 5, this measure is used to describe the similarity between theoretical and experimental spectra and the mutual agreement between theoretical spectra.
In the next section the introduced triangular function will be used to define a similarity measure that takes into account neighborhoods.

4.4.3 Neighborhood similarity

When calculating vibrational frequencies using ab initio methods, usually a harmonic potential is applied to describe nuclear vibrational motion. In combination with finite basis sets, the predicted frequencies are overestimated. It is common use to correct for this overestimation by scaling the frequencies with a uniform factor. This scaling depends on the applied method and basis set.[11,12]
Evidently, it is important to take this scaling into consideration when comparing the experimental and simulated spectra. The similarity measure in Equation (4.17) introduces a scaling factor σ that allows the correction for the overestimated calculated frequencies. Linear scaling is far from perfect, as simulated bands can still be shifted with respect to their corresponding experimental bands.
A good similarity measure should therefore take into account the neighborhood in direct proximity of the bands. If, in Equation (4.17), a triangular shaped weighting function as defined in Equation (4.15) is chosen, neighborhood comparison can be performed.
The fold criterion is not used, because the implementation of this function is more complex due to the parameters α and β. These have no intuitive meaning in contrast to the parameter l in the triangular weighting function. l (in cm^{-1}) defines the interval for which the relative shift is taken into account. A triangular function is also easy to implement and is was shown that these functions give stable results for XRD spectral comparison.[9]

In Figure 4.7, the experimental and simulated IR spectra (1500–1325 cm^{-1} interval) for di-epoxy-*as*-indacene is given. The corresponding bands are labeled based on the fundamental assignment (see Chapter 6). The frequencies of $f(\nu)$ are not scaled, which can clearly be seen in Figure 4.7.
Evaluation of the spectral similarity using the scaled overlap defined in Equation (4.18) yields a value of 66.8% for an optimal scaling factor $\sigma = 0.954$.
It can be observed that band 52/51 is shifted relative to the two other labeled bands. The spectral similarity assessment can only be effective when this effect is taken into account considering the neighborhoods of the bands. Using the triangular weight function with a windows size l = 40 cm^{-1}, the neighborhood similarity expression in Equation (4.17) yields a value of 94.0% with $\sigma^{opt} = 0.957$.
The latter is clearly a better quantification for the similarity of both spectra compared to the scaled overlap measure.

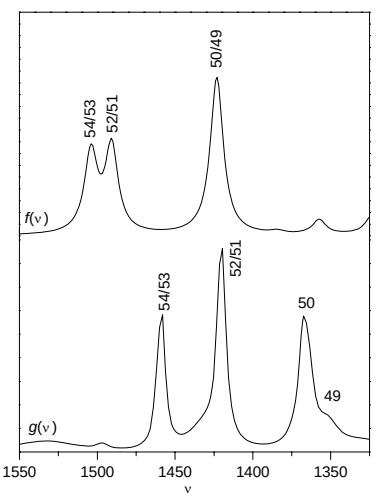

Figure 4.7 1500–1325 cm^{-1} part of the experimental and B3LYP/6-31G* simulated (frequencies are not scaled) IR spectra for di-epoxy-*as*-indacene (Chapter 6). Bands are numbered based on calculated fundamentals.

The size and the shape of the window/weighting function is chosen based on the observation that corresponding bands can be shifted towards each other, but only locally. If they are shifted more than 40 cm^{-1}, after scaling, it is unlikely that these bands are correlated.

The calculation of neighborhood similarities for VCD spectra, is somewhat more complicated because the positive and negative part of the spectrum need to be evaluated separately. Using the positive and negative correlation functions that were

defined previously, two similarity expressions can be written, i.e., $S^{\sigma,+}$ and $S^{\sigma,-}$. The neighborhood similarity measure S^{σ} for VCD spectra is then defined as the arithmetic mean of $S^{\sigma,+}$ and $S^{\sigma,-}$,

$$S^{\sigma} = \frac{S^{\sigma,+} + S^{\sigma,-}}{2} \tag{4.19}$$

4.4.4 Numerical integration

The calculation of the neighborhood similarity using a triangular window function is implemented using Fortran. To evaluate correlation functions and correlation integrals for discrete functions, that is, sampled spectra, numerical integration methods are needed. IR and VCD spectra are a set of two dimensional points, for which an intensity is specified for certain discrete wavenumbers/frequencies.
The objective of numerical integration is to compute an approximate solution to the definite integral:

$$I = \int_{a}^{b} f(x)\,dx \tag{4.20}$$

There are a wide range of methods available to perform numerical integration.[13] For our purpose, Simpson's rule is applied in combination with Richardson extrapolation.[14]
Our implementation was written in Fortran on the basis of the "*Numerical Recipes in Fortran77*" code[14] which was altered for a better performance.
The performance of the numerical integration routine is illustrated, using the product of two Gaussian functions. Gaussians are chosen here, because the product of two Gaussians has a well known analytical expression.[15]

$$\begin{aligned} f_1 &= e^{-(x-10)^2} \\ f_2 &= e^{-(x-11)^2} \end{aligned} \tag{4.21}$$

For this integral an analytical expression of the solution is known,

$$\int e^{-(x-10)^2} e^{-(x-11)^2} dx = \sqrt{\frac{\pi}{2}} \cdot e^{-\frac{1}{2}} = 0.760173450536$$

For the numerical integration with a grid of 0.1, our routine yielded

$$\int_0^{20} f_1(x) f_2(x) dx = 0.\underline{760173450533}$$

which is in good agreement with the analytical result.

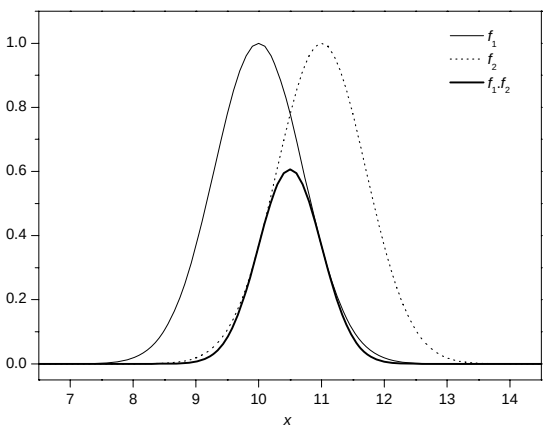

Figure 4.8 Sample Gaussian functions

4.5 Reference list

1. Freedman, T. B.; Cao, X. L.; Dukor, R. K.; Nafie, L. A. *Chirality* **2003**, *15*, 743-758.

2. Herndon, W. C.; Bertz, S. H. *J. Comput. Chem.* **1987**, *8*, 367-374.

3. Schellman, J. A. *Chem. Rev.* **1975**, *75*, 323-331.

4. Devlin, F. J.; Stephens, P. J.; Cheeseman, J. R.; Frisch, M. J. *J. Phys. Chem. A* **1997**, *101*, 6322-6333.

5. Devlin, F. J.; Stephens, P. J.; Cheeseman, J. R.; Frisch, M. J. *J. Phys. Chem. A* **1997**, *101*, 9912-9924.

6. Aamouche, A.; Devlin, F. J.; Stephens, P. J. *J. Am. Chem. Soc.* **2000**, *122*, 7358-7367.

7. He, J. T.; Petrovich, A.; Polavarapu, P. L. *J. Phys. Chem. A* **2004**, *108*, 1671-1680.

8. Kuppens, T.; Vandyck, K.; Van der Eycken, J.; Herrebout, W.; van der Veken, B. J.; Bultinck, P. *J. Org. Chem.* **2005**, *70*, 9103-9114.

9. De Gelder, R.; Wehrens, R.; Hageman, J. A. *J. Comput. Chem.* **2001**, *22*, 273-289.

10. Karfunkel, H. R.; Rohde, B.; Leusen, F. J. J.; Gdanitz, R. J.; Rihs, G. *J. Comput. Chem.* **1993**, *14*, 1125-1135.

11. Scott, A. P.; Radom, L. *J. Phys. Chem.-US* **1996**, *100*, 16502-16513.

12. Wong, M. W. *Chem. Phys. Lett.* **1996**, *256*, 391-399.

13. Davis, P. J.; Rabinowitz, P. Methods of Numerical Integration, New York: Academic Press, **1984**.

14. Press, W. H.; Teukolsky, S. A.; Vetterling, W. T.; Flannery, B. P. *Numerical Recipes in Fortran 77;* 2nd ed.; Cambridge University Press: **1992**.

15. Szabo, A.; Ostlund, N. S. *Modern Quantum Chemistry;* Dover Publications, Inc.: New York, **1996**.

5

determination of the stereochemistry of hydroxymethyl dihydrodioxinopyridine by VCD and the effect of DFT integration grids

5.1 Introduction

It is well known that optical isomers may demonstrate a different biological activity.[1] Therefore, in the pharmaceutical industry, the knowledge of the absolute configuration is of the utmost importance. Among several methods available to determine the absolute configuration, X-ray diffraction (XRD) is often the method of choice because it yields the most reliable results. This relatively labor-intensive method requires the availability of well-defined crystals and the presence of heavy atoms, which is often a problem. A second popular method, nuclear magnetic resonance (NMR), is not always applicable either. Often specific methods have to be

Kuppens, T.; Langenaeker, W.; Tollenaere, J. P.; Bultinck, P. *J. Phys. Chem. A* **2003**, *107*, 542-553

applied to eliminate the degeneracy of the enantiomers e.g., the use of chiral solvents or chiral shift-reagents. These methods are sometimes troublesome and may give contradictory results.[2-4] Retro-synthesis also has several drawbacks, and is usually labor-intensive.
A technique that holds great promise for the determination of the absolute configuration and gains importance quite rapidly, is the measurement of vibrational circular dichroism (VCD). This technique is based on the differential absorption of left and right circularly polarized infrared (IR) radiation. Because circularly polarized light (CPL) itself has handedness, different interactions of the two forms of light occur with chiral molecules, i.e., the differential CPL absorptions of two enantiomers are opposite in sign.

For VCD to be applicable, the acquired spectra should be interpretable. However, interpretation of VCD spectra is not straightforward and it requires an algorithm that relates both the structure and spectra. Hence the necessity to predict spectra for different stereoisomers. By comparing the predicted spectrum with the experimental spectrum, identification of the stereoisomer present in solution is possible. The main issue in the calculation of the theoretical spectra is the sign of the differential transitions and the prediction of the rotational strength, which is proportional to the area of the VCD band. A reliable quantum chemical method for molecules of variable size was developed by Stephens et al. in 1996.[5-8] Several studies have already illustrated the applicability of this method in determining the absolute configuration of a chiral molecule.[9,10]
From an experimental point of view, VCD exhibits several important advantages. Nowadays, VCD spectra can be measured almost routinely, using specially adapted IR spectrometers. An even more important advantage over XRD techniques is that measurements are possible in solvents, i.e., there is no need for crystals or “heavy” atoms.
In this study, the absolute configuration of 3-hydroxymethyl-2,3-dihydro-[1,4]dioxino[2,3-*b*]pyridine, **1**, shown in Figure 5.1 is known by its synthesis route.[11] The *R* and *S* enantiomers respectively correspond to the samples with positive and negative optical rotation.

VCD spectra have been recorded for the *R* and *S* enantiomer. Both spectra were made available to the authors of the present study without revealing any stereochemical information. DFT calculations were used to simulate VCD spectra for both the *R* and *S* enantiomer, and by comparison between the experimental and

theoretical spectra, the absolute configuration could be assigned. The first aim of the present study is to find out whether these assignments can be made correctly by comparison to the absolute configuration that was known via the synthesis route.
Another objective is to study the effect of the basis set size and the DFT integration grid on calculated VCD properties. It was also investigated if it is possible to make the calculation less expensive without affecting the quality of the simulated VCD spectra.

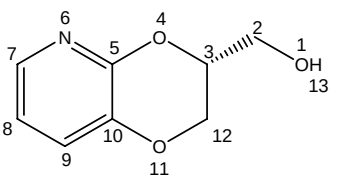

Figure 5.1 (*R*)-3-hydroxymethyl-2,3-dihydro-[1,4]dioxino[2,3-*b*]pyridine ≡ (*R*)-**1** and atom numbering for modeling purposes

5.2 Experimental

The *R* and *S* enantiomers of **1** were obtained with a 98% ee. Synthesis routes were previously described in the literature.[11,12] The IR and VCD spectra for both enantiomers of **1** were recorded in a 90 µm CaF_2 cell on a Bruker IFS66/S FTIR spectrometer coupled to a PMA37 module. The unpolarized absorption spectra have a resolution of 2 cm^{-1} and a recording time of 25 seconds each. The resolution of the VCD spectra is 6 cm^{-1} with recording times of 3 h each. Samples of **1** were dissolved in $CDCl_3$ at a concentration of 0.27 M. The spectral window was set to 1000–1650 cm^{-1}. Experimental spectra of (+)-**1** are shown in Figure 5.2.

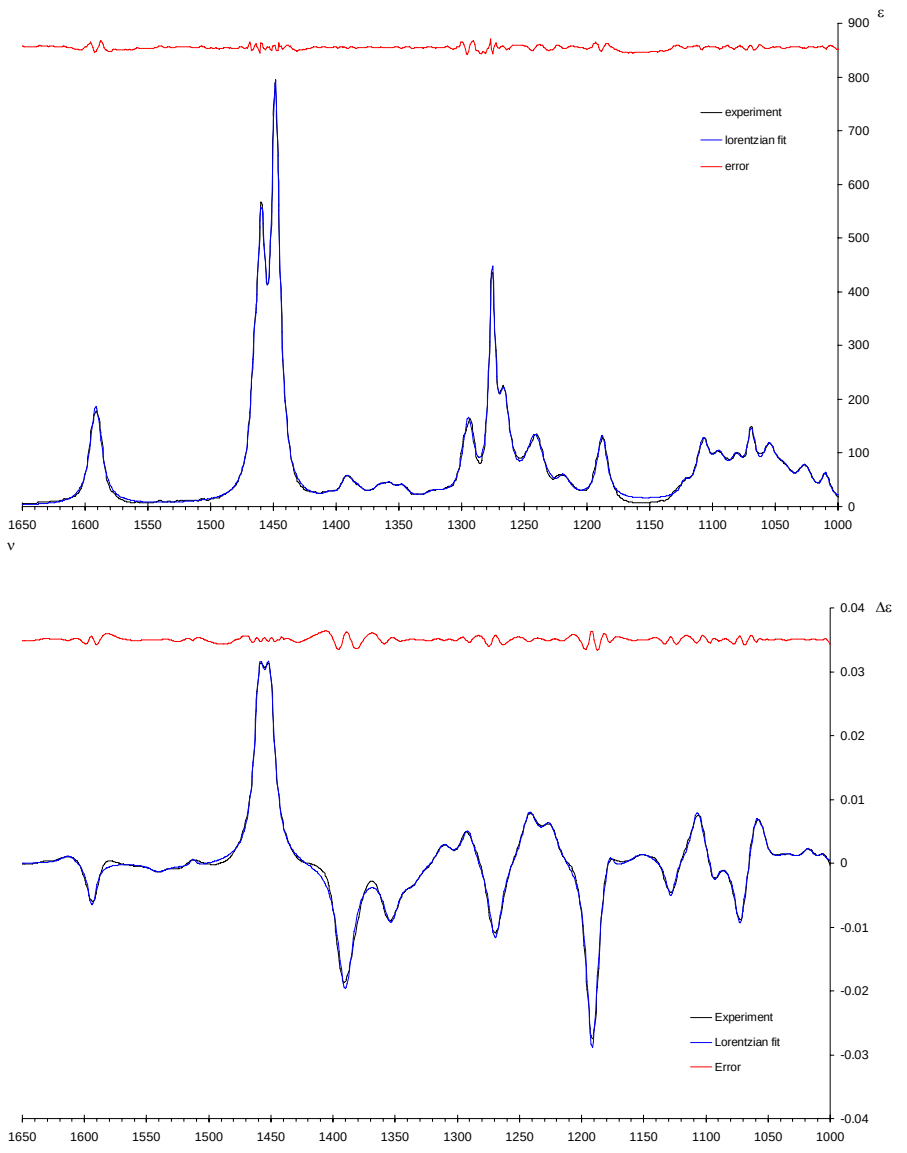

Figure 5.2 IR (top) and VCD (bottom) spectra for (+)-**1**, including Lorentzian fit and error. Intensities and differential intensities are in molar absorptivity units, frequencies in cm^{-1}.

5.3 Computational methodology

Multiple conformations of **1** are possible and each conformation contributes to the IR and VCD spectra of the molecule. Because calculated spectra depend heavily on the molecular conformation,[13] a thorough conformational analysis is needed.

To find the different minimum energy conformations of the molecule, a two-way conformational analysis approach is used. In the first approach, B3LYP/6-31G* calculations are used. The pyridine ring is considered rigid, whereas the dioxane ring, as well as all other fragments, are considered flexible. The dihedral angles are developed in a 60° grid. Not all resulting structures are chemically sound, and prior to initiating a geometry optimization the search tree is pruned by the application of a bump check and ring constraints. The remaining conformations are then optimized on the B3LYP/6-31G* level. The resulting minima are collected for further geometry optimizations and spectroscopic calculations.
A major problem with systematic searches is the combinatorial explosion, which hampers systematic searches for larger molecules and finer dihedral angle grids. The computational requirements of DFT calculations are such that finer dihedral grids in a systematic search are not practicable.[‡] Therefore a stochastic search was also applied using the MM3 force field.[14]
This method, as implemented in the MM3(96) program,[15] optimizes the geometry of a molecule and randomly moves (kicks) each atom in an atom-centered sphere with a predefined radius. The new structure is then reoptimized, yielding a new or possibly previously located stationary point, after which the geometry of this new stationary point is again randomly kicked. Own routines are used to automate the entire search and check for convergence. The conformational search is considered converged if all minima with a relative energy – compared to the global minimum – below 20 kcal/mol are found more than 20 times and a new stochastic search does not yield any new minima.[16] Redundant structures are also removed by compiling the lists of stationary points from different stochastic searches.
DFT molecular geometries were obtained by the minimization of the MM3 geometries of the stationary points found during the MM3 conformational search. These were supplemented with the B3LYP/6-31G* geometries from the ab initio conformational analysis. DFT calculations are performed with Gaussian98 rev A6[17]

[‡] At that moment, i.e., 2002

using the B3LYP hybrid density functional[7,18,19] and DZ and TZ Pople style basis sets, i.e., 6-31G, 6-31G*, 6-31G** and 6-311G**.[20] The cc-pVDZ, cc-pVTZ and cc-pVQZ Dunning basis sets are also applied. Default Gaussian98 basis set parameters are used.

For the geometry optimization and the calculation of the spectroscopic properties different integration grids are applied. Euler-Maclaurin-Lebedev grids of the type (*m*,*n*) are used, having *m* radial shells and *n* angular points per shell. Pruned[21] versions of these grids are also applied. In the latter the number of angular points varies with the shell with a maximum of *n* on radii that are relevant for chemical bonding.[22] The default grid in Gaussian98 is a pruned version of the (75,302) grid further denoted as (75,302)p, invoked with the keyword GRID=FineGrid. The (50,194)p grid[21] is invoked with the keyword GRID=SG1Grid and the (35,110)p grid with GRID=CoarseGrid.[23] Other grids can be used by specifying the INT(GRID=mn) keyword.

Gauge including/invariant atomic orbitals (GIAO) are used to calculate atomic axial tensors (AAT). Together with harmonic force fields and atomic polar tensors (APT) the rotational strengths are calculated.[5-7]

For each DFT energy minimum in the potential surface, the dipole and rotational strengths are calculated. The resulting line spectra are then broadened using a Lorentzian band shape giving single conformer spectra. For the total frequency range, the total broadened dipole and rotational strength is calculated as the weighted sum of the single conformer spectra (Equation (5.1)). In other words; the IR and VCD spectra of a molecule is computed as a linear combination of the spectra for the different conformations.

$$\begin{aligned} D_{\mathrm{tot}}(v) &= \sum_{\mathrm{A}} \mathrm{P(A)} \cdot D_{\mathrm{A}}(v) \\ R_{\mathrm{tot}}(v) &= \sum_{\mathrm{A}} \mathrm{P(A)} \cdot R_{\mathrm{A}}(v) \end{aligned} \tag{5.1}$$

P(A), being the population of conformer A, is calculated assuming a Boltzmann distribution (Equation (5.2)) where *i* runs over all conformers,

$$\mathrm{P(A)} = \frac{e^{-H_{\mathrm{A}}^{0}/RT}}{\sum_{i} e^{-H_{i}^{0}/RT}} \tag{5.2}$$

We omit the entropic contributions to the Gibbs free energy and, consequently, use the enthalpy to calculate the conformational populations.[24] The enthalpy is calculated via DFT using the standard thermochemical expressions and under the usual assumptions.[25]

A quantitative measure has to be introduced to discuss the similarity of spectra. We use a measure based on the overlap integral given in Equation (5.3),

$$S^{\sigma} = \frac{\int f(\sigma\nu)g(\nu)d\nu}{\sqrt{\int f^2(\sigma\nu)d\nu \int g^2(\nu)d\nu}} \tag{5.3}$$

where f and g are the functions that represent the spectral intensities at each frequency ν. Identical spectra have an overlap integral equal to 1. For IR spectra, with no negative values, the overlap integral tends to 0 when the similarity becomes smaller. For VCD spectra however the overlap can become negative, and S^{σ} is equal to −1 when the spectra are the opposite of each other, that is, when both spectra are from enantiomers. Frequency scaling is introduced by the factor σ.

Experimental IR and VCD spectra are Lorentzian fitted to calculate the experimental dipole and rotational strengths via following relations;[26]

$$\begin{aligned} D_i &= 9.184 \cdot 10^{-39} \int \varepsilon_i \frac{d\nu}{\nu} \\ R_i &= 2.296 \cdot 10^{-39} \int \Delta\varepsilon_i \frac{d\nu}{\nu} \end{aligned} \tag{5.4}$$

Here, ε and Δε are the absorptivity and differential molar absorptivity in $l.mol^{-1}cm^{-1}$. D and R are in esu^2cm^2.

5.4 Results and discussion

5.4.1 Conformational analysis

Conformational isomers of **1** differ by :

- the orientation of the exocyclic bond (τ_1, $O^{11}C^{12}C^3C^2$), i.e., pseudo-equatorial or pseudo-axial,
- the rotameric dihedral angle about the C^2–C^3 bond (τ_2, $O^4C^3C^2O^1$) and
- the rotameric dihedral angle about the O^1–C^2 bond (τ_3, $C^3C^2O^1H^{13}$).

The position of the exocyclic substituent, that is, the methylhydroxyl group, is either designated as *eq* or *ax*. Assuming three typical minima in the torsion potential energy, that is, 60°, 180° and −60°, the dihedral angles are respectively denoted as gauche clockwise (G), trans (T) and gauche counterclockwise (G') for the C–C bond torsion (τ_2), and similarly g, t and g' for the O–C bond torsion (τ_3).

The combined conformational search yielded 10 stationary points, all corresponding to minima on the MM3 PES. These are shown in Table 5.1 and Figure 5.3 with their corresponding notation, relative MM3 energies and corresponding values for τ_1, τ_2 and τ_3.

Table 5.1 MM3 minima, conformational description, relative MM3 energy (RE, in kcal/mol) and key dihedral angles (τ_1, τ_2 and τ_3, in degrees).

		RE MM3	τ_1 $O^{11}C^{12}C^3C^2$	τ_2 $O^4C^3C^2O^1$	τ_3 $C^3C^2O^1H^{13}$
1	eqGg'	0.00	179	63	−54
2	eqG'g	0.08	178	−61	58
3	axGg'	0.64	−59	61	−57
4	eqG't	1.60	176	−68	170
5	eqTt	1.63	179	179	−177
6	eqGt	1.80	178	69	−172
7	axG'g	1.84	−67	−68	39
8	axGt	2.43	−59	69	−169
9	axTt	2.45	−60	177	179
10	axG't	4.72	−67	−68	170

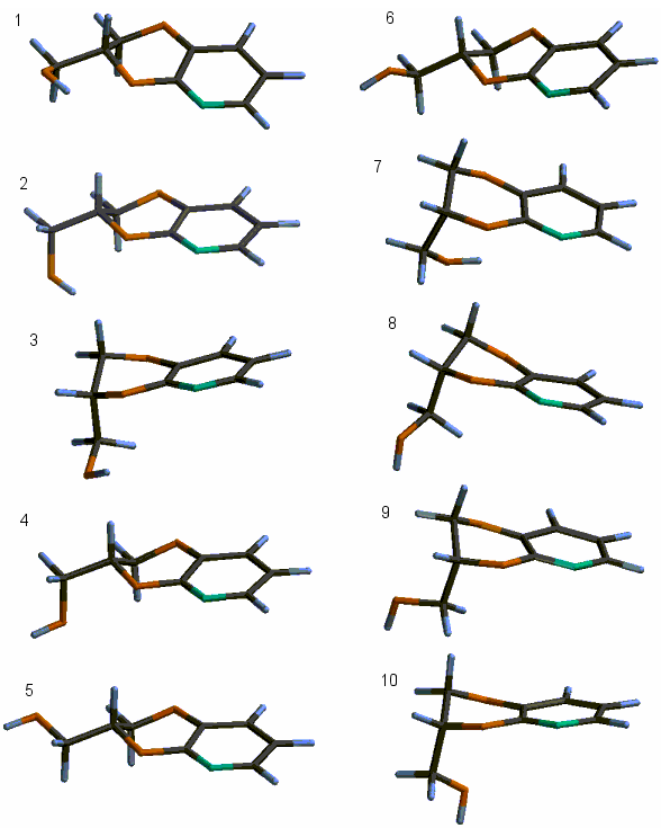

Figure 5.3 Visualization of the PES minima for (*R*)-**1**.

All 10 minima were used as starting geometries for geometry optimizations using the B3LYP functional and the different basis sets mentioned above. These geometry optimizations were not straightforward. Through application of constrained geometry optimizations, we succeeded in locating most minima with the different Pople style basis sets. A common feature for these basis sets is the fact that no axG't structure could be located. The 6-31G basis set was found to be severely lacking in giving a good description of the molecular PES. Given the conformational dependence of the VCD spectra, this basis set was not further considered. For the cc-pVDZ and cc-pVTZ basis set only conformations with a relative energy below 3 kcal/mol (according to 6-311G**) were minimized. A summary of the results of these different geometry optimizations is presented in Table 5.2.

Table 5.2 B3LYP relative energies (in kcal/mol) for the located minima, the conformational description and MM3 energy ranking. For the cc-pVDZ and cc-pVTZ basis set only the 5 lowest energy conformations are considered.

	6-31G*	6-31G**	6-311G**	cc-pVDZ	cc-pVTZ
2 eqG'g	0.00	0.00	0.00	0.00	0.00
1 eqGg'	0.81	0.84	0.81	0.85	0.55
3 axGg'	1.60	1.61	1.60	1.63	1.55
5 eqTt	2.49	2.49	2.06	2.56	1.78
9 axTt	2.94	2.91	2.52	2.90	2.40
4 eqG't	3.59	3.54	3.21	-	-
7 axG'g	4.28	4.30	4.14	-	-
6 eqGt	4.96	4.92	4.47	-	-
8 axGt	5.41	5.36	4.97	-	-

Tables 5.1 and 5.2 clearly show that the relative energies of the different structures differ quite strongly between the MM3 and DFT levels of theory. The energetic ordering of the minima also undergoes a number of changes. Most notably, on the MM3 level, the structures with an equatorial exocyclic bond were lower in energy than those with an axial exocyclic bond (except for the axGg' structure). On the DFT level there is no longer such a clear distinction between both types of structures. The relative energies found using the 6-31G* and 6-31G** basis sets differ little, but when going to the 6-311G** basis set, the energetic spread of the minima is reduced. This effect is also found when going from the cc-pVDZ to the cc-pVTZ basis set. As mentioned above, the 6-31G basis set yields fewer minima, and for those that were found, the relative energies differ strongly from the more extended basis sets (data not shown).

Table 5.3 MM3 ranking, conformational description, relative B3LYP/6-31G* energy (RE, in kcal/mol) and optimized key dihedral angles (τ_1, τ_2 and τ_3, in degrees).

		RE	τ_1 $O^{11}C^{12}C^3C^2$	τ_2 $O^4C^3C^2O^1$	τ_3 $C^3C^2O^1H^{13}$
2	eqG'g	0.00	−177.1	−60.4	58.0
1	eqGg'	0.81	−178.4	58.1	−53.4
3	axGg'	1.60	−64.1	56.1	−52.2
5	eqTt	2.49	−178.9	176.6	−178.7
9	axTt	2.94	−65.2	171.4	174.5
4	eqG't	3.59	178.5	−74.3	163.2
7	axG'g	4.28	−69.7	−59.0	70.3
6	eqGt	4.96	179.6	73.2	−162.3
8	axGt	5.41	−63.5	68.4	−162.5

Table 5.3 gives the dihedral angles τ_1, τ_2 and τ_3 for the optimized B3LYP/6-31G* geometries. The comparison with Table 5.1 clearly shows that the dihedral angles in the MM3 structures agree quite well with the DFT values.

Table 5.4 gives the relative energies using various DFT integration grids. Only small distinctions between the different grids are found, with the exception of the (35,110)p grid. The extent of the difference between the (35,110)p grid and the other grids also depends on the conformations involved. Table 5.5 gives the energy difference (in μhartree) for the eqGg' conformer relative to the (99,974) grid energy. Again, only minor effects are seen, except for the (35,110)p grid, where the deviation is an order of magnitude larger. Geometries (expressed through τ_1, τ_2 and τ_3) differ very little between the various grids, again except for the (35,110)p grid.

Table 5.4 B3LYP/6-31G* relative energies (in kcal/mol) for the located minima, using different DFT integration grids.

	(35,110)p	(50,194)p	(75,302)p	(50,302)	(75,194)	(75,434)	(99,302)
2 eqG'g	0.00	0.00	0.00	0.00	0.00	0.00	0.00
1 eqGg'	0.69	0.83	0.81	0.80	0.84	0.82	0.80
3 axGg'	1.91	1.56	1.60	1.60	1.56	1.59	1.59
5 eqTt	2.42	2.52	2.49	2.48	2.54	2.49	2.48
9 axTt	2.90	2.91	2.94	2.94	2.92	2.96	2.94
4 eqG't	3.48	3.60	3.59	3.59	3.60	3.59	3.59
7 axG'g	4.22	4.33	4.28	4.26	4.33	4.28	4.26
6 eqGt	4.70	4.97	4.96	4.95	4.98	4.96	4.95
8 axGt	5.64	5.39	5.41	5.41	5.38	5.40	5.40

Table 5.5 B3LYP/6-31G* relative energies with respect to the (99,974) grid (RE, in μhartree) and optimized dihedral angles (τ_1, τ_2 and τ_3, in degrees) for conformation eqGg'.

DFT Grid	RE	τ_1 $O^{11}C^{12}C^3C^2$	τ_2 $O^4C^3C^2O^1$	τ_3 $C^3C^2O^1H^{13}$
(35,110)p	189.07	−178.0	59.6	−53.4
(50,194)p	−13.58	−178.4	58.1	−53.8
(75,302)p	16.58	−178.4	58.1	−53.8
(50,194)	−20.19	−178.3	58.1	−53.3
(50,302)	21.92	−178.4	58.0	−53.3
(50,434)	6.96	−178.4	58.0	−53.3
(50,974)	9.51	−178.4	58.2	−53.7
(75,194)	−27.24	−178.4	58.1	−53.2
(75,302)	14.68	−178.4	58.1	−53.3
(75,434)	−0.48	−178.4	58.0	−53.2
(75,974)	1.63	−178.4	58.0	−53.2
(99,194)	−28.49	−178.4	58.2	−53.7
(99,302)	12.96	−178.4	58.1	−53.2
(99,434)	−1.89	−178.4	58.1	−53.2
(99,974)	0.00	−178.4	58.0	−53.2

5.4.2 Single conformational spectra

Basis set dependence for the single conformational spectra was studied. Vibrational frequencies calculated with various basis sets, scale differently with respect to each other. A maximization of the overlap integral S^{σ} was carried out by varying the scale factor σ in Equation (5.3), using the cc-pVQZ basis set as reference. In Table 5.6 S^{σ}_{max} and σ_{max} are given for the eqGg' conformation, both for the IR and VCD spectra.

Table 5.6 Maximized overlap integrals (S^{σ}_{max}, in percent) and optimal scaling factor σ_{max} relative to the B3LYP/cc-pVQZ broadened spectra for the eqGg' conformation.

		6-31G	6-31G*	6-31G**	6-311G**	cc-pVDZ	cc-pVTZ
IR	S^{σ}_{max}	81.8	84.1	77.5	83.5	75.0	96.0
	σ_{max}	0.998	0.989	0.992	1.000	0.994	0.999
VCD	S^{σ}_{max}	35.6	56.3	53.7	58.6	30.3	70.1
	σ_{max}	0.997	0.988	0.993	0.999	1.000	0.999

The 6-31G basis set, being the smallest basis set used, produces an IR spectrum that has a large overlap with the cc-pVQZ IR spectrum. However, this overlap integral is fortuitously large; both spectra differ significantly from each other. For the eqGg' single conformer VCD spectra, the performance of the 6-31G basis set is poor compared to the larger basis sets (Table 5.6), again indicating the 6-31G set to be of little use for our purposes. This agrees with the findings of Stephens et al.[9] The performance of the cc-pVDZ basis set is also inferior to comparable basis sets. The cc-pVTZ basis set surpasses the other basis sets.

One may expect properties calculated with denser grids to be more accurate than those calculated with smaller, less dense grids. The IR and VCD overlap integrals with σ equal to 1.000 for the eqGg' conformer are calculated with the (99,974) grid spectra as reference, and are given in Table 5.7. The grids with 194 angular points have a performance that is less compared to the other grids with the same number of shells. The overlap integrals for the VCD and IR spectra calculated with 50 radial shell grids are all surprisingly high. This seems to be an artifact, attributed to a small

but noticeable frequency shift of the peak at approximately 448 cm^{-1} (mode 9b[‡]: O−H out-of-plane bending vibration) relative to the (99,974) grid. For the (75,194) and (99,194) grids this relative shift is larger than for the (50,194) grid (respectively 4.48 and 4.98 against 1.60 cm^{-1}). Because of the considerably high dipole and rotational strengths of mode 9b these shifts have a substantial effect on the overlap integral. When the number of angular points per shell is augmented, *S* increases, but a dip in the overlap integral for the grids with 434 angular points is observed. This can also be attributed to the frequency shift at 448 cm^{-1}, which is larger for the 434 than for the 302 and 974 angular point grids, resulting in a poorer overlap for the 434 angular point grids. When looking at the quality of the least squares fitting (correlation coefficient) of the dipole and rotational strength with respect to the reference grid it is seen that the effect of the 448 cm^{-1} artifact is absent. The performance of the 75 and 99 radial shell grids is equal. Pruned grids with 50 and 75 shells have also similar performances compared to those of the non-pruned versions. The (35,110)p grid shows only poor agreement with the (99,974) grid.

The computational cost is an important parameter in the applicability of a method. In Table 5.7 the computational load for the calculation of the spectroscopic properties for the conformation eqGg' is given relative to the (75,302)p grid. It can be observed that the CPU load increases when the grid becomes denser. The (75,302)p and (75,302) grids give virtually the same results as well as the (50,194)p and (50,194) grids, however with less CPU load for the pruned grids; 0.7 against 1.8 for the (50,194) type grid and 1.0 against 3.7 for the (75,302) type grid.
The (50,194)p VCD spectrum of conformer eqGg' is shown in Figure 5.4 along with the (99,974) spectrum for the 1000–1650 cm^{-1} interval. Agreement with the reference grid, as seen and discussed above, is still very good, with an overlap integral of 99%. With the former grid the computational cost is reduced by 30% compared to the (75,302)p Gaussian98 default grid.

[‡] Vibrational modes are denoted with the fundamental number (on the basis of the calculated spectrum) and the corresponding conformation, i.e., a ≡ eqG'g, b ≡ eqGg', c ≡ axGg' and d ≡ eqTt.

Table 5.7 Correlation coefficient for dipole and rotational strengths (r^2, in percent) and overlap integrals (*S*, in percent) for IR and VCD spectra (σ=1.000) relative to the (99,974) grid for the simulated IR and VCD spectra for conformation eqGg'. The computational load is given relative to the (75,302)p grid.

DFT Grid	r^2 *D*	r^2 *R*	S_{IR}	S_{VCD}	Rel CPU
(35,110)p	93.56	94.96	82.4	64.7	0.5
(50,194)p	99.71	99.67	98.5	97.2	0.7
(75,302)p	99.99	99.98	99.8	99.7	1.0
(50,194)	99.63	99.66	98.8	97.7	1.8
(50,302)	99.86	99.96	99.3	98.7	2.6
(50,434)	99.90	99.94	98.5	97.8	3.2
(50,974)	99.84	99.93	99.6	99.3	7.2
(75,194)	99.91	99.86	95.5	93.0	2.5
(75,302)	99.99	99.98	100	99.9	3.7
(75,434)	99.99	99.99	99.5	99.3	5.0
(75,974)	100.0	99.99	100	100	11.3
(99,194)	99.88	99.84	95.1	92.1	3.1
(99,302)	99.99	99.98	100	99.9	4.3
(99,434)	100.0	99.99	99.7	99.6	5.7
(99,974)	100.0	100.0	100	100	13.4

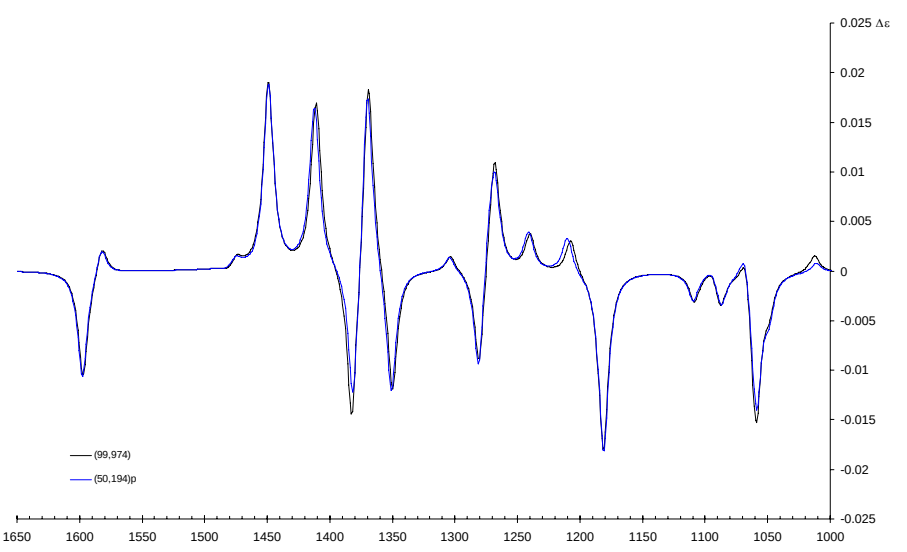

Figure 5.4 VCD spectra of conformer eqGg' for the (50,194)p and (99,974) reference grid. Differential intensities are in molar absorptivity units, frequencies in cm^{-1}.

One of the fundamental mathematical problems with numerical integration using a finite grid is the rotational invariance.[27] Rotation of the molecule as a whole leaving the grid axes fixed, may cause an unphysical change in the computed energy. This effect is even more pronounced with derivative calculations, such as the calculation of harmonic frequencies.[28]

The single point energy, harmonic frequencies and the dipole and rotational strengths were calculated for 3 different orientations of the eqG'g B3LYP/6-31G* equilibrium geometry; the standard orientation rotated by respectively 10° and 20° about the *x* axis (10x and 20x), and the standard orientation successively rotated by 20° about the *x* axis and 30° about the *y* axis (20x30y). These calculations were performed in the (75,302)p and (50,194)p grids.

Table 5.8 B3LYP/6-31G* relative single point energies (RE, in kcal/mol) for the eqG'g equilibrium geometry, correlation coefficient for dipole and rotational strengths (r^2, in percent) and overlap integrals (*S*, in percent) for IR and VCD spectra (σ=1.000) with respect to the standard orientation for 3 different orientations (described in the text). Two grids are considered, i.e. the (50,194)p and (75,302)p. The overlap integrals are given for two frequency intervals, i.e., 300–2000 cm^{-1} and 1000–2000 cm^{-1} (in italics).

(50,194)p	RE	r^2 *D*	r^2 *R*	S_{IR}	S_{VCD}
10x	−0.0096	99.35	99.42	97.7 *99.1*	91.6 *97.4*
20x	0.0248	97.03	97.71	95.9 *99.2*	92.6 *98.0*
20x30y	0.1079	99.02	97.58	93.3 *94.7*	89.3 *92.6*

(75,302)p	RE	r^2 *D*	r^2 *R*	S_{IR}	S_{VCD}
10x	−0.0049	99.67	99.75	99.5 *99.9*	99.2 *99.6*
20x	0.0052	99.86	99.92	99.9 *100*	99.8 *99.9*
20x30y	0.0027	99.86	99.88	99.3 *99.6*	98.9 *99.1*

As can be seen in Table 5.8, for both grids the relative energies are not rotation invariant. For the (50,194)p grid there is a rather large effect on the relative energy for orientation 20x30y, i.e., 0.1079 kcal/mol compared to the standard orientation. This behavior is undesirable, because of the significant influence on the conformational populations. The energy differences for the (75,302)p grid are in the order of 10^{-3} kcal/mol, which is not significant for our purposes.
The dipole and rotational strengths are not rotationally invariant for both grids, but differences with the standard orientation are minimal. For the (50,194)p grid there is one significant sign inversion for orientation 20x at approximately 477 cm^{-1} (mode 10a: O−H and pyridine out-of-plane bending vibration). For the (75,302)p grid, no significant sign inversions are observed.
Also in Table 5.8, the correlation coefficients for dipole and rotational strengths and overlap integrals of the IR and VCD spectra are given for different orientations with respect to the standard orientations. The overlap integral is calculated for two frequency intervals, i.e., 300–2000 cm^{-1} and 1000–2000 cm^{-1}.
It can be seen that the (50,194)p overlap integrals are larger for the 1000–2000 cm^{-1} interval. This due to the poor agreement of the low vibrational frequencies.[28] For the 1000–2000 cm^{-1} interval, differences are observed between the spectra from the different orientations, but these are not considered significant.
The (75,302)p spectra are virtually rotationally invariant for the 1000–2000 cm^{-1} interval. The (75,302)p vibrational frequencies beneath 500 cm^{-1} are not rotationally invariant, and if these are of interest, a denser grid should be used.

To illustrate the strong conformational dependence of VCD, in Figure 5.5 the (75,302)p B3LYP/6-31G* eqGt and eqGg' single conformer VCD spectra are shown. They differ in energy by 4.15 kcal/mol. Geometrical differences are negligible except for one dihedral angle τ_3 ($\Delta\tau_1 = 2.0°$ / $\Delta\tau_2 = 15.1°$ / $\Delta\tau_3 = 108.9°$). The VCD spectra for both conformations are very different. Some vibrational frequencies are shifted and multiple peak inversions can be seen.

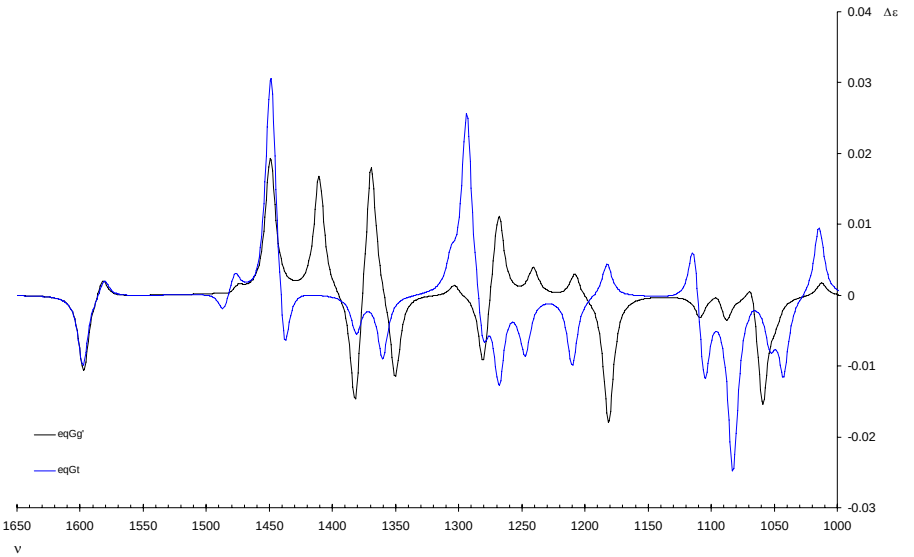

Figure 5.5 Single conformer spectra of eqGt and eqGg' calculated at B3LYP/6-31G* level and the (75,302)p grid. Differential intensities are in molar absorptivity units, frequencies in cm^{-1}.

5.4.3 Boltzmann weighted spectra

In Figure 5.6 the Lorentzian fitted experimental IR and VCD spectra are given for (*R*)-(+)-**1**. Every peak is fitted to a Lorentzian type band, with variable width. The peak numbering is based on the simulated (Boltzmann weighted) B3LYP/6-31G* and B3LYP/cc-pVTZ spectra.

Table 5.9 gives Boltzmann populations for all minima, calculated using the 6-31G* and cc-pVTZ basis sets and the (75,302)p grid. The major contributions to the 6-31G* IR and VCD spectra are from eqG'g, eqGg' and axGg' conformations.

Table 5.9 Relative B3LYP/6-31G* and B3LYP/cc-pVTZ enthalpies (ΔH^0, in kcal/mol) and Boltzmann populations (% P, T = 298.15 K) for the (75,302)p grid.

	6-31G*		cc-pVTZ	
Conf	ΔH^0	% P	ΔH^0	% P
eqG'g	0.00	73.13	0.00	64.43
eqGg'	0.79	19.25	0.55	25.66
axGg'	1.57	5.19	1.53	4.85
eqTt	2.32	1.46	1.66	3.88
axTt	2.83	0.61	2.37	1.18
eqG't	3.35	0.25	-	-
axG'g	4.22	0.06	-	-
eqGt	4.63	0.03	-	-
axGt	5.15	0.01	-	-

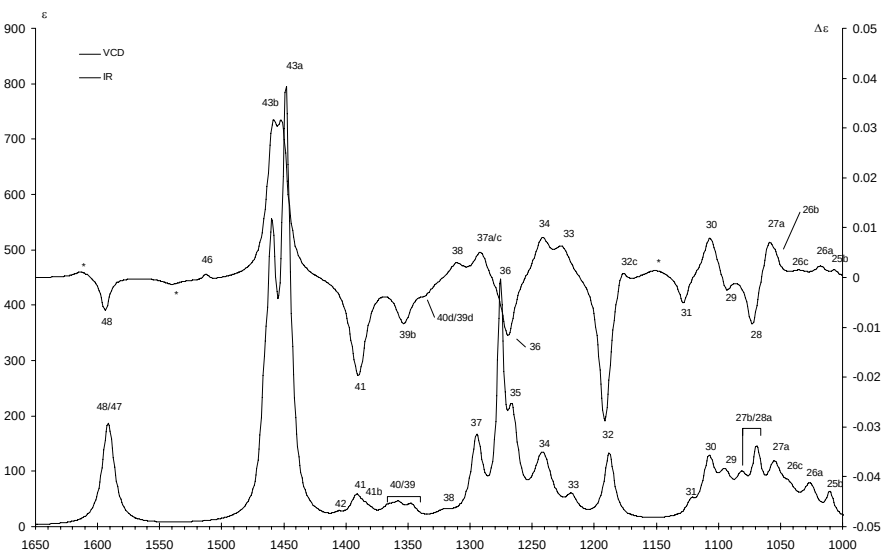

Figure 5.6 Lorentzian fitted experimental IR and VCD spectra for (+)-**1**. Fundamentals are numbered based on B3LYP/6-31G* and B3LYP/cc-pVTZ calculations. Intensities and differential intensities are in molar absorptivity units, frequencies in cm^{-1}.

The 6-31G* basis set is often used as a sufficiently good basis set for VCD calculations.[9] Using Equation (5.3) for the experimental and the broadened IR 6-31G* spectrum, an optimized scaling factor of 0.9669 (yielding a maximized IR overlap integral of 85%) was found. This agrees well with the scaling factor cited in the literature, being 0.9614.[29]

The absolute values of the experimental dipole strengths, given in Table 5.10, do not agree with the calculated, but a proportional agreement is observed. There is also a good agreement between the experimental and simulated spectra and most of the experimental peaks can be assigned as can be seen in Figure 5.6 and Table 5.10.
Experimental IR peaks 39 and 40 are not resolved but have small intensities and a doublet is observed for mode 43.
Most experimental VCD peaks can be assigned based on the B3LYP/6-31G* calculations (Table 5.10). Good agreement is seen between the calculated and the experimental rotational strengths.
Some experimentally observed peaks can not be assigned, that is, the peak between 26b and 26a, the one between 31 and 32c, between 38 and 39b, between 48 and 46 and the one left to 48. Peaks 30 and 26b have the wrong sign, as can be seen in Table 5.10 and Figure 5.7.

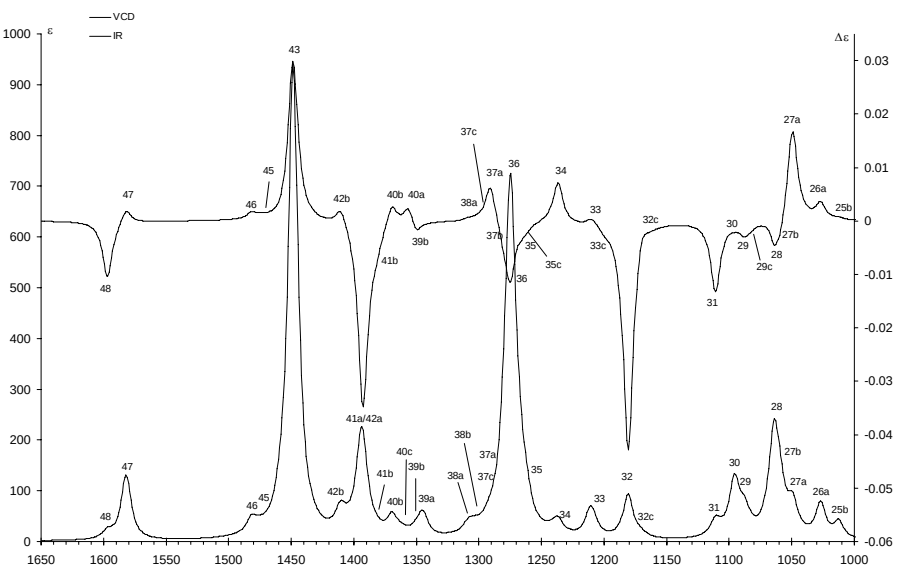

Figure 5.7 B3LYP/6-31G* simulated IR and VCD spectra for (*R*)-**1**, considering all conformations. Intensities and differential intensities are in molar absorptivity units, frequencies in cm^{-1}.

In order to find the reason for these peak inversions, particularly for mode 30 (being the only visible inversion), B3LYP/cc-pVTZ IR and VCD spectra were also simulated and are given in Figure 5.8. The frequency scaling factor was determined to be 0.9779 (yielding a maximized IR overlap integral of 86%).

The peak assignment is given in Table 5.11. It can be observed that there are more visible peaks compared to the 6-31G* spectrum. The conformational energy separation is smaller which gives higher populations for the considered minima which can be seen in Table 5.9. Peaks of conformation eqTt are visible, which was not the case for the 6-31G* spectrum.

All experimental IR and VCD peaks can be assigned based on the cc-pVTZ spectrum. The rotational strengths for modes 39 and 40 (Table 5.11 and Figure 5.8) are predicted with the wrong sign. The peak in the experimental IR spectrum that could not be assigned based on the 6-31G* spectrum corresponds with the B3LYP/cc-pVTZ 26c mode. Other small differences between the IR spectra for both basis sets are the intensities for peak 28a and peak 42a. The negative experimental VCD peak between 38 and 39b agrees with the coinciding cc-pVTZ 39d and 40d modes. Again the experimental VCD peak between peaks 32c and 31, between peaks 46 and 48 and the one left from peak 48 can not be assigned. It can be observed that mode 30 is predicted with the corrected sign for the cc-pVTZ basis set. The overall agreement of the cc-pVTZ simulated VCD spectrum compared with the experimental spectrum is very good.

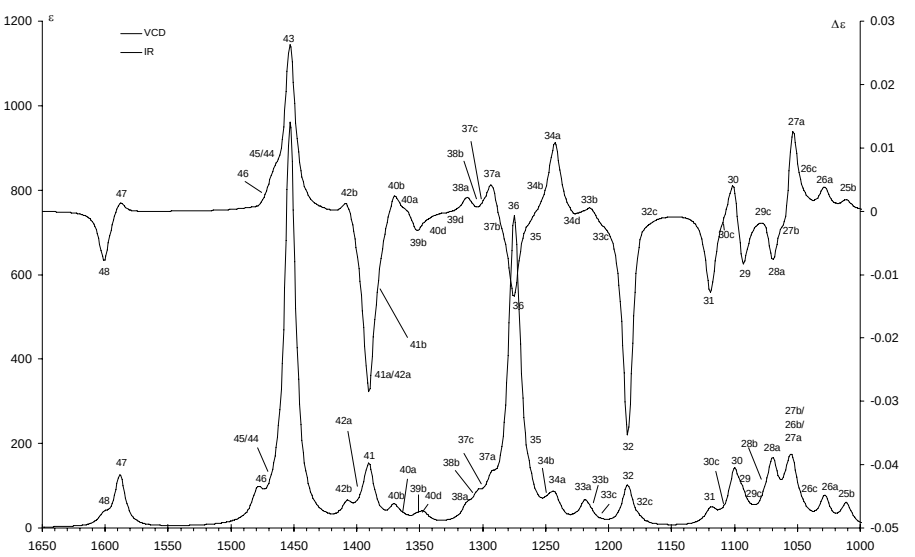

Figure 5.8 B3LYP/cc-pVTZ simulated IR and VCD spectra for (*R*)-**1**, considering only the five lowest energy conformers. Intensities and differential intensities are in molar absorptivity units, frequencies in cm^{-1}.

Table 5.10 Assignment of the experimental peaks based on the B3LYP/6-31G* calculated spectra. The experimental values of the vibrational frequencies (in cm^{-1}), dipole (*D*, in 10^{-40} esu^2cm^2) and rotational strength (*R*, in 10^{-44} esu^2cm^2) were calculated by Lorentzian fitting. Fundamentals are assigned according to the minimum (a ≡ eqG'g, b ≡ eqGg', c ≡ axGg'). Calculated values of *D* and *R* are Boltzmann weighted according to Table 5.9.

Fund	experiment			B3LYP/6-31G*		
	frequency	*D*	*R*	frequency*	*D*	*R*
25b	1009.98	41.19	2.37	1012.51	12.06	1.30
26a	1026.19	97.63	7.61	1026.95	24.46	11.33
	1043.26	94.67	7.21			
26b	1054.93	142.70	7.21	1049.20	0.06	−1.71
27a	1059.53		23.28	1049.34	19.78	59.78
27b			−36.47	1059.19	20.39	−10.35
28a	1069.07	120.22		1063.90	63.47	−19.45
28b	1081.27	88.44		1067.90	6.74	2.67
29c	1094.70	114.74	−10.10	1082.90	2.01	−2.52
29a				1087.83	11.80	−5.08
29b				1087.89	3.75	−2.20
30b	1107.59	149.14	35.89	1095.25	6.43	0.71
30a				1095.84	34.04	−1.93
31b	1122.07	21.95	−17.67	1108.79	1.78	−1.87
31a				1111.05	10.06	−41.61
32c	1187.96	138.10	11.23	1170.11	2.64	10.27
32a	1191.43		−98.52	1180.59	26.02	−122.52
32b				1181.27	5.64	−10.66
33c	1218.25	41.32	28.68	1199.93	0.23	−1.90
33b				1207.86	5.30	2.01
33a				1211.08	18.45	2.54
34a	1241.47	229.52	33.81	1236.60	9.52	21.38
34b				1240.77	2.51	2.09
35c	1265.98	210.45		1261.93	12.40	−2.17
35a				1267.19	4.81	−9.59
35b				1268.06	23.27	6.39
36b	1275.65	244.56	−46.67	1272.30	18.24	0.81
36a				1274.97	232.39	−31.60
37b		169.61		1280.50	19.79	−6.06
37a	1294.65		21.69	1290.68	4.00	20.36
37c				1294.57	3.22	1.10
38b	1321.13	25.34	12.31	1303.33	4.13	0.89
38a				1308.63	7.03	1.08
39a				1344.93	16.80	0.15
39b	1347.16	23.20	−34.64	1350.40	3.46	−6.44
40a	1357.45	26.42		1356.42	0.73	9.09
40c	1365.61	25.89		1362.71	3.28	−0.32
40b	1383.48	24.14		1369.45	13.33	10.53
41b	1391.62	41.49	−78.20	1381.98	2.36	−8.85
41a				1392.64	52.83	−90.56
42a				1395.46	31.54	0.40
42b	1405.91	5.16		1410.69	15.81	8.27
43a	1448.25	556.84	63.91	1448.47	261.14	67.22
43b	1459.64	402.54	64.16	1449.18	62.99	9.21
44a				1458.61	3.10	−2.24
44b				1459.40	3.51	−0.07
45b				1474.28	2.06	0.48
45a				1474.41	0.32	0.67
46b	1512.77		1.58	1481.38	0.93	−0.19
46a				1481.68	9.00	2.73
47a				1581.99	35.64	4.80
47b				1582.11	9.05	1.27
48a	1591.44	190.67	−13.05	1596.76	3.56	−20.54
48b				1597.21	1.08	−4.76

* Scaled with factor 0.9669

Table 5.11 Assignment of the experimental peaks based on the B3LYP/cc-pVTZ calculated spectra. The experimental values of the vibrational frequencies (in cm^{-1}), dipole (*D*, in 10^{-40} esu^2cm^2) and rotational strength (*R*, in 10^{-44} esu^2cm^2) were calculated by Lorentzian fitting. Fundamentals are assigned according to the minimum (a ≡ eqG'g, b ≡ eqGg', c ≡ axGg', d ≡ eqTt). Calculated values of *D* and *R* are Boltzmann weighted according to Table 5.9.

Fund	experiment			B3LYP/cc-pVTZ		
	frequency	*D*	*R*	frequency*	*D*	*R*
25b	1009.98	41.19	2.37	1008.86	17.22	5.12
26a	1026.19	97.63	7.61	1026.02	19.50	12.67
26c	1043.26	94.67	6.16	1042.17	3.97	4.91
27a	1054.93	142.70	23.28	1051.61	27.95	46.92
26b				1053.28	10.00	1.73
27b				1056.24	13.80	−22.82
28a	1069.07	120.22	−36.47	1067.22	38.40	−25.99
28b				1072.95	9.53	4.12
29c	1081.27	88.44	−10.10	1083.04	5.96	−4.02
29a	1094.70	114.74		1090.90	10.65	−27.37
29b				1092.15	1.42	−1.38
30b	1107.59	149.14	35.89	1096.77	11.17	−1.87
30a				1098.21	27.33	24.69
30c				1107.88	3.04	−0.29
31b	1122.07	21.95	−17.67	1115.01	2.39	−1.14
31a				1116.77	8.13	−37.30
32c	1187.96	138.10	11.23	1173.59	5.17	20.20
32a			−98.52	1182.12	21.38	−90.57
32b				1182.82	7.73	−9.08
33c	1218.25	41.32	28.68	1202.75	0.89	−4.40
33b				1211.84	5.42	4.34
33a				1216.52	13.59	0.49
34d				1225.00	1.91	−6.57
34a	1241.47	229.52	33.81	1239.74	15.19	26.68
34b				1244.00	5.84	5.42
35b	1265.98	210.45		1269.88	67.63	4.55
35a				1271.07	13.14	−14.62
36a	1275.65	244.56	−46.67	1272.86	160.95	−24.13
36b				1273.78	0.88	0.25
37b	1294.65	169.61	21.69	1281.39	3.37	−3.58
37a				1289.93	18.80	12.71
37c				1295.11	6.97	2.36
38b	1321.13	25.34	12.31	1301.14	13.59	−1.70
38a				1309.50	9.74	5.65
39d				1325.31	0.48	−0.77
40d	1336.03		−9.15	1341.16	0.67	−2.47
39a	1347.16	23.20		1343.97	6.62	−0.10
39b	1357.45	26.42	−9.15	1349.38	3.43	−7.18
40a	1365.61	25.89	−34.64	1357.47	1.37	2.31
40b	1383.48	24.14		1367.40	12.48	10.20
41b	1391.62	41.49		1380.81	1.66	−8.74
41a			−78.20	1387.41	41.61	−59.24
42a				1393.07	6.04	−7.99
42b	1405.91	5.16		1405.00	12.44	7.29
43a	1448.25	556.84	63.91	1449.81	207.16	46.17
43b	1459.64	402.54	64.16	1450.52	78.24	10.90
44b				1461.33	5.60	2.29
44a				1461.84	1.34	4.52
45a				1464.95	0.45	1.50
45b				1465.94	0.86	1.24
46b	1512.77		1.58	1474.35	5.17	−1.57
46a				1476.59	12.85	0.02
47a				1584.80	26.11	3.30
47b				1585.11	10.42	1.15
48a	1591.44	190.67	−13.05	1597.13	4.46	−12.38
48b				1598.00	2.12	−4.76

* scaled with factor 0.9779

The overlap integrals for the 6-31G* and cc-pVTZ VCD spectra with the experiments are respectively 59% and 70%. These spectra are shown in Figure 5.9. Based on the good agreement and the knowledge that simulated spectra were modeled for the *R* configured compound, the absolute configuration can be assigned

as (*R*)-(+)-**1**. This agrees with the absolute configuration determined via the synthesis route.

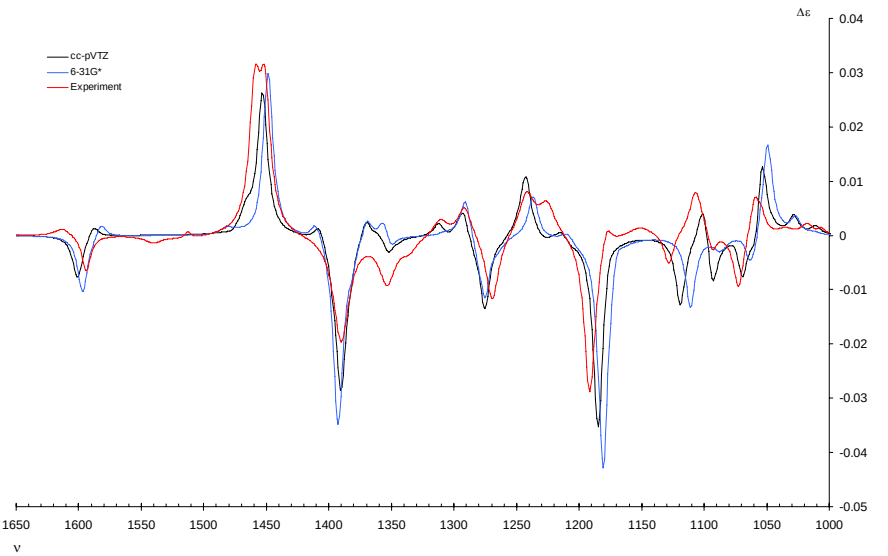

Figure 5.9 B3LYP/6-31G* (based on all conformations) and B3LYP/cc-pVTZ (based on the 5 lowest energy conformations) simulated VCD spectra for (*R*)-**1** together with the experimental spectrum for (+)-**1**. Differential intensities are in molar absorptivity units, frequencies in cm^{-1}.

The influence of basis sets and grids on the single conformer IR and VCD spectra is discussed above. For the basis sets listed in Table 5.2 the Boltzmann weighted spectra were calculated and compared with experiment, i.e., the overlap integral S^{σ} between simulated and experimental spectra was maximized, by scaling the calculated frequencies for the 1000–1650 cm^{-1} frequency interval. Results are given in Table 5.12. The overlap integrals for the IR spectra do not change much. For the VCD spectra there is clearly an increase of the overlap integral with the basis set, especially for the cc-pVTZ basis set. This is probably due to the lower conformational energies compared to 6-31G*, which cause that in the simulated cc-pVTZ spectrum more peaks appear. This gives a better agreement with the experimental spectrum. A second reason is the inherently better quality of the cc-pVTZ VCD characteristics due to the basis set size.

Table 5.12 Maximized overlap integrals (S^{σ}_{max}, in percent) and optimal scaling factor σ_{max} for the simulated spectra calculated with various basis sets with respect to the experimental spectrum.[30]

		6-31G*	6-31G**	6-311G**	cc-pVDZ	cc-pVTZ
IR	S^{σ}_{max}	83.9	85.3	84.2	85.4	84.5
	σ_{max}	0.967	0.969	0.980	0.974	0.978
VCD	S^{σ}_{max}	59.0	60.8	61.3	55.4	69.6
	σ_{max}	0.973	0.976	0.984	0.984	0.983

Table 5.13 Maximized overlap integrals (S^{σ}_{max}, in percent) and optimal scaling factor σ_{max} for the simulated spectra calculated with various grids with respect to the experimental spectrum. [30]

Grid	S^{σ}_{max} IR	σ_{max}	S^{σ}_{max} VCD	σ_{max}
(35,110)p	83.9	0.968	60.8	0.973
(50,194)p	84.0	0.967	60.3	0.973
(75,302)p	83.9	0.967	59.0	0.973
(50,302)	84.0	0.967	59.4	0.973
(75,194)	84.1	0.967	59.2	0.973
(75,434)	84.0	0.967	58.6	0.973
(99,302)	84.3	0.967	58.8	0.973

Weighted spectra were also calculated with the grids given in Table 5.4 and the 6-31G* basis set. The 1000–1650 cm^{-1} part of these spectra were compared with experimental spectra. Results are given in Table 5.13.

The IR overlap integrals for the different grids are virtually the same. A surprisingly, but fortuitously high VCD overlap integral for the (35,110)p grid is found. In Figure 5.10 the simulated VCD spectra for the pruned grids are depicted. One can clearly see that some (35,110)p grid peaks are inverted, that is, peaks corresponding with modes 29 and 42b. Nonetheless, the (50,194)p and (75,302)p VCD spectra are very comparable. The slightly augmented overlap integral value for the (50,194)p grid is due the sign of the rotational strength of mode 30. This is certainly not an indication that the sparse (50,194)p grid performs better than denser grids. On the contrary, the agreement in sign of mode 30 with the experiment is merely coincidental.

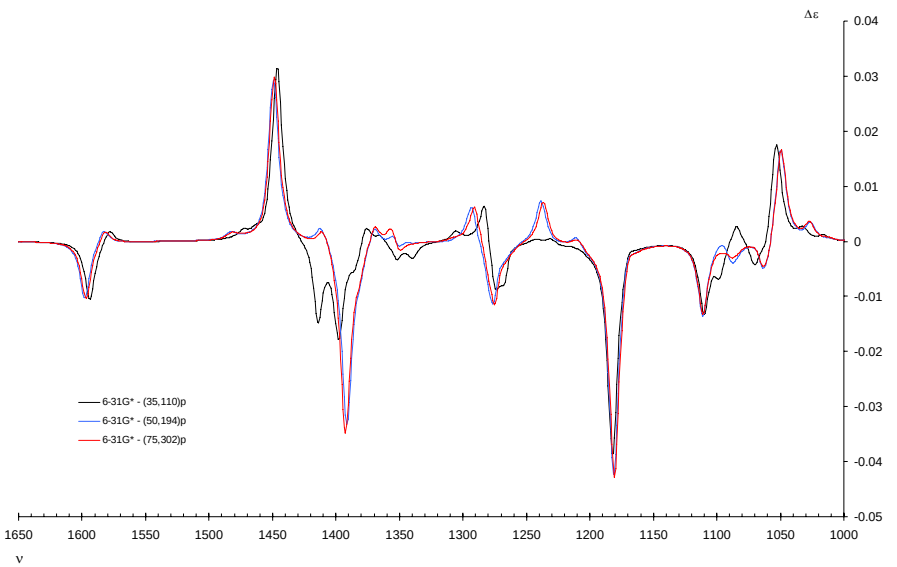

Figure 5.10 Simulated B3LYP/6-31G* VCD spectra calculated for (*R*)-**1** calculated with the (35,110)p, (50,194)p and (75,302)p grids. Intensities and differential intensities are in molar absorptivity units, frequencies in cm^{-1}.

Although it seems that the smaller (50,194)p grid performs similarly to the larger (75,302)p grid, care must be taken. More molecules need to be considered in order to establish whether this is generally valid. It was, however, found that the individual VCD spectra show only minor differences between the different grids, except for the smallest grid (35,110)p. The good agreement and correct assignment based on the (50,194)p grid may be fortuitous, because the use of a smaller grid may well cause several errors, that possibly cancel each other. A similar argument may be formulated for basis sets.

5.5 Conclusion

This study shows that VCD spectroscopy in combination with DFT is an excellent technique for the determination of the absolute configuration. Reducing the computational cost by varying basis set and grid size, this study showed that the 6-31G basis set is too small to produce good spectra. The 6-31G* basis set is an acceptable basis set, and cc-pVTZ yields the best agreement.

The small (35,110)p grid gives inferior results. The (50,194)p grid gives good results for the simulation of VCD spectra together with 6-31G* basis set using the B3LYP hybrid density functional in this specific case. CPU cost for the calculation

of the spectroscopic properties is approximately 30% less than those for the standard Gaussain98 (75,302)p grid. Although this study suggests that this grid would be an acceptable choice, care should be taken. Rotational invariance may be lost, which is not only unphysical but will also influence the calculated Boltzmann distribution. On the other hand, VCD spectra were found to be very similar for the (50,194)p and (75,302)p grids. More molecules should be tested to establish whether this is not due to a fortuitous cancellation of errors.[‡]

The use of the overlap integral as a quantitative measure for the similarity of VCD spectra is very useful, but one has to be careful in drawing conclusions on solely the value of the overlap integral, especially when anomalies are observed. The next step will be the tuning of this overlap index to make it proximity sensitive.

[‡] No further efforts were taken to investigate the applicability of sparser grids, because further research showed that the rotational invariance could not be preserved.

5.6 Reference list

1. Ariens, E. J. *Med. Res. Rev.* **1986**, *6*, 451-466.
2. Aamouche, A.; Devlin, F. J.; Stephens, P. J. *J. Am. Chem. Soc.* **2000**, *122*, 2346-2354.
3. Specht, K. M.; Nam, J.; Ho, D. M.; Berova, N.; Kondru, R. K.; Beratan, D. N.; Wipf, P.; Pascal, R. A.; Kahne, D. *J. Am. Chem. Soc.* **2001**, *123*, 8961-8966.
4. Parker, D. *Chem. Rev.* **1991**, *91*, 1441-1457.
5. Cheeseman, J. R.; Frisch, M. J.; Devlin, F. J.; Stephens, P. J. *Chem. Phys. Lett.* **1996**, *252*, 211-220.
6. Devlin, F. J.; Stephens, P. J.; Cheeseman, J. R.; Frisch, M. J. *J. Phys. Chem. A* **1997**, *101*, 9912-9924.
7. Stephens, P. J.; Devlin, F. J.; Chabalowski, C. F.; Frisch, M. J. *J. Phys. Chem.-US* **1994**, *98*, 11623-11627.
8. Stephens, P. J.; Ashvar, C. S.; Devlin, F. J.; Cheeseman, J. R.; Frisch, M. J. *Mol. Phys.* **1996**, *89*, 579-594.
9. Stephens, P. J.; Devlin, F. J. *Chirality* **2000**, *12*, 172-179.
10. Ashvar, C. S.; Stephens, P. J.; Eggimann, T.; Wieser, H. *Tetrahedron-Asymmetr.* **1998**, *9*, 1107-1110.
11. van Emelen, K.; de Bruyn, M. F. L.; Alcazar-Vaca, M. J.; Andres-Gil, J. I.; Fernandez-Gadea, F. J.; Matesanz-Ballesteros, M. E.; Bartolome-Nebreda, J. M. WO 2001098306, 2001.
12. Soukri, M.; Lazar, S.; Akssira, M.; Guillaumet, G. *Org. Lett.* **2000**, *2*, 1557-1560.
13. Polavarapu, P. L. *Spectroscopy* **1994**, *9*, 48-55.
14. Allinger, N. L.; Yuh, Y. H.; Lii, J. H. *J. Am. Chem. Soc.* **1989**, *111*, 8551-8566.
15. *Allinger, N. L. MM3(96)*, **1996**

16. Bultinck, P.; Van Alsenoy, C.; Goeminne, A.; Van de Vondel, D. *J. Phys. Chem. A* **2000**, *104*, 11801-11809.

17. Frisch, M. J.; Trucks, G. W.; Schlegel, H. B.; Scuseria, G. E.; Robb, M. A.; Cheeseman, J. R.; Montgomery Jr, J. A.; Vreven, T.; Kudin, K. N.; Burant, J. C.; Millam, J. M.; Iyengar, S. S.; Tomasi, J.; Barone, V.; Mennucci, B.; Cossi, M.; Scalmani, G.; Rega, N.; Petersson, G. A.; Nakatsuji, H.; Hada, M.; Ehara, M.; Toyota, K.; Fukuda, R.; Hasegawa, J.; Ishida, M.; Nakajima, T.; Honda, Y.; Kitao, O.; Nakai, H.; Klene, M.; Li, X.; Knox, J. E.; Hratchian, H. P.; Cross, J. B.; Bakken, V.; Adamo, C.; Jaramillo, J.; Gomperts, R.; Stratmann, R. E.; Yazyev, O.; Austin, A. J.; Cammi, R.; Pomelli, C.; Ochterski, J. W.; Ayala, P. Y.; Morokuma, K.; Voth, G. A.; Salvador, P.; Dannenberg, J. J.; Zakrzewski, V. G.; Dapprich, S.; Daniels, A. D.; Strain, M. C.; Farkas, O.; Malick, D. K.; Rabuck, A. D.; Raghavachari, K.; Foresman, J. B.; Ortiz, J. V.; Cui, Q.; Baboul, A. G.; Clifford, S.; Cioslowski, J.; Stefanov, B. B.; Liu, G.; Liashenko, A.; Piskorz, P.; Komaromi, I.; Martin, R. L.; Fox, D. J.; Keith, T.; Al-Laham, M. A.; Peng, C. Y.; Nanayakkara, A.; Challacombe, M.; Gill, P. M. W.; Johnson, B.; Chen, W.; Wong, M. W.; Gonzalez, C.; Pople, J. A. *Gaussian98,* Revision A6; Gaussian, Inc.: Pittsburgh, **1998**.

18. Becke, A. D. *J. Chem. Phys.* **1993**, *98*, 5648-5652.

19. Lee, C. T.; Yang, W. T.; Parr, R. G. *Phys. Rev. B-Condens. Matter* **1988**, *37*, 785-789.

20. Hehre, W. J.; Radom, L.; Schleyer, P. R.; Pople, J. A. *Ab initio molecular orbital theory;* Wiley: **1986**.

21. Gill, P. M. W.; Johnson, B. G.; Pople, J. A. *Chem. Phys. Lett.* **1993**, *209*, 506-512.

22. Murray, C. W.; Handy, N. C.; Laming, G. J. *Mol. Phys.* **1993**, *78*, 997-1014.

23. Frisch, A. E.; Frisch, M. J.; Trucks, G. *Gaussian 98 User's Reference;* 5th ed.; Gaussian, Inc.: Pittsburgh, **1998**.

24. Stephens, P. J. Vibrational circular dichroism spectroscopy: A new tool for the stereochemical characterization of chiral molecules. In *Computational medicinal chemistry for drugs discovery*, Bultinck, P., De Winter, H., Langenaeker, W., Tollenaere, J. P., Eds.; Marcel Dekker, Inc.: New York, **2004**; pp 699-725.

25. McQuarrie, D. A. *Statistical Thermodynamics;* Harper and Row: New York, **1973**.

26. Schellman, J. A. *Chem. Rev.* **1975**, *75*, 323-331.

27. Johnson, B. G.; Gill, P. M. W.; Pople, J. A. *Chem. Phys. Lett.* **1994**, *220*, 377-384.

28. Johnson, B. G.; Frisch, M. J. *Chem. Phys. Lett.* **1993**, *216*, 133-140.

29. Scott, A. P.; Radom, L. *J. Phys. Chem.-US* **1996**, *100*, 16502-16513.

30. The neighborhood similarities are also computed and can be found in Supplementary Material

6

determination of the AC of three *as*-hydrindacene compounds by VCD

6.1 Introduction

Because the absolute configuration of molecules plays a dominant role in many fields of chemistry, methods to establish absolute configurations are of prime importance. One of the techniques that is continuously gaining more attention is the measurement of the vibrational circular dichroism (VCD). Essentially, VCD is based on the fact that when a molecule is irradiated with circularly polarized infrared radiation, different absolute configurations will exhibit different spectra. The most pictorial case is that of two enantiomers. Both enantiomers of a molecule will

Kuppens, T.; Vandyck, K.; Van der Eycken, J.; Herrebout, W.; van der Veken, B. J.; Bultinck, P. *J. Org. Chem.* **2005**, *70*, 9103-9114.

exhibit the same unpolarized infrared (IR) spectrum. When using circularly polarized IR radiation and measuring the spectrum with left and right circularly polarized light separately, the differential absorbance spectrum will exhibit mirror symmetry. Therefore, although the location of the absorbance peaks remains the same in VCD as in unpolarized IR spectra, in VCD the peaks have different sign. As a result, a VCD spectrum contains information on the absolute configuration of a molecule. The interpretation of an experimental VCD spectrum and its connection with a specific stereochemistry has long remained a difficult task, however. A breakthrough was realized when Stephens et al. developed and implemented a quantum chemical algorithm for the computation of VCD spectra.[1-3] This has contributed greatly to the increasing popularity of the VCD technique. Essentially, one performs the necessary VCD calculations using some quantum chemical code for the different possible stereoisomers, and subsequently compares the resulting theoretical spectrum with the experimental one. Despite this conceptually simple approach, some problems remain in the routine application of VCD, so it remains important to check the outcome of the VCD assignments, if possible, with other ways of determining absolute configurations.[3-6] Some of the problems mentioned are related to the quantum chemical methodology used.[2,5,7-11] Density functional theory (DFT) has previously been shown to give gratifying agreements between theory and experiment, but basis set effects can still play an important role.[7,12,13] The advent of commercially available VCD spectrometers and the implementation of the VCD algorithms in widely available software packages, together with the increase in speed and power of computers will only extend the range of molecules that can be handled with the VCD technique.

In this paper, a vibrational circular dichroism study on three 1,8-disubstituted *as*-hydrindacenes is presented i.e. (+)-1,2,3,6,7,8-hexahydro-*as*-indacene-1,8-diol ((+)-**1**), (+)-8-hydroxy-3,6,7,8-tetrahydro-2*H*-*as*-indacen-1-one ((+)-**2**) and $(-)_{365}$-1,2,7,8-di-epoxy-3,6-dihydro-*as*-indacene ((−)-**3**).[‡] The VCD assignments are checked against stereochemistry information based on ECD measurements and/or predictions based on the applied asymmetric methods in the synthetic route.[14]

[‡] (+)-**1**: α_D^{20} = +70.5 (c = 1.09, $CHCl_3$, >99% ee); (+)-**2**: α_D^{25} = +98.2 (c = 1.04, $CHCl_3$, >99 % ee); $(-)_{365}$-**3**: α_{365}^{25} = −128.6 (c = 0.99, $CHCl_3$, >99% ee)

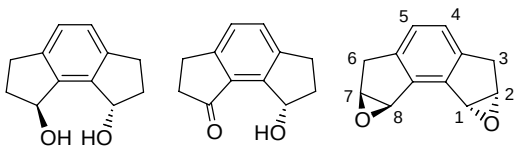

(1*S*,8*S*)-**1** (8*S*)-**2** (1*R*,2*S*,7*S*,8*R*)-**3**

Figure 6.1 (+)-1,2,3,6,7,8-hexahydro-*as*-indacene-1,8-diol ((+)-**1**), (+)-8-hydroxy-3,6,7,8-tetrahydro-2*H*-*as*-indacen-1-one ((+)-**2**) and $(-)_{365}$-1,2,7,8-di-epoxy-3,6-dihydro-*as*-indacene ((−)-**3**)

Compounds **1**–**3** provide a chiral synthetic platform for the synthesis of a new class of rigid enantiopure hexahydro-*as*-indacene based chiral ligands for application in asymmetric catalysis.[15] The *as*-hydrindacenes can be viewed as C_2-symmetric analogues of indane systems which themselves have found numerous applications in asymmetric synthesis.

Derivatives of compounds **1** were recently studied with the circular dichroism exciton chirality method.[14] The determined absolute configurations of (+)-**1** and (+)-**2** are in agreement with what one would predict on the basis of the applied asymmetric reduction.

6.2 Results and discussion

6.2.1 Synthesis

Asymmetric transfer hydrogenation of the C_2-symmetric prochiral diketone **4** applying an *in situ* prepared catalyst (**A**) derived from commercial (1*S*,2*S*)-(+)-*N*-*p*-tosyl-1,2-diphenylethylenediamine and $[RuCl_2(\eta^6\text{-cymene})]_2$ in a 5:2 formic acid-triethylamine mixture,[16] resulted in alcohols (+)-**1** and (+)-**2** in good yield and high enantiomeric excess.[14] Depending on the catalyst loading, reaction time and reaction temperature, (+)-**1** or (+)-**2** could be isolated as the main product (Scheme 6.1). The reduction is expected to yield the (*S*)-alcohols using the (*S*,*S*)-Ts-DPEN ligand by analogy with the reduction of indanone to (*S*)-indanol with the same ligand. Furthermore, reduction of **4** with $NaBH_4$ in MeOH provided a 3/1 mixture of *meso*/(±)-**1** alcohols in 99% yield. Concentration sensitive dehydration[17] in the presence of no more than 1% *p*-TSA yielded one C_2-symmetric isomer **5**. This prochiral alkene can be transformed into the bisepoxide **3** using the low temperature

Jacobsen epoxidation conditions.[18] Noteworthy is the isomerisation of diene **5** by NMO at room temperature, emphasizing the importance of adding **5** at low temperature (−78 °C) to the mixture of catalyst and NMO, not at room temperature. The use of the (*R*,*R*)-catalyst allows to predict the absolute configuration to be (1*R*,2*S*) deduced from the formation of (1*S*,2*R*)-indene oxides when using the (*S*,*S*)-Jacobsen catalyst.[19,20]

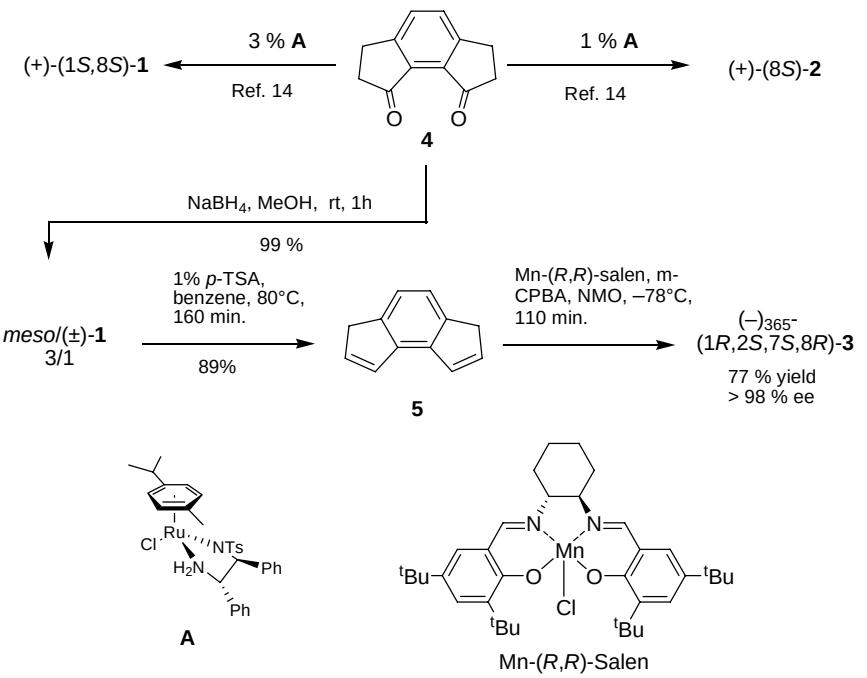

Scheme 6.1

6.2.2 IR and VCD spectroscopy

The IR and VCD spectra for (+)-**2** and (−)-**3** were recorded in a demountable cell with KBr windows and a 105 µm spacer. The spectra for (+)-**1** were recorded in a CaF_2 cell with a 200 µm spacer. The unpolarized IR absorbance spectra were recorded at a resolution of 4 cm^{-1}, the VCD spectra were recorded on a Bruker IFS 66v/S FTIR interferometer coupled to a Bruker PMA37 VCD module[21] at a resolution of 6 cm^{-1}. To improve the VCD S/N ratio an 1830 cm^{-1} long wave-pass filter was used.

The collection time for the VCD spectrum was 2h each, in 4 blocks of 30 minutes. (+)-**1** was dissolved in $CDCl_3$ at a concentration of 0.11 M. For (+)-**2**, $CDCl_3$ was used as solvent at a concentration of approximately 0.19 M. (−)-**3** was dissolved in $CDCl_3$ at a concentration of 0.20 M.

To obtain a good estimate for the baseline artifacts, usually the VCD of the racemic mixture or both enantiomers is measured.[22] As these are not always available, the VCD of the solvent, measured in the same conditions as the sample, is often a good approximation. In this study, a racemic mixture is only available for **1.** For (±)-**1**, the VCD was measured at the exactly the same conditions as the solvent and the enantiopure solution. In Figure 6.2 the racemic and solvent corrected spectra are given. No significant differences involving the signs of any peaks can be seen.

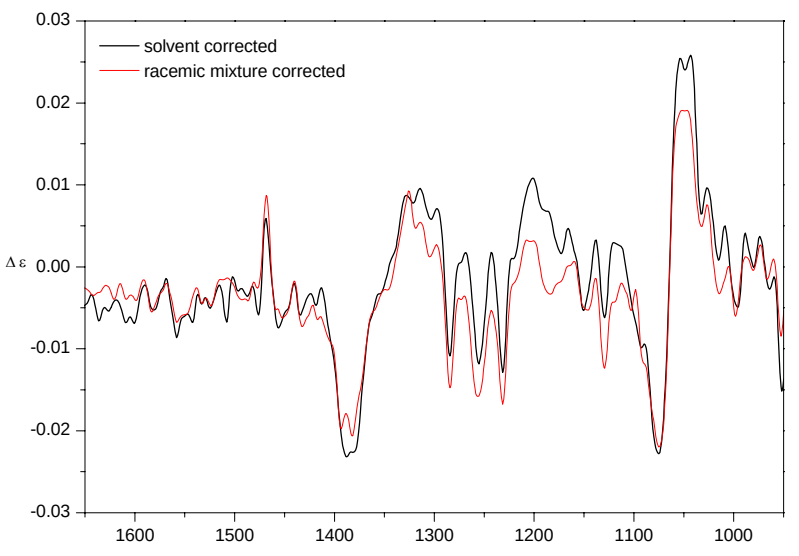

Figure 6.2 Baseline corrected VCD spectra for (+)-**1**, i.e., solvent corrected and racemic corrected. Differential intensities are in molar absorptivity units, frequencies in cm^{-1}.

6.2.3 Computational methods

Because VCD spectra are composed of all contributions of the different conformations, a conformational search has to be performed. In the scope of absolute configuration (AC) determination by VCD, this is very important because of the strong dependence of VCD on the conformations present.[23]

The conformational landscape is explored by molecular mechanics (MM) as well as DFT. A systematic search is carried out at B3LYP/6-31G* level. The aromatic ring of the *as*-hydrindacene skeleton is considered rigid, whereas the attached five-membered rings and exocyclic hydroxyl groups are considered flexible. The dihedral angles are varied in a 60° grid. A bump check and ring constraints[24] assure that only the chemically sane starting structures are minimized on B3LYP/6-31G* level.
Also, a systematic search (with a 10° dihedral grid) is performed with MMFF[25] supplemented with a MM3 stochastic search[26,27] to identify possible further minima. The located MMFF and MM3 geometries are then optimized at B3LYP/6-31G* level and supplemented with these found from the B3LYP/6-31G* systematic search.
The DFT calculations are performed with Gaussian03 revision B5[28] in a distributed computing environment. The B3LYP[4,29,30] functional is used together with the 6-31G* and cc-pVTZ basis sets. Eight additional functionals (B1LYP, B3LYP, B3P86, B3PW91, B98, BHandH, BHandHLYP, MPW1PW91, PBE1PBE)[31] were employed using the 6-31G* basis set.

The agreement between spectra is expressed via the similarity measures given in Equation (6.1) and (6.2). The normalized overlap in Equation (6.1) has been discussed earlier.[7]

$$S^{\sigma} = \frac{\int f(\sigma\upsilon)g(\upsilon)d\upsilon}{\sqrt{\int f^2(\sigma\upsilon)d\upsilon \int g^2(\upsilon)d\upsilon}} \tag{6.1}$$

$$S^{\sigma} = \frac{\int w_{fg}(r)c_{fg}(r)dr}{\sqrt{\int w_{ff}(r)c_{ff}(r)dr \int w_{gg}(r)c_{gg}(r)dr}} \tag{6.2}$$

with

$$\begin{aligned} w(r) &= 1 - \frac{|r|}{l} && if\ |r| < l \\ w(r) &= 0 && if\ |r| \geq l \end{aligned} \tag{6.3}$$

and

$$c_{ff}(r) = \int f(\upsilon)f(\upsilon + r)d\upsilon \tag{6.4}$$

The simple overlap is less robust because of the fundamental difference between experimental and simulated spectra. Although the theoretical frequencies are linearly scaled to correct for the harmonic approximation and basis set incompleteness, some peaks can still be shifted with respect to their corresponding experimental peak. A similarity measure that takes into account the neighborhood around the peaks, results in a more accurate and precise measure for their similarity. Equation (6.2)[32] allows the consideration of the neighborhood with a width of $-l$ and $+l$ around each point in the spectrum.

6.2.4 Theoretical spectra

The dipole and rotational strengths are calculated for each DFT minimum on the potential energy surface. The results are single conformer line spectra, which are broadened using a Lorentzian band shape. Throughout the paper, Lorentzian broadening is always accomplished with a fwhm of 10 cm^{-1}.
Each minimum contributes to the total spectrum in a Boltzmann weighted manner. Conformational populations are based on the free energy. The enthalpy and free energy are calculated under the usual assumptions using standard thermochemical expressions.[33] Appropriate frequency scaling factors are used to correct for the harmonic approximation.

6.2.5 Conformational analysis

Hexahydro-*as*-indacene-1,8-diol (1)

Molecule **1** has two asymmetric carbon atoms. Because the sample of (+)-**1**, which is analyzed, is optically active (> 99% ee), the possible configurations of (+)-**1** are limited to enantiomers $\mathbf{1}^{(RR)}$ or $\mathbf{1}^{(SS)}$ (mesomers $\mathbf{1}^{(RS)}$ and $\mathbf{1}^{(SR)}$, are identical and not optically active).
The conformational space can be described by means of the orientation of the exocyclic substituents. The position of the alcohol group in the context of the five-membered ring is either designated as equatorial (“e”) or axial (“a”). For the CO(H) dihedral angle three typical minima in the torsion potential energy are observed, i.e., for dihedral angles of 60°, 180° and −60°. The dihedral angles are characterized as G, T, and G’ respectively for gauche clockwise, trans and gauche counter clockwise.

Due to the C_2-symmetry of **1**, both substituents are indistinguishable, which is reflected in the conformational notation; the group-ring orientation and CO(H) bond torsion are given successively for both functional groups. In this fashion the global minimum of **1** can be written as eG'eG or eGeG'.
The combined conformational searches, using different techniques that are described in §6.2.3, yielded 13 minima in total. These minima are shown in Figure 6.3.

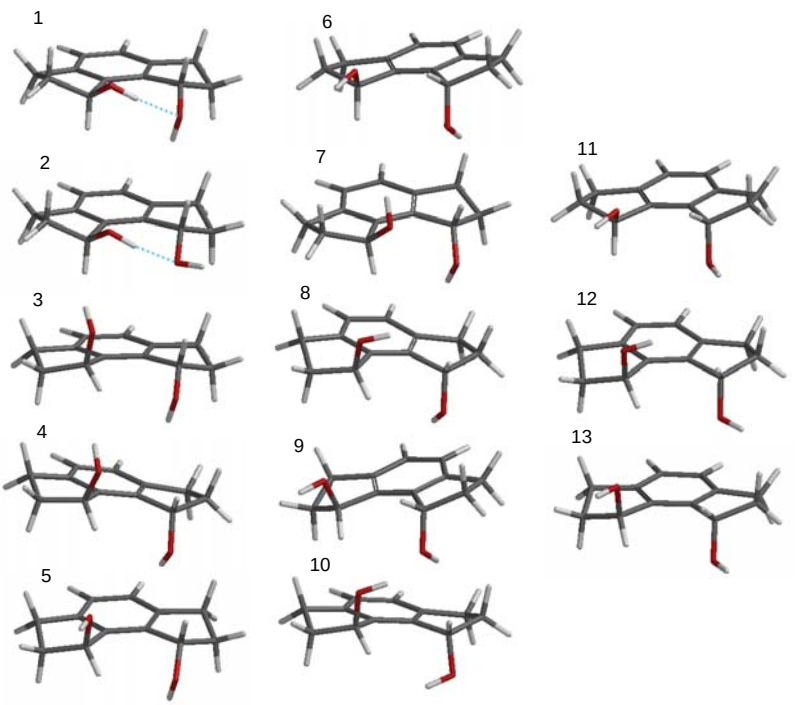

Figure 6.3 Pictorial representation of the B3LYP/6-31G* PES minima for **1**.

Their corresponding notation and energy can be found in Table 6.1. For each minimum the B3LYP 6-31G* and cc-pVTZ relative total energies are given. Some higher energy cc-pVTZ conformers have a different energy order compared to the 6-31G*. Also, the expected eTaG minimum could not be located at the B3LYP/cc-pVTZ level. Starting from the B3LYP/6-31G* eTaG geometry, cc-pVTZ optimization converged in the eG'eG structure. Conformational populations are calculated based on the Boltzmann distribution using free energies at 298.15 K. From Table 6.1 it is clear that eG'eG and eG'eT are the dominant minima, the populations of both conformers summing more than 90%. This can be attributed to

two effects i.e. an internal OH···O hydrogen bond and the gauche effect.[34] This stabilization is more pronounced for the 6-31G* basis set.

Table 6.1 The B3LYP/6-31G* (a) and B3LYP/cc-pVTZ (b) relative energies for the located conformations (RE, in kcal/mol) of **1**, the conformation description, relative enthalpies (ΔH^0 in kcal/mol), relative free energies (ΔG^0, in kcal/mol) and the Boltzmann populations (% P, T = 298.15 K).

a		RE	ΔH^0	ΔG^0	% P
1	eG'eG	0.00	0.00	0.00	84.1
2	eG'eT	1.10	1.05	1.05	14.3
3	aGeG	4.42	4.16	3.20	0.38
4	aGaG	4.50	4.24	3.47	0.24
5	aTeG	4.89	4.57	3.61	0.19
6	eTaG	5.01	4.66	4.13	0.08
7	eGeG	4.97	4.68	3.46	0.24
8	aGaG'	5.14	4.82	3.64	0.18
9	aTaG	5.18	4.87	3.76	0.15
10	aG'aG'	5.84	5.40	4.72	0.03
11	eTaT	5.89	5.48	4.42	0.05
12	aG'aT	6.22	5.80	5.18	0.01
13	aTaT	6.19	5.81	4.74	0.03

b		RE	ΔH^0	ΔG^0	% P
1	eG'eG	0.00	0.00	0.00	71.3
2	eG'eT	0.78	0.73	0.73	20.7
4	aGaG	3.20	3.07	2.49	1.07
3	aGeG	3.35	3.19	2.29	1.50
5	aTeG	3.68	3.44	2.43	1.19
8	aGaG'	3.73	3.52	2.43	1.17
9	aTaG	3.74	3.52	2.47	1.10
6	eGeG	4.02	3.82	3.25	0.29
11	eTaT	4.28	3.94	3.11	0.37
10	aG'aG'	4.29	3.93	2.85	0.59
12	aTaT	4.58	4.26	3.21	0.32
13	aG'aT	4.65	4.28	3.11	0.38

Hydroxy-tetrahydro-*H*-*as*-indacen-one (2)

In hydroxyketone **2**, only one group-ring orientation and CO*(H)* bond torsion is present; a conformational notation comparable to the notation for compound **1** is used.

Figure 6.4 Pictorial representation of the B3LYP/6-31G* PES minima for **2**. Conformation numbering conforms to that of Table 6.2.

A combined stochastic MM3 and systematic MMFF search resulted in three B3LYP/6-31G* minima. These are shown in Figure 6.4 and listed in Table 6.2 accompanied with the 6-31G* and cc-pVTZ relative energies, enthalpies, free energies and Boltzmann populations. Remarkably, the expected minima eT, aT and aG' are not found. Therefore a B3LYP/6-31G* systematic search around the C-C-O-H dihedral angle is performed for an equatorial and axial substitution. In Figure 6.5 the two dimensional PES is shown for the equatorial and axial scan, where the C-C-O-H dihedral angle is varied in steps of 1° and held fixed during optimization. As can be seen, no new minima are encountered. A transition from the axial surface to the equatorial surface can be observed in the proximity of the global minimum. This minimum is stabilized due to a strong internal OH···O hydrogen bond (1.95 Å – B3LYP/cc-pVTZ).

Table 6.2 The B3LYP/6-31G* (a) and B3LYP/cc-pVTZ (b) relative energies for the localized conformations (RE, in kcal/mol) of **2**, the conformation description, relative enthalpies (ΔH^0, in kcal/mol), relative free energies (ΔG^0, in kcal/mol), and the Boltzmann populations (% P, T = 298.15 K).

a		RE	ΔH^0	ΔG^0	% P
1	eG'	0.00	0.00	0.00	100.0
2	aG	6.85	6.59	5.75	0.00
3	eG	8.19	7.87	6.75	0.00

b		RE	ΔH^0	ΔG^0	% P
1	eG'	0.00	0.00	0.00	99.97
2	aG	5.97	5.73	4.90	0.03
3	eG	7.41	7.17	6.03	0.00

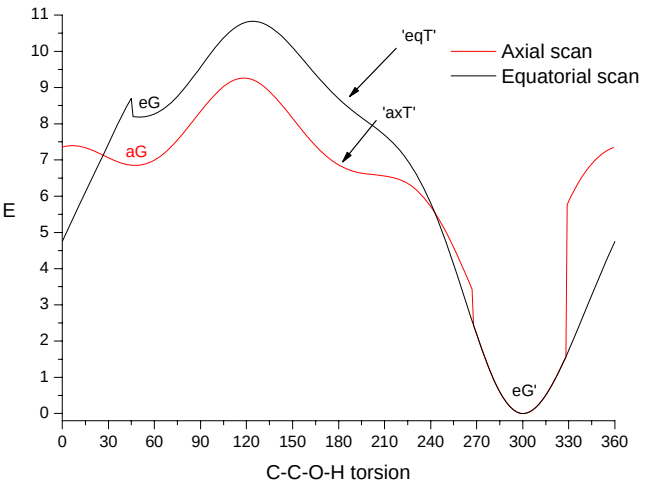

Figure 6.5 PES scan (C-C-O-H torsion) at B3LYP/6-31G* level of the equatorial and axial surface of **2** in steps of 1°. The dihedral angle is held fixed during optimization. Relative energies are in kcal/mol.

Di-epoxy-dihydro-*as*-indacene (3)

Because the four stereocentra of **3** are in a ring-attached epoxide system, they are two-by-two correlated. Due to the optical activity of the molecule, only the $\mathbf{3}^{(RS,SR)}$ and $\mathbf{3}^{(SR,RS)}$ enantiomers are likely.

Due to the rigidity of compound **3** only one conformation could be found (depicted in Figure 6.6) using a stochastic and systematic search, as described in the §6.2.3.

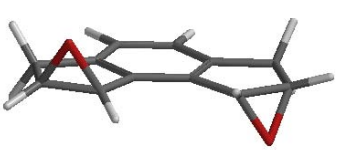

Figure 6.6 Pictorial representation of the B3LYP/6-31G* PES minimum for **3**.

6.2.6 IR and VCD spectra

In Figures 6.7 and 6.8, the Lorentzian fitted experimental IR and VCD spectra of (+)-**1** are given (residual fitting errors are given in Figure S6.1 – *Supplementary Material*). From the Boltzmann populations in Table 6.1 it can be seen that only two conformations have a considerable contribution. All conformations, however, are taken into account to simulate the spectra. Only eG'eG and eG'eT are needed to assign the experimental bands. Fundamentals designated as *a*, originate from conformation eG'eG, those designated as *b* represent eG'eT. No label is used when fundamentals of both conformations coincide or have a very small frequency separation.

In Figures 6.7 and 6.8 the simulated spectra are shown for (1*S*,8*S*)-**1**. The B3LYP/6-31G* theoretical frequencies are uniformly scaled with a factor of 0.967; the B3LYP/cc-pVTZ spectra with a factor 0.977.

The experimental assignments could be performed relatively easy due to the good agreement between theory and experiment, although peak broadening makes the assignment of the low intensity peaks (38–52) somewhat less straightforward. The peak assignment is primarily based on the IR spectrum. Nevertheless, due to the extra discriminating power provided by VCD, that is, the sign of intensity, some unresolved IR bands could be localized, because of their corresponding resolved VCD bands. The extensive assignment tables can be found in *Supplementary Material*, i.e., Tables S6.1 and S6.2.

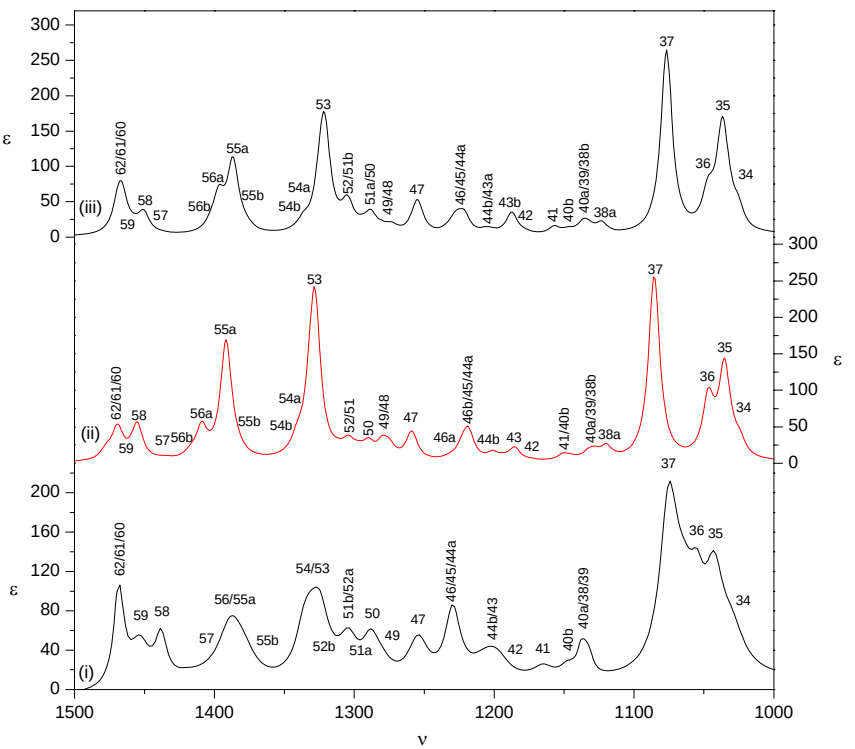

Figure 6.7 Lorentzian fitted unpolarized IR absorption spectrum for (+)-**1** (i), B3LYP/6-31G* (ii) and B3LYP/cc-pVTZ (iii) simulated IR spectrum for (1*S*,8*S*)-**1**. Intensities are in molar absorptivity units, frequencies in cm^{-1}.

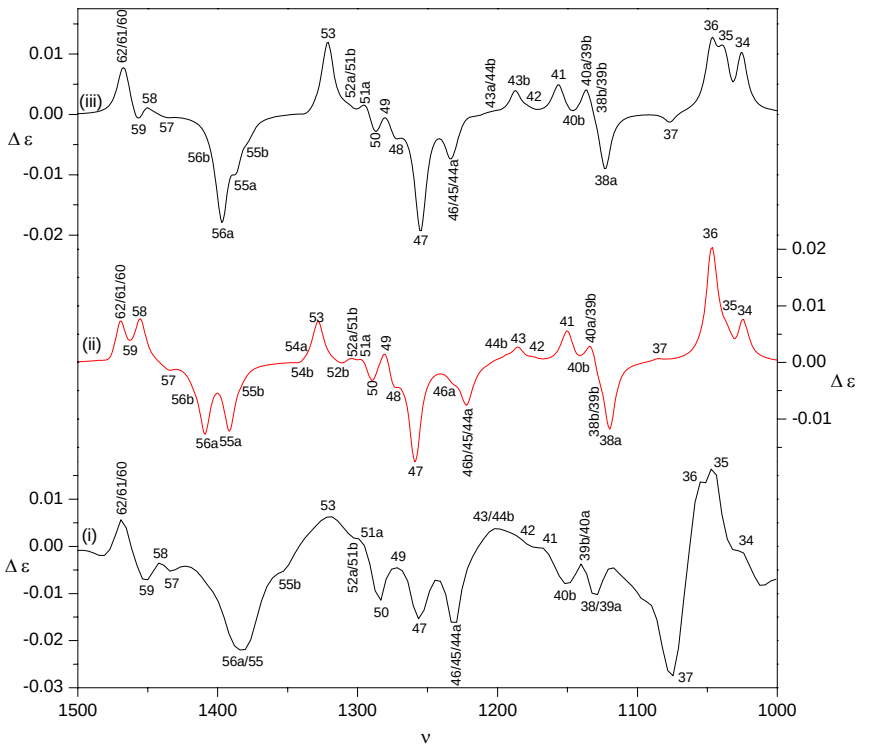

Figure 6.8 Lorentzian fitted experimental VCD spectrum for (+)-**1** (i), B3LYP/6-31G* (ii) and B3LYP/cc-pVTZ (iii) simulated VCD spectrum for (1*S*,8*S*)-**1**. Differential intensities are in molar absorptivity units, frequencies in cm^{-1}.

In the experimental IR absorption spectrum fundamentals 48 and 57 are not clearly visible. Fundamentals 44b/43, 55b and 56/55a are not well resolved. Fundamentals 40a/38/39, 46/45/44a and 62/61/60 are not resolved either, but their predicted frequency separations are also very small. In the experimental VCD spectrum peak 56b is not well resolved, and peak 48 is not visible.

In Figure 6.8, clearly a difference in sign for fundamental 37 can be observed compared to the 6-31G* spectrum. In the cc-pVTZ spectrum, however, the peak is predicted with the correct sign, though strongly underestimated. The better agreement with the cc-pVTZ basis set is coherent with earlier studies.[7] Other functionals (B1LYP, B3P86, B3PW91, B98, MPW1PW91, PBE1PBE, BHandH, BHandHLYP) are also used along with the 6-31G* basis set to simulate spectra for **1**. It seems that only the B1LYP functional predicts the correct sign for fundamental

37. This functional also predicts fundamental 54, which is experimentally not resolved, to be positive in agreement with the cc-pVTZ basis set. When looking at the overall performance of the various functionals, only BHandH and BHandHLYP perform rather poorly. The other functionals have a comparable performance. The B3LYP functional has the best overall agreement (Figures S6.2 and S6.3 in *Supplementary Material*). In Table S6.7a (*Supplementary Material*) the neighborhood overlap (Equation (6.2)) between experimental and simulated IR/VCD spectra is given for different functionals. This type of overlap takes into account the local shift of the simulated band with respect to the experimental one. In addition, the scaling factor is given for which the normalized overlap between experimental and simulated IR spectra is maximized. The overlap is calculated for the 1700–1000 cm^{-1} wavenumber interval.

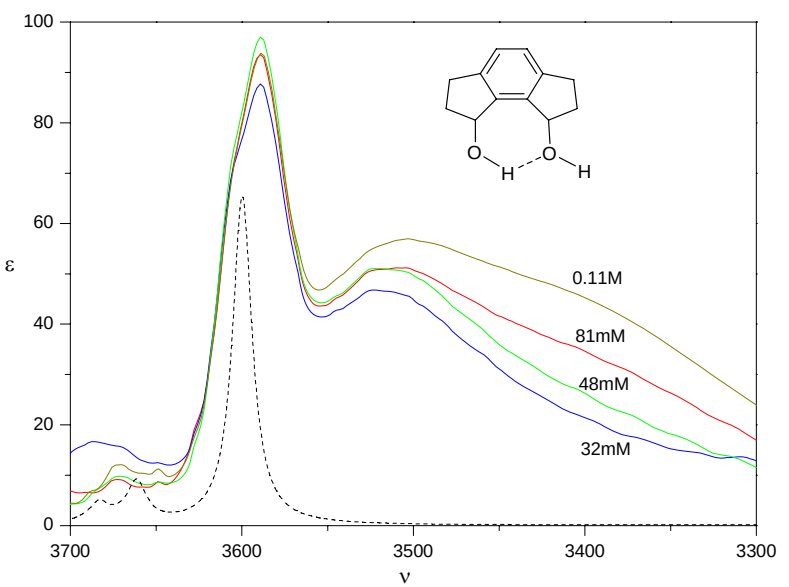

Figure 6.9 Infrared spectrum in the OH stretch region for different concentrations of **1** (0.11 M, 81 mM, 48 mM, and 32 mM). The dashed line is the B3LYP/6-31G* simulated spectrum. Intensities are in molar absorptivity units, frequencies in cm^{-1}.

For **1**, intermolecular interactions with solvent or solute molecules are possible via the OH groups, which could perturb the spectra notably.[35] These interactions are not taken into account in our calculations, as these are performed on isolated molecules. In Figure 6.9 the IR spectra in the OH stretch region for 4 different concentrations are given i.e. 0.11 M (saturated solution), 81 mM, 48 mM, and 32 mM. Two OH

stretch bands can be observed, i.e. an unresolved doublet due to non-interacting OH groups, and a doublet at 3589 cm^{-1} caused by the OH stretching involved in OH···O intramolecular hydrogen bonds. Doublets are due to the two most significant conformations. Figure 6.9 also contains the B3LYP/6-31G* simulated spectrum. The predicted frequencies for the OH stretching fundamental in the OH···O intramolecular hydrogen bond in conformation eG'eG and eG'eT nearly coincide, giving rise to only one peak. The broad band at 3513 cm^{-1} is due to self-association (hydrogen bonding between different solute molecules). The intensity of this band becomes somewhat smaller with lower concentrations. Comparing its intensities with those of the two monomeric bands, it is clear that self-association is less important. Furthermore, there is no concentration effect observed for the VCD spectra of the concentration series.
Given the excellent agreement between the experimental and simulated spectra, the absolute configuration of (+)-**1** can be assigned as (1*S*,8*S*)-**1**. This is in agreement with earlier ECD studies.[14]

In Figures 6.10 and 6.11 the Lorentzian fitted experimental IR and VCD spectra of (+)-**2** are shown (residual fitting errors are given in Figure S6.1 – *Supplementary Material*) simultaneously with the B3LYP/6-31G* and B3LYP/cc-pVTZ simulated spectra for the *S* enantiomer of compound **2**. The 6-31G* and cc-pVTZ frequency scaling factors used are 0.967 and 0.977 respectively. Based on the populations (Table 6.2) it can be seen that only conformation eG' should be considered when assigning the peaks in the experimental spectrum. This assignment was based on the B3LYP/6-31G* and cc-pVTZ calculations. The extensive assignment tables can be found in *Supplementary Material*, i.e., Tables S6.3 and S6.4.

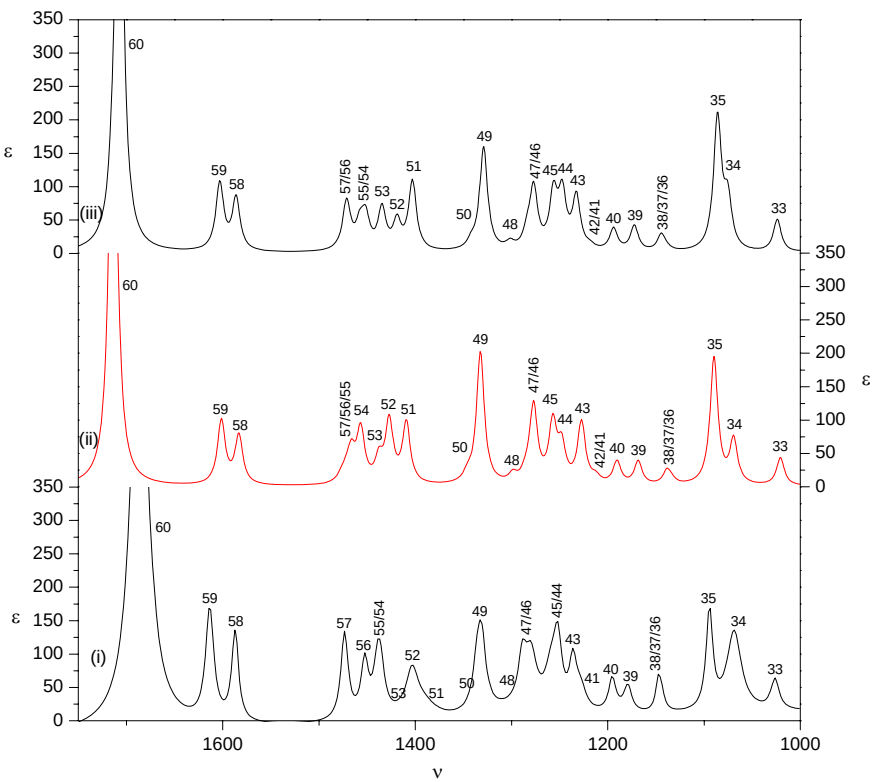

Figure 6.10 Lorentzian fitted unpolarized IR absorption spectrum for (+)-**2** (i), B3LYP/6-31G* (ii) and B3LYP/cc-pVTZ (iii) simulated IR spectrum for (*S*)-**2**. Intensities are in molar absorptivity units, frequencies in cm^{-1}.

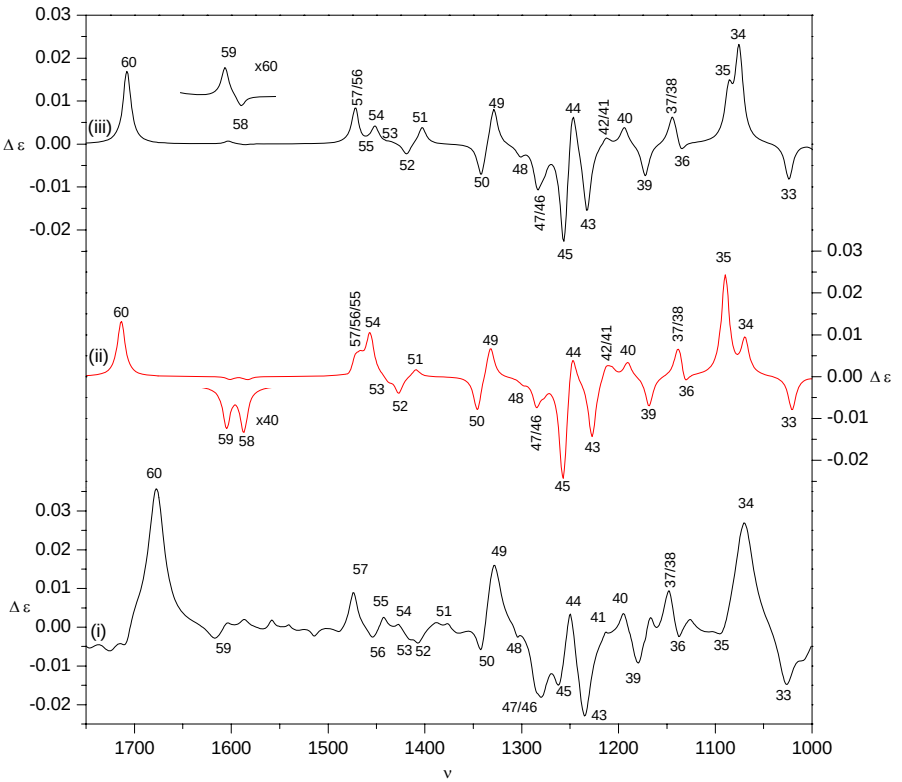

Figure 6.11 Lorentzian experimental VCD spectrum for (+)-**2** (i), B3LYP/6-31G* (ii) and B3LYP/cc-pVTZ (iii) simulated VCD spectrum for (*S*)-**2**. Differential intensities are in molar absorptivity units, frequencies in cm^{-1}.

In the experimental IR spectrum it can be seen that peaks 36/37/38, 45/44 and 54/55 are not resolved, which is in agreement with the predicted small frequency separation. Peaks 53, 51, 50 and 42 are not visible.

In the experimental VCD spectrum peaks 46/47, and 38/37 are not resolved, in agreement with simulations. Peaks 58, 53 and 42 are not visible.

When looking at the signs of the VCD peaks for (+)-**2** in Figure 6.11, it can be seen that the sign of fundamental 35 is not correctly predicted for both basis sets. For 6-31G* fundamentals 56 and 57 have the wrong predicted sign. For the cc-pVTZ simulated spectra, fundamental 59 is erroneously predicted, i.e. slightly positive. However, predicted VCD intensities for fundamental 59 are very small, and the noise level in that area of the experimental spectrum is rather high.

Different functionals are used to simulate spectra at 6-31G* level. None of the functionals manage to correctly predict the sign for fundamental 35. B3P86,

MPW1PW91 and PBE1PBE succeed in calculating the correct signs for fundamentals 57 and 56 but fail for fundamental 55. An overview of the overall performance of the different functionals, in given in *Supplementary Material*, i.e. Table S6.7 (neighborhood overlap along with the scaling factor) and Figures S6.5 and S6.6 (simulated IR and VCD spectra). It shows again that, for our purposes, BHandH and BHandHLYP have a bad performance at 6-31G* level. The other functionals perform similarly.

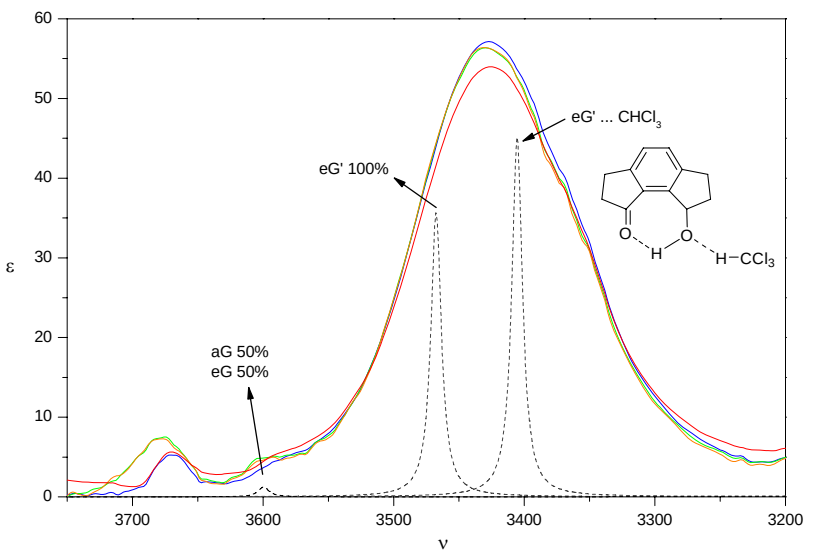

Figure 6.12 Infrared spectrum in the OH stretch region for different concentrations of **2** (0.19 M, 0.14 M, 95 mM, and 57 mM). The dashed lines are B3LYP/6-31G* simulated spectra. Intensities are in molar absorptivity units, frequencies in cm^{-1}.

In the OH stretch region three distinct bands can be observed. One band at 3672 cm^{-1}, a small shoulder at 3594 cm^{-1} and a broad asymmetric band at 3430 cm^{-1}. In agreement with the B3LYP/6-31G* "force field" calculations, the OH stretch band for the intramolecular hydrogen bonded system is shifted to a lower wavenumber and can be found at approximately 3430 cm^{-1} (Figure 6.12). This band is asymmetric and relatively broad. As can be seen, there is no concentration effect, meaning that this broadening can not be attributed to self-association, as diluting affects the aggregation. However, $CDCl_3$ solvent molecules can interact with the solute ($CCl_3D\cdots O(H)-C$), further reducing the OH stretch frequency. This was confirmed at B3LYP/6-31G* level, taking this interaction explicitly into account (Figure 6.12). In this manner the asymmetric broad band can be explained. The band

at 3672 cm^{-1} and its small shoulder can be explained by taking into account the conformations without intramolecular hydrogen bonding. Based on gas-phase calculations their contributions are insignificant compared to the global minimum (Table 6.2), but due to solvent stabilization these conformations apparently gain importance. More evidence can be found at the C=O stretch region, where a doublet is observed in the VCD spectrum (Figure 6.11, fundamental 60). However, the relative intensities of these stabilized conformation bands are low compared to those of the intramolecular hydrogen bonds. Calculations in which the experimental spectrum was reproduced by averaging the calculated VCD spectra and manual adjustment of the conformational populations, shows that the experimental spectra are largely dominated by the global minimum eG'.
For the C−O(H) stretching mode, fundamental 35, the calculations always yield a positive VCD signal, while the experimental data clearly shows that for this mode a negative signal is present. A similar pattern is also observed for fundamental 37 in **1**. The B3LYP/6-31G* calculations for **1** gives a wrong sign for fundamental 37. The calculations using the cc-pVTZ basis set yields a correct sign, but seriously underestimated the rotational strength.

The agreement for some areas is not as excellent as for **1**, but the overall agreement allows to conclude with high certainty that the absolute configuration of (+)-**2** corresponds to (8*S*)-**2**. This is in agreement with the earlier ECD exciton chirality assignment and the prediction based on the selectivity of the asymmetric reduction of indanone with the same catalyst.[14]

In Figures 6.13 and 6.14, the Lorentzian fitted experimental IR and VCD spectra of (−)-**3** are given (residual fitting errors are given in Figure S6.1 – *Supplementary Material*). Also the simulated spectra are shown for (1*R*,2*S*,7*S*,8*R*)-**3**. The B3LYP/6-31G* theoretical frequencies are uniformly scaled with a factor of 0.967; the B3LYP/cc-pVTZ spectra with a factor 0.977.

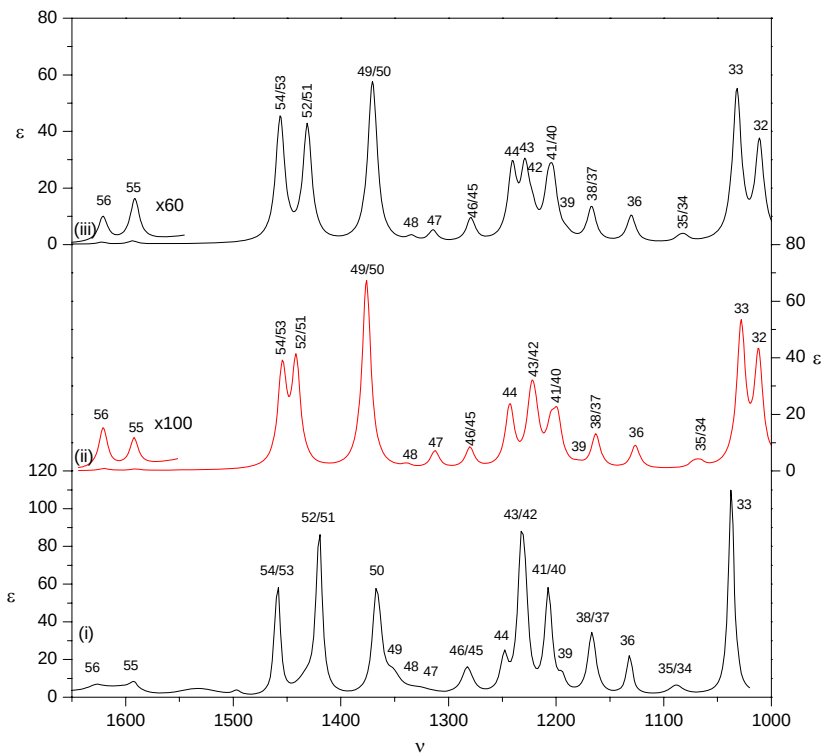

Figure 6.13 Lorentzian fitted unpolarized IR absorption spectrum for (−)-**3** (i), B3LYP/6-31G* (ii) and B3LYP/cc-pVTZ (iii) simulated IR spectrum for (1*R*,2*S*,7*S*,8*R*)-**3**. Intensities are in molar absorptivity units, frequencies in cm^{-1}.

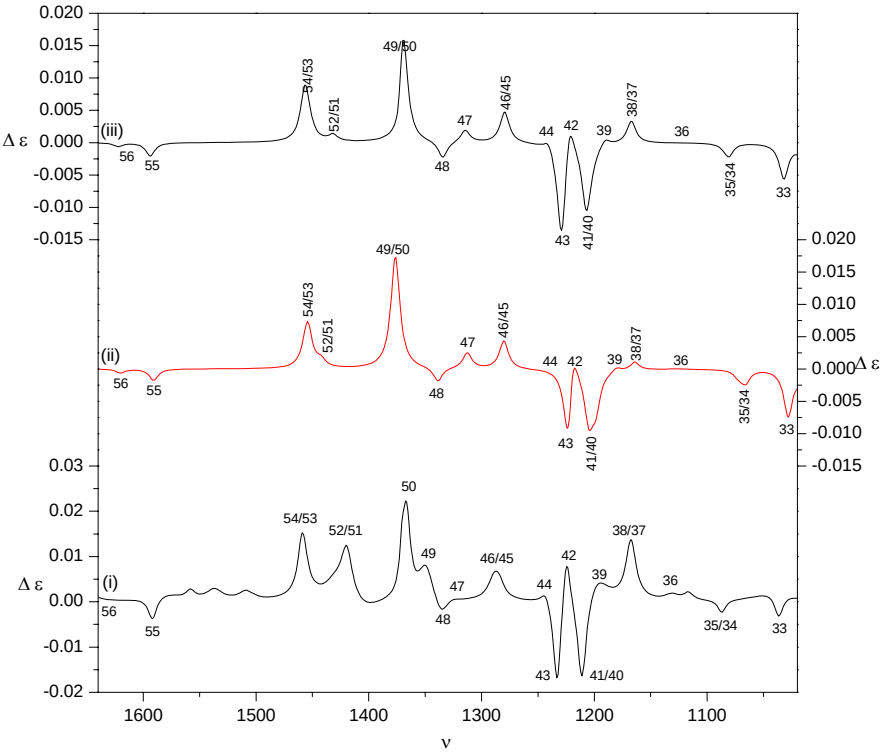

Figure 6.14 Lorentzian fitted experimental VCD spectrum for (−)-**3** (i), B3LYP/6-31G* (ii) and B3LYP/cc-pVTZ (iii) simulated VCD spectrum for (1*R*,2*S*,7*S*,8*R*)-**3**. Differential intensities are in molar absorptivity units, frequencies in cm^{-1}.

The assignment of the fundamentals was relatively easy because only one conformation needs to be taken into account, thereby reducing the complexity of the spectrum and assignment.

For the experimental spectra of (−)-**3**, peak 32 is not visible. Peaks 54/53, 46/45, 43/42, 41/40, 38/37 and 35/34 are not well resolved, in agreement with the predicted small frequency splitting. Peaks 47 and 48 give measurable VCD but are not resolved. The broad left shoulder of peak labeled 52/51 is presumably attributable to fundamental 52.

In the VCD spectrum peaks 56 and 47 are not well resolved.

Comparing the experimental and B3LYP/6-31G* VCD data (Extensive assignment tables can be found in *Supplementary Material*, i.e., Tables S6.5 and S6.6) it can be seen that fundamentals 49 and 51 have wrong predicted signs. For the cc-pVTZ basis set fundamental 51 has still the wrong predicted sign. Fundamental 50 is also wrongly predicted. These discrepancies, however, can only be seen when comparing

the rotational strengths and not in the broadened spectra because of the small frequency separations between mode 49/50 and 51/52 (Tables S6.5 and S6.6, *Supplementary Material*). Comparing the calculated rotational strengths for different functionals, it shows that fundamental 49 is predicted to have a wrong (negative) sign. The functionals which predict the sign of fundamental 51 correctly (B3P86, B3PW91, MPW1PW91 and PBE1PBE) fail to predict the sign correctly for fundamentals 44 and 52. All functionals have a comparable performance, apart from BHandH and BHandHLYP which have a bad performance. In Table S6.7 and Figures S6.6 and S6.7 (*Supplementary Material*) this is shown through the neighborhood overlap values for experimental and the simulated spectra.

Comparing experimental spectra with simulated spectra, we can see an excellent agreement, allowing an assignment of the absolute configuration of (−)-**3** to (1*R*,2*S*,7*S*,8*R*)-**3**.

Comparing the performance of the basis sets for the three molecules, it shows again[7,13] that the 6-31G* basis set is adequate to perform absolute configuration assignments, with the cc-pVTZ basis set being superior. This is shown in the above discussion, but is also clear from Table 6.3, where the neighborhood overlap (Equation (6.2)) is given for experimental IR/VCD spectra and the simulated spectra. The cc-pVTZ neighbourhood overlap values are all closer to 1 compared to the 6-31G* values indicating a better agreement with experiment.

Table 6.3 Neighbourhood similarity (S^{σ}, in percent) for IR and VCD spectra for theory versus experiment for (a) 6-31G* and (b) cc-pVTZ basis set and maximizing scaling factor for default IR overlap.

a	S^{σ} IR	S^{σ} VCD	σ
1	93.6	74.6	0.960
2	92.0	74.3	0.952
3	87.1	62.2	0.975

b	S^{σ} IR	S^{σ} VCD	σ
1	97.2	79.5	0.977
2	93.8	80.4	0.965
3	94.1	80.6	0.978

6.3 Conclusion

Absolute configurations of (+)-**1**, (+)-**2** and (−)-**3** were determined respectively as (1*S*,8*S*)-**1**, (8*S*)-**2** and (1*R*,2*S*,7*S*,8*R*)-**3**. This was accomplished on B3LYP/6-31G* and cc-pVTZ level. cc-pVTZ spectra were proven to be superior to the 6-31G* spectra, which confirms earlier studies. Also, it is shown that small differences between theory and experiment are not the effect of the choice of functional, as the performance of most functionals is very comparable.
The use of VCD to assign absolute configurations is a powerful method, which allows determination of the absolute configurations based on quantum chemical calculations and experimental spectra of dilute solutions. In contrast to the ECD determination for compound **1** and **2**, the VCD method does not require extra synthesis steps to introduce chromophore groups in order to induce exciton coupling.

6.4 Supplementary material index

For this chapter Supplementary Material is provided. It can be downloaded from http://www.quantum.UGent.be/tksup.pdf

Table S6.1 Assignment of the experimental peaks of (+)-**1** (B3LYP/6-31G*)
Table S6.2 Assignment of the experimental peaks of (+)-**1** (B3LYP/cc-pVTZ)
Table S6.3 Assignment of the experimental peaks of (+)-**2** (B3LYP/6-31G*)
Table S6.4 Assignment of the experimental peaks of (+)-**2** (B3LYP/cc-pVTZ)
Table S6.5 Assignment of the experimental peaks of (−)-**3** (B3LYP/6-31G*)
Table S6.6 Assignment of the experimental peaks of (−)-**3** (B3LYP/cc-pVTZ)
Table S6.7 Neighborhood similarity S^{σ} for theoretical versus experimental IR and VCD spectra using different functionals

Figure S6.1 IR absorption and VCD spectrum for (+)-**1**, (+)-**2** and (−)-**3**, including Lorentzian fit and residual fitting error
Figure S6.2 Simulated (1*S*,8*S*)-**1** IR DFT/6-31G* for different functionals and experimental spectra
Figure S6.3 (1*S*,8*S*)-**1** VCD DFT/6-31G* for different functionals and experimental spectra.

6.5 Reference list

1. Cheeseman, J. R.; Frisch, M. J.; Devlin, F. J.; Stephens, P. J. *Chem. Phys. Lett.* **1996**, *252*, 211-220.

2. Devlin, F. J.; Stephens, P. J.; Cheeseman, J. R.; Frisch, M. J. *J. Phys. Chem. A* **1997**, *101*, 9912-9924.

3. Stephens, P. J.; Ashvar, C. S.; Devlin, F. J.; Cheeseman, J. R.; Frisch, M. J. *Mol. Phys.* **1996**, *89*, 579-594.

4. Stephens, P. J.; Devlin, F. J.; Chabalowski, C. F.; Frisch, M. J. *J. Phys. Chem.-US* **1994**, *98*, 11623-11627.

5. Stephens, P. J. Vibrational circular dichroism spectroscopy: A new tool for the stereochemical characterization of chiral molecules. In *Computational medicinal chemistry for drugs discovery*, Bultinck, P., De Winter, H., Langenaeker, W., Tollenaere, J. P., Eds.; Marcel Dekker, Inc.: New York, **2004**; pp 699-725.

6. Wang, F.; Wang, Y.; Polavarapu, P. L.; Li, T. Y.; Drabowicz, J.; Pietrusiewicz, K. M.; Zygo, K. *J. Org. Chem.* **2002**, *67*, 6539-6541.

7. Kuppens, T.; Langenaeker, W.; Tollenaere, J. P.; Bultinck, P. *J. Phys. Chem. A* **2003**, *107*, 542-553.

8. Aamouche, A.; Devlin, F. J.; Stephens, P. J.; Drabowicz, J.; Bujnicki, B.; Mikolajczyk, M. *Chem.-Eur. J.* **2000**, *6*, 4479-4486.

9. Aamouche, A.; Devlin, F. J.; Stephens, P. J. *J. Am. Chem. Soc.* **2000**, *122*, 2346-2354.

10. Polavarapu, P. L.; Zhao, C. X.; Ramig, K. *Tetrahedron-Asymmetr.* **1999**, *10*, 1099-1106.

11. Wang, F.; Polavarapu, P. L.; Lebon, F.; Longhi, G.; Abbate, S.; Catellani, M. *J. Phys. Chem. A* **2002**, *106*, 5918-5923.

12. Freedman, T. B.; Cao, X. L.; Dukor, R. K.; Nafie, L. A. *Chirality* **2003**, *15*, 743-758.

13. Stephens, P. J.; Devlin, F. J. *Chirality* **2000**, *12*, 172-179.

14. Vandyck, K.; Matthys, B.; Van der Eycken, J. *Tetrahedron Lett.* **2005**, *46*, 75-78.

15. *Catalytic Asymmetric Synthesis;* 2nd ed.; Wiley-VCH: New York, **2000**.

16. Fujii, A.; Hashiguchi, S.; Uematsu, N.; Ikariya, T.; Noyori, R. *J. Am. Chem. Soc.* **1996**, *118*, 2521-2522.

17. Moglioni, A. G.; Tombari, D. G.; Iglesias, G. Y. M. *J. Chem. Research (S)* **1998**, 9, 606-607.

18. Palucki, M.; Pospisil, P. J.; Zhang, W.; Jacobsen, E. N. *J. Am. Chem. Soc.* **1994**, *116*, 9333-9334.

19. Kobayashi, T.; Tanaka, K.; Miwa, J.; Katsumura, S. *Tetrahedron-Asymmetr.* **2004**, *15*, 185-188.

20. Larrow, J. F.; Roberts, E.; Verhoeven, T. R.; Ryan, K. M.; Senanayake, C. H.; Reider, P. J.; Jacobsen, E. N. *Org. Synth.* **1999**, *76*, 46-56.

21. Urbanova, M.; Setnicka, V.; Volka, K. *Chirality* **2000**, *12*, 199-203.

22. Nafie, L. A. *Appl. Spectrosc.* **2000**, *54*, 1634-1645.

23. Polavarapu, P. L. *Spectroscopy* **1994**, *9*, 48-55.

24. Sadowski, J.; Schwab, C. H.; Gasteiger, J. 3D structure generation and conformational searching. In *Computational medicinal chemistry for drugs discovery*, Bultinck, P., De Winter, H., Langenaeker, W., Tollenaere, J. P., Eds.; Marcel Dekker, Inc.: New York, **2004**; pp 151-212.

25. Halgren, T. A. *J. Comput. Chem.* **1996**, *17*, 490-519.

26. *Allinger, N. L. MM3(96)*, **1996**

27. Allinger, N. L.; Yuh, Y. H.; Lii, J. H. *J. Am. Chem. Soc.* **1989**, *111*, 8551-8566.

28. Frisch, M. J.; Trucks, G. W.; Schlegel, H. B.; Scuseria, G. E.; Robb, M. A.; Cheeseman, J. R.; Montgomery Jr, J. A.; Vreven, T.; Kudin, K. N.; Burant, J. C.; Millam, J. M.; Iyengar, S. S.; Tomasi, J.; Barone, V.; Mennucci, B.; Cossi, M.; Scalmani, G.; Rega, N.; Petersson, G. A.; Nakatsuji, H.; Hada, M.; Ehara, M.; Toyota, K.; Fukuda, R.; Hasegawa, J.; Ishida, M.; Nakajima, T.; Honda, Y.; Kitao, O.; Nakai, H.; Klene, M.; Li, X.; Knox, J. E.; Hratchian, H. P.; Cross, J. B.; Bakken, V.; Adamo, C.; Jaramillo, J.; Gomperts, R.; Stratmann,

R. E.; Yazyev, O.; Austin, A. J.; Cammi, R.; Pomelli, C.; Ochterski, J. W.; Ayala, P. Y.; Morokuma, K.; Voth, G. A.; Salvador, P.; Dannenberg, J. J.; Zakrzewski, V. G.; Dapprich, S.; Daniels, A. D.; Strain, M. C.; Farkas, O.; Malick, D. K.; Rabuck, A. D.; Raghavachari, K.; Foresman, J. B.; Ortiz, J. V.; Cui, Q.; Baboul, A. G.; Clifford, S.; Cioslowski, J.; Stefanov, B. B.; Liu, G.; Liashenko, A.; Piskorz, P.; Komaromi, I.; Martin, R. L.; Fox, D. J.; Keith, T.; Al-Laham, M. A.; Peng, C. Y.; Nanayakkara, A.; Challacombe, M.; Gill, P. M. W.; Johnson, B.; Chen, W.; Wong, M. W.; Gonzalez, C.; Pople, J. A. *Gaussian03*, Revision B5; Gaussian, Inc.: Wallingford CT, **2004**.

29. Becke, A. D. *J. Chem. Phys.* **1993**, *98*, 5648-5652.

30. Lee, C. T.; Yang, W. T.; Parr, R. G. *Phys. Rev. B-Condens. Matter* **1988**, *37*, 785-789.

31. Frisch, A. E.; Frisch, M. J.; Trucks, G. *Gaussian 03 User's Reference;* 5th ed.; Gaussian, Inc.: Pittsburgh, **2003**.

32. De Gelder, R.; Wehrens, R.; Hageman, J. A. *J. Comput. Chem.* **2001**, *22*, 273-289.

33. McQuarrie, D. A. *Statistical Thermodynamics;* Harper and Row: New York, **1973**.

34. Wolfe, S. *Acc. Chem. Res.* **1972**, *5*, 102-111.

35. He, J. T.; Polavarapu, P. L. *Spectrochim. Acta A* **2005**, *61*, 1327-1334.

7

elucidation of the AC of JNJ-27553292, a CCR2 receptor antagonist

7.1 Introduction

The chemokine receptor CCR2 has a central role in the establishment and maintenance of chronic inflammatory processes. CCR2 and its primary ligand, MCP1, represent a critical signaling pathway for the recruitment of peripheral blood monocytes to sites of immune-mediated inflammation, where they become inflammatory macrophages.[1] Macrophages are among the predominant cell types found at sites of chronic inflammation, and clinical observations show a close correlation between lower macrophage burden and reduced severity of disease.
The inhibition of the CCR2 receptor is a promising target for various inflammatory diseases such as rheumatoid arthritis, multiple sclerosis, chronic obstructive

Kuppens, T.; Herrebout, W.; van der Veken, B. J.; Corens, D.; De Groot, A.; Doyon, A.; Van Lommen, G.; Bultinck, P. *Chirality* **2006**, *18*, 609-620.

pulmonary disease and atherosclerosis.[1] Recently, a new class of CCR2 antagonists were described, i.e., the 2-mercapto-imidazoles[2-5], with compound **1** being one of the most active representatives of this series. It was found that the CCR2 antagonistic activity resides primarily in one enantiomer hence the need to elucidate the absolute configuration for this compound. The synthesis of **1** is described in Scheme 7.1.

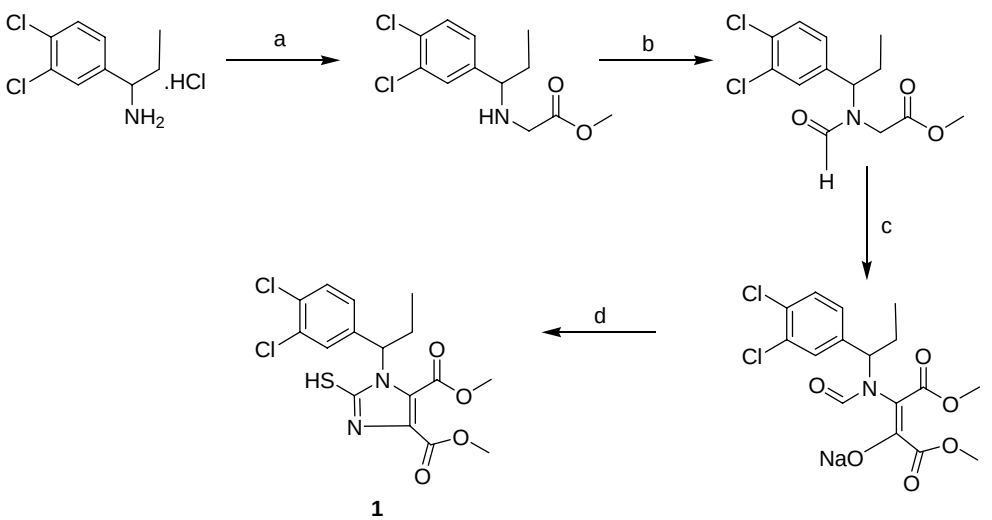

Scheme 7.1 Synthetic route to 2-mercaptoimidazole **1**. Reagents and conditions (yields): a. Methylbromoacetate, Di-isopropyl-ethylamine (DIPEA), THF [room temperature, 1 days] (80%) b. HCOOH, xylene [reflux, 6 h] (100%) c. methyloxalate, NaOtBu, THF [room temperature, 20 h] d. KSCN, HCl–H_2O, MeOH [60 °C, 20 h] (70% over c and d)

Both enantiomers of **1** were prepared following Scheme 7.1, starting from the corresponding enantiomers of 1-(3',4'-dichlorophenyl)-propanamine (**5**) that can be synthesized enantioselectively according to Scheme 7.2.[6-8]

Although 1-(3',4'-dichlorophenyl)-propanol (**3**) has not been described before, very close analogues (phenyl and 4'-chlorophenyl) have been published.[7,8]
The more active enantiomer of **1** was found to be (−)-**1**, derived from amine (−)-**5** that by analogy with the published data should have the *S* configuration.
To confirm this assignment a vibrational circular dichroism (VCD) analysis was performed on amine (−)-**5**. The analysis of the antagonist **1** itself would not render the same reliability, due to the higher density of vibrational transition (and consequently more unresolved bands). The starting alcohol (+)-**3** was analyzed to confirm the inversion of absolute configuration (step b in Scheme 7.2) unambiguously. VCD has become a good technique as an alternative for other

absolute configuration determination methods such as X-ray diffraction and NMR, and has proven its reliability for a wide range of molecules.[9,10]

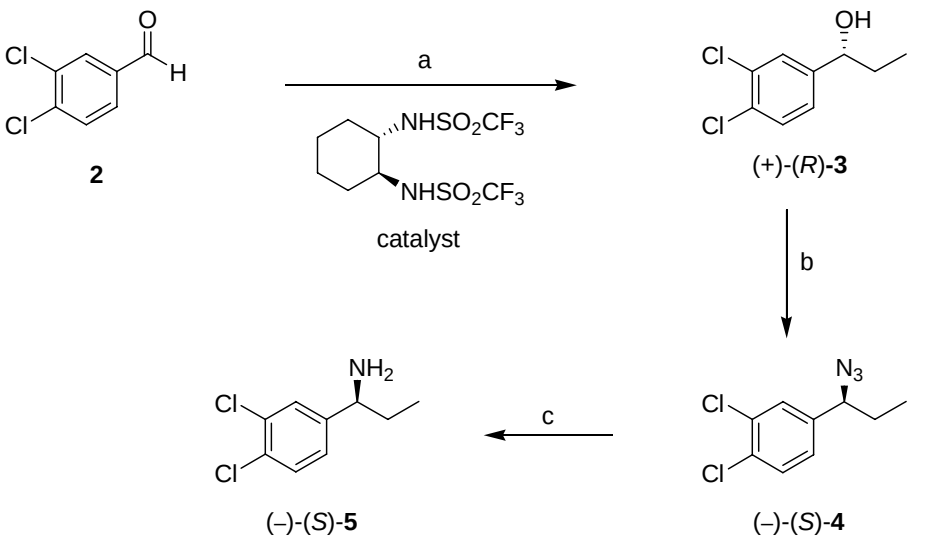

Scheme 7.2 Stereospecific synthesis of 1-(3,4-chloro-phenyl)-1-amino-propane. Reagents (yields) : a. Et_2Zn, $Ti(i\text{-}PropO)_4$, catalyst N,N'-((1*S*,2*S*)-cyclohexane-1,2-diyl)bis(trifluoromethanesulfonamide), toluene, −78 °C (100%) b. Diphenylphosphorylazide, 1,8-diazabicyclo[5.4.0]undec-7-ene, toluene (75%) c. Pt/C (10%), H_2, methanol (75%).

The circular dichroism (CD) phenomenon is in principle the differential absorption (by a molecular species) of left and right circularly polarized light.[11] CD is only observable for chiral molecules or species for which the mirror image of a molecule cannot be brought in coincidence with itself. Vibrational CD applies circularly polarized infrared (IR) radiation. The first measurements of VCD date back to the early 1970s.[12,13] Since then, the technique has improved continuously, and nowadays, VCD spectra for the 800–1800 cm^{-1} mid-IR region can be measured almost routinely.[14]

As VCD is a differential form of spectroscopy, intensities can be negative. The intensities of the VCD of enantiomers are equal in magnitude but opposite in sign. However, extracting the absolute configuration from the VCD spectra is not straightforward, but nevertheless can be done using quantum chemical calculations. A relatively fast and accurate algorithm was developed that allows to calculate VCD intensities[15-17] using density functional theory (DFT).[18] As a result, VCD spectra for

molecules with known stereochemistry can be computed and compared to experimental spectra.
The availability of VCD spectrometers and software that allows the calculation of VCD intensities makes VCD a highly practical method in the elucidation of the absolute configuration. Moreover, measurements can be done in diluted solutions, and no extra synthesis steps or additives are required, in contrast to other techniques.[19]

7.2 Methods

7.2.1 Preparation of the catalyst

To an ice-cold solution of trans-(1*S*,2*S*)-cyclohexyl diamine (5 g, 44 mmol) and di-isopropylethylamine in 250 ml of dichloromethane was added dropwise trifluoromethane sulfonylchloride (16.8 g, 100 mmol) in 50 ml of dichloromethane. The reaction mixture was allowed to warm to room temperature and stirred overnight. The reaction mixture was poured in water and the organic phase was washed three times with 100 ml of 1 N HCl. After drying and concentration of the organic phase 15.9 g of a very light yellow solid (96%) was obtained. Melting point 184–186 °C.

7.2.2 Preparation of (+)-(*R*)-1-(3',4'-dichlorophenyl)-propanol (3)

A 3 liter flask was charged with 1 liter of dry toluene, the catalyst (2 g, 0.0053 mol) and Ti(*i*-PrO)$_4$ (193 g, 0.68 mol). The resulting solution was degassed by three freeze-thaw cycles under argon. This solution was then heated to 40 °C for 20 minutes and cooled to −78 °C. Pure Et_2Zn (85 g, 0.68 mol) was carefully transferred under argon via a large-gauge cannula into an addition funnel and then added over 20 minutes to the reaction mixture. The light orange solution was left 15 minutes and the aldehyde **2** (100 g, 0.57 mol), dissolved in toluene, was added dropwise over 30 minutes. The reaction mixture was allowed to slowly warm up to 0 °C over a few hours. After 4 h the reaction mixture was carefully quenched by addition of 1 M HCl. The aqueous layer was extracted with CH_2Cl_2 and the combined organic phases were filtered through celite, washed with water, dried over $MgSO_4$ and concentrated to give 120 g of a light yellow liquid containing traces of toluene but otherwise pure

by GC-MS and NMR; α_D^{20} = +27 (*c*=0.47, $CHCl_3$); IR 3346, 2966, 2933, 2877, 1687, 1587, 1466, 1383, 1029, 819 cm^{-1}; ^1H NMR ($CDCl_3$, 360 MHz) δ (ppm) 7.42 (d, *J*=2.2 Hz, 1 H), 7.39 (d, *J*=8.4 Hz, 1 H), 7.14 (dd, *J*=2.2, 8.4 Hz, 1 H), 4.55 (t, *J*=6.6 Hz, 1 H), 2.30–2.10 (brd s, 1 H), 1.85–1.60 (m, 2 H), 0.89 (t, *J*=7.3 Hz, 3 H); ^{13}C NMR ($CDCl_3$, 90 MHz) δ (ppm) 144.7, 130.2, 127.9, 125.3, 74.6, 31.8, 9.8.

7.2.3 Preparation of (−)-(*S*)-4-(1-azidopropyl)-1,2-dichlorobenzene (4)

The alcohol **3** (26 g, 0.127 mol) and DPPA (42 g, 0.153 mol) were placed in a 1 liter flask containing 0.5 liter of dry toluene and the mixture was cooled to 0 °C. 1,8-diazabicyclo[5.4.0]undec-7-ene (DPU) (23.3 g, 0.153 mol) was added dropwise over 30 minutes. The reaction mixture was allowed to slowly warm-up to room temperature and further stirred for 12 h. The reaction mixture was diluted with toluene and washed three times with 200 ml each of 1M HCl. The organic phase was washed with water, dried over $MgSO_4$, concentrated and purified by column chromatography on silica gel (elution with CH_2Cl_2 then with 1% MeOH in CH_2Cl_2) giving 23.5 g of a colorless liquid.
α_D^{20} = −125 (*c*=0.58, $CHCl_3$), IR (film) 2093 (s); ^1H NMR ($CDCl_3$, 360 MHz) δ (ppm) 7.45 (d, *J*=8.4 Hz, 1 H), 7.39 (d, *J*=2.2 Hz, 1 H), 7.14 (dd, *J*=2.2, 8.4 Hz, 1 H), 4.33 (app. t, *J*=6.95 Hz, 1 H), 1.92–1.66 (m, 2 H), 0.93 (t, *J*=7.3 Hz, 3 H); ^{13}C NMR ($CDCl_3$, 90 MHz) δ (ppm) 140.1, 132.9, 132.2, 130.7, 128.9, 126.2, 66.6, 29.4, 10.5.

7.2.4 Preparation of (−)-(*S*)-1-(3',4'-dichlorophenyl)-propanamine (5)

A solution of the azide **4** (50 g, 0217 mol) in methanol (800 ml) and Pt/C 5% (2 g) was placed in a Parr apparatus and flushed with three cycles of vacuum/hydrogen. The flask was then placed under 50 psi of hydrogen. The reaction was monitored by TLC. The catalyst was filtered-off and the solvent evaporated under reduced pressure. The light yellow oil obtained was dissolved in DIPE and treated with HCl/*i*-PrOH. The solid was collected, washed with DIPE and dried giving 38 g of a white solid.
For the free base : α_D^{20} = –119 (*c*=0.65, $CHCl_3$), ^1H NMR ($CDCl_3$, 360 MHz) δ (ppm) 7.43 (d, *J*=2.2 Hz, 1 H), 7.38 (d, *J*=8.0 Hz, 1 H), 7.15 (dd, *J*=8.0, 2.2 Hz, 1

H), 3.79 (app. t, *J*=6.6 Hz, 1 H), 1.72–1.58 (m, 2 H), 1.55–1.45 (bs, 2H), 0.86(t, *J*=7.3 Hz, H);

7.2.5 Spectroscopy

Spectra are measured using a Bruker Vector 22 and a Bruker IFS66v/S FTIR spectrometer coupled to a PMA37 module.[20] The infrared (IR) and VCD spectra for (+)-**3** are recorded in a demountable cell with KBr windows and a 105 µm Teflon spacer. The spectra for (−)-**5** are recorded with CaF_2 windows and a 200 µm Teflon spacer. The unpolarized IR absorbance spectra are recorded at a resolution of 4 cm^{-1}, the VCD spectra at a resolution of 6 cm^{-1}. To improve the VCD S/N ratio a long wave-pass filter with an 1830 cm^{-1} cutoff is used. The collection time for the VCD spectrum is 90 minutes each. (+)-**3** is dissolved in $CDCl_3$ at a concentration of 0.39 M. For (−)-**5** CD_2Cl_2 is used as solvent at a concentration of approximately 0.29 M.

To get a good estimate for baseline artifacts one can measure the VCD of the racemic mixture or both enantiomers.[21] As these are not always available, the VCD of the solvent, measured in the same conditions as the sample, is often a good approximation.[22,23]

For both the infrared and VCD spectra, there was no effect seen of possible self-association for compounds **3** and **5**

7.2.6 Computation

Geometry optimizations and the calculation of the dipole strengths *D* and rotational strengths *R* are performed using Gaussian03 revision B5.[24] The B3LYP[25,26] hybrid functional is used throughout this study, generally giving good results when calculating VCD intensities.[17,22,27] The conformational search is performed with the 6-31G* basis set[28], using a systematic search method.[29] For each located B3LYP/6-31G* stationary point, Hessian matrices are calculated to ensure that the obtained structure corresponds to a minimum. The 6-31G* basis set is regarded as an adequate basis set for the description of geometries, vibrational frequencies and IR/VCD intensities.[27] However, the cc-pVTZ basis set is considered to be superior compared to the 6-31G* basis set.[9,27] Therefore, all the unique minima were further optimized at the B3LYP/cc-pVTZ[30,31] level and Hessian matrices, atomic polar tensors (APT) and atomic axial tensors (AAT) are calculated using gauge

including/invariant atomic orbitals (GIAOs)[32,33], allowing the calculation of the dipole and rotational strengths. The enthalpy and free energy are calculated under the usual assumptions using standard thermochemical expressions.[34] An appropriate scaling factor is used to correct for the harmonic approximation.[28] All calculations were performed on the Ghent Quantum Cluster.

7.2.7 Conformational analysis

Experimental IR and VCD spectra are averaged spectra over all conformations that are present in solution. As VCD is very sensitive to conformational differences,[35] it is of the utmost importance that all lower energy conformers (less than 5 kcal/mol) are located. A thorough analysis of the potential energy surface (PES) is therefore required.

For this specific case, the conformational properties of the two compounds, i.e. **3** and **5**, are probed using a systematic search method. The key dihedral angles shown in Figure 7.1 are systematically varied, producing a set of starting geometries. These starting geometries are optimized on the B3LYP/6-31G* level.

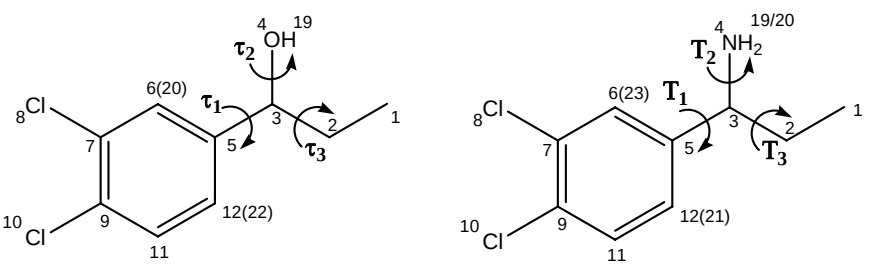

Figure 7.1 Definition of the dihedral angles explored in the conformational search for compound **3** (τ) and **5** (T); $\tau_1 \equiv C^6C^5C^3O^4$, $\tau_2 \equiv H^{19}O^4C^3C^2$, $\tau_3 \equiv C^5C^3C^2C^1$, $T_1 \equiv C^6C^5C^3N^4$, $T_2 \equiv H^{19}N^4C^3C^2$ and $T_3 \equiv C^5C^3C^2C^1$.

For alcohol **3** the *R* configuration is modeled. The dihedral angles $C^6C^5C^3O^4$ (τ_1) and $C^5C^3C^2C^1$ (τ_3) are developed in a 30° grid and the $H^{19}O^4C^3C^2$ torsion (τ_2) in a 60° grid. This resulted in 864 unique and chemically sound starting geometries. Optimization of all these geometries yielded 24 unique minima. These minima were further optimized at B3LYP/cc-pVTZ level and finally resulted in a total of 20 unique minima. All B3LYP/6-31G* minima that could not be located with the

cc-pVTZ basis set have a B3LYP/6-31G* relative energy of above 2.7 kcal/mol. In Table 7.1 the essential B3LYP/cc-pVTZ structural parameters are given. For each conformation, a related structure can be found with almost the same enthalpy. The geometries of these nearly equal enthalpic conformations are different, i.e. the 3,4-dichloro-benzene moiety is rotated over 180° about the C^3–C^5 bond. In Table 7.1 this is expressed by the C−C−C−O torsion (τ_1). The barrier of interconversion is approximately 6 kcal/mol.

Table 7.1 Overview of the localized B3LYP/cc-pVTZ minima for 3: conformational numbering, label (a-i), description, key dihedral angles (τ_1, τ_2 and τ_3, in degrees), relative enthalpies (ΔH^0, in kcal/mol), relative free energy (ΔG^0, in kcal/mol) and the Boltzmann population based on ΔG^0 (% P, T = 298.15 K).

		τ_1 $C^6C^5C^3O^4$	τ_2 $H^{19}O^4C^3C^2$	τ_3 $C^5C^3C^2C^1$	ΔH^0	ΔG^0	% P
1/a	1gT+	−145.8	61.5	−174.9	0.00	0.00	30.67
2/b	1gT	33.0	62.0	−174.5	0.00	0.16	23.50
3/c	2gG'+	−135.9	55.9	−65.2	0.62	0.79	8.08
4/d	2gG'	42.5	55.7	−64.9	0.66	0.90	6.77
5/g	3gG	23.9	61.4	64.0	1.11	1.58	2.14
6/e	4tT+	−155.4	178.3	−177.1	1.12	0.92	6.54
7/f	4tT	22.7	179.0	−176.7	1.13	1.01	5.56
8/h	3gG+	−156.3	61.8	63.8	1.18	1.61	2.04
9	5g'T	8.5	−80.1	−172.3	1.55	1.76	1.58
10/j	5g'T+	−171.5	−79.5	−172.5	1.64	1.64	1.93
11/i	6tG'	40.4	−170.5	−64.9	1.67	1.62	2.01
12	7tG	14.0	−179.7	62.4	1.67	1.86	1.34
13	6tG'+	−139.8	−171.9	−65.3	1.68	1.93	1.19
14	7tG+	−165.7	−180.0	62.1	1.72	1.82	1.43
15	8g'T+	−110.7	−59.8	−174.6	2.24	1.73	1.65
16	8g'T	76.1	−56.8	−173.6	2.26	1.82	1.42
17	9g'G	4.2	−79.9	63.8	2.35	2.70	0.32
18	9g'G+	−174.5	−79.6	64.1	2.42	2.53	0.43
19	10g'G'	75.2	−60.4	−63.1	2.59	2.27	0.66
20	10g'G'+	−100.0	−59.2	−62.9	2.61	2.19	0.76

For the C−C−O−H torsion (τ_2) and the C−C−C−C torsion (τ_3) of the propanol substituent, classical PES minima can be recognized, i.e. for values of approximately 60, −60 and 180°. For τ_2, this value appears to deviate (±30°) for a few conformations. This can be attributed to a strong intra-molecular $C{-}H^{20/22(ortho)}\cdots O^4$ interaction and a weaker OH···π interaction that considerably

stabilizes some conformations. The C−C−O−H torsion is labeled as g, g' and t for respectively 60, −60 and 180°. For the C−C−C−C torsion identical labels are used, yet in uppercase. The '+' label gives the position of the hydroxyl group relative to the dichloro-benzene moiety. In Table 7.1 an apt notation for alcohol **3** to identify the minima in the PES is given.

Table 7.2 Overview of the localized B3LYP/cc-pVTZ minima for 5: conformational numbering, label (a−m), description, key dihedral angles (T_1, T_2 and T_3, in degrees), relative enthalpies (ΔH^0, in kcal/mol), relative free energy (ΔG^0, in kcal/mol) and the Boltzmann population based on ΔG^0 (% P, T = 298.15 K)

		T_1 $C^6C^5C^3N^4$	T_2 $H^{19}N^4C^3C^2$	T_3 $C^5C^3C^2C^1$	ΔH^0	ΔG^0	% P
1/a	1gT+	−36.5	−62.0	174.5	0.00	0.00	19.73
2/b	1gT	143.6	−62.0	175.0	0.05	0.22	13.51
3/e	2gG	135.9	−62.2	64.4	0.08	0.35	10.84
4/d	2gG+	−43.6	−62.3	63.9	0.09	0.35	10.96
5/f	3tT+	−47.1	67.5	169.7	0.64	0.46	9.13
6/c	3tT	128.7	65.6	169.7	0.65	0.27	12.59
7/i	4gG'+	−25.5	−63.8	−63.3	0.75	1.22	2.50
8/j	4gG'	155.1	178.2	−63.2	0.85	1.29	2.23
9/g	5tG+	−59.1	69.0	61.3	0.86	0.81	5.04
10/h	5tG	118.7	68.0	61.0	0.87	0.90	4.35
11/m	6g'T+	−7.7	−160.0	172.1	1.44	1.62	1.28
12/l	6g'T	171.5	−159.7	172.1	1.54	1.62	1.29
13	7g'T	−133.0	69.3	175.7	1.84	2.10	0.57
14	8tG'+	−22.6	70.0	−67.4	1.85	2.23	0.46
15	8tG'	157.7	67.0	−66.4	1.99	2.16	0.51
16	9g'G'+	0.4	−165.9	−63.5	2.22	2.62	0.24
17/k	11g'T+	−63.5	67.9	173.4	2.27	1.36	1.99
18	9g'G'	178.1	75.9	−63.3	2.28	2.37	0.36
19	10g'G+	−74.8	178.1	62.0	2.29	2.06	0.61
20	10g'G	104.4	178.1	62.6	2.32	2.13	0.54
21	11g'T	117.1	67.8	174.0	2.32	2.14	0.53
22	12g'G+	−98.8	−179.9	64.6	2.37	1.95	0.73
23	13gG'+	−127.8	−49.1	−72.7	5.41	5.27	0.00
24	13gG'	58.3	−165.7	−73.9	5.46	5.43	0.00

The *S* configuration is modeled for amine **5.** Dihedral angles $C^6C^5C^3N^4$ (T_1), $H^{19}N^4C^3C^2$ (T_2) and $C^5C^3C^2C^1$ (T_3) are varied in a 30° grid, giving a set of 1728 starting geometries. All starting geometries are optimized at B3LYP/6-31G* level. 27 unique geometries are found, all corresponding to a minimum in the PES. These

geometries were further optimized at B3LYP/cc-pVTZ level of theory. Four 6-31G* higher energy minima (at least 2.54 kcal/mol above global minimum) could not be located on the cc-pVTZ PES. The essential geometric parameters for the located minima are shown in Table 7.2 along with the relative enthalpy and free energy. To identify all minima, the same notation is used as for compound **3.**

Some conformations of compound **5** are intramolecularly stabilized through interaction between the N lone pair and the ortho-hydrogens ($H^{21/23}$). There is also indication for a weaker NH···π interaction.

7.2.8 IR and VCD data

Dipole and rotational strengths are calculated via DFT. The discrete line spectra are broadened using Lorentzian shapes with a full width at half maximum of 10 cm^{-1} and converted to molar absorptivity units using Equation (7.1) and (7.2).[36] As, for the compounds studied, different conformations coexist, the contributions of each conformation have to be taken into account. A Boltzmann weighed distribution is applied to determine the population of each minimum, using relative free energies. In Figures 7.2, 7.3, 7.4 and 7.5 (ii), the simulated IR and VCD spectra are shown i.e. broadened and Boltzmann weighed over all conformations. The calculated frequencies are scaled with a factor 0.98, to correct for the overestimation of the calculated frequencies.[37,38]

Agreement between experimental and theoretical IR and VCD spectra allows the determination of the absolute configuration of the experimental sample. However, simple comparison is not enough to determine an absolute configuration, and a more thorough analysis of the available data has to be performed. First of all, the different fundamentals need to be assigned in the experimental spectra based on the theoretical data. As VCD is a differential form of IR spectroscopy, IR and VCD transition frequencies are the same. Because of the differential intensities, VCD spectra have extra discriminating potential. As a result, assignment of unresolved IR bands can be performed using the experimental VCD counterpart. Vice versa, assignment of unresolved VCD bands can sometimes be based on IR information.

The next step is to determine the experimental dipole and rotational strengths. Here, the assumption is made that the shape of the experimental bands is Lorentzian. The area under the bands can be related to their dipole and rotational strengths.[39] Using a Lorentzian peak fitting procedure[27], and applying Equations (7.1) and (7.2) the experimental dipole and rotational strengths can be approximated.

$$D_i = 9.184 \cdot 10^{-39} \int \varepsilon_i \frac{d\nu}{\nu} \approx 9.184 \cdot 10^{-39} \frac{1}{\nu_{i,\max}} \int \varepsilon_i d\nu \quad (7.1)$$

$$R_i = 2.296 \cdot 10^{-39} \int \Delta\varepsilon_i \frac{d\nu}{\nu} \approx 2.296 \cdot 10^{-39} \frac{1}{\nu_{i,\max}} \int \Delta\varepsilon_i d\nu \quad (7.2)$$

In Equations (7.1) and (7.2), $\nu_{i,\max}$ is the frequency (in cm^{-1}) where the fitted Lorentzian *i* is centered. Here, ε and Δε are respectively the molar absorptivity and differential molar absorptivity in $l.mol^{-1}cm^{-1}$. *D* and *R* are in esu^2cm^2. In Tables 7.3, 7.4, 7.5 and 7.6 experimental values for *D* and *R* are given with corresponding frequency. The theoretical *D* and *R* values in these tables are summed contributions from different conformations. The theoretical frequencies are averaged. In *Supplementary Material*, tables are given in which the contribution of the significant fundamentals are explicitly reported.

7.3 Results and discussion

The assignment of the fundamentals for compound **3** is not straightforward due to the fact that the contributions of 10 different conformations can be observed. These conformations are situated in a 1.70 kcal/mol energy window (Table 7.1). The main features of the spectra can be explained in terms of the conformations within 1.01 kcal/mol, i.e. 1gT+ (a), 1gT (b), 2gG'+ (c), 2gG' (d), 4tT+ (e) and 4tT (f). Taking into account conformations 3gG (g), 3gG+ (h), 6tG' (i) and 5g'T+ (j) allows the assignment of some small bands in the VCD spectrum. In Figures 7.2 and 7.3 the Lorentzian fitted experimental IR and VCD spectra of (+)-**3** are given. In these figures the simulated spectra of (*R*)-**3** also can be found.

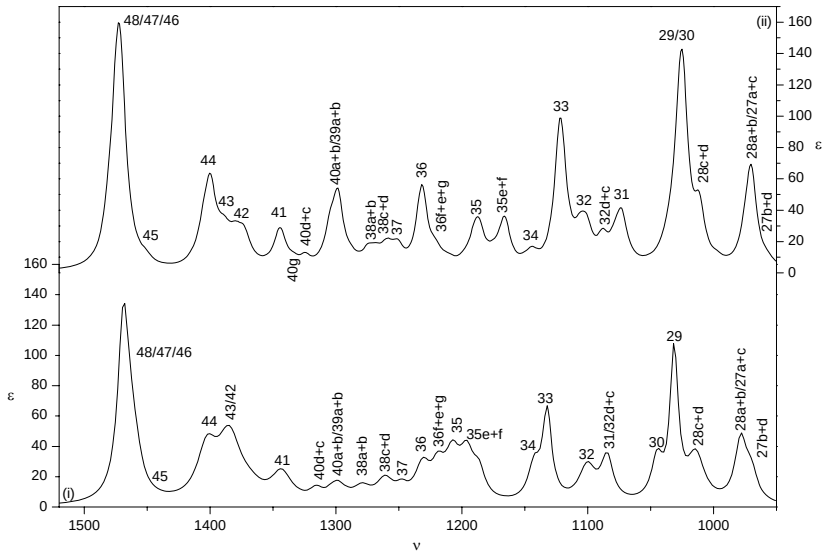

Figure 7.2 Lorentzian fitted experimental IR spectrum (i) for (+)-**3** and B3LYP/cc-pVTZ (ii) simulated IR spectrum for (*R*)-**3**. Experimental and simulated spectra are given in molar absorptivity units, frequencies in cm^{-1}.

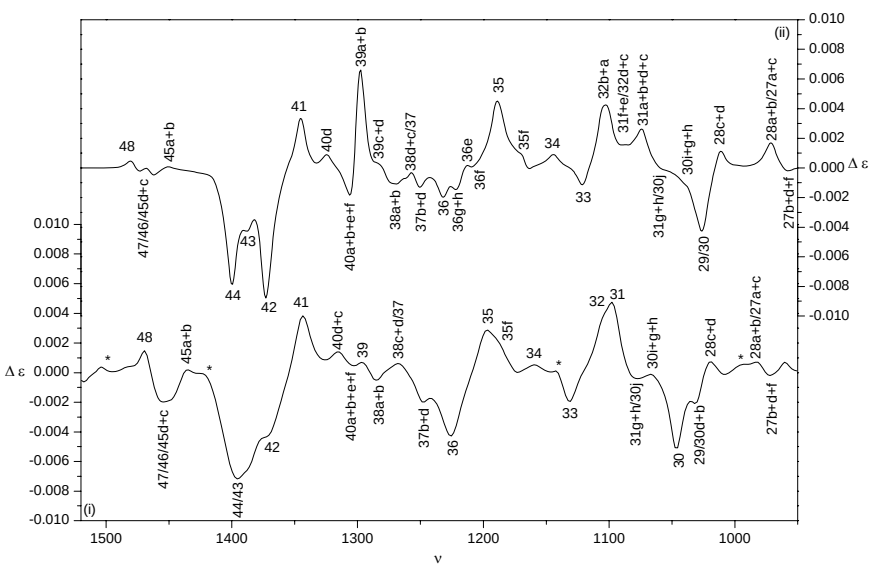

Figure 7.3 Lorentzian fitted experimental VCD spectrum (i) for (+)-**3** and B3LYP/cc-pVTZ (ii) simulated VCD spectrum for (*R*)-**3**. Experimental and simulated spectra are given in molar absorptivity units, frequencies in cm^{-1}.

The fundamentals corresponding to different conformations are designated using characters (a, b c, etc.) that can be found in Table 7.1. If for two or more conformations the fundamentals coincide or have a small frequency separation, the conformational labels are not given.

The small negative and positive shoulders between bands 29/30 and 31 (Figure 7.3) can be attributed to fundamentals 31gh and 30j for the negative one, and 30igh for the positive. The presence of peaks due to these rather high energy conformations can be attributed to the large rotational strengths for a number of fundamentals.

In Tables 7.3 and 7.4 the experimental and B3LYP/cc-pVTZ values of *D* and *R* are lined up, with their associated frequencies. These tables are a reduced version of the tables that can be found in *Supplementary Material*. The theoretical frequencies in these tables are averaged over all the pertinent fundamentals. The predicted IR and VCD frequencies are identical, but when comparing the calculated frequencies in Tables 7.3 and 7.4 for identical bands these can be different. This can be explained by the fact that, in these cases, different fundamentals are taken into account. For example, based on the calculated IR data, fundamentals 27/28baef have a predicted B3LYP/cc-pVTZ averaged frequency of 968 cm^{-1} (Table 7.3). The rotational strengths for fundamentals 27bfd and 27cae/28baef are opposite in sign however (Table 7.4), and can therefore be discerned from each other. In Table 7.4, the calculated frequencies for these two bands (27bfd and 27cae/28baef) are consequently given separately, i.e. 959 cm^{-1} and 972 cm^{-1}.

Table 7.3 For compound **3**: Lorentzian fitted experimental and broadened B3LYP/cc-pVTZ IR frequencies (υ, in cm^{-1}) and dipole strengths (*D*, in 10^{-40} esu^2cm^2) taking into account the fundamentals of 6 lowest energy minima[*1] (a–f)

Fundamental	Experiment		B3LYP/cc-pVTZ	
	υ	*D*	υ [*2]	*D* [*3]
27/28baef	969.92	29.81	967.96	95.70
	978.31	67.55		
28dc	1014.15	73.00	1011.37	44.24
29/30+30ighj	1031.30	105.69	1028.89	197.97
	1044.81	40.24		
31/32dc	1084.61	43.44	1082.07	65.48
32bafge	1100.34	49.88	1107.12	43.14
33	1132.22	65.31	1121.41	101.35
34	1142.57	32.03	1143.98	8.58
35+35ij	1186.36	22.53	1180.94	75.16
	1196.02	45.66		
	1207.46	47.86		
36+36gh	1218.88	26.91	1224.44	72.56
	1231.12	37.56		
37/38cd	1247.72	9.06	1257.99	26.04
	1261.07	26.75		
38feab/39dc	1279.31	15.60	1273.65	17.14
39efba/40ebaf	1299.34	23.14	1299.22	71.28
40dc	1315.95	8.10	1324.38	6.18
40hg/41	1343.28	39.69	1342.67	31.54
42/43	1384.81	104.44	1381.81	42.48
44	1402.56	60.50	1402.81	57.31
45/46/47/48	1461.03	43.83	1469.54	160.88
	1468.77	128.65		

[*1] higher energy minima that are used are explicitly mentioned (g,h,i and j)
[*2] averaged frequencies over the appropriate fundamentals, scaled with factor 0.98
[*3] summed over the appropriate fundamentals

Table 7.4 For compound **3**: Lorentzian fitted experimental and broadened B3LYP/cc-pVTZ VCD frequencies (υ, in cm^{-1}) and rotational strengths (R, in 10^{-44} esu^2cm^2) taking into account the fundamentals of 6 lowest energy minima[*1] (a–f).

Fundamental	Experiment		B3LYP/cc-pVTZ	
	υ	R	υ [*2]	R[*3]
27bfd	973.22	−2.58	959.00	−1.35
27cae/28baef	981.54	3.29	971.80	4.79
28dc	1020.41	6.91	1011.37	5.38
29/30dcbafe	1030.27	−6.94	1026.38	−18.68
	1046.54	−22.22		
30igh	1065.66	1.82	1035.20	1.52
30j/31gh	1082.45	−8.73	1052.44	−1.72
31/32+32g	1096.68	21.05	1091.71	26.19
	1105.69	10.94		
33	1131.37	−10.43	1121.41	−4.76
34	1158.96	2.22	1143.98	2.26
35+35ij	1188.29	7.09	1180.94	16.27
	1198.46	14.49		
36+36gh	1225.62	−27.60	1224.44	−7.95
37bd	1248.71	−5.09	1251.33	−4.15
37fcae/38cd	1266.90	5.03	1260.20	0.65
38feab	1282.73	−0.35	1269.56	−2.16
	1286.56	−1.44		
39	1295.85	2.57	1289.82	22.81
40ebaf	1302.87	−1.48	1304.63	−12.27
40dc	1315.13	6.36	1324.38	2.48
40hg/41	1343.87	20.83	1342.67	9.08
42	1369.39	−17.13	1374.30	−32.81
43/44	1385.27	−5.37	1396.06	−25.43
	1397.21	−50.56		
45eabf	1436.67	3.51	1450.73	0.40
45dc/46/47	1446.92	−4.74	1470.20	−2.10
	1457.68	−7.44		
48	1468.83	6.25	1480.56	1.73

[*1] higher energy minima that are used are explicitly mentioned (g,h,i and j)
[*2] averaged frequencies over the appropriate fundamentals, scaled with factor 0.98.
[*3] summed over the appropriate fundamentals

Based on the IR assignment (Table 7.3), the frequencies are predicted with a maximum error of 15 cm^{-1}. The VCD bands can be localized more accurately, due

to the extra discriminating power via the negative and positive intensities. Based on the frequency agreement for the VCD fundamental assignment (Table 7.4) a larger frequency error of maximum 30 cm^{-1} is therefore observed. For example, fundamental 48 is unresolved in the IR spectrum, and is observed as one band simultaneously with fundamental 47, 46 and 45. In the VCD spectrum, fundamental 48 is clearly resolved, with its predicted frequency overestimated by 12 cm^{-1}. The error that can be observed for the predicted frequencies, even after scaling with a factor 0.98, can be ascribed to the harmonic approximation and the finite basis sets that are used in the calculations.[37,38]

The relative IR intensities of band 44 and 43/42 are different than predicted, and the intensity of the 40ab/39ab is seriously overestimated. Inspection of the VCD of compound **3** (Figure 7.3) shows that the VCD intensities for fundamentals 40abef and 39 are overestimated. This is due to conformations 1gT+ (a) and 1gT (b) that have a predicted contribution that is clearly too large.

Tables 7.3 and 7.4 allow quantitative comparison of the dipole and rotational strengths, in addition to the visual evaluation. From this table it can be seen that the predicted dipole strength for fundamentals 42/43 and 34 are seriously underestimated. The rotational strengths for fundamentals 30j/31gh, 36, 37fcae/38cd, 45dc/46/47 are clearly underestimated, and for fundamental 39 overestimated. More important, no fundamental is predicted with a wrong sign compared to the experiment.

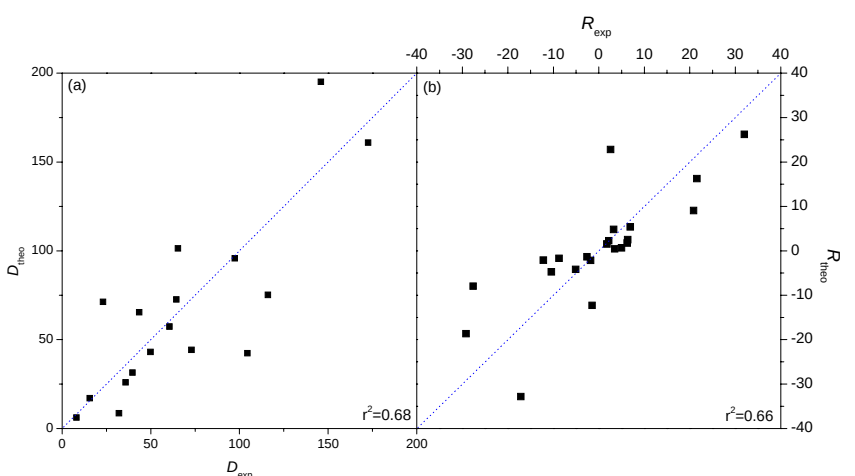

Figure 7.4 Correlation plot for theoretical (for (*R*)-**3**) versus experimental (for (+)-**3**) (a) dipole strengths (*D*, in 10^{-40} esu^2cm^2) and (b) rotational strengths (*R*, in 10^{-44} esu^2cm^2). Correlation coefficients r^2 are given. The blue dotted line has a slope of +1 and intercept of 0.0.

The correlation coefficients for the dipole and rotational strengths are respectively 0.68 and 0.66 (correlation plots are given in Figure 7.4). These values are acceptable. However, three fundamentals could be identified (39, 40abef and 42) which lower the correlation coefficient drastically for both dipole and rotational strengths. If these fundamentals are taken out, correlation coefficients of 0.81 and 0.91 are obtained for respectively dipole and rotational strength. The difference in experimental and theoretical values for these selected fundamentals could be due to intermolecular association, but no evidence for this was found as the normal modes of these fundamentals could not be related to such interactions.

Based on the agreement between experimental and simulated data, and taking into account that the *R* enantiomer is modeled, it can be concluded that the absolute configuration of (+)-**3** can be assigned as (*R*)-**3** in agreement with the proposed configuration.

For compound **5**, the assignment of fundamentals is even more complex than for the previous compound. Fundamentals from 13 minima can be recognized, all situated within 1.62 kcal/mol interval relative to the global minimum (Table 7.2). The majority of the experimental bands can be explained by the lowest 8 energy conformations, i.e. 1gT+ (a), 1gT (b), 3tT (c), 2gG+ (d), 2gG (e), 3tT+ (f), 5tG+ (g) and 5tG (h). These minima are within a 0.90 kcal/mol energy window. In the IR spectrum (Figure 7.5) one band (37klm) can only be explained by taking conformations 11g'T+ (k), 6g'T (l) and 6g'T+ (m) into account. Also conformations 4gG'+ (i) and 4gG' (j) have a considerable contribution.

Again, in the region 1200–1400 cm^{-1} the number of fundamentals is very high and IR intensities are low, which complicates their assignment.
The maximum error for the predicted frequencies based on the IR results is 13 cm^{-1}, and 16 cm^{-1} based on the VCD results. It can also be seen in Figure 7.4 and 7.5 that scaling with 0.98 gives better agreement with experiment than for compound **3**. The negative shoulder in the experimental spectrum at 1277 cm^{-1} can not be assigned based on the simulated spectrum. Though, when examining the extended table (in *Supplementary Material*) it can be seen that fundamentals 40g and 40h have small negative intensities, and are centered at 1284 and 1286 cm^{-1} respectively. Therefore this negative shoulder at 1277 cm^{-1} is assigned as 40gh.

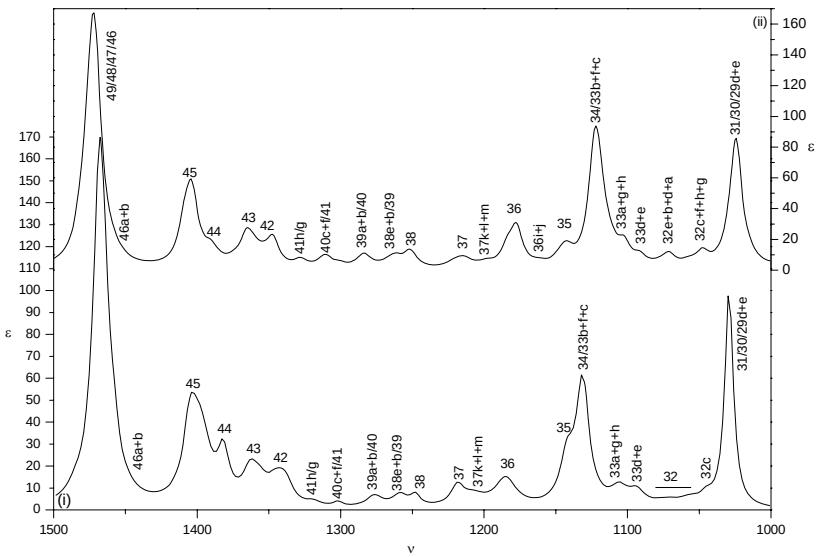

Figure 7.5 Lorentzian fitted experimental IR spectrum (i) for (−)-**5** and B3LYP/cc-pVTZ (ii) simulated IR spectrum for (*S*)-**5**. Experimental and simulated spectra are given in molar absorptivity units, frequencies in cm^{-1}.

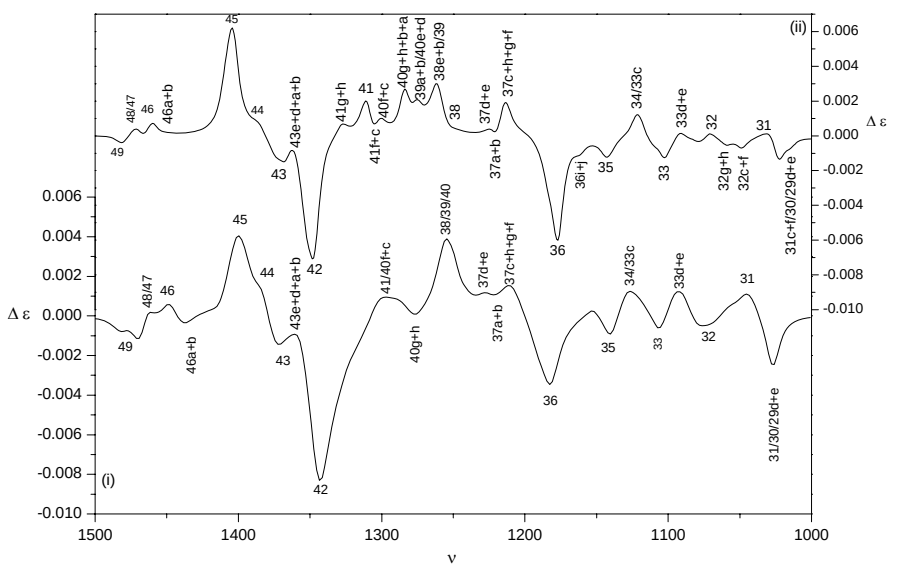

Figure 7.6 Lorentzian fitted experimental VCD spectrum (i) for (−)-**5** and B3LYP/cc-pVTZ (ii) simulated VCD spectrum for (*S*)-**5**. Experimental and simulated spectra are given in molar absorptivity units, frequencies in cm^{-1}.

Table 7.5 For compound **5**: Lorentzian fitted experimental and broadened B3LYP/cc-pVTZ IR frequencies (υ, in cm^{-1}) and dipole strengths (D, in 10^{-40} esu^2cm^2) taking into account the fundamentals of 8 lowest energy minima[*1] (a–h)

Fundamental	Experiment		B3LYP/cc-pVTZ	
	υ	D[*2]	υ	D[*3]
29de/30/31	1029.22	97.97	1024.61	107.81
	1044.73	5.52		
32	1056.28	7.84	1061.99	25.56
	1072.63	7.56		
33de	1093.60	10.40	1091.57	5.14
33hga	1105.71	14.29	1102.11	15.16
33bfc/34	1131.34	78.38	1119.38	120.58
35	1142.15	28.37	1143.28	16.11
36	1184.90	27.23	1179.86	43.54
37klm	1207.97	12.77	1198.75	2.93
37	1218.68	10.17	1217.53	11.20
38hgfcad	1247.86	4.31	1249.92	11.32
38eb/39gcdhef	1258.61	8.36	1262.38	8.46
39ab/40edbagh	1276.45	7.39	1281.24	10.32
40fc/41cfdeab	1301.97	1.51	1307.17	10.60
41hg	1319.07	2.00	1328.02	5.31
42	1338.42	11.38	1346.34	22.02
	1345.05	13.85		
43+43lkm	1356.26	10.95	1367.88	27.96
	1362.91	17.92		
44	1381.79	20.21	1388.58	9.12
45	1397.58	52.24	1405.92	60.86
	1404.76	37.56		
46ab	1448.49	1.37	1452.79	1.18
46fcdegh/47/48/49	1458.79	15.05	1471.32	174.67
	1467.59	186.74		
	1485.27	2.98		

[*1] higher energy minima that are used are explicitly mentioned (k,l and m)
[*2] averaged frequencies over the appropriate fundamentals, scaled with factor 0.98.
[*3] summed over the appropriate fundamentals

Table 7.6 For compound **5**: Lorentzian fitted experimental and broadened B3LYP/cc-pVTZ VCD frequencies (υ, in cm^{-1}) and rotational strengths (R, in 10^{-44} esu^2cm^2) taking into account the fundamentals of 6 lowest energy minima[*1] (a–h)

Fundamental	Experiment		B3LYP/cc-pVTZ	
	υ	R	υ [*2]	R[*3]
29de/30/31cf	1027.08	−12.03	1022.40	−6.24
31adbghe	1044.31	8.56	1029.02	1.94
32	1058.06	1.84	1061.99	−2.52
	1069.71	−3.31		
	1079.42	−3.07		
33ed	1089.42	3.29	1091.57	3.14
	1094.95	4.70		
33ghabf	1106.33	−4.92	1105.93	−5.73
33c/34	1121.67	4.15	1121.09	4.79
	1128.72	5.78		
35	1140.08	−5.96	1143.28	−3.66
36	1182.17	−15.89	1179.86	−22.44
	1190.99	−5.08		
37hcgf	1209.91	10.54	1213.17	6.02
37ab	1220.39	−1.89	1219.20	−2.51
37de	1228.71	2.75	1224.57	1.28
38/39/40edba	1246.23	−1.18	1263.95	17.47
	1249.31	8.50		
	1255.82	11.88		
40gh	1276.65	−2.81	1284.76	−0.25
40fc/41	1288.58	4.96	1311.34	8.72
	1301.71	7.33		
42	1343.57	−36.50	1346.34	−23.36
43edab	1357.01	5.27	1364.00	4.72
43fgch+43lkm	1373.47	−6.24	1370.10	−6.36
44	1383.72	3.92	1388.58	2.10
45	1395.96	5.05	1405.92	18.11
	1401.30	14.91		
46ab	1438.10	−2.30	1452.79	0.09
46fcdegh/47fc	1448.25	2.30	1461.76	1.29
47bdag/48	1463.52	2.02	1471.86	1.32
49	1468.95	−4.21	1479.94	−1.29
	1482.76	−2.05		

[*1] higher energy minima that are used are explicitly mentioned (k,l and m)
[*2] averaged frequencies over the appropriate fundamentals, scaled with factor 0.98.
[*3] summed over the appropriate fundamentals

The rotational strengths of fundamentals 46a and 46b are respectively 0.61 and −0.52 and are centered at 1453 cm^{-1}. Their sum is positive and consequently its sign does not agree with the experimental observation as is shown in Table 7.6 and can be seen in Figure 7.6.

The signs of the rotational strengths vary for the different conformations for fundamental 32 as can be seen in Figure 7.6 and the extended table in *Supplementary Material*. In the experimental spectrum, the band assigned as fundamental 32 is not resolved and has a negative sign. Summing over all the rotational strengths for the significant conformations (a–h) for fundamental 32, this value also appears to be negative in agreement with experiment, as can be seen in Table 7.6.

Further, dipole strengths for fundamentals 37klm and 40 are underestimated, and for fundamentals 40fc/41cfdeab they are overestimated. The rotational strength for fundamental 31adbghe is found to be underestimated.

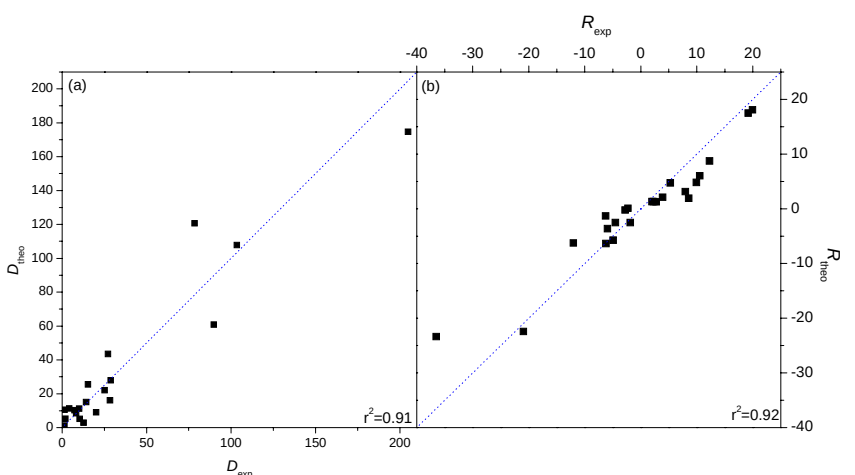

Figure 7.7 Correlation plot for theoretical (for (*S*)-**5**) versus experimental (for (−)-**5**) (a) dipole strength (*D*, in 10^{-40} esu^2cm^2) and (b) rotational strengths (*R*, 10^{-44} esu^2cm^2). Correlation coefficients r^2 are given. The blue dotted line has a slope of +1 and an intercept of 0.0.

The correlation coefficients between theoretical and experimental values of *D* en *R* are 0.91 for the dipole strengths and 0.92 for the rotational strengths, which is excellent (Figure 7.7).

Given the good agreement between experimental and theoretical data, and taking into account that the *S* enantiomer is modeled, the absolute configuration of (−)-**5** can be assigned to (*S*)-**5**, in agreement with the proposed configuration.

7.4 Conclusion

In this study the absolute configurations for two related compounds (+)-**3** and (−)-**5** are determined with success. Both are successive precursors of JNJ-27553292 (−)-**1**, a CCR2 receptor antagonist. The absolute configurations for both (+)-**3** and (−)-**5** were proposed based on a reaction performed on a similar compound, and were found to be in agreement with absolute configurations based on the VCD determination. Starting with the prochiral 3,4-dichlorobenzaldehyde, using the N,N'-((1*S*,2*S*)-cyclohexane-1,2-diyl)bis(trifluoromethanesulfonamide) catalyst it could be determined that (+)-(*R*)-**3** is formed and consequently (−)-(*S*)-**5**. Further, using (−)-(*S*)-**5** to synthesize (−)-**1**, no racemization occurs, which means that based on the reaction mechanism shown in Scheme 7.1, the absolute configuration of the active enantiomer of **1** can be assigned to be (−)-(*S*)-**1**

7.5 Supplementary material index

For this chapter Supplementary Material is provided. It can be downloaded from http://www.quantum.UGent.be/tksup.pdf

Table S7.1 For compound **3**: Experimental Lorentzian fitted and B3LYP/cc-pVTZ vibrational frequencies, dipole strengths and rotational strengths taking into account the fundamentals of the 10 lowest energy minima (a–j).
Table S7.2 For compound **5**: Experimental Lorentzian fitted and B3LYP/cc-pVTZ IR frequencies, dipole strengths and rotational strengths taken into account the fundamentals of the 13 lowest energy minima (a–m).

Figure S7.1 Pictorial representation of the most contributing B3LYP/cc-pVTZ PES minima for (*R*)-**3**.
Figure S7.2 representation of most contributing B3LYP/cc-pVTZ PES minima for (*S*)-**5**

7.6 Reference list

1. Dawson, J.; Miltz, W.; Mir, A. K.; Wiessner, C. *Expert Opin. Ther. Targets* **2003**, *7*, 35-48.

2. Van Lommen, G.; Doyon, J.; Coesemans, E.; Boeckx, S.; Cools, M.; Buntinx, M.; Hermans, B.; VanWauwe, J. *Bioorg. Med. Chem. Lett.* **2005**, *15*, 497-500.

3. Boeckx, G. M.; Van Lommen, G.; Doyon, J.; Coesemans, E. WO 2005118574, 2005.

4. Boeckx, G. M.; Van Lommen, G.; Doyon, J.; Coesemans, E. WO 2005118578, 2005.

5. Van Lommen, G.; Doyon, J.; Van Wauwe, J. P.; Cools, M.; Coesemans, E. WO 2004069809, 2003.

6. Thompson, A. S.; Humphrey, G. R.; Demarco, A. M.; Mathre, D. J.; Grabowski, E. J. J. *J. Org. Chem.* **1993**, *58*, 5886-5888.

7. Yoshioka, M.; Kawakita, T.; Ohno, M. *Tetrahedron Lett.* **1989**, *30*, 1657-1660.

8. Kitamura, M.; Suga, S.; Kawai, K.; Noyori, R. *J. Am. Chem. Soc.* **1986**, *108*, 6071-6072.

9. Stephens, P. J.; Devlin, F. J. *Chirality* **2000**, *12*, 172-179.

10. Stephens, P. J. Vibrational circular dichroism spectroscopy: A new tool for the stereochemical characterization of chiral molecules. In *Computational medicinal chemistry for drugs discovery*, Bultinck, P., De Winter, H., Langenaeker, W., Tollenaere, J. P., Eds.; Marcel Dekker, Inc.: New York, **2004**; pp 699-725.

11. Berova, N.; Nakanishi, K.; Woody, R. W. *Circular Dichroism: Principles and Applications;* 2nd ed.; Wiley-VCH: New York, **2000**.

12. Holzwart, G.; Hsu, E. C.; Mosher, H. S.; Faulkner, T. R.; Moscowit, A. *J. Am. Chem. Soc.* **1974**, *96*, 251-252.

13. Nafie, L. A.; Keiderling, T. A.; Stephens, P. J. *J. Am. Chem. Soc.* **1976**, *98*, 2715-2723.

14. Freedman, T. B.; Cao, X. L.; Dukor, R. K.; Nafie, L. A. *Chirality* **2003**, *15*, 743-758.

15. Cheeseman, J. R.; Frisch, M. J.; Devlin, F. J.; Stephens, P. J. *Chem. Phys. Lett.* **1996**, *252*, 211-220.

16. Devlin, F. J.; Stephens, P. J.; Cheeseman, J. R.; Frisch, M. J. *J. Phys. Chem. A* **1997**, *101*, 9912-9924.

17. Stephens, P. J.; Devlin, F. J.; Chabalowski, C. F.; Frisch, M. J. *J. Phys. Chem.-US* **1994**, *98*, 11623-11627.

18. Ayers, P. W.; Yang, W. Density-functional theory. In *Computational medicinal chemistry for drugs discovery*, Bultinck, P., De Winter, H., Langenaeker, W., Tollenaere, J. P., Eds.; Marcel Dekker, Inc.: New York, **2004**; pp 89-118.

19. Kuppens, T.; Bultinck, P.; Langenaeker, W. *Drug Discovery Today: Techn.* **2004**, *1*, 269-275.

20. Urbanova, M.; Setnicka, V.; Volka, K. *Chirality* **2000**, *12*, 199-203.

21. Nafie, L. A. *Appl. Spectrosc.* **2000**, *54*, 1634-1645.

22. Kuppens, T.; Vandyck, K.; Van der Eycken, J.; Herrebout, W.; van der Veken, B. J.; Bultinck, P. *J. Org. Chem.* **2005**, *70*, 9103-9114.

23. Setnicka, V.; Urbanova, M.; Bour, P.; Kral, V.; Volka, K. *J. Phys. Chem. A* **2001**, *105*, 8931-8938.

24. Frisch, M. J.; Trucks, G. W.; Schlegel, H. B.; Scuseria, G. E.; Robb, M. A.; Cheeseman, J. R.; Montgomery Jr, J. A.; Vreven, T.; Kudin, K. N.; Burant, J. C.; Millam, J. M.; Iyengar, S. S.; Tomasi, J.; Barone, V.; Mennucci, B.; Cossi, M.; Scalmani, G.; Rega, N.; Petersson, G. A.; Nakatsuji, H.; Hada, M.; Ehara, M.; Toyota, K.; Fukuda, R.; Hasegawa, J.; Ishida, M.; Nakajima, T.; Honda, Y.; Kitao, O.; Nakai, H.; Klene, M.; Li, X.; Knox, J. E.; Hratchian, H. P.; Cross, J. B.; Bakken, V.; Adamo, C.; Jaramillo, J.; Gomperts, R.; Stratmann, R. E.; Yazyev, O.; Austin, A. J.; Cammi, R.; Pomelli, C.; Ochterski, J. W.; Ayala, P. Y.; Morokuma, K.; Voth, G. A.; Salvador, P.; Dannenberg, J. J.; Zakrzewski, V. G.; Dapprich, S.; Daniels, A. D.; Strain, M. C.; Farkas, O.; Malick, D. K.; Rabuck, A. D.; Raghavachari, K.; Foresman, J. B.; Ortiz, J. V.; Cui, Q.; Baboul, A. G.; Clifford, S.; Cioslowski, J.; Stefanov, B. B.; Liu, G.; Liashenko, A.; Piskorz, P.; Komaromi, I.; Martin, R. L.; Fox, D. J.; Keith, T.; Al-Laham, M. A.; Peng, C. Y.; Nanayakkara, A.; Challacombe, M.; Gill, P.

M. W.; Johnson, B.; Chen, W.; Wong, M. W.; Gonzalez, C.; Pople, J. A. *Gaussian03*, Revision B5; Gaussian, Inc.: Wallingford CT, **2004**.

25. Becke, A. D. *J. Chem. Phys.* **1993**, *98*, 5648-5652.

26. Lee, C. T.; Yang, W. T.; Parr, R. G. *Phys. Rev. B-Condens. Matter* **1988**, *37*, 785-789.

27. Kuppens, T.; Langenaeker, W.; Tollenaere, J. P.; Bultinck, P. *J. Phys. Chem. A* **2003**, *107*, 542-553.

28. Hehre, W. J.; Radom, L.; Schleyer, P. R.; Pople, J. A. *Ab initio molecular orbital theory;* Wiley: **1986**.

29. Sadowski, J.; Schwab, C. H.; Gasteiger, J. 3D structure generation and conformational searching. In *Computational medicinal chemistry for drugs discovery*, Bultinck, P., De Winter, H., Langenaeker, W., Tollenaere, J. P., Eds.; Marcel Dekker, Inc.: New York, **2004**; pp 151-212.

30. Woon, D. E.; Dunning, T. H. *J. Chem. Phys.* **1993**, *98*, 1358-1371.

31. Kendall, R. A.; Dunning, T. H.; Harrison, R. J. *J. Chem. Phys.* **1992**, *96*, 6796-6806.

32. Ditchfield, R. *Mol. Phys.* **1974**, *27*, 789-807.

33. Stephens, P. J. *J. Phys. Chem.-US* **1987**, *91*, 1712-1715.

34. McQuarrie, D. A. *Statistical Thermodynamics;* Harper and Row: New York, **1973**.

35. Polavarapu, P. L. *Spectroscopy* **1994**, *9*, 48-55.

36. Schellman, J. A. *Chem. Rev.* **1975**, *75*, 323-331.

37. Wong, M. W. *Chem. Phys. Lett.* **1996**, *256*, 391-399.

38. Scott, A. P.; Radom, L. *J. Phys. Chem.-US* **1996**, *100*, 16502-16513.

39. Rauk, A. Vibrational circular dichroism Intensities: Ab initio calculations. In *New developments in molecular chirality*, Mezey, P. G., Ed.; Kluwer academic publishers: **1991**; pp 57-92.

8

self-association behavior of carboxylic acids in solution: a VCD perspective

8.1 Introduction

Carboxylic acids are known for their strong intermolecular associations[1,2] which can appear in solid, liquid and gas-phase state, but also in solutions. Even in diluted solution, self-association can be observed and, depending on solvent, concurrent association between the solvent and the carboxylic acid moiety can be observed.[3]
Aggregation can considerably influence the conformational properties of the compound. In solutions with non-polar solvents, solvent-solute interaction can be possible, as was touched upon discussing $CDCl_3$–OH interaction in Chapter 6. These kind of solvent-solute aggregations are not regarded as a general problem, as the spectra, simulated without considering the aggregation, still show a high degree of agreement with experimental spectra. The differences which sometimes can be seen, often can be explained by taking into account the solvent effects.
Interaction between carboxylic acids groups are a complete different story. It is generally known that carboxylic acids form strong dimeric complexes which have

complete different conformational properties compared to the monomer form. This implicates that the vibrational properties of monomer and dimer are also completely different, which complicates the simulation of their vibrational spectra. If, for example, the absolute configuration of a chiral carboxylic acid needs to be determined and one results to the analysis of the compound without considering the self-associative behavior, these monomeric spectra will probably show no agreement with experiment. Therefore, no conclusions can be drawn from such a study. A solution to this problem is, to explicitly take into account dimer formation.[4] Problems inherent with this approach are the size of the problem, i.e., larger molecular systems, and the need for larger basis sets to correctly describe the hydrogen bonding. In dilute solutions, often an equilibrium between monomer and dimer structures exists which means that the measured spectra can be attributed to both the properties of monomer and dimer structures. It is difficult, however, to asses and determine the equilibrium constant, which complicates the simulation of monomer/dimer spectra considerably.

Another approach is to form the corresponding methyl-ester of the carboxylic acid under study. No major intermolecular association will occur for a methyl-ester, compared to the acid.[5] If no racemization occurs during the methyl-ester forming reaction, the absolute configuration of the methyl-ester will be correlated to the absolute configuration of the parent carboxylic acid.

In this chapter, tetrahydrofuran-2-carboxylic acid is studied and spectra are simulated on the basis of both monomeric and dimeric structures using experimentally determined equilibrium constants. The corresponding methyl-ester is also studied, for which the spectra are simulated using different hybrid density functionals. The absolute configuration determination performed for Johnson & Johnson Pharmaceutical Research and Development on tetrahydrofuran-3-carboxylic acid is also described in this chapter.

8.2 Intermolecular association of tetrahydrofuran-2-carboxylic acid in solution: a vibrational circular dichroism study

8.2.1 Introduction

In this study tetrahydrofuran-2-carboxylic acid **1** is studied using vibrational spectroscopy including both unpolarized infrared (IR) and vibrational circular dichroism (VCD) spectroscopy. (*R*)-tetrahydrofuran-2-carboxylic acid is a chiral building block for faropenem (7-(1-hydroxyethyl)-6-oxo-3-oxolan-2-yl-2-thia-5-azabicyclo[3.2.0]hept-3-ene-4-carboxylicacid),[6,7] a clinically effective nonnatural β-lactam antibiotic.[8]

In combination with density functional theory (DFT) calculations,[9] VCD spectroscopy allows the elucidation of the absolute configuration and the conformational behavior of chiral compounds.[10-12] By doing DFT calculations on a compound with known stereochemistry, one can simulate IR and VCD spectra and consequently compare them with experimental spectra. The IR spectra of enantiomers are identical but the VCD spectra, which are in essence differential IR spectra recorded with left and right circularly polarized infrared light, have intensities with opposite sign. As each vibrational transition band has a corresponding VCD band, each one of these bands can be compared with the simulated spectrum, allowing a very reliable assignment of the stereochemistry of the measured enantiomerically pure sample. At the same time, information about the primary conformations is obtained, as VCD is very sensitive to conformational change. The VCD method was proven very successful in the past[13-19] and further development in spectroscopic techniques and computational algorithms will further increase the reliability of this method.[20,21]

1 is a carboxylic acid, and these types of compounds are known to form intermolecular aggregates.[1,2] In the solid and liquid phase, associations mainly involve cyclic dimers. These are also formed in the gas phase and in solutions. In protic solvents, hydrogen bonding with solvent molecules appears concurrent to dimer formation.[3] As self-association considerably influences the conformational

---

Kuppens, T.; Herrebout, W.; van der Veken, B. J.; Bultinck, P. *J. Phys. Chem. A* **2006**, *100*, 10191-10200.

and vibrational properties of the molecules,[22-24] a suitable model has to be used when computing IR and VCD spectra. In the past, only a few studies were carried out on dimers, in which the focus was on relatively rigid structures.[25,26] A more recent and extensive paper[4] from He et al. describes a VCD study on α-(aryloxy)propanoic acid cyclic dimers; however, the equilibrium between monomer and dimer was not further investigated. Also, recently Urbanová et al.[27] published a VCD study concerning a tetrameric dimethylbiphenyldicarboxylic acid structure. In both studies the calculations are performed with the B3LYP hybrid functional using the 6-31G* basis set.

In this study the computational level is extended, by means of the use of different functionals and larger basis sets. The focus of the present paper is first to establish whether the dimerization has an important effect on the experimental spectra. Second, it is investigated if this effect can be simulated using DFT calculations. Further, a semiquantitative model is defined to obtain estimates of monomer and dimer populations. Combining the semiquantitative populations and DFT results, the experimental IR and VCD will be assessed.

8.2.2 Experimental methods

(*R*)-(+)-**1** (α_D^{20} = +30.0 (*c* = 0.34, $CHCl_3$))[6] and (*S*)-(−)-**1** (α_D^{20} = −12.6 (*c* = 7.70, H_2O)[28] were obtained from Acros with a 97.5% ee and were used without further purification. IR spectra are measured with a Bruker Vector 22 FTIR spectrometer. The VCD is measured with an IFS 66v/S FTIR spectrometer coupled to a PMA37 module, set up as described in Urbanová et al.[29] Long wave pass filters are used to select an operational frequency window to improve the signal-to-noise (S/N) ratio. Because it can induce large artifacts in the CO stretching region for compound **1**, the default 1830 cm^{-1} filter is unusable. Therefore, a 1960 cm^{-1} filter is used instead,[30] which allows measurement in the CO stretch region. As this filter has a rather high long wave cutoff at 1250 cm^{-1}, the 1830 cm^{-1} filter is used for the measurements for (*R*)-(+)-**1** and (*S*)-(−)-**1** below 1200 cm^{-1}, using CS_2 as solvent and KBr cell windows. Above 1200 cm^{-1}, the 1960 cm^{-1} filter is used, in combination with $CDCl_3$ as solvent and CaF_2 cell windows. The collection time for the VCD spectra is 90 minutes (3x30 minutes) each. The demountable cells are equipped with a 105 µm Teflon spacer. (*R*)-(+)-**1** and (*S*)-(−)-**1** are dissolved in $CDCl_3$ at a concentration of 0.42 M, 0.25 M and 0.21 M. **1** has a low solubility in CS_2 and a solution is prepared at an approximate concentration of 0.11 M. Because both enantiomers are available,

half-difference spectra[31] are computed as $(\Delta\varepsilon_- - \Delta\varepsilon_+)/2$, which provides spectra with an improved S/N ratio.
An infrared concentration study with (*R*)-(+)-**1** in $CHCl_3$ was performed using a KBr cell with a 200 µm Teflon spacer.

8.2.3 Computational methods

Geometry optimizations and calculations of the dipole strengths (*D*) and rotational strengths (*R*) are performed using Gaussian03.[32] In this study the B3LYP[33,34] hybrid functional is used, which has proven its reliability in the calculation of VCD intensities,[16,17,35] and the description of strong hydrogen bonded complexes.[36] The potential energy surface for the monomer and dimer are scanned using different methods, which are described in §8.2.4. The located monomer and dimer minima are optimized with the aug-cc-pVTZ basis set. This basis set was previously found capable of describing hydrogen bonded systems.[37] Six additional functionals (B1LYP, B3P86, B3PW91, B98, MPW1PW91, PBE1PBE)[38] are also employed in combination with the 6-31++G** basis set for which the results can be found in *Supplementary Material* (Figures S8.3 and S8.4).
Hessian matrices, atomic polar tensors (APT) and atomic axial tensors (AAT) are calculated using gauge-including/invariant atomic orbitals (GIAOs),[39,40] at the same level as the optimization, allowing the calculation of dipole and rotational strengths. The free energy is calculated under the usual assumptions using standard thermochemical expressions.[41] A scaling factor of 0.980 is used to correct for the harmonic approximation.[42]
The calculations were performed on the Ghent Quantum Cluster at Ghent University and CalcUA located at the University of Antwerp.

8.2.4 Conformational search

The potential energy surfaces of the monomer and dimer of **1** with the *S* configuration were thoroughly analyzed to find the lower energy minima. For the monomer, a conformational analysis was done using MM3[43] and MM4[44] stochastic search methods, for which the implementation is described in more detail in earlier work,[16] and a Monte Carlo search using the MMFF[45] force field. All unique minima were subsequently optimized on the B3LYP/6-31G* level. A systematic

B3LYP/6-31G* DFT search was also performed, which did not yield any new minima. The unique B3LYP/6-31G* minima were further optimized using the aug-cc-pVTZ basis set. For the located minima, the conformational description is given in Table 8.1. To describe the tetrahydrofuran (THF) ring conformations, Cremer-Pople pseudorotational coordinates[46] are used as defined in Equation (8.1) :

$$z_i = \sqrt{\frac{2}{5}} \cdot q \cos\left(\frac{4\pi(i-1)}{5} + \varphi\right) \qquad with \qquad \sum_{i=1}^{5} z_i^2 = q^2 \qquad and \qquad \varphi \in [0, 360] \quad (8.1)$$

The puckering amplitude q describes the degree of ring puckering and the pseudo-rotational phase angle φ describes the mode of ring puckering.[47] The position of the carboxyl substituent relative to the THF ring is given by τ_1. The configuration of the carboxyl group is specified by τ_2 (see Figure 8.1); τ_2 is found to be ~0° and ~180°; that is, the hydroxyl group can be orientated respectively cis or trans relative to the carbonyl group.

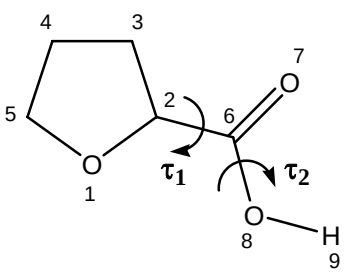

Figure 8.1 Depiction of **1** and definition of dihedral angles τ_1 and τ_2

Table 8.1 B3LYP/aug-cc-pVTZ label, pseudo-rotational coordinates (q in Å and φ in degrees), key dihedral angles (τ_1 and τ_2 in degrees), relative free energies (ΔG^0 in kcal/mol) and Boltzmann populations (% P, 298.15 K) for the unique monomer minima of **1**.

Label	q	φ	τ_1 $O^8C^6C^2O^1$	τ_2 $O^7C^6O^8H^9$	ΔG^0	% P
A	0.36	263	−3	182	0.00	40.59
B	0.36	76	4	180	0.16	31.14
C	0.34	106	154	−1	0.92	8.63
D	0.36	228	156	−1	1.06	6.73
F	0.36	240	−35	−1	1.08	6.61
E	0.34	100	−25	−1	1.10	6.30
G	0.34	105	153	177	6.02	0.00
H	0.36	227	154	176	6.11	0.00

For the dimer of **1**, an MM3 and MM4 stochastic search was performed. This search yielded two relatively stable classes of geometries, which are given schematically in Figure 8.2. The most stable dimer is the classical one in which the two carboxylic acid groups form a strong hydrogen bonded association (Figure 8.2a). Cyclic associations are also observed in which the THF oxygen of one monomer is involved in forming cyclic dimers (Figure 8.2b). Noncyclic dimers with only one OH···O hydrogen bond were located as well but were discarded due to their high energy.[48] Further optimization at the 6-31++G** level showed that the dimers, in which the THF oxygen is involved, have a relative free energy of at least 5.5 kcal/mol compared to the other more stable carboxylic acid bonded cyclic dimers.
Consequently, it can be concluded that, when the dimers are considered, the classic cyclic dimers are most contributing. As the stochastic search did not yield many cyclic dimer geometries, a B3LYP/6-31++G** systematic search was performed in which T_1 and $T_{1'}$ (the position of the carboxyl substituent relative to THF for the dimers as defined in Figure 8.2) were varied in a 30° grid for different values of *q* and φ for both THF rings. Using this approach, a total of 10 unique minima was located. These geometries were further optimized at the aug-cc-pVTZ level for which the conformational description is given in Table 8.2.

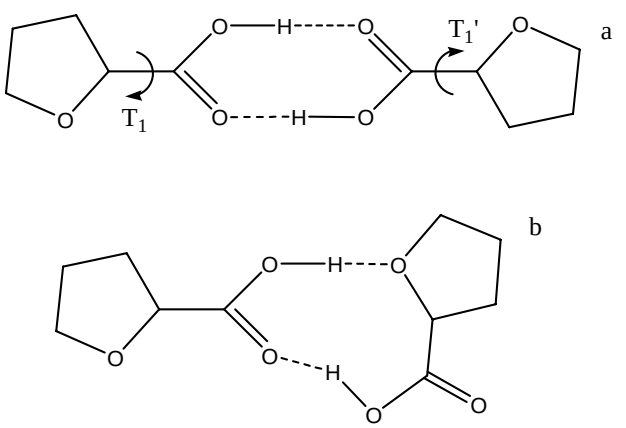

Figure 8.2 Two different possibilities to form cyclic dimers of **1**. Definition of dihedral angles T_1 and T_1'.

Table 8.2 B3LYP/aug-cc-pVTZ label, symmetry, pseudo-rotational coordinates (q in Å and φ in degrees), key dihedral angles (T in degrees), relative enthalpies (ΔH^0 in kcal/mol), relative free energies (ΔG^0 in kcal/mol) and Boltzmann populations (% P, 298.15 K) for the unique dimer minima of **1**.

Label		q_1	φ_1	T_1 $O^8C^6C^2O^1$	q_2	φ_2	$T_{1'}$ $O^{8'}C^{6'}C^{2'}O^{1'}$	ΔH^0	ΔG^0	% P
DC	C_1	0.36	232	156	0.34	102	156	0.06	0.00	24.2
FC	C_1	0.36	237	−35	0.34	108	155	0.12	0.19	17.5
EC	C_1	0.33	100	−29	0.34	105	156	0.27	0.52	10.1
CC	C_2	0.34	103	155	0.34	103	155	0.09	0.57	9.3
FD	C_1	0.36	237	−34	0.36	232	155	0.04	0.58	9.1
FF	C_2	0.36	238	−37	0.36	238	−37	0.37	0.59	8.9
ED	C_1	0.34	96	−31	0.36	232	154	0.23	0.63	8.4
FE	C_1	0.36	240	−36	0.34	105	−26	0.58	0.91	5.2
DD	C_2	0.36	234	154	0.36	234	154	0.00	0.94	5.0
EE	C_2	0.34	101	−27	0.34	102	−27	0.75	1.40	2.3

It can be seen that each of these dimers are in fact combinations of monomer geometries, more precisely, the 4 monomers of **1** that have a cis carboxylic acid group configuration (C, D, E and F) and that are conformationally capable of forming cyclic dimers. However, clearly not all monomer geometries for **1** are able to form dimer structures as can be seen in Figure 8.3, as these are intramolecular hydrogen bonded structures in which the trans carboxylic OH interacts with the THF oxygen. There are also two trans carboxylic monomer structures located in which no intramolecular hydrogen bonding is present (conformation G and H in Table 8.1). Because of their high energies these minima are not significant.

If the relative enthalpy is compared to the relative free energy of the dimer structures, a different order can be observed. This is due to the various entropy contributions of each dimer minimum, e.g., dimers structures with C_2 symmetry have a lower rotational entropy contribution compared to C_1 structures.

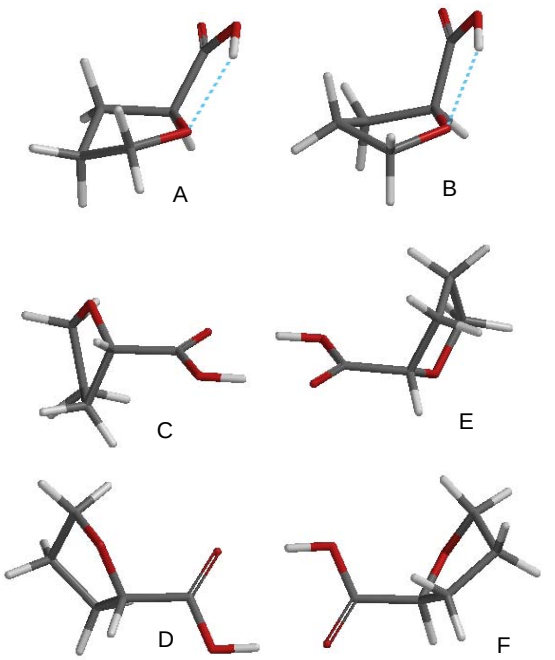

Figure 8.3 Model representations of the monomer conformations A–F and at the same time exemplary models of cyclic dimers EC and FD.

8.2.5 Results and discussion

In Figure 8.4a, the CO stretch region of the IR spectrum is presented for (*R*)-(+)-**1** solutions in $CHCl_3$, with typical concentrations varying between 0.01 and 0.40 M. Two intense bands can be observed in this region, with a rather large frequency separation, which, in the case of carboxylic acids, is often an indication for coexistence of dimer and monomer in solution.[49] This is confirmed in the OH stretch region, given in Figure 8.4b, in which two monomer bands can be observed near 3390 and 3500 cm^{-1} and a broad dimer band near 3000 cm^{-1}. In both the CO and OH stretch region the bands can be identified on the basis of DFT results. In Figure 8.4 the monomer and dimer calculated spectra are concurrently given (Tables S8.4 and S8.5 in *Supplementary Material* describe the fundamentals for monomer and dimer conformations). From these data it can be seen that band P^1 can be assigned to the monomer with conformations A and B and P^2 to the cis-configured monomer (C, D, E and F). For conformations A and B, the carbonyl stretch frequency is somewhat higher and the hydroxyl stretch frequency is somewhat lower compared to the non-

hydrogen bonded monomers C, D, E and F. Also, the intensity of the hydrogen bonded monomer bands is higher compared to the cis configured monomers. These findings agree with the B3LYP intensities and populations. Further, band P^3 can be ascribed to the dimer conformations in the same manner. The typical concentration dependence of the three bands also confirms the assignment of monomer and dimer bands.

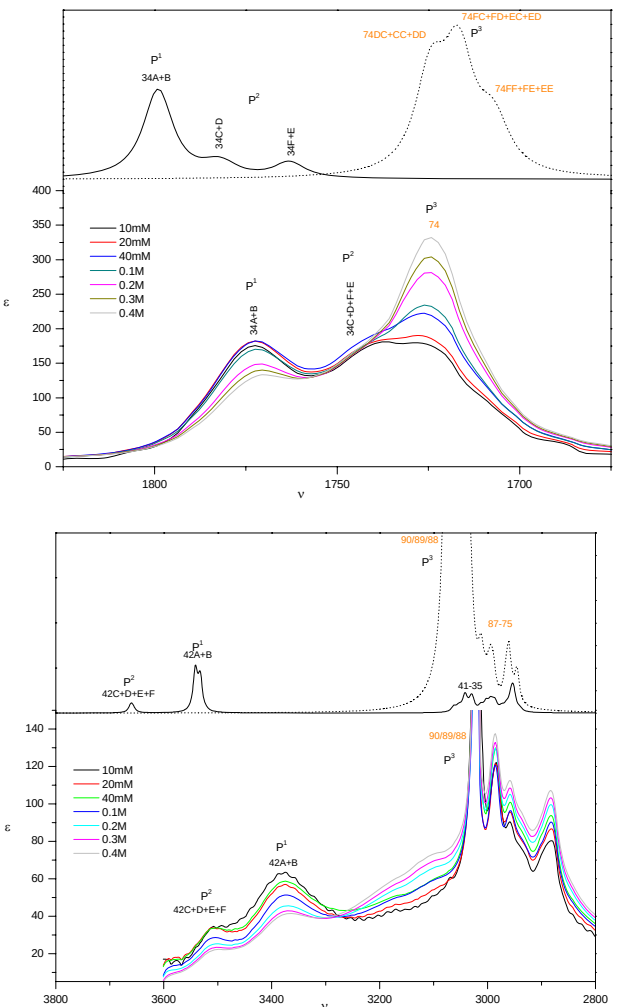

Figure 8.4 IR spectra of (*R*)-(+)-**1** in $CHCl_3$ for different concentrations varying between 0.4 M and 10 mM) in the CO stretch (top) and OH stretch (bottom) region concurrent with the B3LYP/aug-cc-pVTZ simulated spectra for monomer (solid line) and dimer (dotted line) and assignments. Intensities in molar absorptivity units, frequencies in cm^{-1}.

Solutions in CS_2 are also studied to extend the VCD frequency range. For (*R*)-(+)-**1** in CS_2 three carbonyl stretch bands can be observed (Figure S8.1 in *Supplementary Material*), similar to the $CHCl_3$ spectra: P^1 centered at 1784 cm^{-1}, P^2 centered at 1756 cm^{-1} and P^3 at 1722 cm^{-1}. It is interesting to observe that these values, compared to the CO stretch frequencies in $CHCl_3$, are shifted to lower wavenumbers by ~11 cm^{-1}. Furthermore, the intensity ratios P^3/P^1 and P^3/P^2 are higher compared to the corresponding ratios in the $CHCl_3$ spectra. As the solubility of **1** in CS_2 is low, it was difficult to get solutions with accurate concentrations.

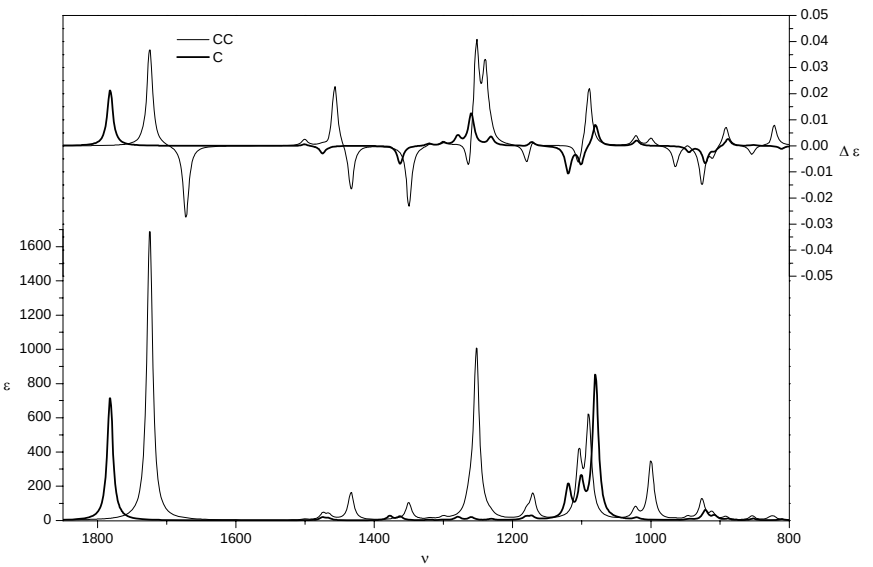

Figure 8.5 Single conformational spectra for monomer conformation C (thick solid line) and dimer conformation CC (solid line). Intensities and differential intensities in molar absorptivity units, frequencies in cm^{-1}.

As it is clear now that both monomers and dimers are present in solution, these have to be taken into account when simulating the spectra for **1** in solution. IR and VCD spectra can be simulated by averaging the single conformation spectra using Boltzmann statistics. These single conformation spectra are obtained by Lorentzian broadening (fwhm = 10 cm^{-1}) of the calculated discrete line spectra based on dipole and rotational strengths and harmonic vibrational frequencies and are transformed to molar absorptivity units.[50] The conformational populations are calculated on the basis of free energies at room temperature (298.15 K) and can be found in Tables 8.1 and 8.2, for the monomer and dimer, respectively. In Figure 8.5, the calculated single conformation spectra are shown for the C monomer and the CC dimer. It can

be seen that there is a significant influence on the IR and VCD spectra due to the dimerization: not only are the dimer intensities systematically higher for both IR and VCD, but also bands of corresponding fundamentals are shifted in frequency.

In Figure 8.6 the simulated B3LYP/aug-cc-pVTZ monomer (*S*)-**1** and dimer (*SS*)-**1** IR and VCD spectra are compared with experimental IR and half-difference VCD spectra for a 0.42 M solution of (*S*)-(−)-**1** in $CDCl_3$. Both the monomer and dimer spectra have some level of similarity compared to the experiment. By taking both monomer and dimer into account, one can explain the major experimental features.

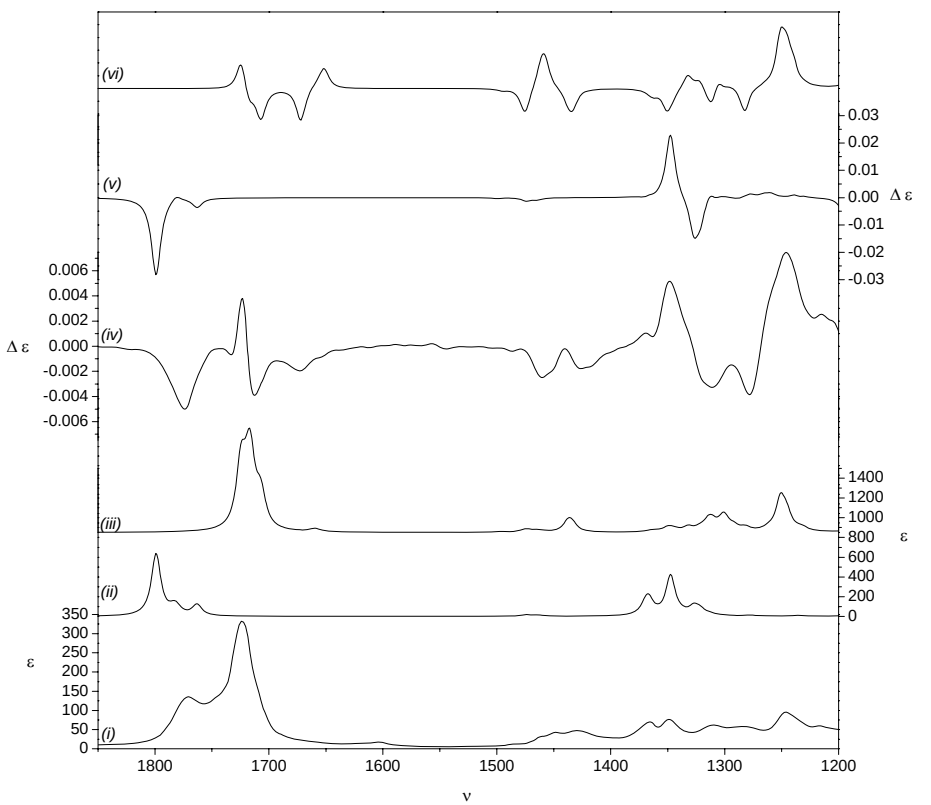

Figure 8.6 Experimental IR (i) and half-difference VCD (iv) spectrum for 0.42 M (*S*)-(−)-**1** in $CDCl_3$. Simulated IR/VCD B3LYP/aug-cc-pVTZ monomer (ii)/(v) and dimer (iii)/(vi) spectra are given. Intensities and differential intensities in molar absorptivity units, frequencies in cm^{-1}

To interpret the experimental IR and VCD spectra in terms of the DFT results, however, the conformational populations need to be assessed for both monomer and dimer. The theoretical populations based on the free energy differences between monomer and dimer structures are often largely overestimated.[25,51] Nonetheless, information on the fractions of monomer and dimer is embedded in the concentration dependence of the IR band intensities. Using a procedure similar to that described in Chen et al.,[52] it was possible to extract this information by determining the equilibrium constant between monomer and cyclic dimer. The equilibrium for dimerization

$$M + M \rightleftharpoons D$$

is characterized by the dimerization constant $K = [D]/[M]^2$. This constant *K* can be determined by analyzing the integrated absorbance in function of the analytical concentration of the dissolved species.[52] In this approach, the experimental data are fitted to

$$\frac{c^0}{A_m^2} = \frac{1}{\varepsilon_m l}\frac{1}{A_m} + \frac{2K}{(\varepsilon_m l)^2} \tag{8.2}$$

in which c^0/A_m^2 is plotted versus A_m^{-1}. c^0 refers to the analytical concentration of the dissolved species **1**, A_m and ε_m are respectively the integrated absorbance and molar absorptivity of a distinct monomer band and *l* is the path length (0.02 cm).

The model used in this study to approximate the monomer/dimer fractions is based on two individual equilibria between monomer and dimer, that is, an equilibrium between hydrogen bonded monomer (A/B) and the dimer and an equilibrium between the cis configured monomer (C, D, E and F) and dimer.

Several approximations are used: First, the formation of trimers and tetramers and other solute-solute associations are not considered. Further, possible solvent-solute aggregation is not taken explicitly into account and the concentrations of the $CHCl_3$/$CDCl_3$ are not exact due to the volatile nature of this solvent. It has also come to our attention that the $CHCl_3$ used in this study contains 0.5 to 1% EtOH for

stabilization.[‡] The mole fraction EtOH is too low, however, to have any influence on the dimerization equilibrium. Taking into account the aforementioned approximations and limitations of the model, the error on the determined populations is expected to be on the order of 10–15%. However, exact populations are not pursued in this study, but merely tentative values are intended that allow the assessment of experimental IR and VCD in terms of DFT results.

The preferred region to extract population dependent data from the concentration series is the carbonyl stretch region, in which both the monomer and dimer bands are separated and do not coincide with other modes. The OH stretch region is less appropriate as there are many intense solvent bands present and also the CH stretch modes overlap with the dimer OH stretch modes. In Figure 8.7, the infrared absorbance spectra are given for the concentration series experiment in $CHCl_3$ (same as Figure 8.4a but in absorbance units). As the solubility of **1** in CS_2 is low, it was difficult to get solutions with accurate concentrations and consequently, the dimerization equilibrium constants for (*R*)-(+)-**1** in CS_2 could not be determined accurately. The integrated intensities for the monomer bands P^1 and P^2 and the dimer band P^3, obtained by Lorentzian fitting, are given in Table 8.3 for the $CHCl_3$ experiment. If c^0/A_m^2 is plotted versus A_m^{-1} (Figure 8.7), for the two equilibria defined in our model, the dimerization constants can be determined with Equation (8.2) on the basis of the intercept and the slope of the linear fit. K_1, being the equilibrium constant for the formation of cyclic dimer from monomer A and B, was determined to be 2.7 (ΔG_1^0 = −0.6 kcal/mol). In the same way, for the equilibrium between the monomers with a cis configured carboxyl (C, D, E and F) and the dimer, K_2 was determined to be 6.9 (ΔG_2^0 = −1.2 kcal/mol). The predicted free energy difference between conformations A/B and C/D/E/F based on our proposed model is 0.6 kcal/mol. This value agrees reasonably well with the B3LYP/aug-cc-pVTZ free energy difference between conformations B and C, i.e., 0.76 kcal/mol (Table 8.1).

[‡] Zhao et al.[53] describe that the polypeptide gramicidin undergoes dimerization in solution. Gramicidin is reported to have a different VCD in $CDCl_3$ compared to $CHCl_3$ solutions (which contains 1% EtOH) in the amide I region. Their IR signatures are the same in this region.

Table 8.3 Integrated absorbances of CO stretching bands from the monomer, A_{m_1} and A_{m_2}, and those of dimer, A_d, for different initial concentrations (c^0, in M) of (*R*)-(+)-**1** in $CHCl_3$.

c^0	A_{m_1}	A_{m_2}	A_d
0.40	33	26	96
0.30	27	19	69
0.20	20	13	44
0.10	10	6	15
0.04	6	4	9
0.02	3	2	4
0.01	2	1	2

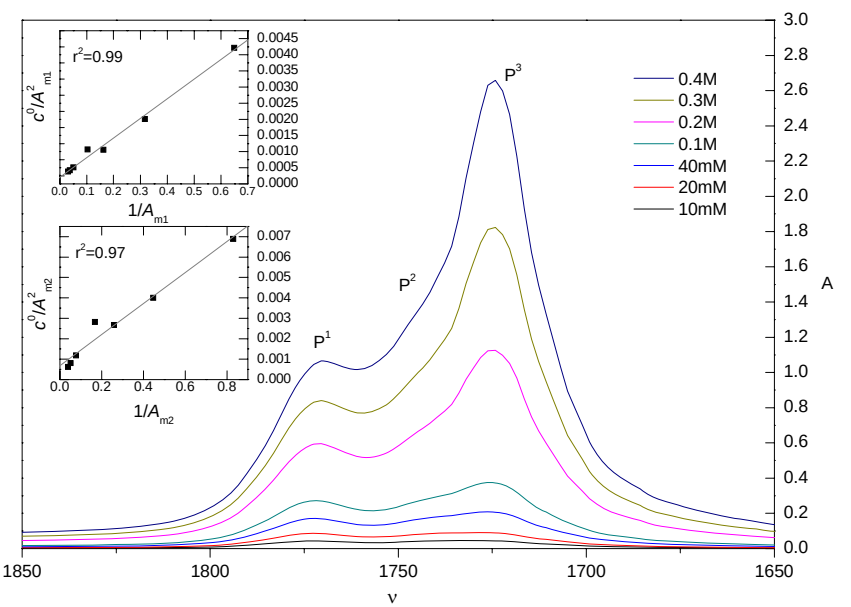

Figure 8.7 IR spectra of (*R*)-(+)-**1** in $CHCl_3$ for different concentrations varying between 0.4 M and 10 mM). The two subplots represent the linear plot based on Equation (8.2) for band P^1 (top) and band P^2 (bottom) – Correlation coefficients r^2 are given. Intensities are in absorbance units, frequencies in cm^{-1}.

Defining f_d as the fraction of dimer, f_{m_1} as the fraction of monomer A/B and f_{m_2} as the fraction monomer C/D/E/F; on can write the following expressions for the different fractions within our proposed model:

$$
\begin{aligned}
f_d + f_{m_1} + f_{m_2} &= 1 \\
f_{m_1}^2 &= f_d \frac{1}{2K_1 c^0} \\
f_{m_2}^2 &= f_d \frac{1}{2K_2 c^0}
\end{aligned}
\tag{8.3}
$$

It is clear that the fractions in (8.3) depend on the analytical concentration for **1**. For a given concentration, the fractions of monomer and dimer can be determined using the obtained equilibrium constants. In Figure 8.8, the fractions of monomers A/B, C/D/E/F and dimer are given as a function of the analytical concentration c^0. It can be seen that for very small concentrations, only monomer species are present; with the relative concentrations being 62% for A and B and 38% for C, D, E and F. These values compare reasonably well with the B3LYP/aug-cc-pVTZ gas-phase values of 72% and 28% summarized in Table 8.1.

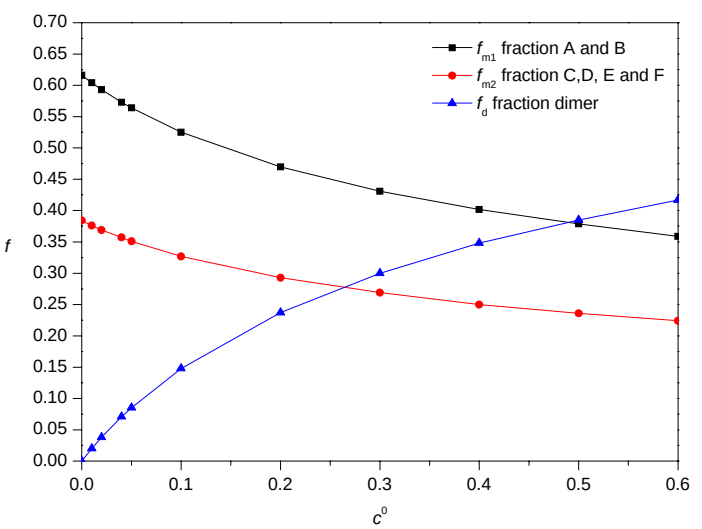

Figure 8.8 Fractions of monomers A/B (f_{m_1}), C/D/E/F (f_{m_2}) and dimers (f_d) based on experimentally determined values of dimerization equilibrium constants.

At a concentration c^0 of 0.42 M in $CDCl_3$, which is required to obtain a good VCD S/N ratio, dimer and monomer coexist in solution, from which the fractions present are determined (see Figure 8.8 and Equation (8.3)) to be f_{m_1} = 0.40, f_{m_2} = 0.25 and f_d = 0.35. Based on these values, the populations for the different conformations were determined, taking into account the Boltzmann populations based on the

relative free energies of each subgroup of structures, that is monomer A/B (f_{m_1}), monomer C/D/E/F (f_{m_2}) and dimer (f_d). In Table 8.4 the experimentally based populations are given for B3LYP/aug-cc-pVTZ data. It has to be mentioned that the experimentally determined equilibrium fractions could be somewhat biased by solvent-solute interaction, which was not taken explicitly into account when modeling the conformations.

Table 8.4 Experiment based populations (B3LYP/aug-cc-pVTZ) for monomer and dimer of **1** in $CDCl_3$.*

	% P		% P		% P		% P
A	23	FC	6	EC	4	ED	3
B	17	D	6	CC	3	FE	2
DC	8	F	6	FD	3	DD	2
C	8	E	6	FF	3	EE	1

* f_{m_1} = 0.40, f_{m_2} = 0.25 and f_d = 0.35

The simulated B3LYP/aug-cc-pVTZ and experimental IR and VCD spectra (experimental VCD spectra are half difference spectra) for three different concentrations (0.21, 0.25, and 0.42 M) are shown in Figure 8.9. The simulated spectra are averaged over all significant dimer and monomer conformations. The populations are calculated by determining the fractions of monomers and dimers for the three different concentrations using Equation (8.3) and taking into account the B3LYP/aug-cc-pVTZ Boltzmann populations. Here, the earlier discussed concentration dependence in the CO stretch region is visible, but a small effect is also seen in the 1300–1400 cm^{-1} area. For the VCD, a more pronounced concentration effect is observed. For higher concentrations more intense CO stretch dimer bands (fundamental 74 and 73) are observed, but the monomer VCD intensities for fundamentals 29A+B and 27/28 are reduced as are the monomer IR intensities of fundamental 34A+B and 30/29A+B. This obviously indicates that the dimer fraction increases at higher concentrations. The same effects can be observed in the simulated spectra (Figure 8.9 (ii) and (iv)), which indicates that our proposed model works.

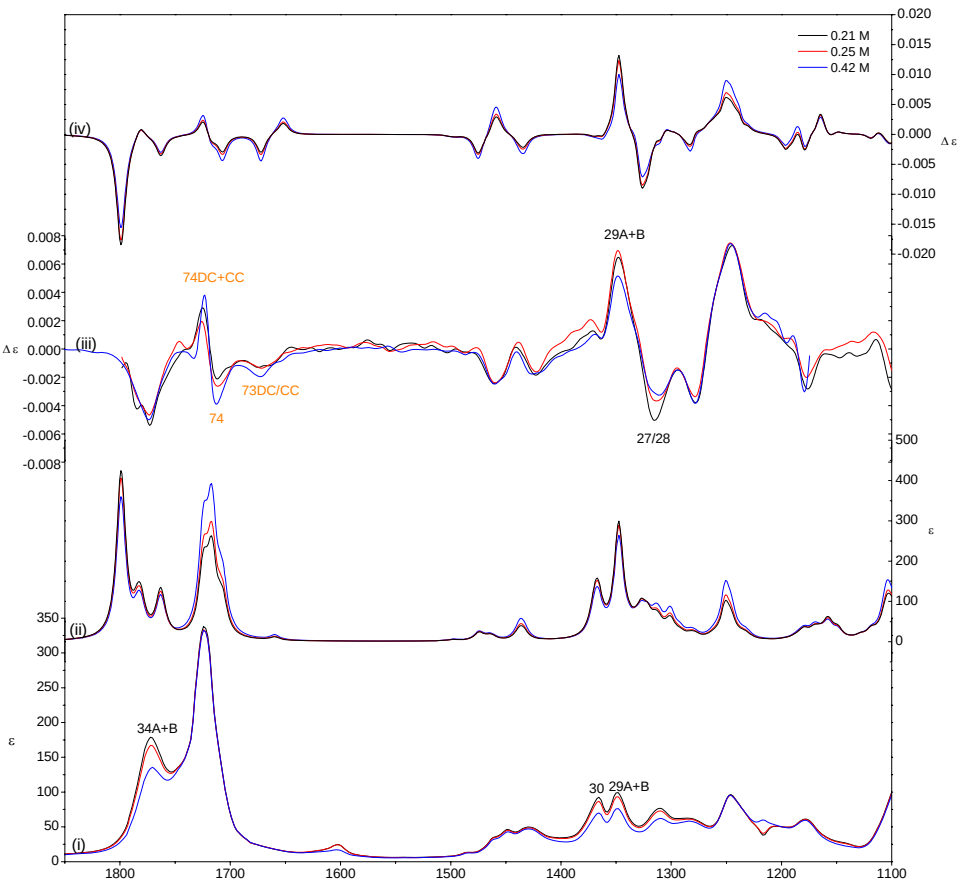

Figure 8.9 Experimental spectra for (*S*)-(−)-**1** in $CDCl_3$ for three concentrations (0.21, 0.25, and 0.42 M) and B3LYP/aug-cc-pVTZ simulated IR/VCD spectra taking into account monomer and dimer of (*S*)-**1** based on experimental populations for different concentrations (0.21 M, 0.25 M and 0.42 M). Intensities and differential intensities in (differential) molar absorptivity units, frequencies in cm^{-1}.

In Figure 8.10 (i) and (iii) the experimental IR and half difference VCD spectra for (*S*)-(−)-**1** are given. The infrared region beneath 1000 cm^{-1} has a bad S/N ratio due to the high absorption of $CDCl_3$ in that region. The long-wave cutoff from the optical filter and the CaF_2 windows make that there is no reliable VCD signal observable below 1200 cm^{-1}. Using a different setup with KBr windows and CS_2 as solvent, the spectroscopic window is extended to 800 cm^{-1}. Using CS_2 as solvent, the fractions of monomer appear to be lower than those in $CHCl_3$, but this effect is rather small on the IR and VCD spectrum, as can be seen in Figure S8.2 in

Supplementary Material. Accordingly, the '$CDCl_3$' weighted spectra can be used without any problems for comparison with the experimental CS_2 spectra.

In Figure 8.10 (ii) and (iv) the simulated B3LYP/aug-cc-pVTZ spectra are shown, which are averaged over all the significant (*S*)-**1** monomer and (*SS*)-**1** dimer conformations using the experimental populations given in Table 8.4 (0.42 M). These simulated spectra can be compared to the experimental (*S*)-(−)-**1** spectra. The B3LYP/aug-cc-pVTZ bands are labeled with their corresponding normal modes. Naturally, monomer and dimer bands overlap, which makes it difficult to assign the bands in much detail. However, where possible, in Figure 8.10 for monomer and dimer, the bands are assigned to the most contributing conformations (indicated by the conformational label). If the normal modes of different conformations have only a small frequency separation, the conformations are not explicitly mentioned in the labeling. The normal modes of the monomers for the 800–1850 cm^{-1} frequency interval run from 12 to 34, for the dimeric structures from 27 to 73. The monomeric labels are given in black, the dimeric in orange.

In the carbonyl stretching region, a complex pattern can be observed in the IR and in the VCD (Figure 8.10). The most intense band in the IR can be attributed to the CO asymmetric stretch in the dimer (fundamental 74).
The dimeric CO stretch modes (fundamentals 73 and 74) have lower vibrational frequencies than their monomeric counterpart (fundamental 34). This is due to the hydrogen bonding, which results in a cooperative lengthening of the C=O and OH bonds and a shortening of the C−O bond.[3] Notwithstanding the fact that the calculated frequency splitting between the monomeric and dimeric CO stretch frequencies is somewhat overestimated, the IR/VCD for the CO stretching region shows a good agreement with the simulated spectra. Monomeric and dimeric bands can be observed and assigned to calculated bands. Bands 34 from conformations C, D, E and F (34C+D, 34F+E) are unresolved in the IR but can be recognized in the VCD. For the asymmetric CO stretch (mode 73), a negative VCD band is observed, mainly attributable to conformation DC and CC. The other dimer conformations are predicted to have a positive VCD for mode 73, but this cannot be observed in the experimental VCD.

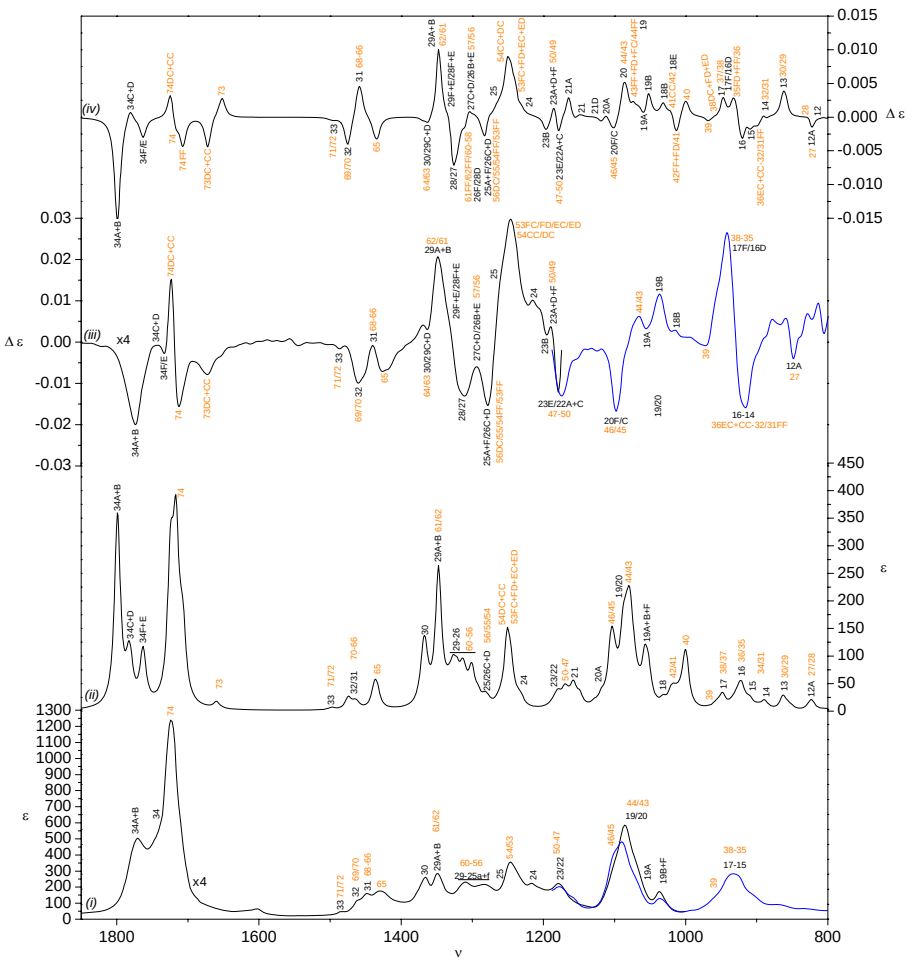

Figure 8.10 IR (i) and half-difference VCD (iii) spectrum for 0.42 M (*S*)-(−)-**1** in $CDCl_3$ (intensities are multiplied with factor four). For the <1200 cm^{-1} region the CS_2 spectrum is given (~0.11 M). B3LYP/aug-cc-pVTZ simulated IR (ii) and VCD (iv) spectra taking into account monomer and dimer of (*S*)-**1** based on experimental populations. Intensities and differential intensities are in molar absorptivity units, frequencies in cm^{-1}.

In the spectral region between 1500 and 850 cm^{-1}, a complex spectrum is observed with several unresolved and broad bands. The VCD spectrum in this region has some distinct features, which allows, in combination with the IR spectrum, the assignment of experimental bands. Monomeric fundamentals 29 to 25 coinciding with dimeric fundamentals 60 to 56 are not resolved in the IR, which is in agreement with predictions. Some IR bands can be exclusively assigned to dimer structure vibrations, i.e., bands 74, 73, 65, 54DC+CC, 53FC+FD+EC+ED, 46/45, 42/41, 40,

and for the VCD, bands 74DC+CC, 74, 74F, 73DC+CC, 73, 65, 54CC+DC, 53FC+FD+EC+ED, 42FF+FD/41, 40, 39. Exclusive monomeric bands in the IR are 34A+B, 34, 30, 19B+F and for the VCD 34A+B, 34C+D, 34 F+E, 27/28, 24, 19A, 19B. The other bands must be assigned to coinciding dimer and monomer fundamentals.

If small differences are neglected, it can be concluded that almost all experimental IR and VCD bands can be assigned with success to the harmonic fundamentals. Some larger bands cannot be observed in the experimental spectra, i.e., VCD band 73 (discussed earlier), VCD band 21A (COH bend), bands 42/41/40 (mainly COH out of plane bend) and VCD band 13/30/29 (CH_2 rocking). As these differences are found for both the 6-31++G** and the aug-cc-pVTZ basis set, it is highly unlikely that this is the effect of the use of an incomplete basis set. To investigate the effect of the density functional, six additional functionals (B1LYP, B3P86, B3PW91, B98, MPW1PW91, PBE1PBE) were used to simulate IR and VCD spectra for **1** using the 6-31++G** basis set. These resulting spectra are given in Figures S8.3 and S8.4 (*Supplementary Material*). The overall agreement between simulated and experimental spectra is best for the B1LYP and B3LYP functionals. It can also be seen that all the functionals fail to correctly predict the rotational strength of fundamental 73 (selected conformations, see above), fundamental 21 for conformation A, and combined fundamentals 13, 30 and 29. For the B3PW91 and B3P86 functionals, the vibrational frequencies for fundamentals 42, 41 and 40 are shifted somewhat to higher wavenumbers and show a better resemblance with the experimental spectrum for this part of the spectrum compared to the B3LYP functional. However, fundamentals 40, 41 and 42 correspond to COH out of plane bending modes. In a recent study,[54] Antony et al. found that the harmonic COH out-of-plane bending frequency for dimeric benzoic acid is gravely overestimated by ~50 cm^{-1} due to the anharmonic character of this vibrational mode. If this argument is pursued, it would mean that the predicted frequencies for fundamental 40–42 are overestimated and these would be shifted to lower wavenumbers in the experimental spectra. If these corresponding bands are lowered by 50 cm^{-1}, these would coincide with intense profiles in both IR and VCD bands. This would also explain the relative intensity of the IR band 17–15/38–35.

Taking into account the approximations that are used to determine the monomer and dimer populations to simulate their IR and VCD spectra, it would be of no use to perform a quantitative comparison of simulated and experimental spectra which is sometimes performed,[13,50] for smaller molecules. In this study the situation is even

more difficult because not only bands of different conformations, belonging to one species coincide, but also bands from dimer conformations can overlap with bands of the monomer conformations. As a result, no quantitative comparison is performed. However, the assignment of the bands to fundamentals by comparison of the experimental and theoretical spectra was still possible and the resulting agreement in both spectra and trends establishes that for this specific molecule, both monomeric and dimeric species are present and that these can be modeled to simulate spectra.

8.2.6 Conclusion

It this study it is shown that for a carboxylic acid **1** in CS_2 and $CDCl_3$, considerable fractions of monomer exist next to cyclic dimers, due to the stabilizing effect of an intramolecular hydrogen bonding for two monomer conformations. The equilibrium between the monomer and the cyclic dimer was evaluated using a concentration variation study in $CHCl_3$. The proposed model that describes the equilibrium between intramolecular stabilized monomer and cyclic dimer and nonintramolecular bonded dimer and cyclic dimer predicts monomer equilibrium concentrations that are 60% higher for the stabilized monomer form. The amount of cyclic dimer was found to be dependent on the initial amount of **1** present in $CHCl_3$. Taking into account the equilibrium between monomer and dimer, IR and VCD spectra were simulated for (*S*)-**1** on the basis of the approximate experimentally determined fractions and B3LYP/aug-cc-pVTZ Boltzmann populations of dimeric and monomeric conformations. Spectra were simulated at the B3LYP/aug-cc-pVTZ level and were compared with experimental spectra for (*S*)-(−)-**1** in $CDCl_3$ and CS_2. A good agreement was obtained which suggests that the proposed model of dimer/monomer equilibrium is valid within the scope of our article.

8.2.7 Supplementary material index

For this paragraph Supplementary Material is provided. It can be downloaded from http://www.quantum.UGent.be/tksup.pdf

Table S8.1 B3LYP/6-31++G** conformational description monomer **1**
Table S8.2 B3LYP/ cc-pVTZ conformational description monomer **1**
Table S8.3 B3LYP/ 6-31++G** conformational description dimer **1**

8.3 Elucidation of the absolute configuration of tetrahydrofuran-3-carboxylic acid

8.3.1 Introduction

In the previous paragraph the intermolecular association of tetrahydrofuran-2-carboxylic acid was described using unpolarized IR and VCD methods. All plausible monomer and cyclic dimer conformations of the carboxylic acid were accounted for in the simulation of theoretical IR and VCD spectra. In this paragraph, the absolute configuration of tetrahydrofuran-3-carboxylic acid, a position isomer of the previous compound, is elucidated taking into account the formation of cyclic dimers. Using DFT, the monomers and cyclic dimers were modeled and the corresponding IR and VCD spectra could be simulated. These theoretical spectra, in turn, could be compared to experimental data, which were provided by Johnson & Johnson Pharmaceutical Research and Development (JNJPRD). This analysis is part of an agreement between Ghent University and JNJPRD in which AC determinations are performed on drugs discovery compounds (for more information see the Appendix). VCD has partially replaced XRD AC determinations at JNJPRD, as VCD has obvious advantages compared to other methods

8.3.2 Experimental

The enantiopure samples, i.e., (+)-**2** (α_D^{24} = +21.44 (EtOH)) and (−)-**2** (α_D^{20} = −21.91 (EtOH)) were obtained by separation of the racemic mixture (Aldrich) using chiral column chromatography.[55] The experimental IR and VCD spectra for both enantiomers were provided by JNPRD. VCD and IR data within the 1000–1500 cm^{-1} frequency interval were available. Details concerning experimental conditions are not known, but the sample concentrations provide a reliable VCD as the majority of IR bands reside within 0.2–0.8 absorbance unit interval. Solutions were prepared with CD_2Cl_2. Further, the half-difference VCD spectrum is reported, calculated as $(\Delta A_+ - \Delta A_-)/2$.

Additional, unpolarized IR data were provided for the CO and OH stretch region.

8.3.3 Computational methods

The conformational search strategy and computational methods are the same as those used in §8.2. The B3LYP functional was used in combination with the 6-31G* and 6-31++G** basis set for respectively the (*R*)-**2** monomer and (*RR*)-**2** dimer. Previously (§8.2) it was shown that the B3LYP/6-31++G** level is sufficient to describe carboxylic acid dimer geometries in the context of IR and VCD comparison. A scaling factor of 0.967 is used to correct for the harmonic approximation.[16]

8.3.4 Results and discussion

8.3.4.1 Conformational description

In Table 8.5, the conformational description is given for the (*R*)-**2** monomer. The same descriptors are used as for **1** in §8.2, i.e., puckering coordinates for the five membered rings and the dihedral angles as defined in Figure 8.11. Based on the configuration of the carboxylic acid moiety (τ_2), the conformations can be categorized in two classes, that is, the hydroxyl group can be *cis* or *trans* relative to the carbonyl group. It can be observed, in Table 8.5, that the *trans* conformers have a higher energy compared to the *cis* isomers. For one *trans* conformations, i.e., conformer F, hydrogen bonding with the THF oxygen is observed, which has a stabilizing effect. Compared to **1**, this stabilizing effect is relatively small and the *cis* conformations are found to be more stable. In Figure 8.12 the 4 *cis* minima (A, B, C and D) and also the intramolecular hydrogen bonded minimum F are depicted.

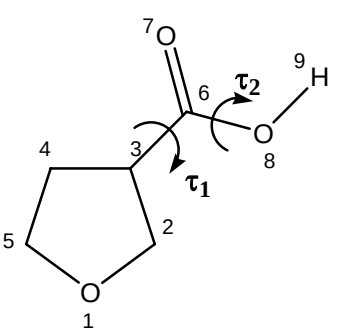

Figure 8.11 Depiction of **2** and definition of dihedral angles τ_1 and τ_2

For the (*R*,*R*)-tetrahydrofuran-3-carboxylic acid dimer a total of 15 conformations were found which are described in Table 8.6.

If Table 8.5 and Table 8.6 are closely compared, it can be seen that the monomer geometries are building blocks that can be used for the construction of cyclic dimer structures, with only one exception, that is conformation B'C. This is the global minimum dimer structure which is constructed from the C and B' monomer. The geometry of the monomeric B' differs from B in the dihedral angle τ_1. Clearly, the dimeric dihedral angles T_1 and T_1' (and also the THF ring geometries) for all dimer structures deviate slightly from their corresponding monomeric dihedral angles τ_1, but in case of dimer B'C the difference is rather large ($\Delta\tau_1 = 27°$). The monomeric B' geometry, however, is not found as an optimum. In Figure 8.12, a model representation for the B'C dimer is given.

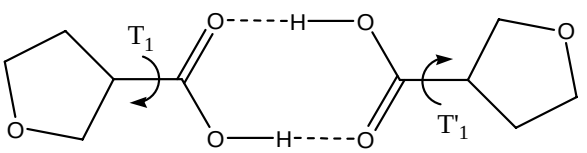

Figure 8.13 Depiction of cyclic dimer **2** and definition of dihedral angles T_1 and T'_1

Table 8.5 B3LYP/6-31G* label, pseudo-rotational coordinates (*q* in Å and φ in degrees), key dihedral angles (τ_1 and τ_2 in degrees), relative free energies (ΔG^0 in kcal/mol) and Boltzmann populations (% P, 298.15 K) for the unique monomer minima of **2**.

	q	φ	τ_1	τ_2	ΔG^0	% P
A	0.38	50	158	−1	0.00	47.7
B	0.38	174	76	0	0.31	28.5
C	0.37	8	71	1	0.65	16.1
D	0.39	156	−61	0	1.50	3.8
E	0.38	38	−59	0	1.51	3.8
F	0.42	329	−42	−178	3.49	0.1
G	0.39	151	107	−179	5.49	0.0
H	0.38	193	171	180	6.66	0.0
I	0.37	305	69	−179	6.83	0.0
J	0.38	137	−57	−179	6.90	0.0
K	0.37	11	72	−178	6.91	0.0
L	0.38	27	−175	−179	6.94	0.0
M	0.37	189	−64	−179	8.24	0.0

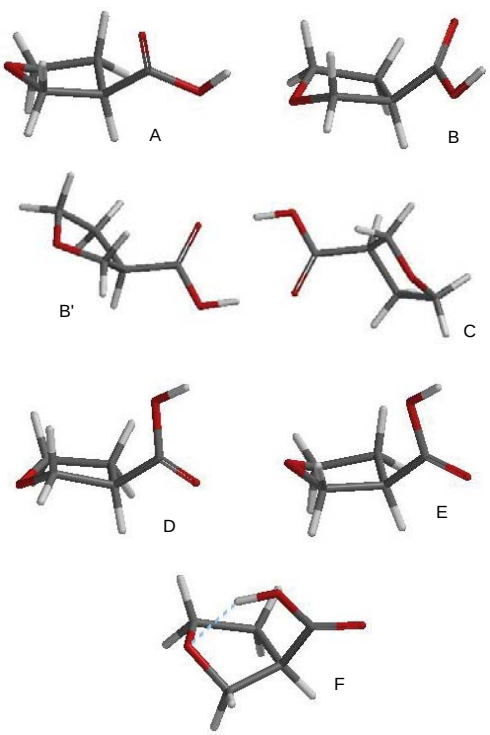

Figure 8.12 Model representations of the monomer conformations A−F and at the same time exemplary models of cyclic dimers B'C and DE.

Table 8.6 B3LYP/6-31++G** label, symmetry, pseudo-rotational coordinates (q in Å and φ in degrees), key dihedral angles (T in degrees), relative enthalpies (ΔH^0 in kcal/mol), relative free energies (ΔG^0 in kcal/mol) and Boltzmann populations (% P, 298.15 K) for the unique dimer minima of **2**.

Label		q_1	φ_1	T_1	q_2	φ_2	T_2	ΔH^0	ΔG^0	% P
B'C	C_1	0.38	167	103	0.37	18	76	0.39	0.00	74.5
DB	C_1	0.38	180	−70	0.38	179	82	0.54	1.49	6.1
EB	C_1	0.38	45	−60	0.37	176	78	0.87	1.64	4.6
BB	C_2	0.38	179	79	0.37	179	80	0.00	1.83	3.4
DA	C_1	0.38	178	−67	0.38	49	149	1.03	2.15	2.0
AC	C_1	0.38	42	156	0.37	14	75	0.72	2.19	1.8
BA	C_1	0.37	180	78	0.38	41	157	0.47	2.20	1.8
CD	C_1	0.37	17	77	0.38	176	−69	0.80	2.43	1.2
EA	C_1	0.38	46	−62	0.38	47	152	1.38	2.44	1.2
ED	C_1	0.38	43	−54	0.38	177	−66	1.39	2.65	0.9
EC	C_1	0.38	46	−65	0.37	11	71	1.10	2.70	0.8
AA	C_2	0.38	39	162	0.38	39	162	0.95	2.89	0.6
DD	C_2	0.38	178	−66	0.38	183	−67	1.09	2.95	0.5
CC	C_2	0.37	17	76	0.37	17	76	0.51	3.01	0.5
EE	C_2	0.38	43	−59	0.38	43	−63	1.73	3.59	0.2

8.3.4.2 IR and VCD spectra

In Figure 8.14 (i) and (iv) the experimental IR and VCD for (+)-**2** are given. The VCD spectrum is actually the half difference spectrum. The simulated spectra for (*R*)-**2** can also be found in Figure 8.14; the monomer spectra in subplots (ii) and (v), the dimer spectra in subplots (iii) and (vi). Due to the unknown concentrations the absorbance spectra could not be converted into molar absorptivity units. However, ignoring the differences in intensity units, a good proportional agreement can be noticed between the simulated dimer and experiment. Also, applying the Lambert-Beer law and Equations (4.2) and (4.3) to creating molar absorptivity spectra, will not change the observed proportional agreement. This approach, albeit pragmatic, allows a reliable assignment of experimental bands based on harmonic fundamentals.

The influence from monomer and dimer conformations on the IR and VCD for this compound is likely to be different than for the 2 isomer. Based on the conformational search, the former compound is not expected to form stabilizing intramolecular hydrogen bonds, ergo compared to **1** the dimer-monomer equilibrium is expected to be shifted more to the dimer.

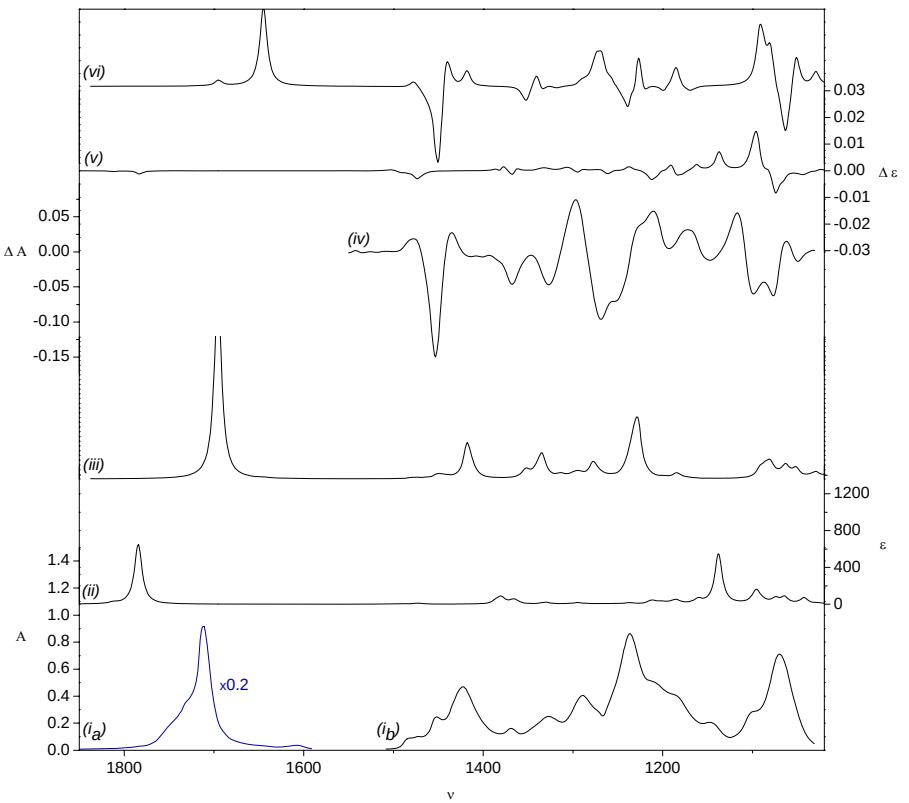

Figure 8.14 Experimental IR (i_a absorbance scaled with factor 0.2 and i_b) and half-difference VCD (iv) spectrum for (+)-**2** in CD_2Cl_2. Simulated IR/VCD B3LYP/6-31++G** monomer (ii)/(v) and dimer (iii)/(vi) spectra for (*R*)-**2**. Experimental intensities and differential intensities in absorbance units. Theoretical intensities and differential intensities in molar absorptivity units, frequencies in cm^{-1}

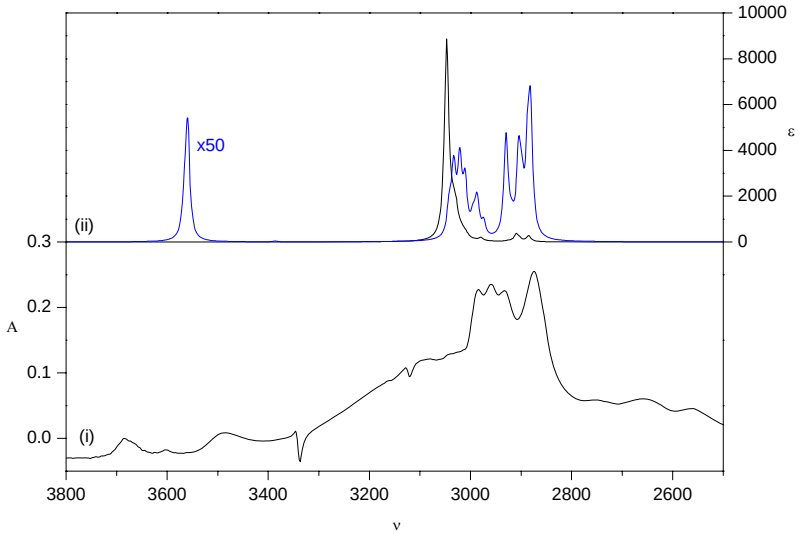

Figure 8.15 (i) OH stretch region IR spectrum of **2** in CD_2Cl_2 and (ii) theoretical 6-31G* (intensities scaled x50) monomer (in blue) and 6-31++G** dimer spectrum.

In Figure 8.14(i) and 8.15(i) the OH and CO stretch spectra are given for a CD_2Cl_2 **2** solution. Based on the CO stretch region, in Figure 8.14(i_a), it is difficult to assess if there is monomer present in solution. Monomer signatures are seen but these are relatively weak. In the OH stretch region, it can clearly be seen that fractions of monomer are present, with two relatively weak bands near 3700 cm^{-1} and 3500 cm^{-1}. However, to draw quantitative conclusions for the equilibrium between monomer and dimer, a concentration study has to be performed, in which multiple solutions with known concentrations should be measured. These kind of data were not provided, and also, the assessment of the equilibrium is not within the scope of this study, which is primarily to establish the absolute configuration of the provided samples.

It can be observed in Figure 8.14, that the predicted monomer IR and VCD intensities are also relatively small. If the monomer structures had any significant populations, which is doubtable based on the previous observations, it can be said that the monomer contribution would be insignificant due to the small predicted intensities and their small influence on the total Boltzmann weighted spectrum.

The VCD spectra are therefore simulated only taking into account cyclic dimer structures, discarding the presumable small fraction of monomer.

8.3.4.3 Fundamental assignment

In Figure 8.16 and 8.17 the experimental bands are assigned based on the B3LYP/6-31++G** dimer fundamentals. The experimental bands can be assigned based on the agreement between simulated and experimental IR and VCD. Virtually all bands can be explained by considering the two lowest energy minima for the dimers, i.e., minima B'C and DB, as they constitute more than 80% of the total population over all the minima listed in Table 8.6. For both conformations, the transition frequency and dipole/rotational strengths can be found in Table 8.7 for fundamentals 41–72. Based on these data and within the applied approximation, a relatively good assignment can be done.

In Figure 8.16 the experimental IR spectrum is given concurrently with the simulated dimer spectrum. The labels indicate the assigned fundamental, i.e., label a represents conformer B'C and b conformer DB. For the VCD data, the same can be seen in Figure 8.17.
Two bands can be assigned to a unique conformation, i.e., bands 55a and 44b. Band 55a is an example of how an unresolved IR band can be identified using the VCD spectrum.
In Figure 8.16 it can be seen that all IR bands have a good proportional agreement, except for band 42, which is predicted to be relatively weak. Fundamentals 54–51 are predicted to have a small frequency separation, giving rise to one band. Experimentally these appear as a broad band with two shoulders corresponding to fundamental 52 and 51/50. One band in the IR, near 1150 cm^{-1}, could possibly be assigned as monomeric, as is was not possible to assign this to any dimer structure fundamental.
In the VCD spectrum, the very small combined rotational strengths for fundamentals 61/60/59a are underestimated compared to the experiment, but have the same sign. Fundamental 47 could not be assigned and is possibly unresolved in agreement with its small predicted intensity. Fundamentals 44b and 43 are predicted to have a small frequency separation, but are experimentally found as 2 different bands.

Table 8.7 B3LYP/6-31++G** vibrational frequencies (ν, in cm^{-1}), dipole strengths (*D*, in 10^{-40} esu^2cm^2) and rotational strengths (*R*, in 10^{-44} esu^2cm^2) for two most significant (*R*,*R*)-dimer conformations, i.e., B'C and DB.

	B'C			DB		
	ν	*D*	*R*	ν	*D*	*R*
41	1029	94	27	1018	53	29
42	1051	173	67	1035	103	4
43	1063	203	−79	1059	153	−100
44	1080	194	66	1066	127	−86
45	1085	72	−30	1086	236	208
46	1092	139	88	1087	129	−15
47	1170	4	−5	1176	19	29
48	1183	23	−15	1177	34	−56
49	1184	51	36	1199	38	2
50	1199	6	−7	1200	5	−14
51	1221	13	−29	1224	93	32
52	1228	688	82	1229	440	−43
53	1230	43	−41	1230	84	5
54	1235	237	16	1258	19	34
55	1239	127	−40	1265	18	−19
56	1268	34	41	1274	159	47
57	1274	44	27	1280	7	11
58	1278	208	7	1291	113	32
59	1313	22	−1	1299	409	−15
60	1317	12	−5	1317	3	5
61	1335	307	−12	1320	7	−12
62	1340	67	22	1334	236	−2
63	1351	35	−12	1354	8	2
64	1352	66	−9	1355	76	−6
65	1418	449	22	1411	314	−3
66	1442	20	43	1437	48	61
67	1450	30	−56	1446	20	−18
68	1452	21	−38	1449	20	−91
69	1462	3	−4	1460	2	−3
70	1464	4	−2	1462	1	1
71	1477	2	0	1477	15	9
72	1478	12	5	1477	4	2

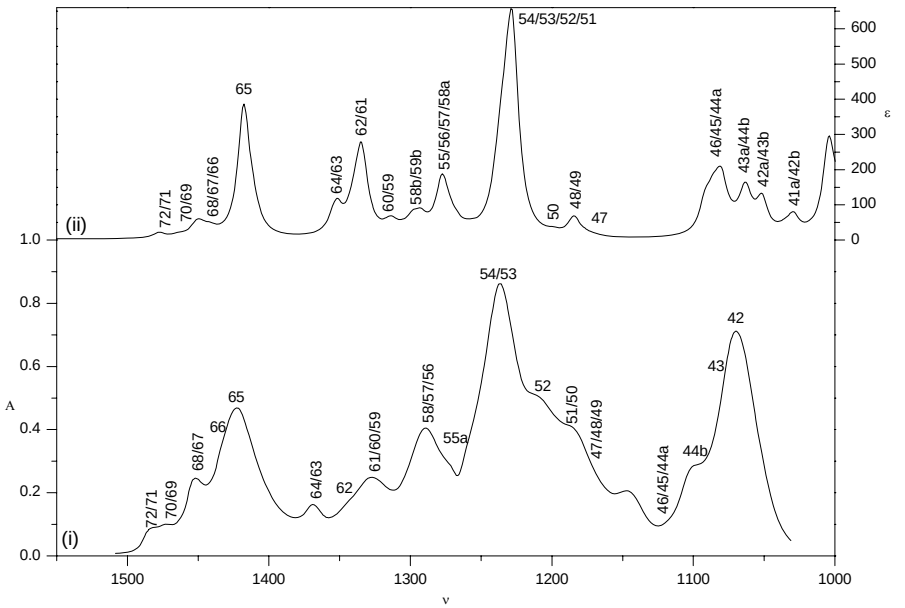

Figure 8.16 Experimental IR spectrum (i) for (+)-**2** and B3LYP/6-31++G** (ii) simulated IR spectrum for (*R*,*R*)-**2**. Experimental spectra are given in absorbance units, simulated spectra in molar absorptivity units, frequencies in cm^{-1}.

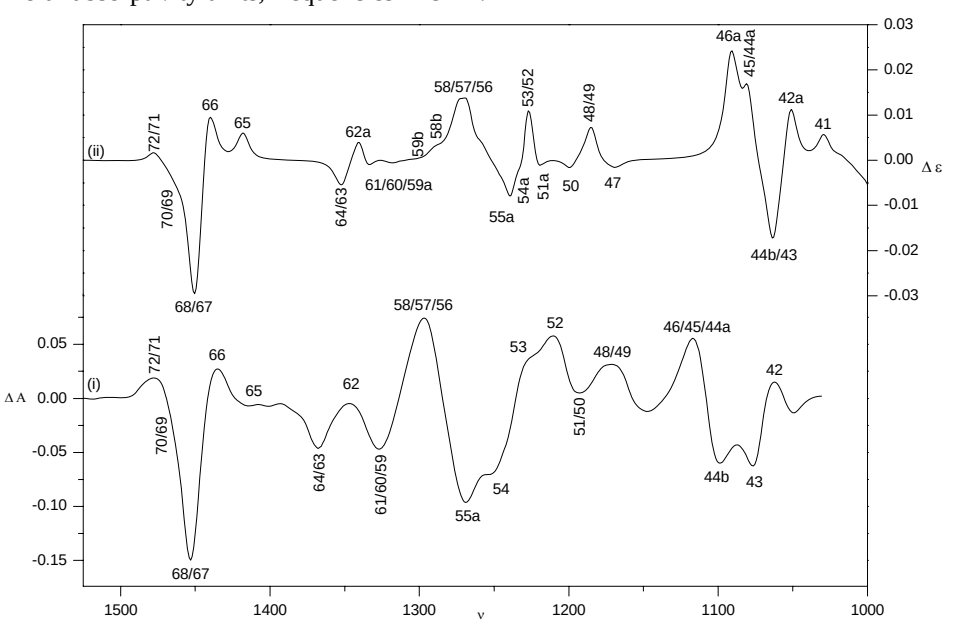

Figure 8.17 Half difference VCD spectrum (i) for (+)-**2** and B3LYP/6-31++G** (ii) simulated IR spectrum for (*R*,*R*)-**2**. Experimental spectra are given in absorbance units, simulated spectra in molar absorptivity units, frequencies in cm^{-1}.

8.3.4.4 Absolute configuration assignment

The identification of the experimental bands is the first step in the process of the determination of the absolute configuration. If a good agreement is seen between vibrational frequencies and IR and VCD intensities, conclusions can be drawn about the three dimensional structure of the studied compound. However, in general, experimental dipole and rotational strengths should be derived from the experimental molar absorptivity spectra by Lorentzian fitting (see Chapter 4). As these molar absorptivity spectra are not available, it is not possible to determine the experimental dipole and rotational strengths and to correlate them with theoretical values. But, as previously reported for other compounds, it is still possible to perform a reliable assignment without this correlation, as the experimental bands are all thoroughly assigned.
Experimental spectra of to (+)-**2** in CD_2Cl_2 were compared to simulated spectra for the *R* configured cyclic dimer of **2**. Based on the proportional agreement between the simulated and experimental IR and VCD, and the agreement of the VCD intensity signs it can be concluded that (+)-**2** can be assigned as the *R* configuration.

8.3.5 Conclusion

For the compound under study, i.e., tetrahydrofuran-3-carboxylic acid, monomer IR and VCD spectra do not reproduce the experimental spectra. This is believed to be due to dimer formations for carboxylic acids in solution. Based on the conformational analysis it could be concluded that cyclic dimers are most significant, compared to other associations. Experimental spectra indicated that mainly dimers are present in solutions. This, combined with the low IR and VCD activity of the monomer, allowed that theoretical spectra could be simulated using B3LYP/6-31++G** cyclic dimers geometries. Based on these spectra, the experimental IR and VCD bands could be assigned using the two lowest energy cyclic dimer conformers. Experimental spectra corresponding to (+)-**2** were presented together with the simulated spectra for the *R* configuration. A qualitative agreement was observed for IR spectra and VCD spectra. For virtually all bands, the VCD was predicted with the correct sign. Based on this agreement, it can be concluded that the sample with positive optical rotation agrees with (*R*)-**2**. Further conclusions on solvent-solute interaction and dimer-monomer equilibrium can not be drawn from this study, due to the lack of experimental data.

8.4 A DFT conformational analysis and VCD study on methyl-tetrahydrofuran-2-carboxylate

8.4.1 Scope and significance

In this last paragraph, a DFT study that was performed on methyl-tetrahydrofuran-2-carboxylate is presented. This compound is the corresponding methyl-ester of the carboxylic acid studied in §8.2.
In the literature it was already established that conversion into the corresponding methyl-ester is a good method to study carboxylic acids with IR and VCD methods, without having to deal with the intermolecular aggregation.[5] This is confirmed in this work. To extend the scope of this study, the potential energy surface and the spectra are thoroughly investigated using different hybrid functionals. Also, a new and promising similarity measure based on neighborhood similarity is introduced, which will be the ansatz for Chapter 9.

8.4.2 Introduction

An interesting approach for the synthesis of tetrahydrofuran-2-carboxylic acid is the enantioselective hydrolysis of its esters.[6] (*R*)-tetrahydrofuran-2-carboxylic acid is a chiral building block for faropenem[7], a clinically effective non-natural β-lactam antibiotic.[8] In this paper, a study is performed on the methyl-ester of tetrahydrofuran-2-carboxylic acid using unpolarized infrared (IR) and vibrational circular dichroism (VCD) spectroscopy and density functional theory (DFT).
VCD spectroscopy has become a powerful method to study the absolute configuration and the conformational properties of chiral molecules in solutions. Vibrational CD is the differential vibrational absorption between left and right circularly polarized IR radiation by a chiral species.[56] In combination with quantum chemical calculations, experimental VCD spectra can be simulated which allows the interpretation of the experimental VCD. For a specific vibrational transition,

---

Kuppens, T.; Vandyck, K.; Van der Eycken, J.; Herrebout, W.; van der Veken, B. J.; Bultinck, P. *Spectrochim. Acta A* **2006**, In Press

enantiomers have identical IR intensities. Their VCD intensities, however, are opposite in sign. Consequently, agreement between a simulated and experimental VCD spectrum should imply that the enantiomerically pure compound measured, has the same absolute configuration as the modeled compound. Evidently, this agreement depends on the reliability of the prediction.

The most applied theoretical framework for the prediction of VCD intensities, consists in using DFT with the B3LYP hybrid functional[10-12,35], combined with the application of the 6-31G* basis set. This combination has been used in numerous studies and gives satisfactory results, allowing the interpretation of the experimental VCD spectra of chiral molecules in solution.[50,57,58]

The absolute configuration of methyl-tetrahydrofuran-2-carboxylate, **3**, is known from the synthesis, i.e., based on the absolute configuration of the corresponding carboxylic acid[28,59] (+)-**3** has the *S* configuration. The spectra measured for (+)-**3** should therefore show a high degree of similarity towards the spectra simulated for (*S*)-**3**. The a priori knowledge of the AC allows to set up a study, in which the performance of the hybrid density functionals are screened for their applicability in the VCD methodology[21,60] for the compound under study, applying the 6-31G* and cc-pVTZ basis sets. For each functional, IR and VCD spectra are simulated and compared in detail with the experiment, assigning experimental bands based on the harmonic fundamentals. Also, a similarity measure is introduced which allows the comparison of experimental and theoretical spectra, to establish the usefulness of the different hybrid functionals.

8.4.3 Methods

8.4.3.1 Preparation of (+)-(S)-methyl-tetrahydrofuran-2-carboxylate

(+)-(*S*)-methyl-tetrahydrofuran-2-carboxylate was made by esterification of (−)-(*S*)-tetrahydrofuran-2-carboxilic acid using diazomethane (98 % ee).[59] This method proved superior over the use of commercial $(CH_3)_3SiCHN_2$ since it resulted in an easier purification of the product.

8.4.3.2 Spectroscopy

IR and VCD spectra are measured using respectively a Bruker Vector 22 and an IFS 66v/S FTIR spectrometer coupled to a PMA37 module.[29] A demountable cell with CaF_2 windows and a 105 µm Teflon spacer are employed. The unpolarized IR absorbance spectra are recorded at a resolution of 4 cm^{-1}, the VCD spectra at a resolution of 6 cm^{-1}. To improve the VCD S/N ratio a long wave-pass filter with an 1830 cm^{-1} cutoff is used. The collection time for the VCD spectrum is 90 minutes. (+)-**3** is dissolved in CD_2Cl_2 at a concentration of 0.42 M and 0.68 M. The sample with high concentration was used to obtain good VCD spectra for the 1400–1500 cm^{-1} range. These spectra are provided in Figure 8.18.

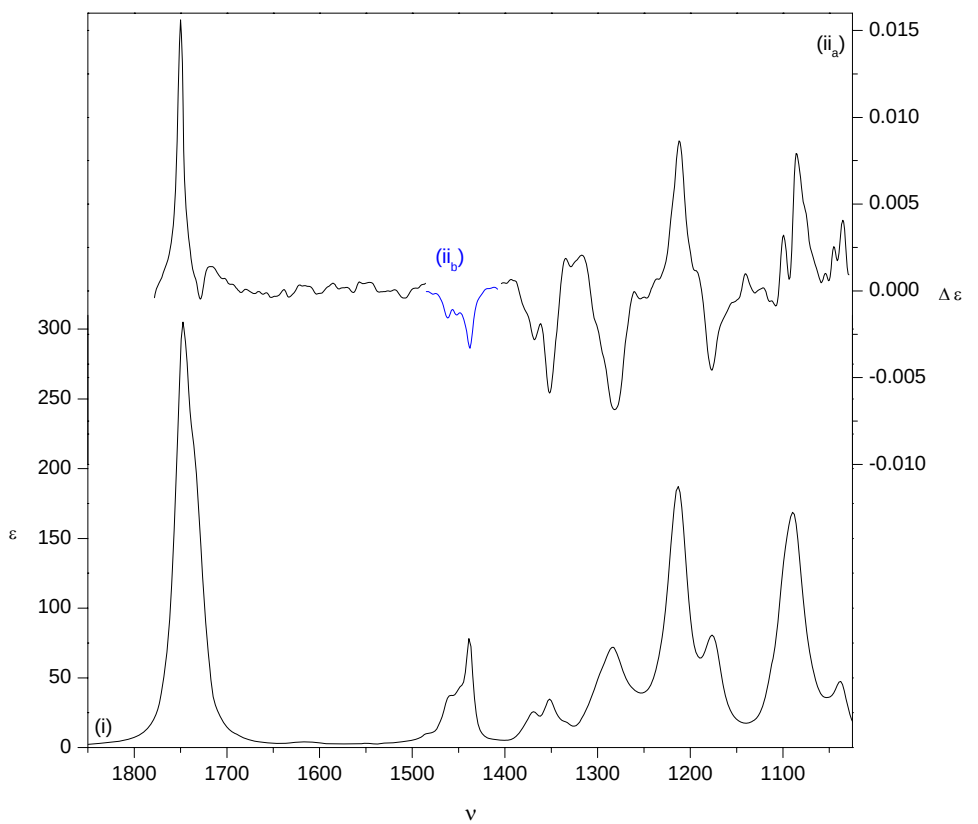

Figure 8.18 Experimental IR (i) and VCD for 0.42 M (ii_a) (*S*)-(+)-**3** solution in CD_2Cl_2. For the region 1400–1500 cm^{-1} the VCD (ii_b) is given for the 0.68 M solution due to the weak VCD in that area.

To compensate for machine and cell artifacts, the VCD of the solvent was used as baseline, and was measured in the same conditions as the sample. In the past this has been proven to be a good approximation.[17,61]

8.4.3.3 Computation

Geometry optimizations and the calculation of the dipole strengths (*D*) and rotational strengths (*R*) are performed using Gaussian03 revision B5[32] using the tight optimization criterion. DFT calculations with the 6-31G* and cc-pVTZ basis set were performed using a set of 9 hybrid functionals, i.e., B1LYP, B3LYP, B3P86, B3PW91, B98, BHandH, BHandHLYP, MPW1PW91 and PBE1PBE.[38] The conformational analysis is described further. For all the allocated DFT minima, for each functional using the cc-pVTZ[62,63] basis set, the Hessian matrices, atomic polar tensors (APT) and atomic axial tensors (AAT) are calculated using gauge-including/invariant atomic orbitals (GIAOs)[39,40], allowing the calculation of the dipole and rotational strengths. The enthalpy and Gibbs energy are calculated under the usual assumptions using standard statistical thermodynamical expressions.[41] An appropriate scaling factor is used to correct for the harmonic approximation.[64,65] All calculations were performed on the Ghent Quantum Cluster.

8.4.4 Results and discussion

Because VCD is very sensitive to conformational changes, the conformational description of the compound studied is very important.[66,67] As a consequence, to ensure that all possible conformations with significant contributions can be located, a conformational search has to be performed with the greatest care.
For this compound, first a preliminary MM3[43] and MM4[68] stochastic search with subsequent B3LYP/6-31G* optimization was performed, which indicated that two different ring conformations are possible for **3**. To describe these ring conformations, Cremer-Pople pseudo rotational coordinates are used; the puckering amplitude *q* describes the degree of ring puckering and the pseudo-rotational phase angle φ describes the mode of ring puckering.[46,47,69] Also, methyl-ester conformations with a *trans* configuration, i.e., $\tau_2 = 180°$ ($O^7C^6O^8C^9$ in Figure 8.19) showed to be higher in energy compared to the *cis* configured minima (ΔH^0_{min}(B3LYP/6-31G*) > 7 kcal/mol).

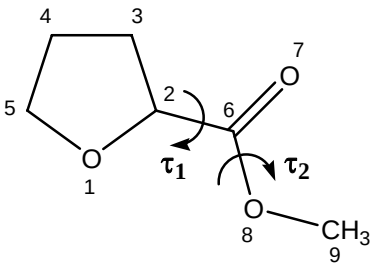

Figure 8.19 Depiction of **3** and definition of dihedral angles τ_1 ($O^1C^2C^6O^8$) and τ_2 ($O^7C^6O^8C^9$)

Subsequently, a systematic B3LYP/6-31G* search was applied for *cis* (τ_2 = 0°) configured (*S*)-**3** in which τ_1 ($O^1C^2C^6O^8$) is varied in steps of 5° for two different sets of puckering coordinates, i.e., q = 0.36 Å/φ = 120° and q = 0.38 Å/φ = 230°. A total of 144 starting geometries were optimized using a tight optimization criterion yielding 4 minima. The same systematic search was performed using a series of alternative hybrid functionals, i.e., B1LYP, B3P86, B3PW91, B98, BHandH, BHandHLYP, MPW1PW91 and PBE1PBE. However, the energy order and the number of located minima were found to depend on the functional used (See Table S8.6 in *Supplementary Material*). In order to gain some transparency on the conformational behavior of the compound under study, a B3LYP/6-31G* constrained potential energy surface scan was performed, developing τ_1 in steps of 1°, for both ring conformations. The constrained energy profile can be found in Figure 8.20 in which 6 possible minima can be distinguished, which are labeled T, U, V, W, X and Y. As can be seen, in Figure 8.20, the constrained energy profiles are not well defined for the $90° < \tau_1 < 160°$ region, probably due to the steric hindrance between the carbonyl moiety and the THF ring.

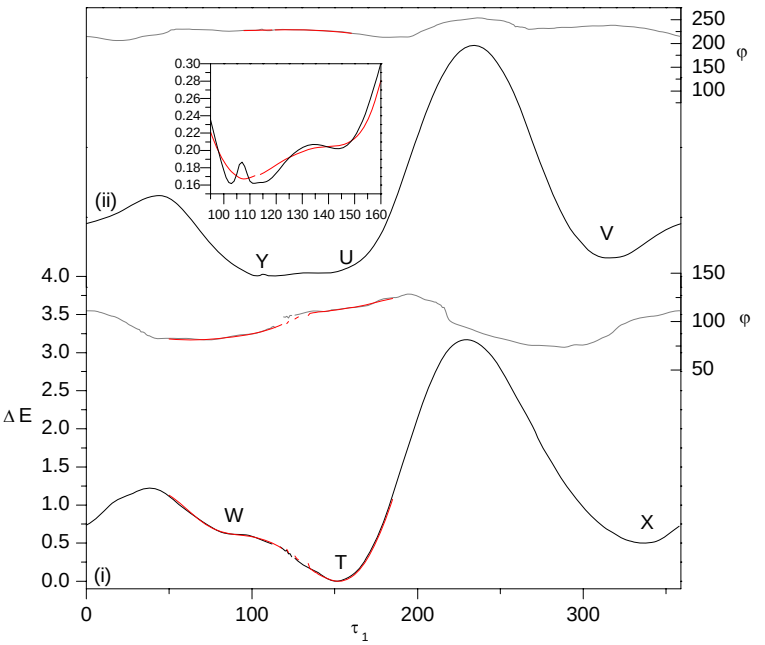

Figure 8.20 B3LYP/6-31G* constrained energy profile for two different ring conformations with initial geometry descriptors q = 0.36 Å/φ = 115° (i) and q = 0.38 Å/φ = 230° (ii). The dihedral angle coordinate τ_1 is kept fixed during the optimization (scanned in steps of 1°). Relative SCF energies are given in kcal/mol. The puckering angle (φ, in degrees) as a function of the dihedral angle coordinate τ_1 is given above each energy profile. The same scans were performed again for the 50° < τ_1 < 190° region, using a tight optimization criterion (red). The subplot in (ii) is a detailed energy plot of the 90° < τ_1 < 160° region

The geometries equivalent to the points labeled T, U, V, W, X and Y on the constrained energy profiles in Figure 8.20 are taken as starting geometries for the tight optimization, employing a cc-pVTZ basis set and a set of 9 different functionals. In previous studies, this large basis set was proven to be excellent for the purpose of VCD.[50,57] The results of this large-scale conformational analysis are given in Table 8.8, in which the geometry descriptors are given concurrently with the Gibbs energy and corresponding Boltzmann population. For each functional the same conformations can be found, albeit that the energy order for the functionals B3PW91, B98 and BHandH differ compared to the other functionals. Surprisingly, conformation Y is not found as a minimum. Optimization of this geometry appears to converge to conformation U, for all functionals.

Table 8.8 DFT (B1LYP, B3LYP, B3P86, B3PW91, B98, BHandH, BHandHLYP, MPW1PW91 and PBE1PBE)/cc-pVTZ label, pseudo-rotational coordinates (q in Å and φ in degrees), key dihedral angle (τ_1 in degrees), relative Gibbs energies (ΔG^0 in kcal/mol) and Boltzmann populations (% P, 298.15 K) for located conformations of **3**.

functional		τ_1 $O^8C^6C^2O^1$	q	φ	ΔG^0	% P
B1LYP	T	153	0.34	109	0.00	27.66
	U	153	0.36	227	0.03	26.30
	X	−24	0.34	101	0.31	16.45
	V	−37	0.36	240	0.32	16.16
	W	89	0.34	82	0.43	13.44
B3LYP	T	152	0.34	109	0.00	26.80
	U	152	0.36	227	0.00	26.62
	X	−23	0.34	102	0.31	15.96
	V	−37	0.36	240	0.32	15.59
	W	90	0.34	82	0.34	15.03
B3P86	T	153	0.35	109	0.00	29.60
	U	154	0.37	225	0.10	25.01
	X	−19	0.35	102	0.29	18.03
	V	−34	0.37	239	0.35	16.31
	W	86	0.35	82	0.58	11.05
B3PW91	U	153	0.36	229	0.00	28.10
	T	154	0.35	107	0.01	27.70
	V	−34	0.37	242	0.31	16.67
	X	−19	0.35	99	0.31	16.61
	W	87	0.35	81	0.56	10.93
B98	T	154	0.35	114	0.00	27.43
	U	155	0.36	224	0.11	22.94
	W	90	0.35	82	0.18	20.12
	X	−21	0.35	106	0.36	15.06
	V	−35	0.36	237	0.38	14.46
BHandH	T	158	0.36	114	0.00	39.67
	X	−17	0.37	109	0.32	23.22
	U	163	0.37	217	0.54	15.89
	V	−33	0.38	235	0.63	13.69
	W	74	0.37	82	0.98	7.54
BHandHLYP	T	156	0.35	109	0.00	31.20
	U	157	0.36	226	0.18	22.92
	X	−24	0.34	101	0.30	18.96
	V	−37	0.36	242	0.33	17.93
	W	81	0.35	80	0.74	9.01

MPW1PW91	T	154	0.35	108	0.00	29.60
	U	155	0.36	227	0.08	25.65
	X	−19	0.35	101	0.29	18.09
	V	−34	0.37	241	0.33	16.92
	W	84	0.35	80	0.66	9.73
PBE1PBE	T	155	0.35	109	0.00	31.13
	U	155	0.37	225	0.15	24.08
	X	−18	0.36	103	0.30	18.87
	V	−33	0.37	239	0.37	16.57
	W	83	0.36	80	0.71	9.35

The most applied framework for the calculation of rotational strengths for common organic compounds is DFT, particularly using the hybrid functional B3LYP.[13,17,70,71] This functional gives good results describing geometries and predicting rotational strengths, using the 6-31G* basis set, which are in good agreement with experimental spectra.[16,57] For the compound under study, however, this default level of theory is unable to describe the potential energy surface unambiguously, which is clearly the effect of the limited basis set size. Therefore, the cc-pVTZ basis set will be applied to study the VCD for **3**, applying the B3LYP and 8 other functionals.

For each functional, dipole and rotational strengths were calculated using the cc-pVTZ basis set, for all minima. Single conformational spectra were produced using a Lorentzian band shape (fwhm = 10 cm^{-1}) to mimic experimental spectra. These spectra were then summed, taking into account their Gibbs energy using Boltzmann statistics and subsequently were converted into molar absorptivity units.[50] In Figure 8.21 and 8.22 the simulated IR and VCD spectra are given for each functional. The frequencies were scaled with a factor 0.98 which will be rationalized further.

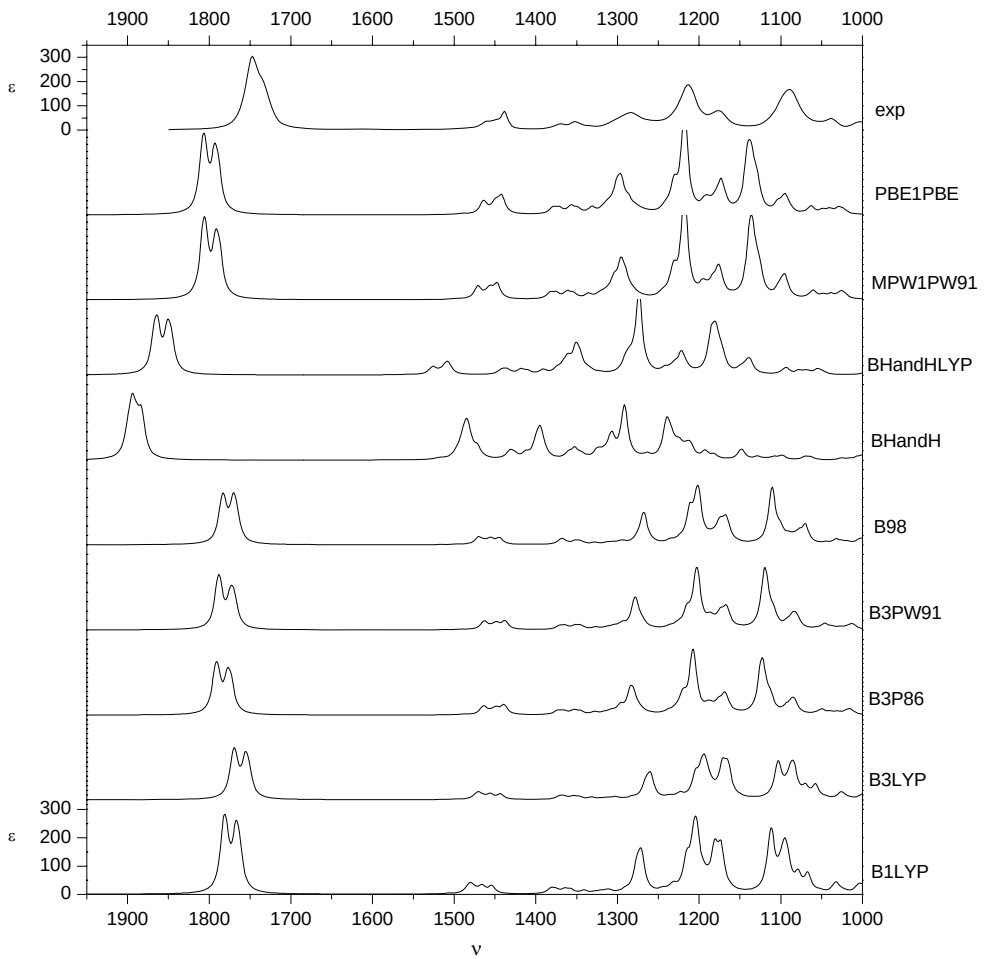

Figure 8.21 Simulated (+)-(*S*)-**3** IR DFT/cc-pVTZ for different functionals and experimental spectra. Intensities are in molar absorptivity units, frequencies in cm^{-1}

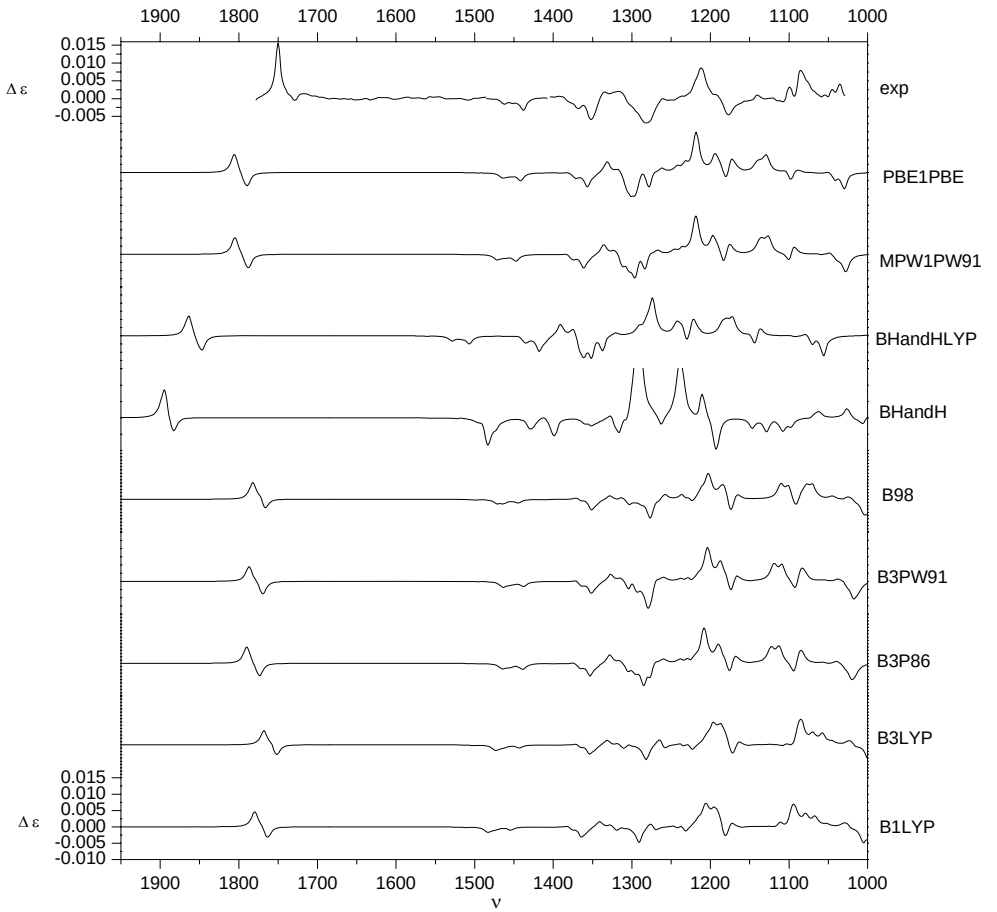

Figure 8.22 Simulated (+)-(*S*)-**3** VCD DFT/cc-pVTZ for different functionals and experimental spectra. Intensities are in molar absorptivity units, frequencies in cm^{-1}

The spectra were simulated for a specific absolute configuration, i.e., the *S* configuration. Generally, agreement with the experimental VCD spectrum, i.e., location and sign of the bands allows the elucidation of the absolute configuration. The absolute configuration of the ester and acid were determined previously[28,59], i.e., (*S*)-(+)-**3**. Therefore, agreement between experiment and theory is expected. This design allows the further evaluation of the density functionals.

First, the B3LYP/cc-pVTZ spectra are compared with experimental spectra. In Figure 8.23 the simulated B3LYP/cc-pVTZ spectra are given concurrently with the experiment.

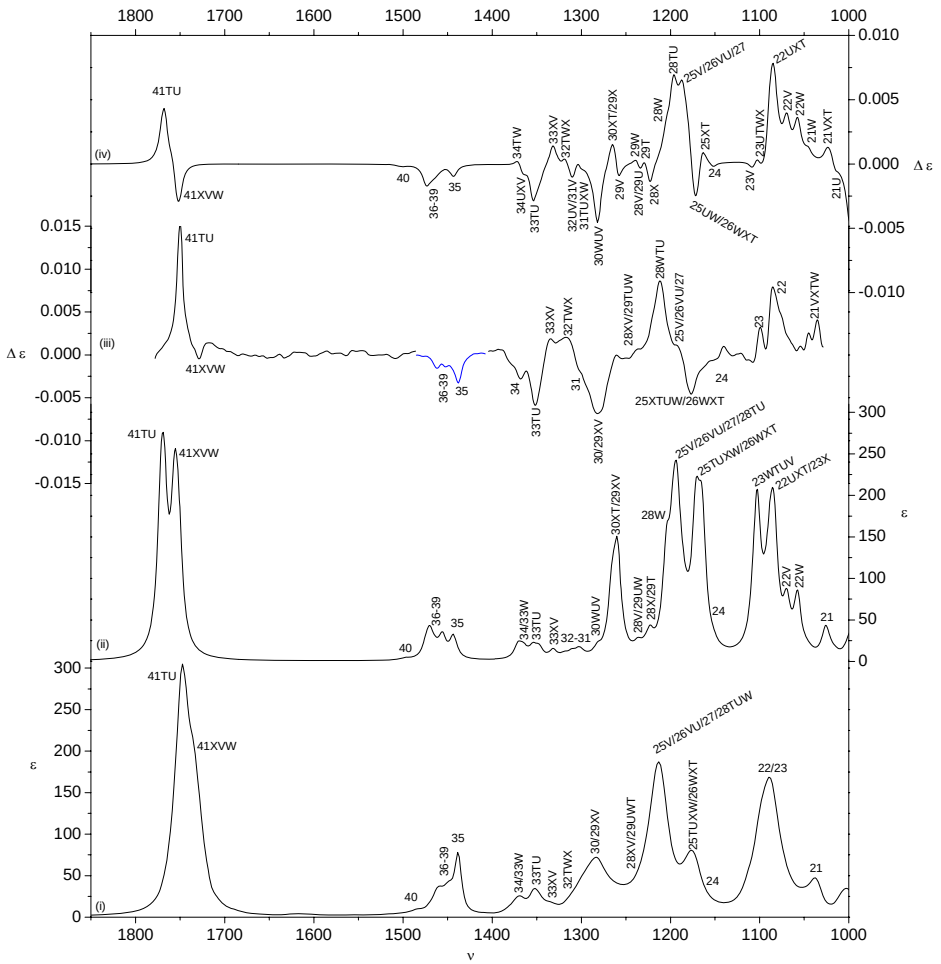

Figure 8.23 IR (i)/(iii) and VCD (ii)/(iv) for 0.42 M (+)-(*S*)-**3** solution (0.68 M for 1400–1500 cm^{-1} VCD region) and simulated B3LYP/cc-pVTZ accounting for all significant minima, i.e., T, U, X, V and W

Good agreement is found between the experimental and the simulated spectra, both for IR and VCD. However, to unequivocally validate the agreement between experiment and theory, each individual band should be compared. Accordingly, the experimental bands have to be identified, so these can be correlated to simulated bands. This can be done by attempting to assign these bands, based on the predicted frequencies and dipole/rotational strengths.[50] In Figure 8.23, the broadened theoretical bands are labeled with their normal mode, indicated by their fundamental number and conformational tag. As can be seen, the 5 minima T, U, X, V and W should all be accounted for. This makes the assignment of the experimental bands

complex, but feasible and is illustrated in Figure 8.23 and Table 8.9 (In *Supplementary Material*, Table S8.7 can be found which is a extended version of Table 8.9 and illustrates the assignment in more detail). In both tables the experimental dipole and rotational strengths are determined by Lorentzian deconvolution of respectively the experimental IR and VCD spectrum. Lorentzian bands[72] are fitted to the experimental spectrum, which allows the evaluation of the area under these bands. The dipole and rotational strengths are proportional to the area under the observed bands[17] in their respective spectrum. This procedure is not regarded as exact[73], nevertheless it is a way to approximate experimental dipole and rotational strengths and has proven its reliability.[13,50]

Table 8.9 Lorentzian fitted experimental and broadened B3LYP/cc-pVTZ IR/VCD frequencies (υ, in cm^{-1}) and dipole/rotational strengths (D in 10^{-40} esu^2cm^2 and R in 10^{-44} esu^2cm^2) accounting for the significant minima, i.e., T, U, X, V and W.

Fundamental	Experiment		B3LYP/cc-pVTZ	
	υ	D^{*1}	υ	D^{*2}
21	1039.0	65.1	1021.6	61.8
21W/22/23	1074.0	81.1	1085.0	736.1
	1086.6	266.4		
	1097.3	193.5		
	1108.9	18.0		
24/25/26WX	1176.1	135.5	1162.3	372.8
25V/26VU/2	1213.6	498.2	1201.7	492.7
	1255.5	77.0		
29VX/30	1281.2	111.4	1271.7	229.3
31/32	1293.3	63.0	1310.2	24.2
	1305.0	13.6		
33VX	1338.2	3.8	1331.6	10.9
33UT	1351.8	40.3	1350.7	26.1
	1369.8	20.1		
33W/34	1377.5	2.2	1365.4	28.9
35	1438.4	58.6	1443.5	26.7
36/37/38/39	1449.9	34.7	1465.1	73.2
	1461.3	38.1		
40	1487.2	5.5	1499.0	2.3
41	1733.9	214.1	1760.5	455.7
	1747.9	405.8		

Fundamental	Experiment		B3LYP/cc-pVTZ	
	υ	R^{*1}	υ	R^{*2}
21TXV	1035.4	9.4	1023.7	6.5
	1045.0	3.8		
	1054.4	0.4		
21W/22/23X	1067.8	2.9	1074.7	47.3
	1075.4	7.7		
	1081.1	7.3		
	1085.9	14.0		
23	1098.4	2.2	1103.0	−2.8
	1101.1	2.6		
24/25TUXW	1163.9	−3.8	1162.3	−9.5
	1177.2	−19.7		
25V/26VU/2	1191.1	2.9	1188.1	43.9
	1210.9	31.4		
	1218.5	6.8		
28XV/29/30	1238.7	1.3	1231.5	−2.0
	1245.6	−1.1		
	1259.1	−1.6		
	1261.2	2.4		
30VUW	1275.8	−12.7	1284.0	−13.7
31/32UV	1283.9	−20.1	1306.0	−2.2
	1293.8	−6.4		
	1302.7	−1.8		
32XTW	1314.3	6.7	1319.9	1.4
	1322.6	3.4		
33VX	1335.2	7.8	1331.6	4.6
33UTW/34	1346.6	−4.3	1361.7	−9.3
	1352.3	−14.3		
	1368.6	−6.4		
35	1436.7	−5.2	1443.5	−2.2
36/37/38/39	1437.6	−5.9	1465.1	−5.9
40	1442.9	−1.8	1499.0	−0.4
	1452.2	−1.9		
	1461.8	−2.5		
	1465.4	−0.3		
41XVW	1729.0	−1.5	1754.5	−7.0
41TU	1746.0	3.1	1769.6	9.8
	1750.2	20.1		

[*1] averaged frequencies over the appropriate fundamentals, scaled with factor 0.98.
[*2] summed over the appropriate fundamentals

In the IR, some broad unresolved bands and low intensity bands can be identified based on their VCD. The agreement of the experiment with the simulated B3LYP/cc-pVTZ spectra is good, with some differences in relative intensity; the band assigned as 25TUXW/26WXT in the IR is overestimated compared to band 25V/26VU/27/28TU, whereas band 35 is underestimated compared to band 36−39, both in IR as in VCD. The CO stretch band 41XVW is overestimated as this band has a predicted intensity that is almost equal in magnitude compared to band 41TU. In the experimental VCD an intense band 41TU is observed and a negative low intensity band 41XVW. The VCD in the region of 1250 cm^{-1} which is assigned to fundamentals 28 and 29 for the selected conformations, is very weak. In the simulated spectrum, multiple bands are predicted with opposite signs. In the assignment, the sum over all these bands, i.e. 28XV/29TUW, is taken and compared to the weak experimental features. For the weak IR band, assigned as fundamental 40, no experimental VCD could be measured, in agreement with the small predicted intensity.

The correlation plots for the experimental and B3LYP/cc-pVTZ theoretical dipole and rotational strengths are given in Figure 8.24. The correlation coefficient is 83% for the dipole strengths and 75% for the rotational strengths. These values illustrate the good agreement, between both the IR and VCD spectra, taking into consideration the observed but also inherent differences.

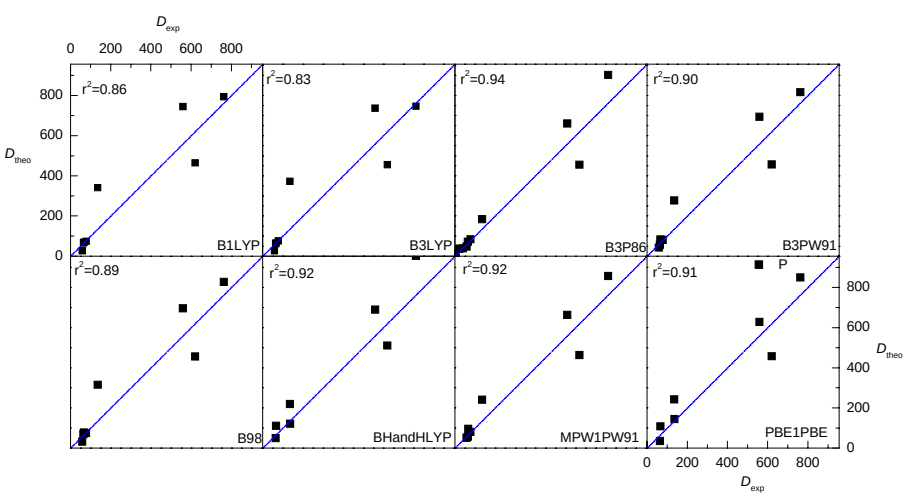

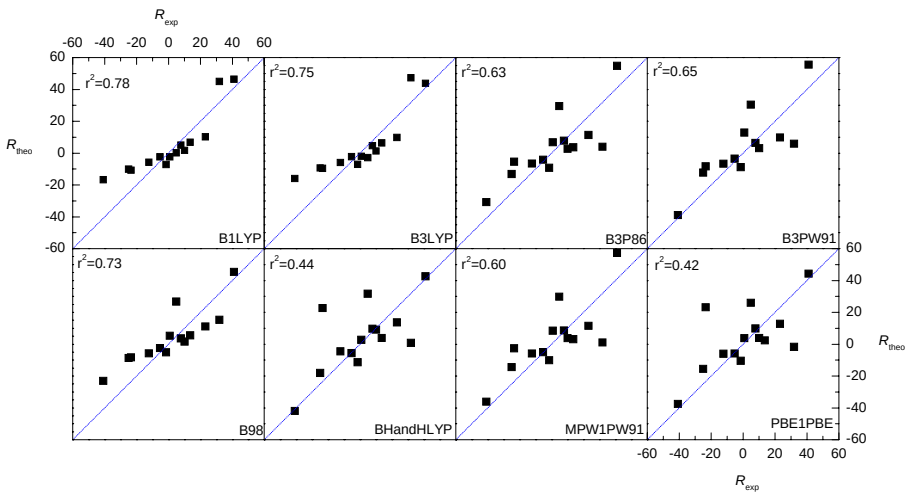

Figure 8.24 Correlation plots for theoretical (DFT/cc-pVTZ, i.e., B1LYP, B3LYP, B3P86, B3PW91, B98, BHandHLYP, MPW1PW91 and PBE1PBE) versus experimental dipole strengths (*D*, in 10^{-40} esu^{2}cm^2) (a) and rotational strengths (*R*, in 10^{-44} esu^{2}cm^2) for (+)-(*S*)-**3**. Correlation coefficients r^2 are given. The blue dotted line has a slope of +1 and intercept of 0.0.

For the eight other functionals, the same comparison can be done as for the B3LYP functional above, assigning the experimental bands and comparing dipole and rotational strengths. This was done exhaustively for seven functionals, i.e., B1LYP, B3P86, B3PW91, B98, BHandHLYP, MPW1PW91 and PBE1PBE. The BHandH functional was not further investigated as BHandH/cc-pVTZ dipole and rotational strengths were found to differ substantially from those compared to the other functionals. In Figures 8.21 and 8.22, the BHandH/cc-pVTZ simulated spectra are notably different compared to the other functionals. Not only is there a large difference in predicted dipole and rotational strengths but the relative free energies of the conformations are also very different compared to those of the other functionals.

For the seven resulting functionals the experimental dipole and rotational strengths are correlated with theory. The actual assignment details, as described for B3LYP assignment, are not being discussed in the main text. The comprehensive assignment tables are given in *Supplementary Material*. Using the same procedure as described for the B3LYP functional, correlation plots could be designed for each of the seven functionals, and can be found in Figure 8.24.

The dipole strengths are predicted in good agreement with experiment for all eight functionals, which all perform equally well. This can be seen in Figure 8.24, with correlation coefficients near 90%.
For the rotational strengths the situation is different. There is an extra dimension when discussing rotational strengths, i.e., its sign, which can be positive, negative (or zero). Wrongly predicted, this would lead to false conclusions when e.g. elucidating conformational populations or absolute configurations. In Figure 8.24 the correlation plots for the rotational strengths are given for the eight functionals. Based on the correlation, three functionals that are significantly better than the rest can immediately be identified, i.e., B1LYP, B3LYP and B98, with correlation coefficients higher than 70%. On the other end, the BHandHLYP and PBE1PBE have a correlation less than 50%. The other three functionals, i.e., B3P86, B3PW91 and MPW1PW91 are in between with a correlation between 60% and 65%. If the plots are studied in more detail, it can be seen that for four functionals rotational strengths are predicted with the wrong sign. The band assigned as 28XV/29/30TX is predicted with the wrong sign for the B1LYP and B3LYP and for mode 23, the B3LYP the rotational strength is also predicted wrongly. However, there the absolute value of the predicted and experimental rotational strengths is rather low. For the BHandHLYP functional the predicted rotational strength for the band assigned as 24/25/26/27 has a value near 23 which contrasts with the experimental value of approximately −23. For the PBE1PBE functional, the same experimental band is assigned as 25/26/27 (mode 24 is predicted with a lower frequency) and gives the same difference as for BHandHLYP, and additionally mode 22/23W is predicted wrongly. For the other three functionals all rotational strengths are predicted with the correct sign.

Another approach to compare experimental and simulated spectra is the use of similarity descriptors.[17] Although the theoretical frequencies are scaled linearly to correct for the harmonic approximation and basis set incompleteness, some bands can still be shifted with respect to their corresponding experimental band. A good similarity measure should therefore take into account the neighborhood in direct proximity of the compared points. Also interesting would be the incorporation of the specific frequency scaling of the simulated spectrum in the similarity measure. This scaling factor is dependent on the applied functional and basis set. The functional dependence on the calculated frequency is illustrated in Figures 8.21 and 8.22, where all simulated spectra were scaled with a factor 0.98 which is in general a good value for B3LYP/cc-pVTZ frequencies.

The neighborhood similarity (NS) measure that is used in this paper is given in Equation (8.4)

$$S^{\sigma} = \frac{\int w_{fg}(r)c_{fg}^{\sigma}(r)dr}{\sqrt{\int w_{ff}(r)c_{ff}^{\sigma}(r)dr \int w_{gg}(r)c_{gg}^{\sigma}(r)dr}} \tag{8.4}$$

In this similarity descriptor, a weighting function w(*r*) is introduced to extract the similarity information concerning neighborhoods. For this purpose a triangular function is used as introduced by De Gelder et al.[74],

$$\begin{aligned} w(r) &= 1 - \frac{|r|}{l} && \Leftrightarrow |r| < l \\ w(r) &= 0 && \Leftrightarrow |r| \geq l \end{aligned} \tag{8.5}$$

For our purposes the window size l = 40 cm^{-1} is chosen, as this gives good results when comparing IR spectra.
$c_{fg}^{\sigma}(r)$ and $c_{ff}^{\sigma}(r)$ are called respectively auto- and cross-correlation functions and are defined as

$$\begin{aligned} c_{fg}^{\sigma}(r) &= \int f(\sigma v)g(v+r)dv \\ c_{ff}^{\sigma}(r) &= \int f(\sigma v)f(v+r)dv \end{aligned} \tag{8.6}$$

A scaling factor σ is introduced to consider the scaling between theoretical and experimental spectrum respectively represented by *f*(ν) and *g*(ν). The scaling factor that gives the highest similarity can be found by optimizing S^{σ} in function of σ.
In Table 8.10, the maximized NS is given comparing experimental and DFT/cc-pVTZ simulated IR spectra. It can be seen that B3LYP gives a scaling factor closest to unity. The BHandH and BHandHLYP vibrational frequencies are notably more overestimated, yielding scaling factors of respectively 0.90 and 0.92. The simulated IR and VCD spectra for the different functionals with scaled frequencies according to Table 8.10 are given in Figure S8.5 and Figure S8.6 in *Supplementary Material*.
These scaling factors are now used for the calculation of the NS between experimental and simulated VCD for the compound with known absolute configuration. The NS, i.e., S^{σ} values for each functional are represented in Figure

8.25 in gray. The same can also done for the simulated spectra for the opposite enantiomer, i.e., (*R*)-**3**. These NS are also given in Figure 8.25, in black.

Table 8.10 Maximized NS for experimental and simulated IR spectrum (DFT/cc-pVTZ) optimized by theoretical frequency scaling. The scaling factor σ gives the optimum, for l = 40 cm^{-1}.

	S^{σ}_{max}	σ
B1LYP	84.4	0.97
B3LYP	82.6	0.98
B3P86	84.6	0.96
B3PW91	83.2	0.96
B98	84.0	0.97
BHandH	81.0	0.90
BHandHLYP	87.6	0.92
MPW1PW91	83.9	0.95
PBE1PBE	83.0	0.95

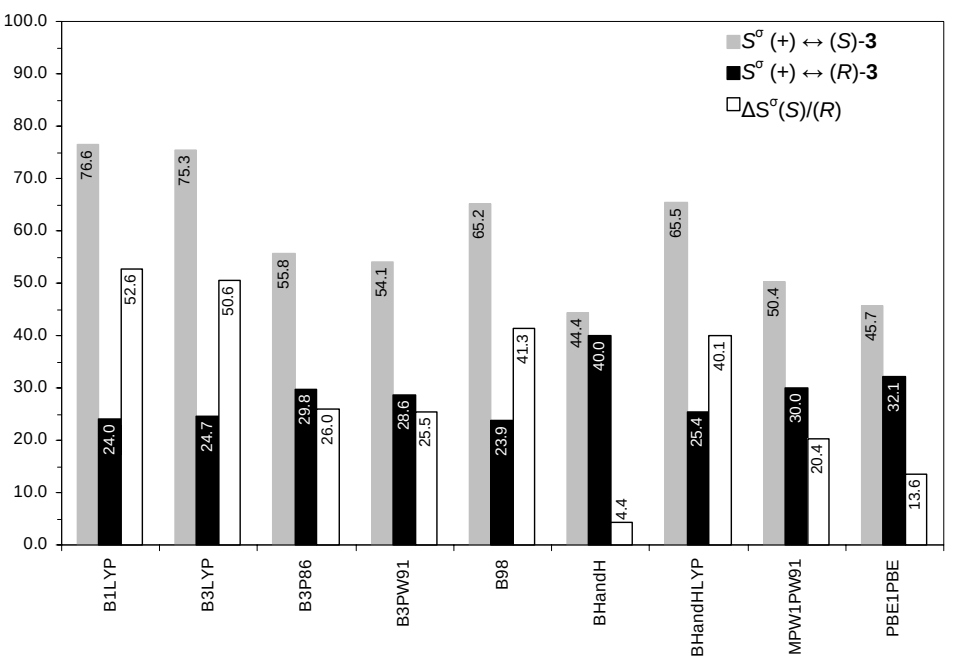

Figure 8.25 NS S^{σ} between experimental (+)-**3** and DFT/cc-pVTZ (i.e., functionals B1LYP, B3LYP, B3P86, B3PW91, B98, BHandH, BHandHLYP, MPW1PW91 and PBE1PBE) simulated spectra for the *S* (correct) and *R* enantiomer. The applied scaling factors are those from Table 8.10. In gray, the NS between experiment and simulated spectrum for the known correct absolute configuration (*S*), in black the NS between experiment and the opposite enantiomer (wrong absolute configuration, i.e., (*R*)), and in white the difference in *S*/*R* NS.

It can be seen that for the B3LYP and B1LYP functionals a S^{σ} of 75% and higher can be found when evaluating the correct enantiomer. Except for the BHandH and PBE1PBE functionals that give a S^{σ} around 45%, the remainder functionals give a similarity between 50 and 66%.

Evaluation of the opposite enantiomer gives much lower S^{σ}, with values between 20 and 30%. The PBE1PBE NS is 32%, and BHandH is an outlier, having a value of 40%.

Rather than looking at the absolute values of the NS, it seems more interesting to consider the differences in S^{σ} evaluated for opposite enantiomers, which are also represented in Figure 8.25 using outlined-white bars. The largest differences in S^{σ} can be found for the B1LYP, B3LYP, B98 and BHandHLYP. The remaining functionals, i.e., PBE1PBE and BHandH gives the smallest difference in S^{σ}, with an extreme small difference of 4.4% for the BHandH functional. B3P86, B3PW91 and MPW1PW91 give intermediate ΔS^{σ} values.

When comparing these findings to the correlation coefficients in Figure 8.24 it can be observed that the functionals yielding high R_{exp}/R_{theo} correlation coefficients also display the largest differential $S/R\ S^{\sigma}$. The same trend for functionals with lower correlation coefficients can be observed. Earlier in this paper, the cc-pVTZ/BHandH spectra were found to be notably different compared to spectra produced using other functionals. The BHandH ΔS^{σ} indicate that the visually observed differences are well reflected in the proposed similarity measure.

This could indicate that the difference in S^{σ} evaluated for the correct and wrong enantiomer could be a useful measure for the quality of the agreement between experimental and theoretical VCD spectra.

Comparing experimental and theoretical rotational strengths is still superior, giving much more information about the agreement. An example which makes this clear is the discrepancy that can be observed for the BHandHLYP functionals, yielding a somewhat higher differential S^{σ} than expected from its R_{exp}/R_{theo} correlation. The cc-pVTZ/BHandHLYP predicted rotational strength for band 24/25/26/27 was predicted with the wrong sign yielding a lower correlation, which can not be deduced based on the differential similarity measure. The differential S^{σ} is still lower compared to the better performing functionals.

However, the assignment and extraction of experimental rotational strengths is very labor intensive. A transparent measure for the agreement, such as the calculation of similarities is undemanding and straightforward and would be desirable. To verify the validity of the proposed quality measure, other compounds should be thoroughly tested.

8.4.5 Conclusion

Based on a thorough conformational search performed at DFT/6-31G* level it could be observed that the 6-31G* basis set is unable to describe the PES unambiguously for (*S*)-**3**, as the number of minima and the relative energies were particularly functional dependent. The cc-pVTZ conformational description, however, gave a uniform conformational picture over all applied functionals. IR and VCD spectra were simulated using this large cc-pVTZ basis set and nine hybrid functionals, calculating dipole and rotational strengths for each located minimum.
Based on both measures, that is, the correlation between experimental and theoretical rotational strengths and the newly introduced differential *S*/*R* neighborhood similarities, it can be seen that three functionals perform very good in predicting rotational strengths for **3** applying the cc-pVTZ basis set. B1LYP, B3LYP and B98 give the highest R_{exp}/R_{theo} correlations and largest differential *S*/*R* neighborhood similarities. The B3PW91, B3P86 and MPW1PW91 also perform very well, but giving intermediate R_{exp}/R_{theo} correlations. The intermediate performance is also illustrated by the differential neighborhood similarity. The BHandHLYP and PBE1PBE give the lowest R_{exp}/R_{theo} correlations mainly due to the wrongly predicted rotational strengths for an intense band.
All tested functionals are found capable of predicting rotational strengths for **3**, except the BHandH functional. The reliability of B1LYP, B3LYP, and B98 rotational strengths is higher than for B3P86, B3PW91, BHandLYP, PBE1PBE and MPW1PW91.

8.4.6 Supplementary material index

For this paragraph Supplementary Material is provided. It can be downloaded from http://www.quantum.UGent.be/tksup.pdf

Table S8.6 DFT/6-31G* conformational description **3**
Table S8.7 DFT/cc-pVTZ fundamental assignment tables
Figure S8.5 Simulated (*S*)-(+)-**1** IR DFT/cc-pVTZ spectra for different functionals and experimental spectrum.
Figure S8.6 Simulated (*S*)-(+)-**1** VCD DFT/cc-pVTZ spectra for different functionals and experimental spectrum.

8.5 Summary

In this chapter, two chiral carboxylic acid compounds and a methyl-ester derivative were studied with the aid of VCD spectroscopy and DFT calculations. The formation of stable carboxylic acid cyclic dimers has a large influence on the vibrational properties of carboxylic acids, which was clearly visible in the vibrational spectra. A wealth of information could be obtained by measuring the IR, but more important, the VCD, because of its conformational sensitivity and differential nature. By modeling the dimer conformations, and simulating IR and VCD spectra, these experimental spectra could be interpreted.

For compound **1** it could be established that next to cyclic dimers, also monomers are present at the concentration range that was studied. For compound **2**, monomer concentrations were found to be low, and spectra could be simulated on the basis of cyclic dimer conformations. The absolute configuration of this compound was assigned this way. The reason for compound **1**, that the monomer concentrations in solution are higher compared to compound **2**, is because of the stabilizing intra-molecular hydrogen bonding for a number of monomers.

Compound **3**, the methyl-ester of compound **1**, was studied and it was shown that a simple esterification can eliminate the self-association difficulties. This compound was thoroughly analyzed, applying different density functionals. The reliability of the B1LYP, B3LYP and B98 functionals was found the highest for the calculation of rotational strengths.

Additionally, a new method for the evaluation of the agreement between experimental and simulated spectra was introduced, i.e., the differential *S*/*R* neighborhood similarity. This measure looks very promising and will be the main topic of the last chapter.

8.6 Reference list

1. Kollman, P. A.; Allen, L. C. *Chem. Rev.* **1972**, *72*, 283-303.
2. Patai, S. *The Chemistry of acid derivatives;* Wiley: New York, **1992**.
3. Wolfs, I.; Desseyn, H. O. *J. Mol. Struc. (THEOCHEM)* **1996**, *360*, 81-97.
4. He, J. T.; Polavarapu, P. L. *J. Chem. Theory Comput.* **2005**, *1*, 506-514.
5. He, J. T.; Polavarapu, P. L. *Spectrochim. Acta A* **2005**, *61*, 1327-1334.
6. Fujima, Y.; Hirayama, Y.; Ikunaka, M.; Nishimoto, Y. *Tetrahedron-Asymmetr.* **2003**, *14*, 1385-1391.
7. Ishigura, M.; Nishihara, T.; Tanaka, R. *Yakugaku Zasshi* **2001**, *121*, 915-927.
8. Hoffman-Roberts, H. L.; Babcock, E. C.; Mitropoulos, I. F. *Expert Opin. Invest. Drugs* **2005**, *14*, 973-995.
9. Ayers, P. W.; Yang, W. Density-functional theory. In *Computational medicinal chemistry for drugs discovery*, Bultinck, P., De Winter, H., Langenaeker, W., Tollenaere, J. P., Eds.; Marcel Dekker, Inc.: New York, **2004**; pp 89-118.
10. Cheeseman, J. R.; Frisch, M. J.; Devlin, F. J.; Stephens, P. J. *Chem. Phys. Lett.* **1996**, *252*, 211-220.
11. Devlin, F. J.; Stephens, P. J.; Cheeseman, J. R.; Frisch, M. J. *J. Phys. Chem. A* **1997**, *101*, 9912-9924.
12. Stephens, P. J.; Ashvar, C. S.; Devlin, F. J.; Cheeseman, J. R.; Frisch, M. J. *Mol. Phys.* **1996**, *89*, 579-594.
13. Aamouche, A.; Devlin, F. J.; Stephens, P. J. *J. Am. Chem. Soc.* **2000**, *122*, 2346-2354.
14. Devlin, F. J.; Stephens, P. J.; Scafato, P.; Superchi, S.; Rosini, C. *Tetrahedron-Asymmetr.* **2001**, *12*, 1551-1558.
15. Dyatkin, A. B.; Freedman, T. B.; Cao, X. L.; Dukor, R. K.; Maryanoff, B. E.; Maryanoff, C. A.; Matthews, J. M.; Shah, R. D.; Nafie, L. A. *Chirality* **2002**, *14*, 215-219.

16. Kuppens, T.; Langenaeker, W.; Tollenaere, J. P.; Bultinck, P. *J. Phys. Chem. A* **2003**, *107*, 542-553.

17. Kuppens, T.; Vandyck, K.; Van der Eycken, J.; Herrebout, W.; van der Veken, B. J.; Bultinck, P. *J. Org. Chem.* **2005**, *70*, 9103-9114.

18. Wang, F.; Polavarapu, P. L. *J. Phys. Chem. A* **2000**, *104*, 1822-1826.

19. Stephens, P. J. Vibrational circular dichroism spectroscopy: A new tool for the stereochemical characterization of chiral molecules. In *Computational medicinal chemistry for drugs discovery*, Bultinck, P., De Winter, H., Langenaeker, W., Tollenaere, J. P., Eds.; Marcel Dekker, Inc.: New York, **2004**; pp 699-725.

20. Nafie, L. A. *Appl. Spectrosc.* **2000**, *54*, 1634-1645.

21. Kuppens, T.; Bultinck, P.; Langenaeker, W. *Drug Discovery Today: Techn.* **2004**, *1*, 269-275.

22. Lewell, X. Q.; Hillier, I. H.; Field, M. J.; Morris, J. J.; Taylor, P. J. *J. Chem. Soc. Faraday Trans. II* **1988**, *84*, 893-898.

23. Devlin, F. J.; Stephens, P. J. *J. Am. Chem. Soc.* **1999**, *121*, 7413-7414.

24. Wang, F.; Polavarapu, P. L.; Lebon, F.; Longhi, G.; Abbate, S.; Catellani, M. *J. Phys. Chem. A* **2002**, *106*, 12365-12369.

25. Cappelli, C.; Corni, S.; Mennucci, B.; Cammi, R.; Tomasi, J. *J. Phys. Chem. A* **2002**, *106*, 12331-12339.

26. Wang, F.; Polavarapu, P. L. *J. Phys. Chem. A* **2000**, *104*, 10683-10687.

27. Urbanova, M.; Setnicka, V.; Devlin, F. J.; Stephens, P. J. *J. Am. Chem. Soc.* **2005**, *127*, 6700-6711.

28. Cervinka, O.; Bajanzulyn, O.; Fabryova, A.; Sackus, A. *Collect. Czech. Chem. Commun.* **1986**, *51*, 404-407.

29. Urbanova, M.; Setnicka, V.; Volka, K. *Chirality* **2000**, *12*, 199-203.

30. Spectrogon AB, Taeby, Sweden - www.spectrogon.com

31. Aamouche, A.; Devlin, F. J.; Stephens, P. J.; Drabowicz, J.; Bujnicki, B.; Mikolajczyk, M. *Chem.-Eur. J.* **2000**, *6*, 4479-4486.

32. Frisch, M. J.; Trucks, G. W.; Schlegel, H. B.; Scuseria, G. E.; Robb, M. A.; Cheeseman, J. R.; Montgomery Jr, J. A.; Vreven, T.; Kudin, K. N.; Burant, J. C.; Millam, J. M.; Iyengar, S. S.; Tomasi, J.; Barone, V.; Mennucci, B.; Cossi, M.; Scalmani, G.; Rega, N.; Petersson, G. A.; Nakatsuji, H.; Hada, M.; Ehara, M.; Toyota, K.; Fukuda, R.; Hasegawa, J.; Ishida, M.; Nakajima, T.; Honda, Y.; Kitao, O.; Nakai, H.; Klene, M.; Li, X.; Knox, J. E.; Hratchian, H. P.; Cross, J. B.; Bakken, V.; Adamo, C.; Jaramillo, J.; Gomperts, R.; Stratmann, R. E.; Yazyev, O.; Austin, A. J.; Cammi, R.; Pomelli, C.; Ochterski, J. W.; Ayala, P. Y.; Morokuma, K.; Voth, G. A.; Salvador, P.; Dannenberg, J. J.; Zakrzewski, V. G.; Dapprich, S.; Daniels, A. D.; Strain, M. C.; Farkas, O.; Malick, D. K.; Rabuck, A. D.; Raghavachari, K.; Foresman, J. B.; Ortiz, J. V.; Cui, Q.; Baboul, A. G.; Clifford, S.; Cioslowski, J.; Stefanov, B. B.; Liu, G.; Liashenko, A.; Piskorz, P.; Komaromi, I.; Martin, R. L.; Fox, D. J.; Keith, T.; Al-Laham, M. A.; Peng, C. Y.; Nanayakkara, A.; Challacombe, M.; Gill, P. M. W.; Johnson, B.; Chen, W.; Wong, M. W.; Gonzalez, C.; Pople, J. A. *Gaussian03*, Revision B5; Gaussian, Inc.: Wallingford CT, **2004**.

33. Becke, A. D. *J. Chem. Phys.* **1993**, *98*, 5648-5652.

34. Lee, C. T.; Yang, W. T.; Parr, R. G. *Phys. Rev. B-Condens. Matter* **1988**, *37*, 785-789.

35. Stephens, P. J.; Devlin, F. J.; Chabalowski, C. F.; Frisch, M. J. *J. Phys. Chem.-US* **1994**, *98*, 11623-11627.

36. Sander, W.; Gantenberg, M. *Spectrochim. Acta A* **2005**, *62*, 902-909.

37. Sadlej, J.; Dobrowolski, J. C.; Rode, J. E.; Jamroz, M. H. *Phys. Chem. Chem. Phys.* **2006**, *8*, 101-113.

38. Frisch, A. E.; Frisch, M. J.; Trucks, G. *Gaussian 03 User's Reference;* 5th ed.; Gaussian, Inc.: Pittsburgh, **2003**.

39. Ditchfield, R. *Mol. Phys.* **1974**, *27*, 789-807.

40. Stephens, P. J. *J. Phys. Chem.-US* **1987**, *91*, 1712-1715.

41. McQuarrie, D. A. *Statistical Thermodynamics;* Harper and Row: New York, **1973**.

42. Hehre, W. J.; Radom, L.; Schleyer, P. R.; Pople, J. A. *Ab initio molecular orbital theory;* Wiley: **1986**.

43. Allinger, N. L.; Yuh, Y. H.; Lii, J. H. *J. Am. Chem. Soc.* **1989**, *111*, 8551-8566.

44. Allinger, N. L.; Chen, K. S.; Lii, J. H. *J. Comput. Chem.* **1996**, *17*, 642-668.

45. Halgren, T. A. *J. Comput. Chem.* **1996**, *17*, 490-519.

46. Cremer, D.; Pople, J. A. *J. Am. Chem. Soc.* **1975**, *97*, 1354-1358.

47. Wu, A.; Cremer, D. *J. Phys. Chem. A* **2003**, *107*, 1797-1810.

48. Fernandez, L. E.; Marigliano, A. C. G.; Varetti, E. L. *Vib. Spectrosc.* **2005**, *37*, 179-187.

49. Eliason, T. L.; Havey, D. K.; Vaida, V. *Chem. Phys. Lett.* **2005**, *402*, 239-244.

50. Kuppens, T.; Herrebout, W.; van der Veken, B. J.; Corens, D.; De Groot, A.; Doyon, A.; Van Lommen, G.; Bultinck, P. *Chirality* **2006**, *18*, 609-620.

51. Yu, Y. B.; Privalov, P. L.; Hodges, R. S. *Biophys. J.* **2001**, *81*, 1632-1642.

52. Chen, J. S.; Wu, C. C.; Kao, D. Y. *Spectrochim. Acta A* **2004**, *60*, 2287-2293.

53. Zhao, C. X.; Polavarapu, P. L. *Biospectroscopy* **1999**, *5*, 276-283.

54. Antony, J.; von Helden, G.; Meijer, G.; Schmidt, B. *J. Chem. Phys.* **2005**, *123*, 014305

55. Janssens, F. E.; Sommen, F.; De Boeck, B.; Benoit, C.; Leenaerts, J. E. WO A2 2004056799, 2003.

56. Nafie, L. A. *Appl. Spectrosc.* **1996**, *50*, A14-A26.

57. Stephens, P. J.; Devlin, F. J. *Chirality* **2000**, *12*, 172-179.

58. Freedman, T. B.; Cao, X. L.; Dukor, R. K.; Nafie, L. A. *Chirality* **2003**, *15*, 743-758.

59. Bélanger, P. C.; Williams, H. W. R. *Can. J. Chem.* **1983**, *61*, 1383-1386.

60. Freedman, T. B.; Cao, X. L.; Oliveira, R. V.; Cass, Q. B.; Nafie, L. A. *Chirality* **2003**, *15*, 196-200.

61. Setnicka, V.; Urbanova, M.; Bour, P.; Kral, V.; Volka, K. *J. Phys. Chem. A* **2001**, *105*, 8931-8938.

62. Woon, D. E.; Dunning, T. H. *J. Chem. Phys.* **1993**, *98*, 1358-1371.

63. Kendall, R. A.; Dunning, T. H.; Harrison, R. J. *J. Chem. Phys.* **1992**, *96*, 6796-6806.

64. Wong, M. W. *Chem. Phys. Lett.* **1996**, *256*, 391-399.

65. Scott, A. P.; Radom, L. *J. Phys. Chem.-US* **1996**, *100*, 16502-16513.

66. Wang, F.; Polavarapu, P. L. *J. Phys. Chem. A* **2000**, *104*, 6189-6196.

67. McCann, J. L.; Rauk, A.; Wieser, H. *Can. J. Chem.* **1998**, *76*, 274-283.

68. Nevins, N.; Chen, K. S.; Allinger, N. L. *J. Comput. Chem.* **1996**, *17*, 669-694.

69. Cremer, D.; Pople, J. A. *J. Am. Chem. Soc.* **1975**, *97*, 1358-1367.

70. Ashvar, C. S.; Devlin, F. J.; Bak, K. L.; Taylor, P. R.; Stephens, P. J. *J. Phys. Chem.-US* **1996**, *100*, 9262-9270.

71. Buffeteau, T.; Ducasse, L.; Brizard, A.; Huc, I.; Oda, R. *J. Phys. Chem. A* **2004**, *108*, 4080-4086.

72. Schellman, J. A. *Chem. Rev.* **1975**, *75*, 323-331.

73. He, J. T.; Petrovich, A.; Polavarapu, P. L. *J. Phys. Chem. A* **2004**, *108*, 1671-1680.

74. De Gelder, R.; Wehrens, R.; Hageman, J. A. *J. Comput. Chem.* **2001**, *22*, 273-289.

9

neighborhood based enantiomeric similarity index

9.1 Introduction

The reliability of AC determinations using the VCD methodology unmistakably depends on the quality of the experimental data and the performance of the DFT calculations. If the compounds provided are enantiomerically pure and the VCD baseline correction can be performed, the obtained spectra should be of very high quality. This is not always the case, however. Samples of chiral compounds can contain small concentrations of impurities and the compounds can also have a lower or unknown enantiomeric excess. Racemic mixtures or both enantiomers are not always available, which ultimately results in less accurate baselines. At the other

end, basis set size, choice of density functional, numerical integration grid size, etc. can have an influence on the usability of the simulated spectra. In addition, if an important conformation is not found during the conformational search, this would a major pitfall.

Taking into account the argumentation from above, the following question can be raised: What is the reliability of an AC assignment using the VCD methodology and can one quantify the quality of an assignment?
Up until now, very few studies are published that discus the criteria to assess whether a reliable prediction can be made. In Reference 1, D. Minick explains the quality assessment at GlaxoSmithKline; "The key to confident predictions at GSK is the value of the […] coefficients of correlation between the intensities of 10–15 corresponding bands in the calculated and measured spectra. Our assignments are considered reliable if r^2 is at least 90%".

In Chapter 4 it was already established that there are different ways to quantify the agreement between the experimental and simulated spectra. The most reliable method, but very time consuming and not transparent, is to determine the correlation between experimental and theoretical rotational strengths. A neighborhood similarity measure was introduced that allows a more transparent quantification of the agreement.

The central problem in AC determination is the capacity to distinguish between two enantiomers.[2] A new quantity was therefore introduced (see §8.3) on the basis of neighborhood similarity, in which the agreement is assessed between the experimental VCD and the simulated spectra of both enantiomers. Only one compound was tested using this differential neighborhood similarity measure (methyl tetrahydrofuran-2-carboxylate).[3]
In this chapter, the main objective is to test the differential neighborhood similarity measure for its applicability in enantiomeric discrimination and whether it can be used to quantify the confidence of an assignment. First, a comprehensive overview is given of this newly proposed quantity and new terminology and symbols are introduced. In what follows, a set of 21 compounds is presented that will be used for the evaluation of the proposed neighborhood similarity measure.

9.2 Enantiomeric similarity index

The neighborhood similarity (NS) was introduced in Chapter 4 in Equation (4.17). This similarity measure does not only takes into account the overestimation of the calculated frequencies via a scaling factor σ, but also deals with the local shift of bands. The latter is done using correlation functions and a triangular weighting function. Equation (4.17) is for convenience reintroduced in this chapter,

$$S^{\sigma} = \frac{\int w_{fg}(r) c^{\sigma}_{fg}(r) dr}{\sqrt{\int w_{ff}(r) c^{\sigma}_{ff}(r) dr \int w_{gg}(r) c^{\sigma}_{gg}(r) dr}} \tag{9.1}$$

with

$$\begin{aligned} w(r) &= 1 - \frac{|r|}{l} && if\, |r| < l \\ w(r) &= 0 && if\, |r| \geq l \end{aligned} \tag{9.2}$$

and the correlation functions defined as

$$c^{\sigma}_{fg}(r) = \int f(\sigma\nu) g(\nu + r) d\nu \tag{9.3}$$

The NS is a quantity within the interval [0, 1]. The optimization of S^{σ} is carried out by searching the optimal σ through scaling of the vibrational frequencies of the theoretical spectrum $f(\nu)$. When evaluating S^{σ} for corresponding IR and VCD data, their maximizing scaling factor σ^{opt} is slightly different, in the order of 1 or 2%. This difference is expected, as the S/N ratio in the VCD spectra is considerably higher than in the IR. Therefore, the scaling factor for theoretical frequency scaling we use, is determined by optimizing S^{σ} for the experimental and theoretical IR spectra. The latter is denoted by $S^{\sigma}(\mathrm{IR})_{\max}$ and the scaling factor is abbreviated as $\sigma^{opt,IR}$. In the same way, $S^{\sigma}(\mathrm{VCD})_{\max}$ and $\sigma^{opt,VCD}$ can be defined.

For VCD purposes, $\overline{f}(\nu)$ can be defined as the perfect mirror image spectrum of $f(\nu)$. From a more practical approach it can be said that if $f(\nu)$ represents the

spectrum of modeled compound and $\overline{f}(\nu)$ represents the simulated spectrum of the opposite enantiomer. $S^{\sigma}(\mathrm{VCD})$ and $\overline{S}^{\sigma}(\mathrm{VCD})$ can be calculated for respectively $f(\nu)$ and $\overline{f}(\nu)$ and the experimental spectrum $g(\nu)$ for a specific scaling factor. If the frequencies of $f(\nu)$ and $\overline{f}(\nu)$ are both scaled with $\sigma^{\mathrm{opt,IR}}$, $S^{\sigma}(\mathrm{VCD})$ and $\overline{S}^{\sigma}(\mathrm{VCD})$ give a measure for the agreement between the experimental VCD and the simulated VCD spectra for both enantiomers separately. $S^{\sigma}(\mathrm{VCD})$ and $\overline{S}^{\sigma}(\mathrm{VCD})$ with $\sigma = \sigma^{\mathrm{opt,IR}}$ will be denoted further respectively as V and $\overline{V}$, the VCD NS.
If it is assumed now, that the measurement and simulation of the spectra can be regarded as reliable, the simulated VCD spectrum for one enantiomer should have a good agreement with the experimental VCD, whilst the spectrum of the opposite enantiomer should hardly show any agreement, that is, should have intensities with opposite sign. This is the basis of the enantiomeric discrimination potential of VCD. This should consequently be reflected in the values of the VCD NS, i.e., V and $\overline{V}$; one should be significantly lower than the other. The difference between both VCD NS, that is, ΔV is defined as the enantiomeric similarity index (ESI),

$$\Delta V = V - \overline{V} \tag{9.4}$$

The ESI is limited to the interval [−1, 1]. A positive ESI indicates that $f(\nu)$ has a better agreement with $g(\nu)$, a negative ESI signifies that $\overline{f}(\nu)$ has a better agreement with $g(\nu)$. The absolute value of ΔV gives a measure for the enantiomeric discrimination power. High absolute values of ΔV indicate that one of the enantiomeric spectra has a significantly better agreement with the experimental spectrum $g(\nu)$ compared to the other. Low absolute values give no information and indicate that both $f(\nu)$ and $\overline{f}(\nu)$ have a comparable agreement with $g(\nu)$.

In the next section, the newly proposed ESI will be screened for its applicability and validity using a set of 21 compounds.

9.3 Results

In Figure 9.1 and Table 9.1 an overview of the set of 21 compounds is given which are utilized to test the functionality and validity of the ESI. For each compound the conformational behavior was thoroughly studied, and IR and VCD spectra were

simulated at different levels of theory. For most compounds these details can be found in the previous chapters. Compounds (e),(m)–(s) are not discussed in detail in this dissertation, but spectra and additional information can be found in the Appendix. Details of compounds (i)–(l) were not integrated in this thesis, but can be found in Reference 4. An overview of references is provided in Table 9.1. Except for compounds (a),(g),(m)–(s), all the experimental spectra were measured ourselves.

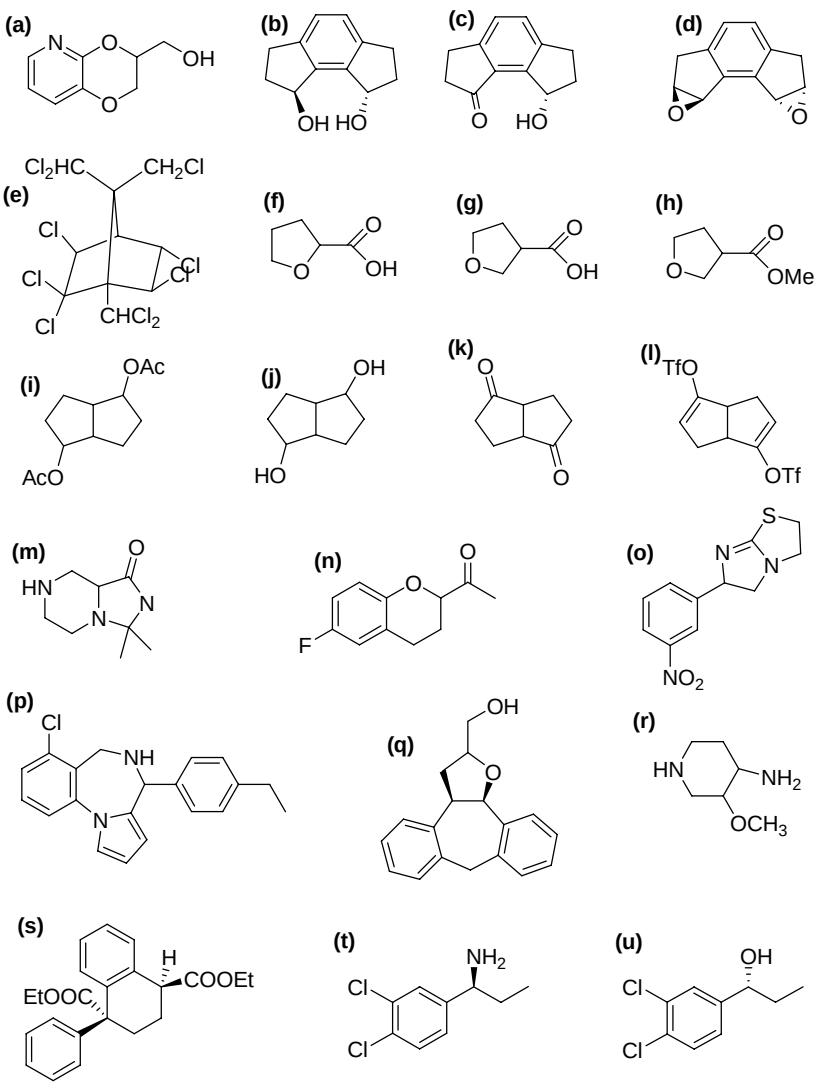

Figure 9.1 Overview of the set of compounds that is used to test the enantiomeric similarity index.

Table 9.1 names and labels for the set of compounds given in Figure 9.1, with references.

	Compound name	Reference
a	3-hydroxymethyl-2,3-dihydro-[1,4]dioxino[2,3-*b*]pyridine	Chapter 5, Ref. 5
b	1,2,3,6,7,8-Hexahydro-*as*-indacene-1,8-diol	Chapter 6, Ref. 6
c	8-Hydroxy-3,6,7,8-tetrahydro-2H-as-indacen-1-one	Chapter 6, Ref. 6
d	1,2,7,8-di-epoxy-3,6-dihydro-as-indacene	Chapter 6, Ref. 6
e	2,2,3-*exo*,5-*endo*,6-*exo*,8,9,9,10,10-decachlorobornane	Appendix, Ref. 7
f	tetrahydrofuran-2-carboxylic acid	Chapter 8, Ref. 8
g	tetrahydrofuran-3-carboxylic acid	Chapter 8
h	methyl tetrahydrofuran-2-carboxylate	Chapter 8, Ref. 3
i	bicyclo[3.3.0]octane-2,6-bisacetate	Ref. 4
j	bicyclo[3.3.0]octane-2,6-diol	Ref. 4
k	bicyclo[3.3.0]octane-2,6-dion	Ref. 4
l	bicyclo[3.3.0]octane-2,6-dieen-bisvinylic-triflate	Ref. 4
m	3,3-Dimethyl-hexahydro-imidazo[1,5-alpha]pyrazin-1-one	Appendix, Ref. 9
n	1-(6-fluorochroman-2-yl)ethanone	Appendix, Refs. 10,11
o	2,3,5,6-tetrahydro-6-(3-nitrophenyl)-imidazo[2,1-*b*]thiazole	Appendix, Ref. 12
p	1-Chloro-8-ethyl-5,6-dihydro-4-phenyl-4H-pyrrolo[1,2-a][1,4]benzodiazepine	Appendix, Refs. 13,14
q	11-fluoro-3,3a,8,12b-tetrahydro-2*H*-dibenzo[3,4:6,7]cyclohepta[1,2-*b*]furan-2-methanol	Appendix, Refs. 15-17
r	3-methoxypiperidin-4-amine	Appendix, Refs. 18,19
s	diethyl1-phenyl-1,2,3,4-tetrahydronaphthalene-1,4-dicarboxylate	Appendix, Ref. 20
t	1-(3',4'-dichlorophenyl)-propanamine	Chapter 7, Ref. 21
u	1-(3',4'-dichlorophenyl)-propanol	Chapter 7, Ref. 21

For the calculation of the NS, the window size l of the triangular weighting function is taken as 40 cm^{-1} (see Chapter 4). In Table 9.2, the results for the different descriptors are given for the 21 compounds in our set. Default, the B3LYP functional and the 6-31G* basis set are used. If different basis sets and/or density functionals were used, this is mentioned. For compound (a), various DFT integration

grids were applied in combination with B3LYP/6-31G* level of theory. If not mentioned, the (75,302)p grid is used. Compounds (f) and (g) are carboxylic acids, and to simulate spectra for these molecules, dimers should be taken into account. More details can be found in Chapter 8.

For each simulated spectrum, the maximized IR NS $S^{\sigma}(\mathrm{IR})_{\max}$ with experiment was determined. This yielded the scaling factor ($\sigma^{\mathrm{opt,IR}}$) which was applied to determine the VCD NS between experiment and simulation for both enantiomers, i.e., V and $\overline{V}$. Here, $f(\nu)$ was chosen as the spectrum that corresponds to the enantiomer with the same AC as the measured compound; $\overline{f}(\nu)$ corresponds with the enantiomer with opposite AC.

Table 9.2 NS based descriptors for 21 compounds at different levels of approximation, i.e., $S^{\sigma}(\mathrm{IR})_{\max}$, $\sigma^{\mathrm{opt,IR}}$, V, $\overline{V}$ and ΔV or ESI (in percent). When not specified, the B3LYP functional with 6-31G* basis set and (75,302)p integration grid is used.

		$S^{\sigma}(\mathrm{IR})_{\max}$	$\sigma^{\mathrm{opt,IR}}$	V	$\overline{V}$	ΔV ESI
a	6-31G*	95.4	0.969	83.6	12.3	71.3
	6-31G**	96.5	0.970	83.6	11.9	71.7
	6-311G**	96.4	0.981	85.7	11.5	74.2
	cc-pVDZ	96.7	0.977	81.6	15.5	66.1
	cc-pVTZ	96.9	0.979	89.7	15.2	74.5
	(35,110)p	95.1	0.971	80.4	14.3	66.1
	(50,194)p	95.4	0.969	83.4	12.1	71.3
	(50,194)p	95.4	0.969	84.0	12.0	72.0
	(50,302)	95.4	0.969	83.9	12.3	71.6
	(75,194)	95.4	0.969	83.1	12.0	71.1
	(75,302)p	95.4	0.969	83.6	12.3	71.3
	(75,434)	95.4	0.969	83.3	12.5	70.8
	(99,302)	95.7	0.969	83.8	13.5	70.3
b	cc-pVTZ	97.2	0.977	79.5	11.8	67.7
	B1LYP	93.8	0.955	76.7	14.3	62.4
	B3LYP	93.6	0.961	75.6	14.6	61.0
	B3P86	90.8	0.944	73.0	26.8	46.2
	B3PW91	91.3	0.947	74.5	24.2	50.3
	B98	92.8	0.958	79.0	17.1	61.9
	BHandH	85.6	0.900	52.2	40.9	11.3
	BHandHLYP	91.4	0.908	75.7	21.8	53.9
	MPW1PW91	90.6	0.936	71.9	27.8	44.1
	PBE1PBE	90.4	0.928	61.8	34.9	26.9
c	cc-pVTZ	93.9	0.966	80.7	11.9	68.8
	B1LYP	91.3	0.945	73.6	11.9	61.7
	B3LYP	92.0	0.952	74.3	12.4	61.9
	B3P86	91.7	0.942	62.6	14.7	47.9
	B3PW91	91.6	0.943	62.9	14.9	48.0
	B98	89.4	0.944	64.6	13.8	50.8
	BHandH	59.4	1.063	23.0	44.2	−21.2
	BHandHLYP	87.1	0.900	62.4	14.8	47.6

	MPW1PW91	91.1	0.932	59.4	16.0	43.4
	PBE1PBE	90.8	0.931	56.6	17.3	39.3
d	cc-pVTZ	94.6	0.975	80.8	19.9	60.9
	B1LYP	89.5	0.957	63.3	26.5	36.8
	B3LYP	89.8	0.963	66.2	25.7	40.5
	B3P86	90.4	0.964	64.9	20.8	44.1
	B3PW91	90.4	0.964	65.0	21.5	43.5
	B98	91.5	0.967	68.2	25.8	42.4
	BHandH	87.0	0.934	55.9	22.8	33.1
	BHandHLYP	87.9	0.927	48.2	26.8	21.4
	MPW1PW91	89.9	0.959	60.9	21.5	39.4
	PBE1PBE	89.7	0.962	60.5	20.0	40.5
e		91.7	0.998	75.6	44.7	30.9
f	6-31++G**	90.3	0.983	76.0	26.4	49.6
	aug-cc-pVTZ	87.2	0.976	84.1	22.3	61.8
g	6-31++G**	93.8	0.967	51.1	46.5	4.6
h	B1LYP	84.4	0.968	76.6	24.0	52.6
	B3LYP	82.6	0.975	75.3	24.7	50.6
	B3P86	84.6	0.960	55.8	29.8	26.0
	B3PW91	83.2	0.962	54.1	28.6	25.5
	B98	84.0	0.966	65.2	23.9	41.3
	BHandH	81.0	0.904	44.4	40.0	4.4
	BHandHLYP	87.6	0.920	65.5	25.4	40.1
	MPW1PW91	83.9	0.951	50.4	30.0	20.4
	PBE1PBE	83.0	0.950	45.7	32.1	13.6
i (*RRSR*)		75.3	0.980	57.9	29.7	28.2
i (*RSSS*)		75.3	0.978	52.8	39.8	13.0
i (*RSSR*)		75.1	0.980	59.0	31.9	27.1
i (*SSSS*)		75.6	0.977	32.7	52.6	−19.9
j (*SRRS*)		95.4	0.967	76.8	25.3	51.5
j (*SRRR*)		91.7	1.037	45.4	25.7	19.7
j (*RRRR*)		88.3	1.044	34.3	28.2	6.1
j (*RRSR*)		86.1	1.013	24.3	40.5	−16.2
k		92.5	0.945	56.1	32.6	23.5
l		81.1	0.966	78.0	20.1	57.9
m	6-31G*	87.0	0.931	40.2	30.1	10.1
	cc-pVTZ	94.6	0.989	74.4	23.6	50.8
n		78.7	0.968	78.6	15.0	63.6
o	6-31G*	79.4	0.949	65.4	43.9	21.5
	cc-pVTZ	82.8	0.965	68.5	29.1	39.4
p		95.9	0.971	88.2	36.5	51.7
q	6-31G*	94.1	0.965	82.4	22.3	60.1
	cc-pVTZ	96.3	0.976	86.4	25.2	61.2
r		97.8	0.963	77.1	39.0	38.1
s		96.9	0.983	79.0	17.2	61.8
t	cc-pVTZ	93.1	0.978	85.1	12.3	72.8
u	cc-pVTZ	93.1	0.979	90.3	13.0	77.3

9.3.1 Scaling factor

In this approach, the IR NS global maximum is determined by scaling the calculated frequencies. From Table 9.2, the influence of the basis set size on the calculated frequencies becomes immediately clear through the IR scaling factor. For larger basis sets the scaling factor is closer to unity than for smaller basis sets. The applied functional even has a larger influence on the calculated frequencies. It can be expected that in some cases over-scaling occurs when aligning the patterns of two spectra.

An example is the BHandH/6-31G* spectrum for compound (c). A maximized IR NS is found for a scaling factor of 1.063. A local minimum can be found near σ = 0.955, which is more likely for a frequency scaling factor, with VCD NS of 45.3% and 20.2%. Irregular scaling factors can also be found for the diastereomers for compound (j): the diastereomer that configurationally corresponds to the experimentally measured compound gives a scaling factor of 0.967, whilst the other diastereomers yield substantially higher values all above unity. As can be seen in Figure 9.6, the three diastereomers with the high scaling factors have completely different IR characteristics compared to the configuration *SRRS*. This will be discussed further in Paragraph 9.3.5.

For compound (e) (spectra can be found in the Appendix, Figure A8 and Figure 9.4), it can be seen that uniform frequency scaling sometimes does not work very well, i.e., aligning experimental and theoretical spectra. Using the $S^{\sigma}(\mathrm{IR})_{\max}$ approach, the most intense IR profiles will always be aligned, sometimes without regard for the smaller IR bands. In Paragraph 9.3.4, this will be discussed in more detail.

Performing the scaling by maximizing the IR NS is certainly not flawless. It maximizes the neighborhood overlap between two spectra without any chemical correlation. For hybrid functionals the uniform scaling factor is found to reside between 0.9 and 1.0. However, nothing guarantees that the global minimum of $S^{\sigma}(IR)$ is found within that range, unless the optimization procedure forces the value of σ to fall within 0.90 and 1.00. In our routine, however, we do not impose this tight restriction, and let σ vary between 0.90 and 1.30. This method gives mostly good results, in cases were experimental and simulated spectra have a good agreement. If the scaling factor is higher than expected, this should give a indication that something could be wrong.

9.3.2 Basis set

The cc-pVTZ basis set is regarded as superior to the smaller 6-31G* basis set when calculating rotational strengths. This does not mean that this smaller basis set is unusable, to the contrary: the 6-31G* basis set provides usable rotational strengths at a much lower computational cost than the cc-pVTZ basis set. The ESI should be able to reflect the basis set effect, i.e., for a certain compound, ΔV should be higher for better performing basis sets. For compound (a), 5 different basis sets were applied in combination with the B3LYP functional. The cc-pVTZ and 6-311G** basis sets gives the highest ESI. The lowest value can be found for the cc-pVDZ basis set, yielding a value lower than the 6-31G* ESI. In Figure 9.2 it can be seen that this is probably due to a underestimated intensity of the positive band near 1240 cm^{-1}.

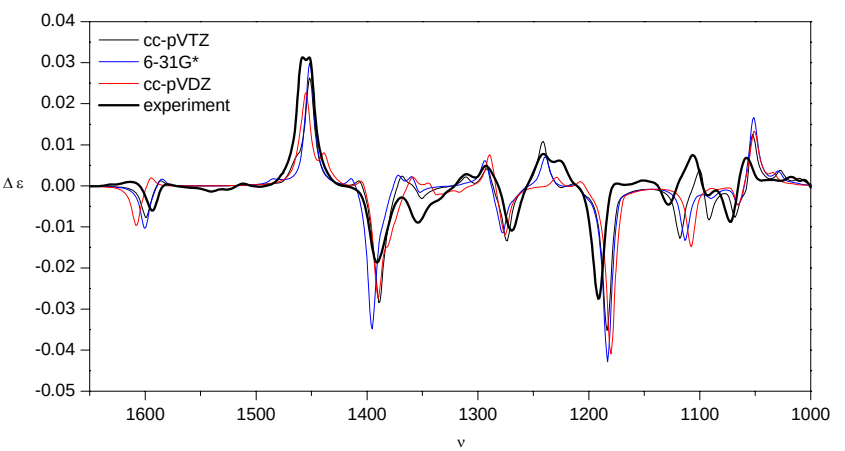

Figure 9.2 B3LYP spectra for three basis sets (cc-pVTZ, 6-31G* and cc-pVDZ) and experimental VCD.

For the other compounds for which cc-pVTZ spectra are available, it can be seen that the obtained ΔV values are all higher than the 6-31G* values. For compound (m) the difference between the 6-31G* and cc-pVTZ is rather large, which is due to the scaling factor 0.931, which is probably too small for the 6-31G* basis set. The quality of the experimental spectra is also somewhat less, which makes the comparison more difficult anyway. The spectra for compound (m) are depicted in Figure A.1 in the Appendix.

For this set of compounds, it seems that the ESI is able to quantify the performance of the basis sets for the calculation rotational strengths.

9.3.3 Functional

In literature, local, non-local and hybrid functionals, specifically LSDA, BLYP, B3LYP and B3PW91[22-26] were mostly studied. Very few explorations of hybrid functionals in the context of VCD simulations are found. Devlin et al. mention very briefly that the B3P86 and B3PW91 functionals "have given extremely similar vibrational spectra".[26]
Similarly as for the basis set, the density functionals can evaluated for a given compound. Calculations were performed on four compounds, using a series of hybrid functionals all available in Gaussian03, i.e., B1LYP, B3LYP, B3P86, B3PW91, B98, BHandH, BHandHLYP, MPW1PW91 and PBE1PBE in combination with the 6-31G* basis set. In Figure 9.3 the ΔV values are depicted for the four compounds. Here, it can be seen that B3LYP and B1LYP have very similar values for ΔV. Also B3P86 and B3PW91 perform similar. This is in agreement with the findings of Devlin et al. The remainder of the functionals do not seem to have any mutual correspondence.

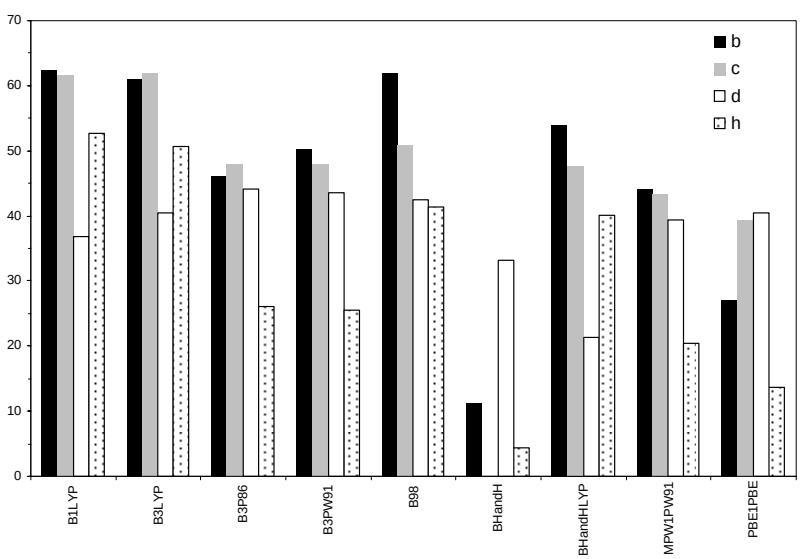

Figure 9.3 ESI for different hybrid functionals and 4 compounds. For compound c, the BHandH/6-31G* ESI value is negative (off-scale).

In a study performed on compound (h)[3], the B3LYP, B1LYP and B98 functionals were found to perform better than the other functionals, based on the correlation between experimental and theoretical rotational strengths. The same conclusion could be formulated based on the ESI, ΔV, also given in Figure 9.3. The only discrepancy found was for the BHandHLYP functional, for which the R_{exp}/R_{theo} correlation coefficient was small (44%) compared to the relatively high value for ΔV. The BHandH functional was found to yield unusable VCD spectra.
For the three other compounds, it can be seen in Figure 9.3 that the B3LYP and B1LYP functionals yield the highest ΔV values. For compound (d), the ESI is more or less 6% lower than the B3P86, B3PW91 and B98 functionals, which yield the highest ΔV values. The BHandH functional clearly gives a low ESI, and for compound (c) ΔV is found to be negative which indicates that the spectrum of the other enantiomer has a higher similarity with the experimental VCD than the spectrum of 'correct' enantiomer (actually when using the a local optimum scaling factor of 0.955 an ESI of 25.1% is found). For the other functionals it can be seen that the value for ΔV depends on the compound and not much conclusions can be drawn from these data.
Based on the ESI, it could be concluded that the B3LYP and B1LYP functionals perform best in the calculation of rotational strengths. However, more compounds should be processed to generalize this conclusion.

9.3.4 Absolute configuration assignment and quality

For the set of 21 compounds the AC were assigned after thorough analysis (assignment of fundamentals) of the agreement between experimental an simulated IR and VCD spectra. An interesting and still open question is if NS measures, and more precisely the ESI, can be used to assign absolute configurations. If the proposed NS measure, i.e., $S^{\sigma}(\mathrm{VCD})$, is reliable enough to quantify the agreement between experimental and simulated VCD spectra, one can argue that this measure can be used to assign the AC of the measured compound. The enantiomer with the highest $S^{\sigma}(\mathrm{VCD})$ has consequently the same absolute configuration as the measured compound. In this argumentation, of course, it is assumed that theory and experimental spectra are of high quality.
Because the spectrum $f(\nu)$ for the 21 compounds tested, was chosen to correspond to the enantiomer having the same AC as the measured compound, each compound in the set should have a positive ESI. If ΔV would be negative, it would mean that

based on the VCD NS, the spectrum corresponding to the opposite (wrong) enantiomer would have a higher resemblance to the experimental spectrum then $f(\nu)$, based on the NS measure.

For all compounds, (i) and (j) not included (this is a case of diastereomers and will be discussed further), it can be seen that, for a reliable level of theory, a positive ESI is found. This indicates that the enantiomeric similarity index can indeed be used for an indicator for the assignment of ACs.

Some prudence is of course advised: this set only counts 21 compounds and it is not our intention to generalize this conclusion to other compounds without further testing on a larger set. Also, above it was already found that for a better performing basis set, larger values can be found for the enantiomeric similarity index. This was also found more or less for functionals, especially the bad performing (for 4 compounds) BHandH which gives a negative ESI.

It is, however, rather difficult to pass a judgment on the quality of the performed experiment. Low S/N ratios and deviating baselines are indicators for spectra with lower reliability. Do these effects show in the ESI for a certain compound? Is the ESI lower when the quality of the spectra is questionable?

Compound (e) is modeled at the B3LYP/6-31G* level and has only one significant conformation. This compound has a low VCD signal, and combined with small sample amounts available, the VCD spectrum has a high S/N ratio as can be seen in Figure A8 in the Appendix and Figure 9.4. The VCD baseline was estimated using a racemic mixture. For this compound, a relatively low ESI is observed. One can argue that this low ESI is due to the bad uniform scaling, as mentioned earlier. However, when only the 1100–800 cm^{-1} region is analyzed, in which experiment and simulation are perfectly aligned with a $\sigma^{opt,IR} = 0.999$, the ESI only rises 1%, i.e., 31.7%.

Another example in which interfering experimental effects occur is solvent-solute or solute-solute interaction. It is not a routine practice to take these kind of effects into account. In case of carboxylic acids it is absolutely necessary to take the intermolecular association into regard as stable dimers can be formed.[8,27] For compound (g) (see §8.3), the dimeric spectrum was modeled and compared to the experimental spectrum. Agreement can be seen between experiment and theory when carboxylic acid dimers are considered and assigning fundamentals (Figures 8.16 and 8.17) However, a small ESI is found, i.e., 4.6%. Can we conclude from this value that the reliability from this assignment is not high? Whatever the case may be, the spectra are simulated on the basis of cyclic dimer conformation, not accounting for the monomers. The low ESI may be an indication that monomer

conformation should be accounted for. For compound (f) (see §8.2), also a carboxylic acid, the simulation of the spectra was more elaborated, taking into account dimers and monomers, using semi-qualitative populations. For these simulated spectra an ESI of 49.6% was found.

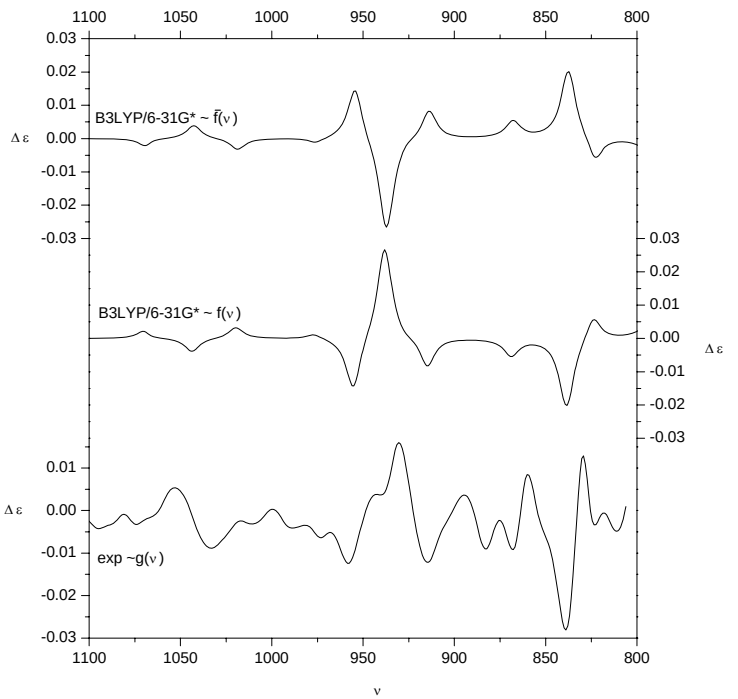

Figure 9.4 Experimental $g(\nu)$ and B3LYP/6-31G* simulated spectra $\overline{f}(\nu)$ and $f(\nu)$ for compound (e) in the 1100–800 cm^{-1} window. Calculated frequencies were scaled with a factor 0.999.

The B3LYP/cc-pVTZ VCD NS for compound (u) are very different from each other, i.e., 90.3% and 13.0%, yielding a ESI of 77.3% In Figure 7.6 the VCD spectra are given. The R_{exp}/R_{theo} correlation coefficient for this compound was determined to be is 91%. Compound (t) has a lower correlation coefficient, i.e., 66%. This lower correlation was attributed to three fundamentals, which lower the correlation (for both dipole and rotational strengths) drastically. If these are discarded a R_{exp}/R_{theo} correlation of 91% can be found. The ESI for this compound is 72.8%.

Other compounds for which a correlation was made between experimental and theoretical values of dipole and rotational strengths are compounds (b), (c) and (d) which are structurally related to each other. These compounds have respectively a R_{exp}/R_{theo} correlation coefficient of 53%, 64% and 38% comparing B3LYP/cc-pVTZ

data to experimental data. From Table 9.2 it can be seen that the ESI for these compounds is respectively 67%, 68% and 60%.

Above examples indicate that if the experimental and simulated spectra are of good quality, the ESI is relatively high. If the experimental spectrum has a somewhat lower quality, or the level of theory used is somewhat inferior, the ESI gives lower values. This could indicate that the ESI has the ability to quantify the agreement, i.e., may be used as an indicator for the reliability of the AC assignment. Again, we do not want generalize this conclusion to other compounds and further testing is needed.

9.3.5 Diastereomer assignment

From the above it can be seen that the ESI is a measure that has the potential to discriminate between enantiomers. Can the ESI also be used for diastereomer discrimination?

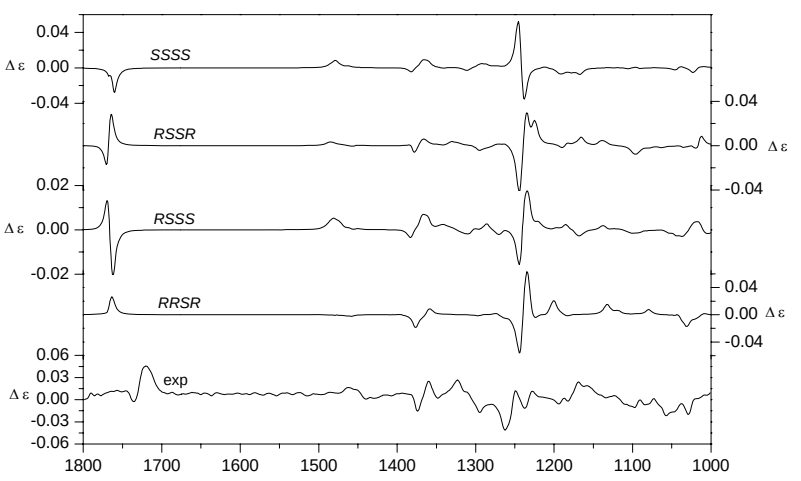

Figure 9.5 Simulated B3LYP/6-31G* VCD spectra for 4 diastereomers and experimental spectrum for compound (i). Theoretical frequencies are scaled with a factor 0.98.

For compounds (i) and (j), the different diastereomers were studied. Due the C_2 symmetry present in both compounds, there are only 4 optically active isomers. For each compound, the IR and VCD spectra were simulated for all optical active diastereomers. Based on thorough analysis of experimental and simulated spectra

and the assignment of fundamentals, we were able to determine the correct absolute configuration of the compound, i.e., the correct enantiomer and diastereomer for compound (i) and (j).[4]
In Figures 9.5 and 9.6 the experimental and simulated VCD spectra are given for both compounds and the different diastereomeric configurations.

For compound (i), the visual agreement between experiment and the simulated VCD spectra is not very good. The AC for compound (i) was assigned as *RSSR*.[4] The ESI for the *RRSR*, *RSSS*, *RSSR* and *SSSS* are respectively (Table 9.2) 28.2%, 13.0%, 27.1% and −19.9%. The configurations with the highest ESI are *RRSR* and *RSSR*. Configuration *RRRR* (enantiomer of SSSS, the *RRRR* spectrum is not shown in Figure 9.5) has a value of 19.9% which is significantly lower. If the spectra of *RRSR* and *RSSR* are compared in Figure 9.5 then it seems that the large features are very similar apart from the CO stretch band. Based on their ESI it is not possible to identify the correct configuration for this compound, and a thorough analysis is needed that identifies each band for 1:1 comparison.
The ESI measure identifies that the enantiomer of *SSSS*, that is, *RRRR* (mirror image VCD spectrum) has a relative good similarity with the experiment. Indeed, the large features near 1250 cm^{-1} and the CO stretch band of the *RRRR* VCD spectrum agree with the experimental spectrum (however, differences for smaller bands allows to discard this configuration in the assignment).

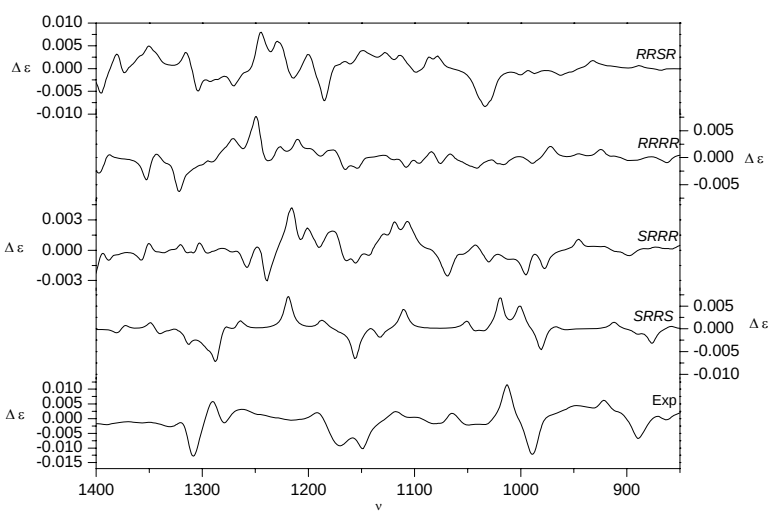

Figure 9.6 Simulated B3LYP/6-31G* VCD spectra for 4 diastereomers and experimental spectrum for compound (j). Theoretical frequencies are scaled with a factor 0.967.

For compound (j), a relative good agreement can be seen between experiment and configuration *SRRS*. This is also being reflected in the ESI value, i.e., for configurations *SRRS*, *SRRR*, *RRRR* and *RRSR* values are respectively 51.5%, 19.7%, 6.1% and −16.2%. The highest ESI value agrees with the diastereomer with the correct configuration. As stated above, the optimal scaling factors are found larger than 1. Local optima (restricting σ within 0.90 and 1.00) for these three configurations are given in Table 9.3 which gives the same picture.

Table 9.3 Local maxima for $S^{\sigma}(\mathrm{IR})$ for the three configurations *SRRR*, *RRRR* and *RRSR*.

	$S^{\sigma}(\mathrm{IR})$	σ^{IR}	V	$\overline{V}$	ESI
j (*SRRR*)	83.1	0.923	38.5	52.1	−13.6
j (*RRRR*)	80.8	0.923	34.9	41.6	−6.1
j (*RRSR*)	84.5	0.999	38.8	38.9	−0.1

9.4 Conclusion

The assignment of the AC based on one descriptor can be very dangerous, certainly if there is no chemical correlation involved. Even if this descriptor is thoroughly tested for a very large set of compounds, artifacts or problems can arise which ultimately can result in assigning the wrong absolute configuration. In this study, a method was proposed that can help to facilitate the assignment of ACs. When the experimental and simulated IR and VCD spectra are provided, the optimization and evaluation of neighborhood similarity is very transparent and within a few seconds the evaluation can be performed. The results from this analysis should not be taken as a general truth; in combination with the assignment of the bands based on IR data and ultimately the correlation between experimental and theoretical rotational strengths the neighborhood similarity measure can help in the AC assignment process.

When the question comes from an organic chemist or the pharmaceutical industry, to determine an absolute configuration of a compound they synthesized, it is reassuring that one has multiple methods that objectively can assign the AC. Still missing today is a measure that allows one to report a value of certainty that the proposed AC based on the VCD assignment is the correct one. The method that we propose based on neighborhood similarity, is hopefully a step in the right direction, allowing the quantification of the reliability of the assignment, but still work has to be done to refine this measure.

9.5 Reference list

1. Rouhi, A. M. *Chem. Eng. News* **2005**, *83*, 32-33.

2. Flack, H. D.; Bernardinelli, G. *Acta. Crystallogr. A* **1999**, *55*, 908-915.

3. Kuppens, T.; Vandyck, K.; Van der Eycken, J.; Herrebout, W.; van der Veken, B. J.; Bultinck, P. *Spectrochim. Acta A* **2006**, In press.

4. Debie, E.; Kuppens, T.; Vandyck, K.; Van der Eycken, J.; van der Veken, B. J.; Herrebout, W.; Bultinck, P. Submitted to *Tetrahedron-Asymmetr.* **2006**

5. Kuppens, T.; Langenaeker, W.; Tollenaere, J. P.; Bultinck, P. *J. Phys. Chem. A* **2003**, *107*, 542-553.

6. Kuppens, T.; Vandyck, K.; Van der Eycken, J.; Herrebout, W.; van der Veken, B. J.; Bultinck, P. *J. Org. Chem.* **2005**, *70*, 9103-9114.

7. Kruchkov, F. A.; Kuppens, T.; Kolehmainen, E.; Nikiforov, V. A. *Organohalogen Compounds* **2006**, *68*. In press.

8. Kuppens, T.; Herrebout, W.; van der Veken, B. J.; Bultinck, P. *J. Phys. Chem. A* **2006**, *100*, 10191-10200.

9. Van Daele, G. EP 68544, 1982.

10. Lesage, A.; Bischoff, F. P.; Janssen, C.; Lavreysen, H. WO 2003082350, 2003.

11. Mabire, D.; Venet, M. G.; Coupa, S.; Poncelet, A. P.; Lesage, A. WO 2002028837, 2001.

12. Janssen, P. A. J.; Heeres, J.; Lewi, P. J.; Vlaminck, K.; Ottevaere, P.; Vanparijs, O. WO 2006079642, 2006.

13. Gilkerson, T.; Nash, R.; Van Gestel, J.; Meerpoel, L. WO 2002034752, 2001.

14. Meerpoel, L.; Van Gestel, J.; Van Gerven, F.; Woestenborghs, F.; Marichal, P.; Sipido, V.; Terence, G.; Nash, R.; Corens, D.; Richards, R. D. *Bioorg. Med. Chem. Lett.* **2005**, *15*, 3453-3458.

15. Cid-Nunez, J. M.; Megens, A.; Trabanco-Suarez, A. A.; Koukni, M.; Hoornaert, G.; Compernolle, F.; Kozlecki, T.; Mao, H.; Jha, S. C.; Fernandez-Gadea, F. J. WO 2006061392, 2005.

16. Mao, H.; Kozlecki, T.; Compernolle, F.; Hoornaert, G. WO 2003048147, 2002.

17. Lang, Y. L.; Medaer, B.; Hoornaert, G.; Brossette, T.; Compernolle, F.; Guillaume, M.; Mao, H.; Kozlecki, T. WO 2003048146, 2002.

18. De Knaep, A.; Moens, L.; Rey, M. WO 9816511, 1997.

19. Van Daele, G.; Bosmans, J. P.; Van Laerhoven, W. US 5674868, 1995.

20. Moehrle, H.; Pycior, M.; Wendisch, D. *Pharmazie* **1992**, *47*, 8-10.

21. Kuppens, T.; Herrebout, W.; van der Veken, B. J.; Corens, D.; De Groot, A.; Doyon, A.; Van Lommen, G.; Bultinck, P. *Chirality* **2006**, *18*, 609-620.

22. Ashvar, C. S.; Devlin, F. J.; Bak, K. L.; Taylor, P. R.; Stephens, P. J. *J. Phys. Chem.-US* **1996**, *100*, 9262-9270.

23. Devlin, F. J.; Stephens, P. J.; Cheeseman, J. R.; Frisch, M. J. *J. Phys. Chem. A* **1997**, *101*, 9912-9924.

24. Devlin, F. J.; Finley, J. W.; Stephens, P. J.; Frisch, M. J. *J. Phys. Chem.-US* **1995**, *99*, 16883-16902.

25. Stephens, P. J.; Devlin, F. J.; Ashvar, C. S.; Chabalowski, C. F.; Frisch, M. J. *Faraday Discuss.* **1994**, *99*, 103-119.

26. Devlin, F. J.; Stephens, P. J.; Cheeseman, J. R.; Frisch, M. J. *J. Phys. Chem. A* **1997**, *101*, 6322-6333.

27. He, J. T.; Polavarapu, P. L. *J. Chem. Theory Comput.* **2005**, *1*, 506-514.

summary and conclusions

The primary aim of this research has been the development of a transparent methodology for the measurement and calculation of vibrational circular dichroism (VCD) spectra with the purpose of absolute configuration assignments of chiral molecules in organic synthesis, medicinal chemistry and pharmaceutical industry.

The first compound that was examined was hydroxymethyl dihydrodioxinopyridine. This study was the first investigation on the applicability of VCD absolute configuration determination in Belgium. The experimental measurements for this compound were performed by Bruker Optics. In Chapter 5, the basis set dependence was explored, and the outcome was that the 6-31G* is a practicable basis set, but when exact rotational strengths are needed, the cc-pVTZ basis set should be used. The numerical integration grid size was also thoroughly tested, which resulted in the conclusion that the SG1 grid produces very similar spectra compared to the *finegrid*, with a computational cost reduction of approximately 30%. However, the rotational invariance was lost. No further efforts were taken to investigate the applicability of sparser grids, because additional calculations showed that the rotational invariance could not be preserved.

The first measurements that were performed on our own VCD spectrometer are described in Chapter 6. A good agreement was observed between the measured and the simulated spectra for three *as*-hydrindacene compounds. On the basis of these agreements and after thorough analysis of the spectra, their absolute configuration could be assigned. For hexahydro-*as*-indacenediol and hydroxy-tetrahydro-*as*-indacenone the absolute configurations were previously determined by other methods and the absolute configuration of di-epoxy-dihydro-*as*-indacene was

previously unknown. Our absolute configurations based on VCD for the first two compounds were in agreement with the known absolute configurations.

In parallel to the previous assignments and following studies, multiple absolute configurations determinations were performed for Johnson & Johnson Pharmaceutical Research and Development (JNJPRD), and are partially listed in the Appendix. Two compounds, studied under the agreement between JNJPRD and Ghent University were published and presented in Chapter 7. The studied compounds, i.e. dichlorophenyl-propanol and dichlorophenyl-propanamine are successive precursors of a potent CCR2 receptor antagonist. The antagonist itself was too large to handle, and would not give as reliable results as the analysis of a smaller precursor molecule. Here, two successive precursors were available in enantiopuric form to assign the absolute configurations of both compounds.
This scheme was only possible because no racemization occurs in the synthesis path. The analysis of both compounds, and their corresponding vibrational spectra were a real challenge, because many significant minima were found, which should all be accounted for in order to explain all experimental bands. Ultimately, this resulted in a highly reliable assignment of the absolute configurations of the alcohol and amine derivative, and therefore also absolute configuration of the CCR2 receptor antagonist.

For tetrahydrofuran-3-carboxylic acid, a compound that was studied for JNJPRD, the simulated IR and VCD showed no agreement with experiment. Because non-polar solvents are used to eliminate significant solvent interaction with the solute molecules, solvent effects could be ruled out. Also, the applied level of theory was proven to be very reliable. Therefore a different explanation had to be found. As it is known that carboxylic acids in solutions form strong hydrogen-bonded cyclic dimers, the dimers of tetrahydrofuran-3-carboxylic acid were modeled. Simulated vibrational spectra for these dimer geometries showed good agreement with experiment.
This result directed the research to the investigation of tetrahydrofuran-2-carboxylic acid. The simulation of spectra for this compound was a real challenge, as neither the dimer nor the monomer structures yielded spectra that were in agreement with experiment. It soon became clear that both monomers and dimers were present in solution. Due to the relative position of the carboxylic acid moiety with respect to the tetrahydrofuran oxygen, intramolecular hydrogen bonding was possible, which stabilized two monomer geometries considerably. Consequently, both monomers

and dimers should be taken into account. To obtain usable populations for the monomer and dimer conformations, a semiquantitative model was proposed. This yielded rational values for the populations, which gave spectra in relative good agreement with experiment.
Further investigations on this compound were performed by converting the carboxylic acid in a methyl ester. For this compound, i.e., methyl-tetrahydrofuran-2-carboxylate, it was shown that no problems arose with respect to intermolecular associations. Additionally, a systematic study to investigate the performance of the available hybrid functionals in Gaussian03 was performed. B3LYP, B1LYP and B98 proved to be the most reliable for the calculation of rotational strengths for this compound.

An important objective of this thesis has been the development of a method allowing transparent and reliable comparison of computed IR and VCD spectra.
This started with the introduction of the scaled and normalized overlap integral for experimental and calculated spectra (Chapter 5). However, the main problem with this method is that the inherent differences between experimental and theoretical spectra can not be managed, that is, the local shift of vibrational bands for theory versus experiment. The next step was the introduction of neighborhood comparison, with the aid of cross-correlation functions and a triangular weighting function. A window size of 40 cm^{-1} was found ideal for the comparison of vibrational spectra. The main problem with this method is the choice of scaling factor. The values in Chapter 6 are achieved, using the maximizing overlap scaling factor. Further development yielded a neighborhood similarity measure that could be optimized by varying the scaling of the theoretical frequencies. Based on this neighborhood similarity measure, the enantiomeric similarity index (ESI) was introduced. This ESI is the difference between the VCD neighborhood similarities for opposite enantiomers for which the scaling factors are obtained by the maximization of the IR neighborhood similarity. The ESI was tested for 21 compounds (Chapter 9) and is shown to be very promising towards the quantification of the reliability of the absolute configuration assignment. Further testing on additional compounds and refinement of the ESI should be performed to confirm these results.

Roughly 30 compounds were analyzed for this thesis, and their absolute configurations were successfully assigned. Based on these results one could propose a transparent methodology or guidelines for absolute configuration determination.
Prior to presenting such guidelines, it is of utmost importance to stress that these guidelines can merely reflect a rough advice. They should never be considered as dogmatic, and it remains an important task for every user to establish whether or not these guidelines are likely to be acceptable. Failure to establishing this may result in poor determinations of absolute configuration, or even the wrong assignment. As such, the guidelines developed here should be considered only a first step. If any elements appear that suggest the necessity for a closer examination of the application of the guidelines, the VCD user should examine closely the source for any disagreement between theory and experiment. For instance, if bands with wrong sign are predicted, the user should question his/her own computational and experimental strategy and be prepared to go beyond the guidelines and improve e.g. basis sets, functionals, experimental setup, … VCD is not likely to become a black box technique, and experience in quantum chemistry techniques and experimental FTIR is essential.

The first step in the process of the AC determination using VCD is the assessment of the behavior of the studied compound in solution. One should have a good understanding of possible intermolecular associations of solute molecules or important solvent/solute interactions. If such interactions are expected, standard gas phase quantum chemical modeling techniques will not suffice and a careful computational and experimental setup should be planned. It may often happen that solvent models in the current state of the art will not sufficiently well describe solvent effects, or could come at a too high computational cost. In such an event, one could study a derivative of the molecule.
It was found that for the compounds studied in this thesis containing alcohol and amine functional groups, solvent effects and self-association does not have a large influence on the absolute configuration determination. For carboxylic acids it is adviced to analyse the corresponding methyl ester.

The conformational analysis should be performed using a systematic search on a sufficiently high level of theory, preferably B3LYP/6-31G*. For larger molecules this is not practical and it has been shown that the combination of molecular mechanics methods most often yields the same qualitative picture as the DFT search. The minima found during the molecular mechanics conformational search

should be optimized further on at least the B3LYP/6-31G* level of theory. A good understanding of the conformational behavior of the studied compound is of the utmost importance as the VCD signature of a molecule is found to be heavily dependent on the conformational properties!
The conformational analysis yields a list of all unique stationary points on the potential energy surface (PES). For each unique geometrie one should calculate the dipole and rotational strengths and vibrational frequencies, and one should check if all stationary points that were found are real minima. The B3LYP/6-31G* yields rotational strengths which are often good enough to be compared with experimental VCD intensities, but it has been shown that small differences can occur. The cc-pVTZ basis set yields better rotational strengths, but at a higher computational cost. It has also been shown that in some cases the B3LYP/6-31G* level of theory has problems describing the PES unambiguously.
IR and VCD spectra can be simulated based on these calculations, using free energies and Boltzmann statistics to determine the conformational populations.

A procedure for the measurement of the experimental VCD spectra on a Bruker PMA37 module can be found in §3.3. For this setup it is extremely important that high quality baselines are acquired by using both enantiomers or the racemic mixture. If these samples are not available, one can use the solvent to approximate the baseline. It goes without saying that the chiral samples should have a high enough enantiomeric excess to perform a reliable assignment.

The final step is the comparison of the experimental and simulated spectra. A method which is very tempting, is the superposition of both the theoretical and experimental spectra and *on sight* comparison. The reliability of this method is not very high, and one should use more elaborate techniques to compare experimental and theoretical spectra. The most reliable technique is to assign the bands in the experimental spectrum based on the fundamental spectrum which was simulated and estimate the area under the experimental bands. The main problem with this method is that it is very time consuming (4–8 hours per compound). The ESI is an alternative to this technique, which gives the same information in a few seconds. Both techniques give the scientist a measure that can be used to quantify the agreement and the reliability of the assignment.

The most important step in the simulation of reliable spectra is intermolecular association assessment and the conformational analysis. For all subsequent steps it

has been shown that they can be automated in a reliable way and little interaction is required. Using this methodology more than 95% of the compounds studied in this dissertation could be assigned.

That VCD has become a powerful method to study absolute configurations and conformational properties of chiral molecules in solution is certain. In Figure 1, an overview of the number of publications per year is presented and it can be seen that more and more scientists are becoming active in the field. Before 1996, most papers where on the fundamentals of FTIR VCD measurements and the theory of VCD intensities. The last 10 years, VCD papers began to appear in experimental and high impact journals e.g., Journal of the American Chemical Society, Journal of Organic Chemistry, Journal of Physical Chemistry, Tetrahedron, etc. More and more experimental scientists and pharmaceutical companies are using this technique combining quantum chemical and experimental expertise.

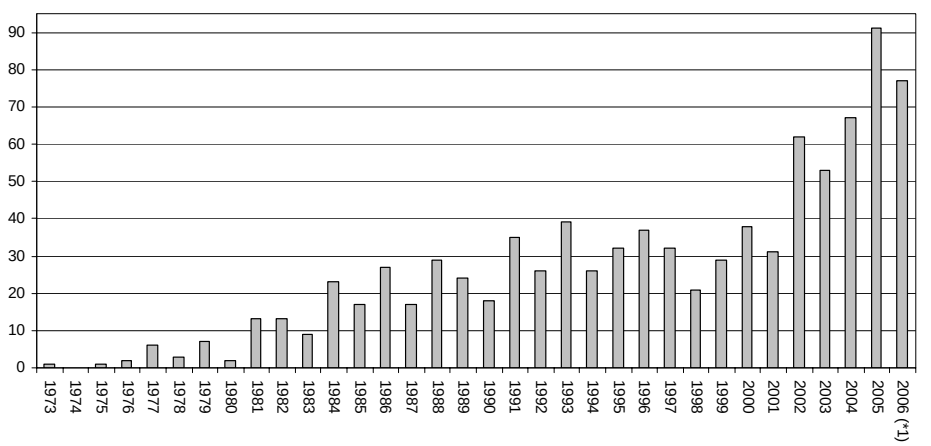

Figure 1 The number of annual publication of VCD related papers. [*1] the cited number for 2006 is incomplete (November 2006). (source: SciFinder Scholar database)

For this dissertation much energy was put in the development of a methodology that allows absolute configuration determination. There was absolutely no expertise on this subject in our laboratory. Currently, much experience has been gained, both on the experimentally and theoretically side. New computational standards were introduced on which VCD spectra can be assigned and analyzed even when the conformational behavior of the compounds is complex (see Chapter 7). Also new

insights were gained on the VCD of carboxylic acids and intermolecular interaction (see Chapter 8).

Based on the results of this dissertation, new and more fundamental questions can be raised. For example, can we perform low temperature measurements, which affect the conformational populations? More interesting is the influence of intermolecular interaction on the vibrational properties of the compounds. In this dissertation it was shown that this is a general problem. There are also indications that the $CDCl_3$ interaction with carbonyl containing compounds has a certain influence on the conformational and vibrational behavior. Further research is needed in this area.

samenvatting

1 Inleiding

De biologische activiteit van enantiomeren van chirale geneesmiddelen kan sterk verschillen. Vaak vertoont het ene enantiomeer een farmacologische activiteit, terwijl het andere minder actief of zelfs toxisch kan zijn. Het is bijgevolg uiterst belangrijk de biologische activiteit van specifieke enantiomeren in chirale geneesmiddelen te kennen. De onderzoeksinspanningen hiernaar zijn de laatste jaren sterk toegenomen, vooral gedreven door de snelle ontwikkeling van betere analyse- en scheidingstechnieken en verbeterde synthese routes voor chirale moleculen.
Een bedrijf of instelling dat wil overgaan tot klinische testen van een geneesmiddel, of dat zijn medicijn op de markt wil brengen, moet eerst een licentie bekomen bij de regulerende instanties. In de Verenigde Staten kan men zo'n licentie verkrijgen via een *New Drug Application* (NDA) bij de *Food and Drug Administration* (FDA). Men moet hiervoor een lijvig rapport samenstellen dat handelt over de actieve component. Voor chirale geneesmiddelen is natuurlijk ook de absolute configuratie van groot belang. Wanneer een farmaceutisch bedrijf zijn intellectuele eigendom op potentiële moleculen wil vrijwaren, dan ook moet de absolute configuratie gekend zijn.

De combinatie van de snel groeiende markt van chirale geneesmiddelen en de behoefte aan de kennis van de absolute configuratie van moleculen maakt dat er nood is aan toegankelijke methoden voor de bepaling van absolute configuraties.

Eenkristal x-straal diffractie is een zeer belangrijke techniek voor het bepalen van absolute configuraties. Deze techniek is echter niet altijd toepasbaar. Een vereiste is

dat de eenkristallen onderhevig zijn aan anomale verstrooiing. Voor standaard x-straal diffractie experimenten komt dit neer op de aanwezigheid van zware atomen.
Een andere methode, elektronisch circulair dichroïsme (ECD), is een vorm van UV/VIS-spectroscopie waarbij links- en rechtsdraaiend circulair gepolariseerd UV/VIS-licht op een verschillende wijze wordt geabsorbeerd door chirale moleculen. Deze methode kan enkel gebruikt worden wanneer de nodige chromofore groepen aanwezig zijn op de moleculen.
Andere methoden zijn nucleaire magnetische resonantie (NMR), optische rotatie en stereospecifieke synthese.
Een betrekkelijk nieuwe techniek is het vibrationeel circulair dichroïsme (VCD).

2 Vibrationeel circulair dichroïsme

Vibrationeel circulair dichroïsme is een techniek, die de structurele specificiteit van infraroodspectroscopie combineert met de stereochemische gevoeligheid van circulair dichroïsme. Het betreft de meting van de differentiële absorptie van circulair gepolariseerde infrarood straling. Deze methode heeft als voordeel dat de metingen op nagenoeg exact dezelfde manier kunnen gebeuren als infrarood experimenten, en dat ze dus relatief weinig eisen stellen aan de moleculen. Zo kunnen de VCD metingen ook in oplossingen gebeuren.
VCD is een zeer interessante techniek aangezien vibrationele transities in chirale moleculen de oorsprong zijn van de VCD-intensiteiten. Gewone IR-spectra bevatten echter geen stereochemische informatie aangezien IR-spectra van enantiomeren identiek zijn; de VCD-spectra zijn echter spiegelbeelden van elkaar (gespiegeld over de frequentie-as). Omdat VCD een differentiële spectroscopische techniek is, kunnen deze intensiteiten dus ook negatief zijn, waarbij de banden zijn gecentreerd op de vibrationele frequenties.

Experimentele spectra werden voor het eerst gerapporteerd in 1973 door Holzwarth et al. De implementatie van Fourier-getransformeerde VCD door Nafie et al. in 1979 en verdere ontwikkelingen van de instrumentatie, maakt dat we tegenwoordig hoge kwaliteit VCD-spectra kunnen opmeten voor de meeste chirale moleculen in oplossing.

De interpretatie en evaluatie van experimentele VCD-spectra is niet voor de hand liggend. In vergelijking met de klassieke infrarood spectroscopie komt er bij de verklaring van VCD-spectra nog een extra dimensie bij, met name het teken van de

VCD-intensiteiten. Deze zijn niet eenvoudig interpreteerbaar. Voor een bepaald enantiomeer zijn sommige banden positief en andere negatief zonder dat dit gemakkelijk kan worden gerationaliseerd. Het is in deze context dat de kwantumchemie een grote ondersteunende rol speelt.

In het midden van de jaren tachtig werd een theorie ontwikkeld die toelaat om ab initio VCD-intensiteiten te bereken. Deze theorie werd dan ook snel geïmplementeerd, gebruikmakend van Hartree-Fock theorie. De resultaten hiervan waren echter niet accuraat genoeg om vergelijking met experimentele resultaten toe te laten. Het gebruik van Møller-Plesset perturbatie theorie leverde wel goede resultaten, maar door de computationele vereisten was deze methode niet echt haalbaar.

De ontwikkeling van *density functional theory* (DFT) en de introductie van hybride functionalen in het begin van de jaren negentig, betekende een doorbraak voor de berekening van VCD-intensiteiten. Met behulp van DFT- en hybride-functionalen kunnen theoretische spectra van goede kwaliteit bekomen worden, in overeenstemming met experimentele waarnemingen en met rationele computationele kost.

3 Doelstelling van dit onderzoekswerk

De implementatie van de theorie voor het berekenen van VCD-intensiteiten op DFT niveau in het commercieel kwantumchemisch rekenpakket Gaussian en de commercialisering van VCD-spectrometers heeft ertoe geleid dat absolute configuratie bepaling d.m.v. VCD meer toegankelijk is geworden. Maar een grote doorbraak zal er enkel komen als ook de methode toegankelijker wordt gemaakt. Momenteel is de drempel voor het uitvoeren van kwantumchemische berekeningen nog te hoog voor niet theoretisch georiënteerde wetenschappers.

Het doel van deze thesis is de kracht van deze techniek te bevestigen en een methodologie te ontwikkelen die toelaat om op een transparante en toegankelijke wijze VCD-spectra te berekenen voor de absolute configuratie bepaling van chirale moleculen.
Deze doelstelling kan als volgt worden onderverdeeld:

- Optimalisatie van de berekening van VCD-spectra en het testen van de verschillende computationele parameters voor middelgrote tot grote moleculen.
- Inzicht verwerven in de metingen en interpretatie van VCD-spectra voor moleculen die typisch voorkomen bij organische synthese, in de medicinale chemie en in de farmaceutische industrie.
- Ontwikkelen van een methode die toelaat experimentele en theoretische spectra op een transparante en snelle manier te vergelijken.

4 Samenvatting van de resultaten en conclusie

De allereerste VCD absolute configuratie toewijzing in België werd gedaan voor hydroxymethyl-dihydro-dioxinopyridine (Figuur 1).

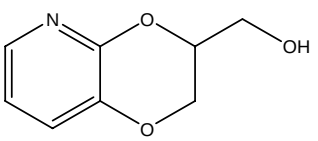

Figuur 1 3-hydroxymethyl-2,3-dihydro-[1,4]dioxino[2,3-*b*]pyridine

Uit deze studie is gebleken dat de 6-31G* basisset goede resultaten oplevert, i.e., een goede overeenkomst tussen theoretische en experimentele spectra. Betere resultaten werden behaald met de cc-pVTZ basisset. Het nadeel bij het gebruik van deze grote basisset is de computationele kost.
De eerste metingen op onze eigen VCD-spectrometer werden uitgevoerd op 3 verwante moleculen, i.e. hexahydro-*as*-indaceen-diol, hydroxy-tetrahydro-*as*-indacenon en di-epoxy-dihydro-*as*-indaceen (Figuur 2). De absolute configuratie van deze drie moleculen is bepaald aan de hand van hun gesimuleerd VCD-spectrum. Voor de eerste twee moleculen werden de absolute configuraties ook al via andere methoden bepaald. Deze waren in overeenstemming met de VCD resultaten. Voor de derde molecule was de absolute configuratie niet te bepalen via een andere methode.

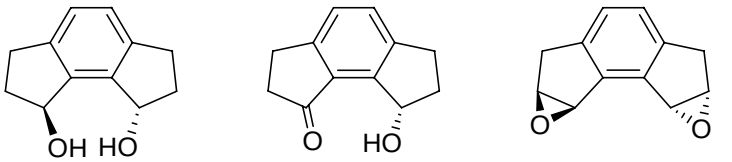

Figuur 2 1,2,3,6,7,8-hexahydro-*as*-indacen-1,8-diol, 8-hydroxy-3,6,7,8-tetrahydro-2*H*-*as*-indacen-1-on en 1,2,7,8-di-epoxy-3,6-dihydro-*as*-indaceen

In deze thesis werden eveneens absolute configuratie bepalingen gedaan voor 21 moleculen van *Johnson & Johnson Pharmaceutical R&D* (JNJPRD). Twee moleculen van deze lijst werden gepubliceerd, i.e. dichlorophenyl-propanol en dichlorophenyl-propaanamine (Figuur 3). Beide zijn opeenvolgende precursoren van een krachtige CCR2 receptor antagonist. Aangezien de moleculaire structuur van de antagonist te groot was om te behandelen, werden de absolute configuraties van de kleinere precursoren bepaald. Dit was mogelijk omdat er in de verdere synthese stappen geen racemisatie optreedt. De simulatie van de spectra werd gedaan op B3LYP/cc-pVTZ niveau en een goede overeenkomst met de experimentele spectra werd gevonden. Dit resulteerde in een betrouwbare toewijzing van de absolute configuratie van de twee precursoren en de eigenlijke CCR2 receptor antagonist.

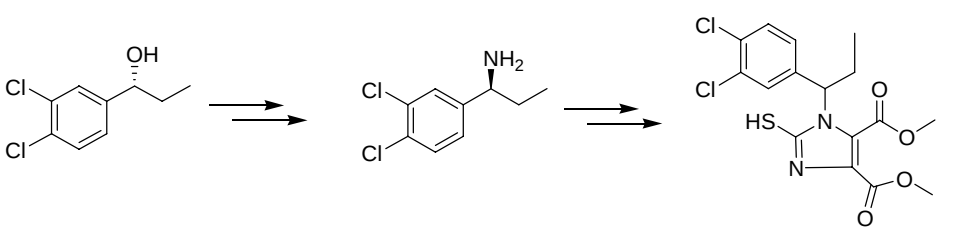

Figuur 3 Dichlorophenyl-propanol, dichlorophenyl-propaanamine en de CCR2 receptor antagonist.

Bij het opnemen van de experimentele spectra worden de te bestuderen moleculen meestal opgelost in apolaire solventen om een mogelijke interactie tussen solvent en opgelost product te vermijden. Voor tetrahydrofuran-3-carboxylzuur stelden we echter vast dat de gesimuleerde IR- en VCD-spectra geen overeenkomst vertoonden met de experimentele spectra. Dit verschil was blijkbaar te wijten aan zelfassociatie van het carbonzuur in de apolaire oplossing. Wanneer theoretische spectra werden gesimuleerd van gemodelleerde dimeer-structuren (Figuur 4), werd wel overeenkomst met het experiment gevonden.

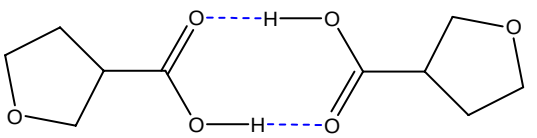

Figuur 4 Cyclische dimeer-structuur van tetrahydrofuran-3-carboxylzuur

Deze bevinding leidde het onderzoek naar een studie rond tetrahydrofuran-2-carbonzuur (Figuur 5). De simulatie van de VCD- en IR-spectra voor deze molecule was niet voor de hand liggend, omdat in dit geval noch de spectra voor het gesimuleerde monomeer, noch de dimeer-spectra overeen kwamen met de experimentele spectra. De conformationele eigenschappen van het 2-isomeer waren immers van die aard dat er stabiliserende intra-moleculaire waterstofbruggen gevormd konden worden in het monomeer. In oplossing was er dus zowel monomeer als dimeer aanwezig. Er werd een semi-kwantitatief model opgesteld om bruikbare conformationele populaties van het monomeer en dimeer te vinden. Op basis van dit model werden spectra gesimuleerd die een goede overeenkomst vertoonden met de experimentele spectra.

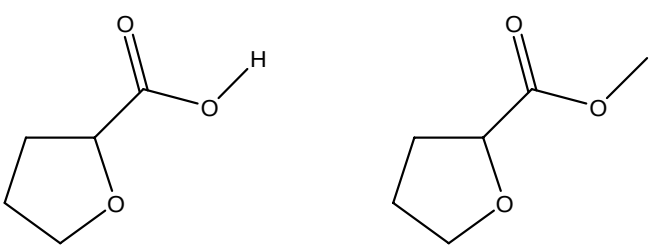

Figuur 5 Tetrahydrofuran-2-carbonzuur en het methyl-tetrahydrofuran-2-carboxylaat

In navolging van dit onderzoek werd er ook een studie uitgevoerd op het methylester van het 2-isomeer, i.e. methyl-tetrahydrofuran-2-carboxylaat (Figuur 5). Hieruit bleek dat er voor het methylester geen hinderlijke intermoleculaire associatie aanwezig was. Verder werd er ook een systematische studie uitgevoerd op verschillende hybride functionalen waaruit volgde dat de B3LYP, B1LYP en B98 functionalen de beste resultaten opleverden voor het simuleren van VCD-spectra.

In dit onderzoek werd ook een transparante methode voor het vergelijken van experimentele en theoretische spectra uitgewerkt.

De aanvankelijk voorgestelde maat voor similariteit van spectra was een genormaliseerde overlap integraal. Het grote probleem bij dergelijk type van vergelijkingen is het inherent verschil tussen experimentele en theoretische vibrationele spectra. De berekende vibrationele frequenties worden systematisch overschat. Hiervoor kan gedeeltelijk worden gecompenseerd via lineaire schaling, maar zelfs dan worden er nog steeds locale verschuivingen waargenomen tussen corresponderende experimentele en theoretische banden.
Om die reden werd een nieuwe maat voor similariteit ingevoerd die rekening houdt met de omgeving van de beschouwde banden door gebruik te maken van een genormaliseerde kruiscorrelatiefunctie en een driehoekige gewichtsfunctie. Deze omgevings-similariteitsmaat is natuurlijk afhankelijk van de frequentie schalings-factor. Verdere ontwikkeling stelde ons in staat om de omgevings-similariteit te optimaliseren door de schalingsfactor te variëren.
Op basis van deze omgevings-similariteitsmaat hebben we de enantiomerische similariteitsindex (ESI) geïntroduceerd. De ESI is het verschil tussen de VCD omgevings-similariteiten (t.o.v. het experimentele VCD) van beide enantiomeren. Deze ESI is getest voor 21 moleculen en de resultaten geven aan dat dit een veelbelovende maat is voor het kwantificeren van de betrouwbaarheid van een absolute configuratie bepaling.

Gedurende dit doctoraal onderzoek werden een dertigtal moleculen geanalyseerd, en hun absolute configuraties werden met succes toegewezen. Gebaseerd op de expertise die aldus werd opgebouwd en in dit werk naar voor komt, zou men een transparante methodologie en een set van richtlijnen voor absolute configuratie bepaling kunnen voorstellen. Deze richtlijnen zijn enkel bedoeld als leidraad en het moet benadrukt worden dat het aan de VCD-gebruiker is om in te schatten of deze richtlijnen voldoen voor het specifieke probleem. Het kan zijn dat er bij het volgen van deze richtlijnen elementen opduiken die wijzen op het feit dat er een verdergaande analyse nodig is. Zo kunnen er bijvoorbeeld banden worden voorspeld met een verkeerd teken. Het is aan de VCD-gebruiker om de relevantie van het probleem in te schatten en eventueel de experimentele en/of reken-strategie te herzien. Het is hoe dan ook noodzakelijk om een grondige expertise in de gebruikte kwantum chemische en experimentele FTIR-technieken te hebben.

De eerste stap in het proces van een absolute configuratie bepaling op basis van VCD is een grondige analyse van het gedrag van de molecule in oplossing. Het is zeer belangrijk dat men een goed zicht heeft op het intermoleculair associatiegedrag

van de opgeloste molecule onderling of van opgeloste molecule en solvent. Als dergelijke interacties te verwachten zijn, voldoen standaard kwantum chemische gas fase berekeningen vaak niet, en is een uitgebreidere modellering nodig, alsook verdere experimentele metingen. Men kan trachten het associatie gedrag te modelleren waarbij verscheidene modellen kunnen aangewend worden. Als blijkt dat deze modellen niet toereikend zijn of een te hoge rekentijd met zich meebrengen dan kan er eventueel worden overgegaan tot het derivatiseren van de molecule.
Voor de alcoholen en amines bestudeerd in dit werk zijn de solvent en zelfassociatie effecten niet significant gebleken voor de toepassing van absolute configuratie bepaling. Voor carbonzuren is het aangeraden om het corresponderende methylester te bestuderen.

De conformationele analyse zou op een zo hoog mogelijk niveau moeten gebeuren, bij voorkeur B3LYP/6-31G* niveau. Voor grotere moleculen is het praktischer om een combinatie van moleculair mechanische methoden te gebruiken. Een dergelijke aanpak geeft veelal hetzelfde conformationele beeld. De minima die gevonden worden gedurende een moleculair mechanische conformationele zoektocht zouden vervolgens geoptimaliseerd moeten worden op het B3LYP/6-31G* niveau. Gezien de conformationele gevoeligheid van VCD is een goed begrip van het conformationele gedrag van de bestudeerde molecule uiterst belangrijk.
Een conformationele analyse levert een lijst op met unieke stationaire punten op het potentiaal oppervlak. Voor alle unieke geometrieën moet men de dipool en rotationele sterktes berekenen samen met de vibrationele frequenties. Men moet zich er ook van vergewissen dat alle stationaire punten echte minima zijn. Het B3LYP/6-31G* krachtveld levert rotationele sterktes op die vergelijkbaar zijn met experimentele VCD-intensiteiten. In sommige gevallen worden er kleine verschillen geobserveerd. Het is ook aangetoond dat het B3LYP/6-31G* soms problemen heeft om het potentiaaloppervlak ondubbelzinnig te beschrijven. De cc-pVTZ basisset is een beter keuze, maar brengt dan ook langere rekentijden met zich mee.
IR- en VCD-spectra kunnen gesimuleerd worden op basis van deze berekening, gebruikmakend van vrije energieën en Boltzmann-statistiek om de conformationele populaties te berekenen.

Voor de meting van VCD verwijzen we naar §3.3 waar uitgebreid staat beschreven hoe men betrouwbare spectra kan bekomen op de PMA37 VCD-module van Bruker. Voor een dergelijke configuratie is het zeer belangrijk om een goede basislijn te bekomen gebruik makend van beide enantiomeren of het racemisch mengsel.

Wanneer deze niet voorhanden zijn kan men de basislijn benaderend bepalen met behulp van het solvent. De chirale samples moeten natuurlijk een voldoende hoge enantiomere overmaat hebben om een betrouwbare toewijzing te kunnen doen.

De finale stap is de vergelijking van experimentele en gesimuleerde spectra. Een voor de hand liggende maar onbetrouwbare methode is het op elkaar leggen van het experimentele en theoretische spectrum. De meest betrouwbare methode is het toewijzen van de experimentele banden op basis van het theoretische spectrum, en het bepalen van de oppervlakte onder de experimentele banden. Het probleem met deze methode is het arbeidsintensieve karakter, i.e., 4 tot 8 uur per molecule. De door ons ontwikkelde ESI is een alternatieve methode die dezelfde informatie geeft in enkele seconden. Beide technieken geven de gebruiker een maat van overeenkomst en betrouwbaarheid van de toewijzing.

De belangrijkste stap in de simulatie van VCD-spectra is de inschatting van mogelijke intermoleculaire associaties en de conformationele analyse. De stappen die hierop volgen werden allemaal geautomatiseerd waardoor de analyse niet veel interactie meer behoeft. Meer dan 95% van de moleculen bestudeerd voor deze thesis konden worden toegewezen gebruikmakend van de hierboven beschreven methodologie.

Het is duidelijk dat VCD een krachtige techniek is geworden om de absolute configuratie en conformationele eigenschappen van chirale moleculen in oplossingen te analyseren. Figuur 6 geeft de evolutie van het aantal VCD gerelateerde publicaties per jaar en hieruit blijkt dat de wetenschappelijke reikwijdte steeds groter wordt. De publicaties daterend vóór 1996 handelen voornamelijk over de theorie van VCD-intensiteiten en FTIR VCD. Gedurende de laatste tien jaar is de frequentie van VCD publicaties sterk toegenomen in tijdschriften met een hoge impact factor en experimentele tijdschriften zoals bijvoorbeeld *Journal of the American Chemical Society*, *Journal of Organic Chemistry*, *Journal of Physical Chemistry*, *Tetrahedron*, enz. De interesse vanuit de experimentele hoek en de farmaceutische industrie neemt sterk toe, waarbij de combinatie van de experimentele en kwantum chemische expertise goed tot uiting komt.

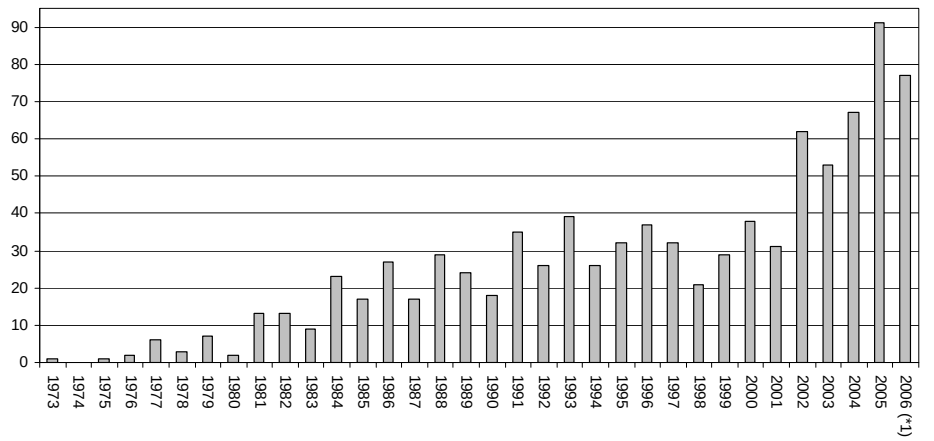

Figuur 6 Het jaarlijkse aantal VCD gerelateerde publicaties. Het geciteerde getal voor 2006 is onvolledig (november 2006). (bron: SciFinder Scholar database)

Gedurende dit werk werd veel aandacht en energie geïnvesteerd in de ontwikkeling van een methodologie voor absolute configuratie bepalingen. Immers, deze methode werd de onderzoeksgroep binnengehaald met dit doctoraatsonderzoek en state-of-the art expertise werd opgebouwd met als resultaat een aanzienlijk aantal publicaties in hoog gewaardeerde wetenschappelijke tijdschriften. Momenteel is zowel de experimentele als de theoretische expertise aanwezig en kunnen toekenningen op een relatief transparante wijze worden voltooid. Met dit werk werden ook nieuwe theoretische standaarden geïntroduceerd op basis waarvan de VCD-spectra kunnen worden toegekend en geanalyseerd, zelfs wanneer het conformationeel gedrag van de moleculen bijzonder complex is (zie Hoofdstuk 7). Er werden bovendien ook bijkomende inzichten verworven in de VCD analyse van carbonzuren en de optredende intermoleculaire interacties (zie Hoofdstuk 8).

Als resultaat van de kennisopbouw bij deze thesis, kunnen nieuwe fundamentele vragen gesteld worden. Zo is er bijvoorbeeld de bemerking of we lage temperatuur VCD analyses kunnen uitvoeren en welke invloed dit zal hebben op de conformationele populaties. Zoals ook naar voor komt in deze thesis is een systematische studie naar de invloed van intermoleculaire interacties op de vibrationele eigenschappen van moleculen van bijzondere interesse. Er zijn aanwijzingen dat de $CDCl_3$ interactie met de carbonyl groepen van een molecule een significante invloed hebben op de conformationele en vibrationele eigenschappen van de verbinding. Verder onderzoek in deze richting is nuttig en uiterst interessant.

Appendix

unreported AC assignments

Background

In the last quarter of 2003, an agreement was closed between Ghent University and Johnson & Johnson Pharmaceutical Research and Development (JNJPRD) in which was declared that Ghent Quantum Chemistry Group would perform the calculations and the actual assignments for AC determination based on VCD. These assignments involve drugs discovery compounds.

Until now, a total of 21 compounds were processed for JNJPRD. Due to intellectual property restrictions not all structures can be published in this dissertation. All successful assignments, for which the intellectual property rights have been secured, are given briefly in this appendix. Experimental and simulated spectra are presented together with additional information on measurement conditions and the structure, name and internal JNJ code.

The calculations were all performed using the B3LYP functional and the 6-31G* basis set. For some compounds also cc-pVTZ spectra were calculated. The figures are arranged in the following fashion,

(B3LYP/cc-pVTZ)
B3LYP/6-31G*
Experimental

The 6-31G* and cc-pVTZ frequencies are respectively scaled with a factor 0.967 and 0.980.

The last assignment in this chapter is an assignment performed for Prof. Dr. V. Nikiforov from the St. Petersburg State University. For this compound the absolute configuration determination was not possible nor with XRD nor with NMR methods.

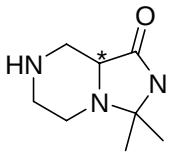

3,3-Dimethyl-hexahydro-imidazo[1,5-α]pyrazin-1-one
JNJ6202391
JNJ16927053

Origin	–	JNJPRD ref 1
Measurements	–	Performed by JNJPRD - Enantiomeric pure sample
Modeled configuration	–	*S*
Number of significant conformations	–	2
Spectra	–	No CO stretch spectra due to high absorbance in this region.

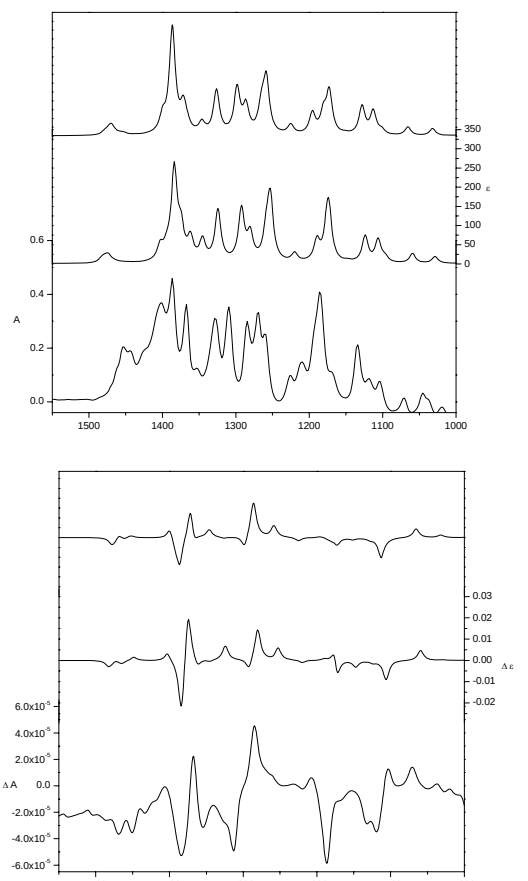

Figure A1

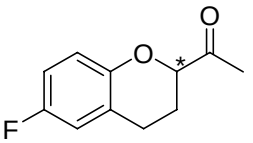

1-(6-fluorochroman-2-yl)ethanone
JNJ17341727

Origin	–	JNJPRD refs 2,3
Measurements	–	Performed by JNJPRD - Both enantiomers in CD_2Cl_2
Modeled configuration	–	*S*
Number of significant conformations	–	2
Spectra	–	Half difference

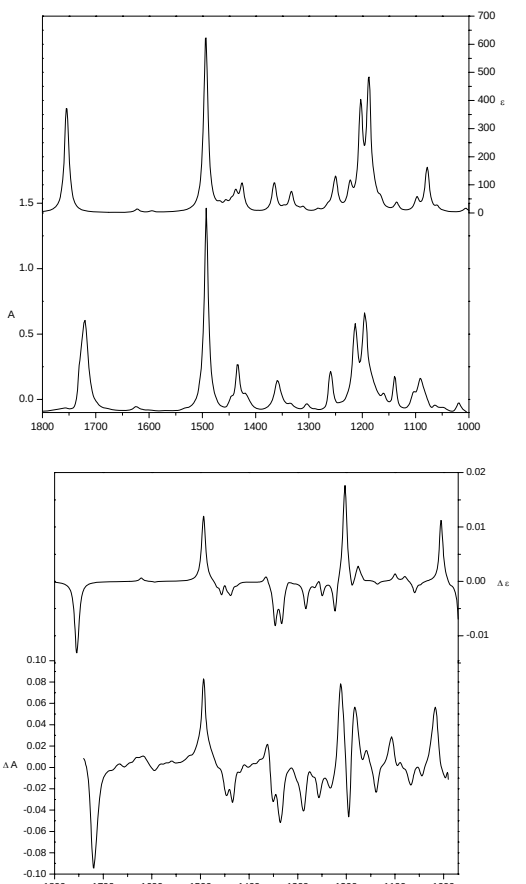

Figure A2

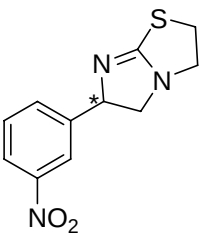

2,3,5,6-tetrahydro-6-(3-nitrophenyl)-
imidazo[2,1b]thiazole
JNJ17139652
JNJ17321343

Origin	– JNJPRD ref 4
Measurements	– Performed by JNJPRD - Both enantiomers in $CDCl_3$
Modeled configuration	– *R*
Number of significant conformations	– 4
Spectra	– Half difference

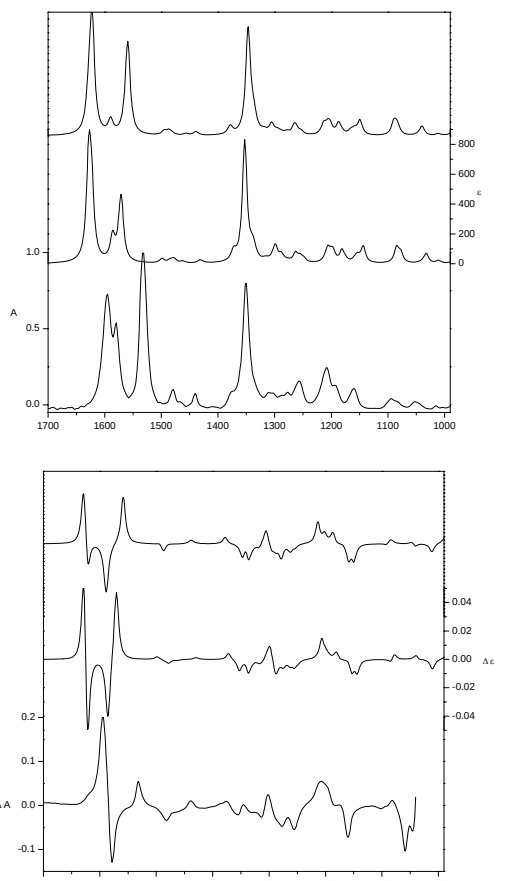

Figure A3

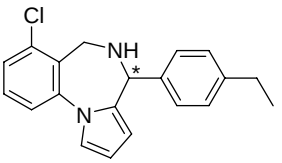

1-Chloro-8-ethyl-5,6-dihydro-4-phenyl-4H-pyrrolo[1,2-a][1,4]benzodiazepine
JNJ16709368
JNJ16709407
JNJ16992508

Origin	–	JNJPRD refs 5,6
Measurements	–	Performed by JNJPRD - Both enantiomers in CD_2Cl_2
Modeled configuration	–	*S*
Number of significant conformations	–	7
Spectra	–	Half difference

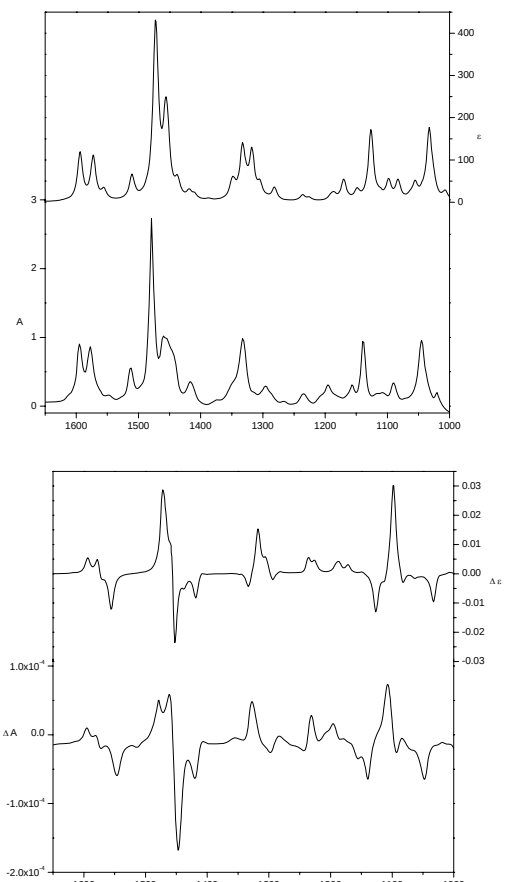

Figure A4

VCD AC determination was published in Meerpoel, L.; Van Gestel, J.; Van Gerven, F.; Woestenborghs, F.; Marichal, P.; Sipido, V.; Terence, G.; Nash, R.; Corens, D.; Richards, R. D. Pyrrolo[1,2-a][1,4]benzodiazepine: A novel class of non-azole anti-dermatophyte anti-fungal agents. *Bioorg. Med. Chem. Lett.* **2005**, *15*, 3453-3458.

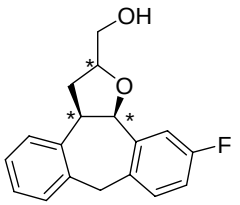

(2*R*,3a*R*,12b*R*)-11-fluoro-3,3a,8,12b-tetrahydro-2*H*-dibenzo[3,4:6,7]cyclohepta[1,2-*b*]furan-2-methanol
JNJ16150433

Origin	– JNJPRD refs 7-9
Measurements	– Performed by JNJPRD
Modeled configuration	– 2*R*,3a*R*,12b*R*
Number of significant conformations	– 8
Spectra	– Half difference

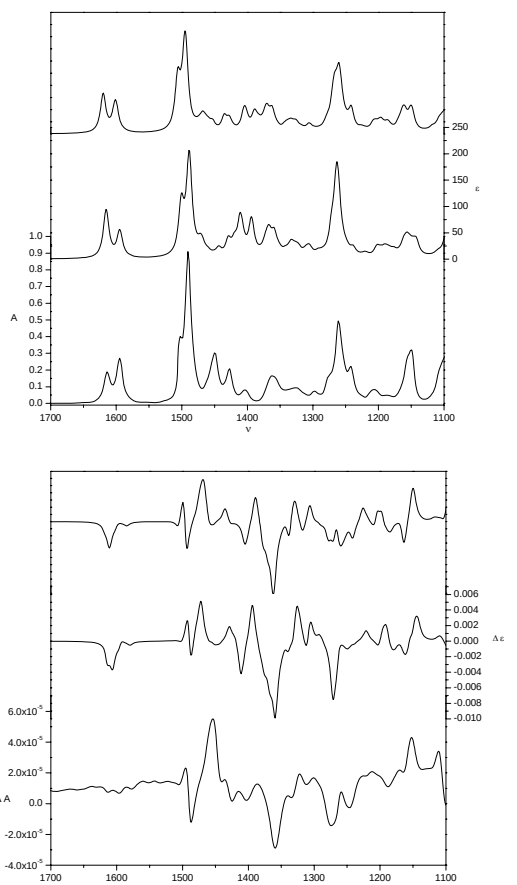

Figure A5

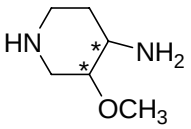

3-methoxypiperidin-4-amine
JNJ16502655
JNJ16159039

Origin	– JNJPRD refs 10,11
Measurements	– Performed by JNJPRD
Modeled configuration	– 3*R*,4*S*
Number of significant conformations	– 13

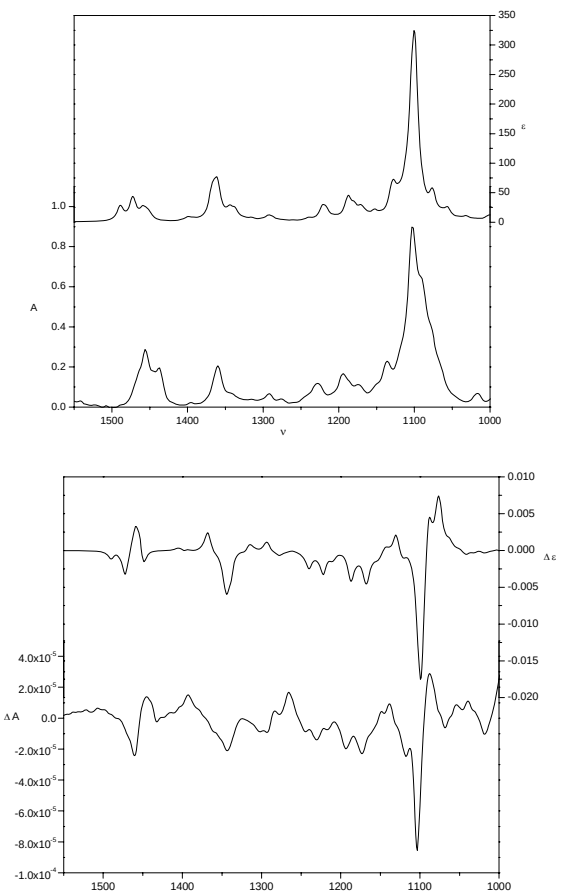

Figure A6

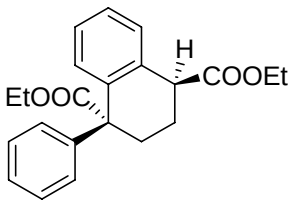

(1*R*,4*S*)-diethyl-1-phenyl-1,2,3,4-tetrahydronaphthalene-1,4-dicarboxylate
JNJ39342095

Origin	–	JNJPRD ref 12
Measurements	–	Performed by JNJPRD
Modeled configuration	–	1*R*,4*S*
Number of significant conformations	–	26
Spectra	–	Half difference

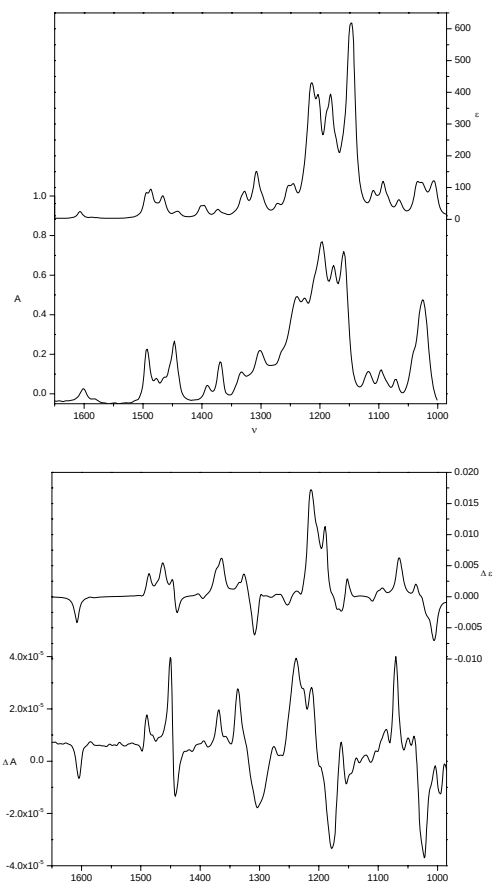

Figure A7

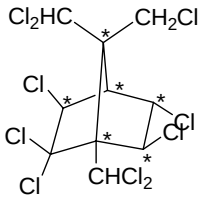

(1*R*,3*S*,4*S*,5*S*,6*S*,7*R*)-2,2,3-*exo*,5-*endo*,6-*exo*,8,9,9,10,10-decachlorobornane

Origin	– Prof. Dr. V. Nikiforov – St. Petersburg State University ref 13
Measurements	– Racemic mixture and enantiomeric pure samples at 0.17M in CS_2. Measured in KBr cell with 105 μm spacers.
Modeled configuration	– 1*R*,3*S*,4*S*,5*S*,6*S*,7*R*
Number of significant conformations	– 1
Spectra	– Racemic baseline corrected.

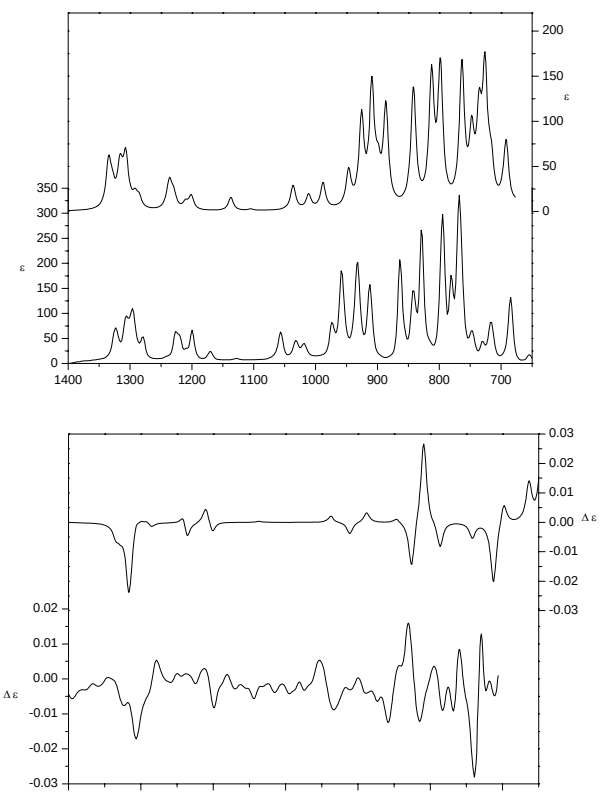

Figure A8

Based on the synthesis, only two enantiomers are possible. The absolute configuration could not be determined by XRD or NMR. AC determination was presented at DIOXIN2006: Structure elucidation of poly-chloroterpenes obtained from optically active pinenes[13]

Reference list

1. Van Daele, G. EP 68544, 1982.

2. Lesage, A.; Bischoff, F. P.; Janssen, C.; Lavreysen, H. WO 2003082350, 2003.

3. Mabire, D.; Venet, M. G.; Coupa, S.; Poncelet, A. P.; Lesage, WO 2002028837, 2001.

4. Janssen, P. A. J.; Heeres, J.; Lewi, P. J.; Vlaminck, K.; Ottevaere, P.; Vanparijs, O. WO 2006079642, 2006.

5. Gilkerson, T.; Nash, R.; Van Gestel, J.; Meerpoel, L. WO 2002034752, 2001.

6. Meerpoel, L.; Van Gestel, J.; Van Gerven, F.; Woestenborghs, F.; Marichal, P.; Sipido, V.; Terence, G.; Nash, R.; Corens, D.; Richards, R. D. *Bioorg. Med. Chem. Lett.* **2005**, *15*, 3453-3458.

7. Cid-Nunez, J. M.; Megens, A.; Trabanco-Suarez, A. A.; Koukni, M.; Hoornaert, G.; Compernolle, F.; Kozlecki, T.; Mao, H.; Jha, S. C.; Fernandez-Gadea, F. J. WO 2006061392, 2005.

8. Mao, H.; Kozlecki, T.; Compernolle, F.; Hoornaert, G. WO 2003048147, 2002.

9. Lang, Y. L.; Medaer, B.; Hoornaert, G.; Brossette, T.; Compernolle, F.; Guillaume, M.; Mao, H.; Kozlecki, T. WO 2003048146, 2002.

10. De Knaep, A.; Moens, L.; Rey, M. WO 9816511, 1997.

11. Van Daele, G.; Bosmans, J. P.; Van Laerhoven, W. US 5674868, 1995.

12. Moehrle, H.; Pycior, M.; Wendisch, D. *Pharmazie* **1992**, *47*, 8-10.

13. Kruchkov, F. A.; Kuppens, T.; Kolehmainen, E.; Nikiforov, V. A. *Organohalogen Compounds* **2006**, *68*, In press.

acknowledgements

> De eekhoorn liep naar het smalle strand van zand en kiezelstenen dat zich uitstrekte langs de rivier.
> Hij was van plan om daar te gaan nadenken.
> Hij wist nog niet waarover, maar dat was altijd zo als hij wilde gaan nadenken.
> Als hij wel had geweten waarover hij wilde nadenken was hij thuis gebleven en had hij daar meteen nagedacht over datgene waarover hij wilde nadenken.
>
> – Toon Tellegen, Er ging geen dag voorbij

Ik dank mijn promotor Prof. Dr. Patrick Bultinck, omdat hij me de kans heeft gegeven dit doctoraatsonderzoek aan te vangen en dat ik nu met succes kan afronden. Bedankt voor het vertrouwen en de hand boven mijn hoofd.
Het was in de eerste jaren echter niet gemakkelijk om een weg te vinden in de wereld van het VCD onderzoek. In die periode kon ik binnen de vakgroep ook rekenen op de steun van Prof. Dr. André Goeminne.

Aan de Universiteit Antwerpen waren het vooral Prof. Dr. Wouter Herrebout en Prof. Dr. Ben van der Veken die me met enthousiasme in dit werk hebben gesteund en ik wil hen dan ook graag bedanken voor hun gastvrijheid en de ondersteuning die ze vanuit hun perspectief gaven aan mijn werk.

De samenwerking met het organische synthese labo van Prof. Dr. Johan Van der Eycken was eveneens heel vruchtbaar. Meerdere interessante resultaten werden samen met Dr. Koen Vandyck bekomen en tot in de puntjes uitgewerkt. Koen ben ik dan ook heel dankbaar.

De inspiratie voor de opzet van dit onderzoeksproject kwam van Dr. Wilfried Langenaeker en Prof. Dr. Jan Tollenaere, toen werkzaam bij Janssen Pharmaceutica, Beerse. Aan de vorm en samenstelling is in de loop van de jaren misschien wel het één en het ander veranderd, maar de samenwerking met Johnson & Johnson Pharmaceutical Research and Development in Beerse is gebleven. Momenteel is Dr. David Corens daar de drijvende kracht achter de VCD absolute configuratie bepalingen en samen met hem heb ik een groot aantal toewijzingen uitgevoerd. Tenslotte ben ik ook Dr. Guy Van Lommen dankbaar voor de vlotte samenwerking.

I would like to thank Prof. Ramon Carbó-Dorca for his kindness and his help on diverse problems.

I'm also grateful for the many constructive comments and remarks I have received from all the *anonymous referees* during the years. They have improved the quality of this work considerably and have stretched it towards the highest possible level.

Dank aan de collega's in Gent en Antwerpen!

Ik wil ook al mijn vrienden danken voor hun steun. In het bijzonder:
Raju, zelfs aan de andere kant van de wereld ben je nog steeds een bron van inspiratie en motivatie. Sabina, wat was het leuk om naar jouw verhaaltjes te luisteren. Ik heb het zelfs niet kunnen laten om hierboven een filosofische noot van Eek te plaatsten. Bedankt ook voor je steeds luisterend oor! Lieve, merci voor de zalige ontspannende dineetjes en de vele gesprekken over de meest uiteenlopende onderwerpen. Driesken, ge hebt een jaar in Gent gewoond en het was leuk om zo kort bij huis familie te hebben. Spijtig dat ik het afgelopen jaar zo wreed druk heb gehad.

Christy, bedankt voor je steun en je engelengeduld.

Mijn ouders en mijn broer Bart wil ik graag bedanken voor de jarenlange en onvoorwaardelijke steun.

Tom Kuppens, december 2006

P.S. Ik zal een marathon lopen binnen dit en twee jaar. (Zo, nu kan ik er niet meer onderuit komen met een flauw excuus)

P.P.S. Ik vergeet nog iemand, nl. mijn gevederde vriend QTux, die mij gezelschap hield bij het creëren van mijn computer cluster ("Ghent quantum cluster" :). Hier staat niets van vermeld in mijn doctoraat. Het is echter praktisch onmogelijk om zware berekeningen uit te voeren zonder een serieuze computer infrastructuur. Ons heterogene en steeds groter wordende computerpark heb ik dan ook op een bepaald moment gebald in een *cluster* waarbij je op 30 computers tegelijk kan rekenen (en makkelijk uitbreidbaar), ook al lijkt het dat je er maar één aan het bedienen bent. Dit is naast mijn doctoraat waarschijnlijk mijn belangrijkste bijdrage aan de onderzoeksgroep.

TOM KUPPENS

development of methodology to assign absolute configurations using vibrational circular dichroism

Supplementary Material

promotor: Prof. Dr. P. Bultinck, Ghent University

co-promotor: Prof. Dr. W. Herrebout, University of Antwerp

Dissertation for the degree of Doctor in Sciences: Chemistry – December 2006
Ghent University, Faculty of Sciences
Department of Inorganic and Physical Chemistry

Chapter 5

Table S5.1 Maximized neighborhood similarity S^{σ}_{max} and optimal scaling factor σ_{max} – basis sets
Table S5.2 Maximized neighborhood similarity S^{σ}_{max} and optimal scaling factor σ_{max} – integration grids

Table S5.1 Maximized neighborhood similarity S^{σ}_{max} and optimal scaling factor σ_{max} for the simulated spectra calculated with various basis sets with respect to the experimental spectrum. IR NS l=40 cm^{-1}

		6-31G*	6-31G**	6-311G**	cc-pVDZ	cc-pVTZ
IR	S^{σ}_{max}	95.4	96.5	96.4	96.7	96.9
	σ_{max}	0.969	0.970	0.981	0.977	0.979
VCD	S^{σ}_{max}	83.6	83.6	85.7	81.6	89.7
	σ_{max}	0.969	0.970	0.981	0.977	0.979

Table S5.2 Maximized neighborhood similarity S^{σ}_{max} and optimal scaling factor σ_{max} for the simulated spectra calculated with various grids with respect to the experimental spectrum. IR NS l=40 cm^{-1}

Grid	S^{σ} IR	σ_{max}	S^{σ} VCD	σ_{max}
(35,110)p	95.1	0.971	80.4	0.971
(50,194)p	95.4	0.969	84.0	0.969
(75,302)p	95.4	0.969	83.6	0.969
(50,302)	95.4	0.969	83.9	0.969
(75,194)	95.4	0.969	83.1	0.969
(75,434)	95.4	0.969	83.3	0.969
(99,302)	95.7	0.969	83.8	0.969

Chapter 6

General experimental methods

Table S6.1 Assignment of the experimental peaks of (+)-**1** based on the B3LYP/6-31G* simulated spectra. The experimental values of the vibrational frequencies (in cm^{-1}), dipole (D in 10^{-40} esu^2cm^2) and rotational strength (R in 10^{-44} esu^2cm^2) were Lorentzian fitted. Fundamentals are labeled according to the minimum (a ≡ eGeG' b ≡ eG'eT). Calculated values of D and R are Boltzmann weighed according to Table 6.1a.

Fund	Experimental			B3LYP/6-31G*		
	freq	D	R	freq*	D	R
34a	1024.83	104.57	14.28	1024.48	27.07	24.45
34b	1034.65	⊥	−12.33	1030.40	9.83	−6.09
35a	1042.73	201.76	116.04	1035.31	169.35	10.25
35b		⊥	⊥	1041.08	3.83	2.48
36b	1054.98	75.22	106.26	1045.43	15.79	14.56
36a	1064.06	165.79	⊥	1047.04	93.08	53.82
37b	1075.09	339.49	−137.13	1085.52	47.18	3.94
37a		⊥	⊥	1085.62	289.06	−2.34
38a	1130.65	17.29	−28.06	1119.84	21.77	−38.96
38b	1137.29	30.95	|	1128.28	3.87	−3.02
39a		|	⊥	1128.49	8.86	−3.15
39b	1139.53	|	18.17	1132.46	1.72	2.60
40a		⊥	⊥	1133.15	8.04	12.59
40b	1147.58	17.66	−36.21	1143.99	3.45	−2.93
41b	1165.08	28.78	15.96	1148.67	4.14	8.63
41a		⊥	⊥	1151.12	7.42	11.04
42b	1187.64	49.24	39.94	1173.48	0.55	0.05
42a		⊥	⊥	1174.57	1.03	1.45
43b	1204.16	48.13	55.55	1185.42	21.25	7.56
43a		|	|	1193.64	3.87	2.47
44b		⊥	⊥	1201.03	11.38	1.46
44a	1226.20	22.62	−54.94	1218.27	41.35	−2.22
45a	1229.94	87.14	|	1221.88	16.76	−14.89
45b		|	|	1222.81	1.96	−1.82
46b		|	|	1224.50	3.00	−3.35
46a		⊥	⊥	1231.82	3.35	−5.41
47a	1256.29	83.32	−66.89	1258.70	38.79	−42.67
47b		|	|	1260.17	5.49	−7.41
48b		|	|	1272.35	0.77	−2.19
48a		⊥	⊥	1275.07	16.58	−10.49
49a	1280.89	27.34	24.52	1279.92	21.74	13.33
49b		⊥	⊥	1280.69	0.68	0.59
50b	1288.31	57.44	−47.59	1289.41	1.04	−2.47
50a		|	⊥	1289.77	19.59	−8.56
51a	1295.42	⊥	13.93	1296.22	7.77	4.69
51b	1304.38	66.34	|	1300.70	4.95	−0.85
52a		|	|	1304.39	19.61	2.72
52b		⊥	⊥	1311.45	6.36	−1.91

53a	1325.15	133.79	93.86	1328.19	225.14	20.39
53b	1334.61	92.61	|	1331.55	44.68	0.58
54a		|	|	1340.82	19.91	−1.80
54b		⊥	|	1344.28	0.32	−0.05
55b	1379.26	46.53	⊥	1383.32	6.76	−3.17
55a	1388.30	115.43	−66.80	1391.64	167.52	−28.64
56a	1388.85	⊥	−84.63	1409.11	42.26	−29.47
56b	1402.34	52.32	|	1416.98	6.86	−3.94
57a	1420.35	13.13	|	1434.65	1.81	−2.65
57b		⊥	⊥	1439.29	0.61	−0.63
58a	1438.23	45.75	4.62	1455.09	41.22	15.18
58b		⊥	⊥	1456.28	7.83	3.45
59a	1453.52	78.36	−28.40	1465.29	1.44	−1.73
59b		⊥	⊥	1466.48	0.31	−0.45
60a	1468.36	85.65	29.74	1469.27	35.92	16.20
60b		⊥	⊥	1469.87	5.79	2.66

* scaled with factor 0.967 Correlation coefficients – *D*: 72% / *R*: 47%

Table S6.2 Assignment of the experimental peaks of (+)-**1** based on the B3LYP/cc-pVTZ simulated spectra. The experimental values of the vibrational frequencies (in cm^{-1}), dipole (*D* in 10^{-40} esu^2cm^2) and rotational strength (*R* in 10^{-44} esu^2cm^2) were Lorentzian fitted. Fundamentals are labeled according to the minimum (a ≡ eGeG' b ≡ eG'eT). Calculated values of *D* and *R* are Boltzmann weighed according to Table 6.1b.

Fund	Experimental			B3LYP/cc-pVTZ		
	freq	*D*	*R*	freq*	*D*	*R*
34a	1024.83	104.57	14.28	1025.47	36.22	34.00
34b	1034.65	⊥	−12.33	1031.87	21.37	−10.81
35a	1042.73	201.76	116.04	1036.53	186.82	17.44
35b		⊥	⊥	1039.70	18.94	15.34
36a	1054.98	75.22	106.26	1047.37	49.35	24.85
36b	1064.06	165.79	⊥	1046.22	13.71	11.46
37a	1075.09	339.49	−137.13	1076.72	272.24	−9.80
37b		⊥	⊥	1076.68	75.90	4.05
38a	1130.65	17.29	−28.06	1123.10	18.43	−31.33
38b	1137.29	30.95	|	1132.21	3.91	−3.48
39a		|	⊥	1132.26	5.28	3.95
39b	1139.53	|	18.17	1135.90	5.87	4.76
40a		⊥	⊥	1136.54	12.24	11.26
40b	1147.58	17.66	−36.21	1147.10	6.51	−2.79
41a	1165.08	28.78	15.96	1157.47	8.23	4.92
41b		⊥	⊥	1155.84	4.57	10.55
42a	1187.64	49.24	39.94	1178.80	0.83	1.62
42b		⊥	⊥	1177.42	1.96	0.05
43a	1204.16	48.13	55.55	1202.88	4.60	0.97
43b		|	|	1187.34	36.87	11.25
44a		⊥	⊥	1221.37	28.76	1.89
44b	1226.20	22.62	−54.94	1206.79	4.52	0.59

45a	1229.94	87.14		1226.62	20.47	1.43
45b				1225.48	0.37	−0.10
46a				1233.94	2.84	−15.22
46b		⊥	⊥	1229.96	6.47	−7.15
47a	1256.29	83.32	−66.89	1254.62	45.35	−43.09
47b				1256.42	11.13	−12.73
48a				1273.32	9.86	−7.34
48b		⊥	⊥	1270.10	0.51	−1.21
49a	1280.89	27.34	24.52	1280.17	5.27	5.19
49b		⊥	⊥	1280.15	1.49	0.47
50a	1288.31	57.44	−47.59	1288.46	24.34	−3.91
50b			⊥	1286.72	3.55	−6.84
51a	1295.42	⊥	13.93	1294.30	6.87	7.23
51b	1304.38	66.34		1303.29	10.18	−2.06
52a				1305.18	33.93	3.08
52b		⊥	⊥	1310.74	2.48	0.94
53a	1325.15	133.79	93.86	1321.09	144.19	30.54
53b	1334.61	92.61		1324.16	55.26	3.66
54a				1336.45	14.25	−1.96
54b		⊥		1340.64	0.41	−0.15
55a	1379.26	46.53	⊥	1386.73	101.65	−16.15
55b	1388.30	115.43	−66.80	1377.96	8.00	−5.45
56a	1388.85	⊥	−84.63	1396.90	49.00	−40.48
56b	1402.34	52.32		1402.41	7.58	−4.98
57a	1420.35	13.13		1435.25	0.64	−0.84
57b		⊥	⊥	1439.14	0.43	−0.36
58a	1438.23	45.75	4.62	1450.43	21.96	2.65
58b		⊥	⊥	1451.00	6.38	1.11
59a	1453.52	78.36	−28.40	1457.06	4.35	−5.04
59b		⊥	⊥	1458.40	1.27	−1.78
60a	1468.36	85.65	29.74	1465.85	33.80	10.81
60b				1466.50	4.57	1.98
61a				1466.66	0.69	−2.05
61b				1467.18	3.37	0.11
62a				1468.43	26.00	8.36
62b		⊥	⊥	1468.90	9.68	3.04

[*] scaled with factor 0.977 Correlation coefficients – *D*: 73% / *R*: 54%

Table S6.3 Assignment of the experimental peaks of (+)-**2** based on the B3LYP/6-31G* simulated spectra. The experimental values of the vibrational frequencies (in cm^{-1}), dipole (*D* in 10^{-40} esu^2cm^2) and rotational strength (*R* in 10^{-44} esu^2cm^2) were Lorentzian fitted. The fundamentals listed are from minimum eG'. −

Fund	experimental			B3LYP/6-31G*		
	freq	*D*	*R*	freq[*]	*D*	*R*
34	1068.74	296.57	222.04	1069.24	89.45	28.21
35	1092.45	160.69	−33.90	1089.67	252.24	79.33
36	1137.94	25.48	−12.99	1132.22	1.71	−18.45
37	1147.67	32.92	27.85	1134.61	7.54	14.06

38		⊥	⊥	1138.62	24.39	19.05
39	1179.41	49.47	−42.38	1168.36	43.47	−22.67
40	1194.59	57.49	15.10	1190.49	41.42	11.15
41	1213.49	53.64	2.13	1206.76	0.52	5.33
42		⊥	⊥	1212.71	11.34	9.29
43	1235.08	72.54	−111.60	1227.28	108.41	−42.98
44	1249.79	104.86	38.00	1247.91	60.56	28.66
45	1257.26	30.37	−48.84	1257.10	100.35	−74.32
	1259.64	73.19	⊥		⊥	⊥
46	1278.90	125.80	−65.43	1277.09	131.08	−6.35
47	1286.09	78.04	−18.54	1284.74	13.93	−16.92
48	1299.15	83.38	−2.72	1298.52	13.48	−3.19
49	1331.65	149.02	84.48	1332.26	214.69	21.33
50	1341.54	44.48	−32.00	1345.75	11.97	−23.31
51	1390.98	55.57	6.17	1409.29	93.06	4.86
52	1406.57	86.00	−11.84	1426.98	93.42	−10.57
53	1416.32	41.12	−6.10	1437.65	34.33	−3.52
	1427.01	⊥	2.09		⊥	⊥
54	1442.73	57.15	6.53	1456.68	78.81	24.64
55	1438.93	70.21	⊥	1466.39	43.45	7.41
56	1454.00	74.69	−10.08	1472.05	14.76	9.22
57	1473.41	116.00	23.56	1477.54	7.52	−3.16
58	1586.97	104.35	-	1583.22	66.62	−1.67
59	1613.42	154.70	−17.25	1601.36	86.44	−1.50
60	1686.50	1215.25	151.90	1713.72	608.98	27.80

[*] scaled with factor 0.967 Correlation coefficients – *D*: 79% / *R*:23%

Table S6.4 Assignment of the experimental peaks of (+)-**2** based on the B3LYP/cc-pVTZ simulated spectra. The experimental values of the vibrational frequencies (in cm^{-1}), dipole (*D* in 10^{-40} esu^2cm^2) and rotational strength (*R* in 10^{-44} esu^2cm^2) were Lorentzian fitted. The fundamentals listed are from minimum eG'.

Fund	experimental			B3LYP/cc-pVTZ		
	freq	*D*	*R*	freq[*]	*D*	*R*
33	1026.20	66.25	−103.77	1023.92	68.95	−29.65
34	1068.74	296.57	222.04	1075.34	97.67	71.77
35	1092.45	160.69	−33.90	1086.02	264.70	36.88
36	1137.94	25.48	−12.99	1135.91	0.89	−11.24
37	1147.67	32.92	27.85	1139.12	3.48	4.59
38		⊥	⊥	1144.39	31.47	20.78
39	1179.41	49.47	−42.38	1172.38	46.84	−23.81
40	1194.59	57.49	15.10	1193.96	40.42	12.98
41	1213.49	53.64	2.13	1212.66	0.32	6.13
42		⊥	⊥	1218.65	5.95	0.41
43	1235.08	72.54	−111.60	1232.60	92.22	−46.70
44	1249.79	104.86	38.00	1247.34	92.79	38.55
45	1257.26	30.37	−48.84	1256.37	92.25	−70.55
	1259.64	73.19	⊥		⊥	⊥
46	1278.90	125.80	−65.43	1277.02	102.59	−11.25

47	1286.09	78.04	−18.54	1283.63	23.51	−23.90
48	1299.15	83.38	−2.72	1301.51	11.16	−6.08
49	1331.65	149.02	84.48	1328.97	168.95	25.48
50	1341.54	44.48	−32.00	1341.69	11.04	−21.88
51	1390.98	55.57	6.17	1402.88	106.45	10.34
52	1406.57	86.00	−11.84	1418.96	42.00	−7.12
53	1416.32	41.12	−6.10	1434.56	61.77	0.84
	1427.01	⊥	2.09		⊥	⊥
54	1442.73	57.15	6.53	1451.52	46.27	9.61
55	1438.93	70.21	⊥	1457.56	34.08	0.18
56	1454.00	74.69	−10.08	1468.08	2.39	−5.60
57	1473.41	116.00	23.56	1471.41	70.55	23.85
58	1586.97	104.35	-	1586.07	71.63	−0.55
59	1613.42	154.70	−17.25	1603.03	90.97	1.47
60	1686.50	1215.25	151.90	1707.75	670.62	35.77

* scaled with factor 0.977 Correlation coefficients – *D*: 86% / *R*: 64%

Table S6.5 Assignment of the experimental peaks of (−)-**3** based on the B3LYP/6-31G* simulated spectra. The experimental values of the vibrational frequencies (in cm^{-1}), dipole (*D* in 10^{-40} esu^2cm^2) and rotational strength (*R* in 10^{-44} esu^2cm^2) were Lorentzian fitted.

Fund	experimental			B3LYP/6-31G*		
	freq	*D*	*R*	freq*	*D*	*R*
34	1088.34	9.94	−7.91	1066.00	2.47	−6.54
35		⊥	⊥	1071.93	2.63	−3.41
36	1131.78	17.90	5.81	1126.37	10.51	0.38
37	1165.18	7.28	43.73	1162.92	12.36	−1.15
38	1167.03	28.66	⊥	1163.87	2.51	4.88
39	1194.46	6.46	38.53	1180.22	0.96	1.96
40	1207.20	50.50	−56.82	1198.71	18.71	−15.41
41		⊥	⊥	1204.84	14.03	−22.18
42	1228.58	23.08	31.82	1219.22	13.94	23.09
43	1232.30	68.18	−49.03	1223.08	25.13	−38.50
44	1248.24	17.30	9.20	1243.04	24.79	0.19
45	1282.52	20.61	3.67	1279.92	4.67	4.14
46	1288.05	⊥	22.77	1280.34	3.55	8.13
47	1327.72	16.19	2.83	1312.62	6.76	6.66
48	1351.85	18.10	−17.56	1338.69	1.25	−5.94
49	1363.04	7.60	32.49	1376.14	25.68	−32.90
50	1367.16	45.17	41.95	1376.29	44.42	78.25
51	1422.65	3.87	33.84	1441.44	9.48	−6.93
52	1431.12	25.48	20.00	1441.67	27.21	9.54
53	1454.67	31.83	11.82	1453.16	2.19	2.51
54	1455.85	|	3.32	1454.53	31.83	15.33
	1459.12	⊥	25.65		⊥	⊥
55	1601.74	23.52	−10.89	1590.68	0.44	−3.94
56	1650.93	21.00	−5.35	1620.19	0.63	−1.33

* scaled with factor 0.967 Correlation coefficients – *D*: 27% / *R*: 28%

Table S6.6 Assignment of the experimental peaks of (−)-**3** based on the B3LYP/cc-pVTZ simulated spectra. The experimental values of the vibrational frequencies (in cm^{-1}), dipole (D in 10^{-40} esu^2cm^2) and rotational strength (R in 10^{-44} esu^2cm^2) were Lorentzian fitted.

Fund	experimental			B3LYP/cc-pVTZ		
	freq	*D*	*R*	freq*	*D*	*R*
33	1037.20	95.81	−18.23	1031.95	74.06	−18.84
34	1088.34	9.94	−7.91	1080.92	2.76	−6.81
35		⊥	⊥	1085.69	1.77	−0.74
36	1131.78	17.90	5.81	1130.17	12.13	0.01
37	1165.18	7.28	43.73	1166.93	11.23	3.20
38	1167.03	28.66	⊥	1167.35	3.85	7.51
39	1194.46	6.46	38.53	1190.18	1.96	3.50
40	1207.20	50.50	−56.82	1202.51	20.32	−3.33
41		⊥	⊥	1207.05	18.27	−29.84
42	1228.58	23.08	31.82	1222.13	7.75	19.53
43	1232.30	68.18	−49.03	1228.94	26.90	−45.83
44	1248.24	17.30	9.20	1240.69	28.86	4.58
45	1282.52	20.61	3.67	1279.20	8.49	6.33
46	1288.05	⊥	22.77	1279.67	0.86	7.23
47	1327.72	16.19	2.83	1314.45	4.42	5.23
48	1351.85	18.10	−17.56	1334.33	1.85	−7.17
49	1363.04	7.60	32.49	1369.96	41.21	65.74
50	1367.16	45.17	41.95	1371.94	20.96	−28.85
51	1422.65	3.87	33.84	1431.08	17.38	−3.13
52	1431.12	25.48	20.00	1431.33	23.68	5.64
53	1454.67	31.83	11.82	1452.46	0.73	1.88
54	1455.85	|	3.32	1456.42	43.03	20.82
	1459.12	⊥	25.65		⊥	⊥
55	1601.74	23.52	−10.89	1593.71	1.00	−4.67
56	1650.93	21.00	−5.35	1622.18	0.59	−1.27

* scaled with factor 0.977 Correlation coefficients – *D*: 45% / *R*: 38%

Table S6.7 Neighborhood similarity S^{σ} (Equation 6.2) and maximizing scaling factor (for default IR overlap) for theoretical versus experimental IR and VCD spectra using different functionals with the 6-31G* basis set for respectively **1** (a), **2** (b) and **3** (c).

a

functional	S^{σ} IR	S^{σ} VCD	σ
B1LYP	0.938	0.758	0.954
B3LYP	0.936	0.746	0.960
B3P86	0.907	0.702	0.942
B3PW91	0.911	0.717	0.945
B98	0.925	0.759	0.955
BHandH	0.854	0.511	0.901
BHandHLYP	0.912	0.723	0.906
MPW1PW91	0.905	0.690	0.934
PBE1PBE	0.903	0.670	0.932

b

functional	S^{σ} IR	S^{σ} VCD	σ
B1LYP	0.913	0.731	0.944
B3LYP	0.920	0.743	0.952
B3P86	0.916	0.622	0.941
B3PW91	0.914	0.624	0.942
B98	0.894	0.646	0.944
BHandH	0.565	0.453	0.900
BHandHLYP	0.855	0.628	0.901
MPW1PW91	0.909	0.592	0.931
PBE1PBE	0.908	0.566	0.930

c

functional	S^{σ} IR	S^{σ} VCD	σ
B1LYP	0.864	0.597	0.969
B3LYP	0.871	0.622	0.975
B3P86	0.899	0.637	0.969
B3PW91	0.897	0.634	0.970
B98	0.891	0.648	0.977
BHandH	0.861	0.550	0.938
BHandHLYP	0.875	0.490	0.930
MPW1PW91	0.895	0.606	0.962
PBE1PBE	0.895	0.604	0.964

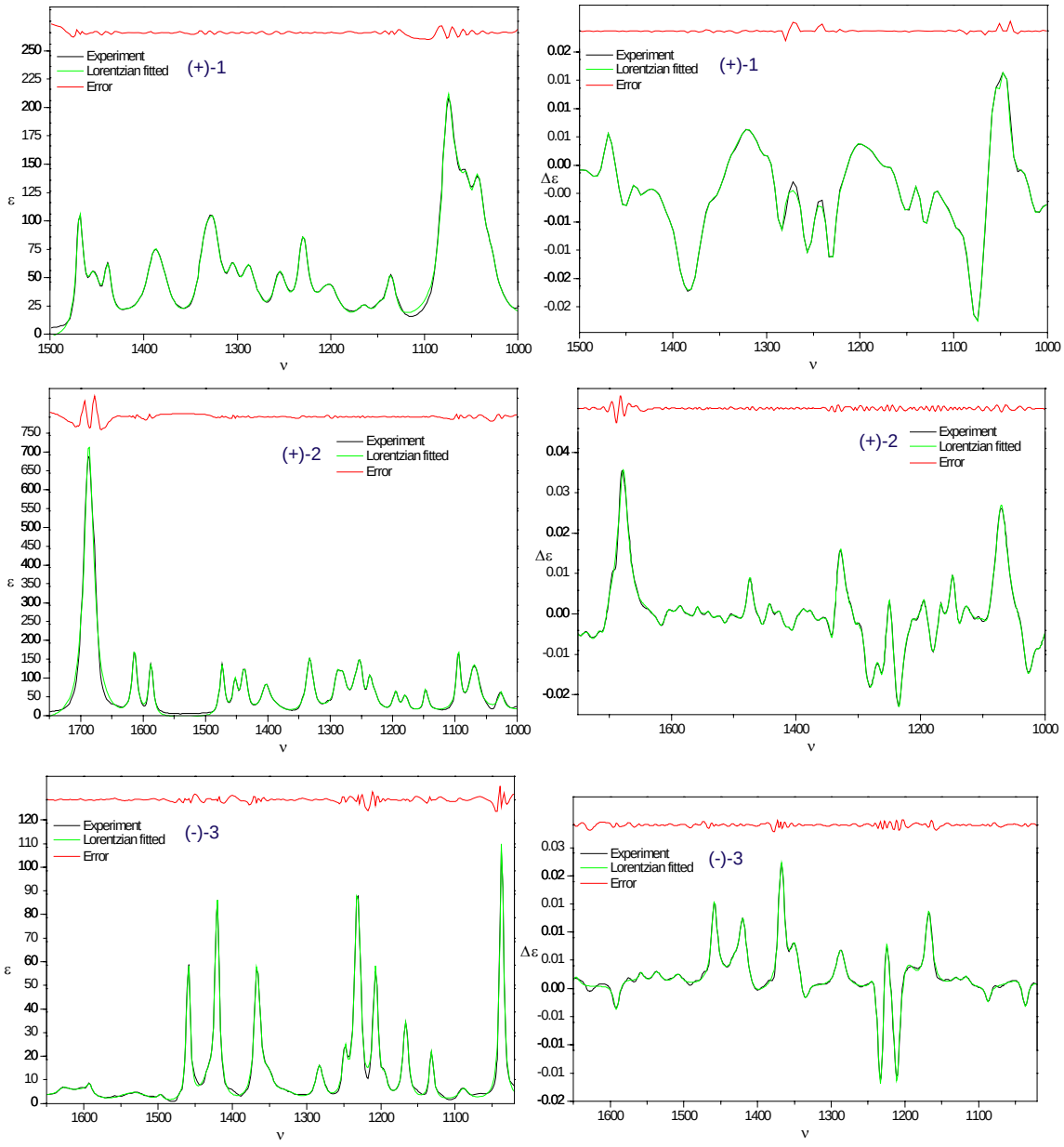

Figure S6.1 Unpolarized IR absorption and VCD spectrum for (+)-**1**, (+)-**2** and (−)-**3**, including Lorentzian fit and residual fitting error (absorptions and differential absorptions in molar absorptivity units).

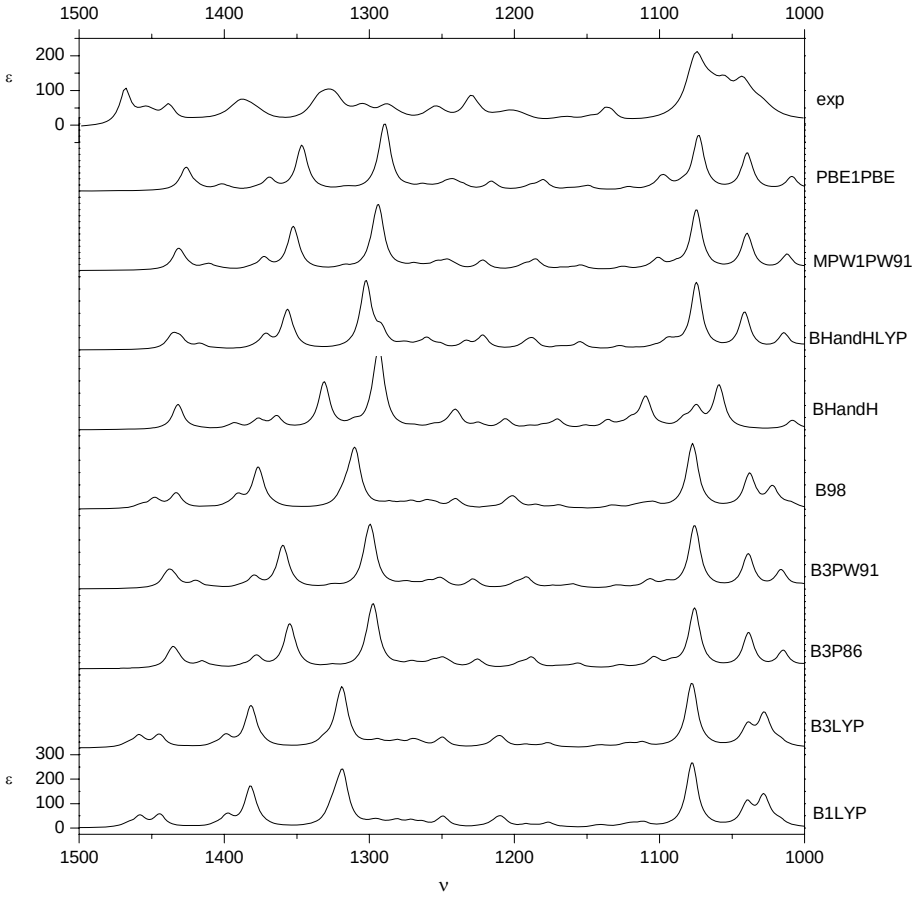

Figure S6.2 Simulated (1*S*,8*S*)-**1** IR DFT/6-31G* for different functionals and experimental spectra. Intensities are in molar absorptivity units, frequencies in cm^{-1}. Frequencies are scaled with functional dependent scaling factors (see Table S6.7).

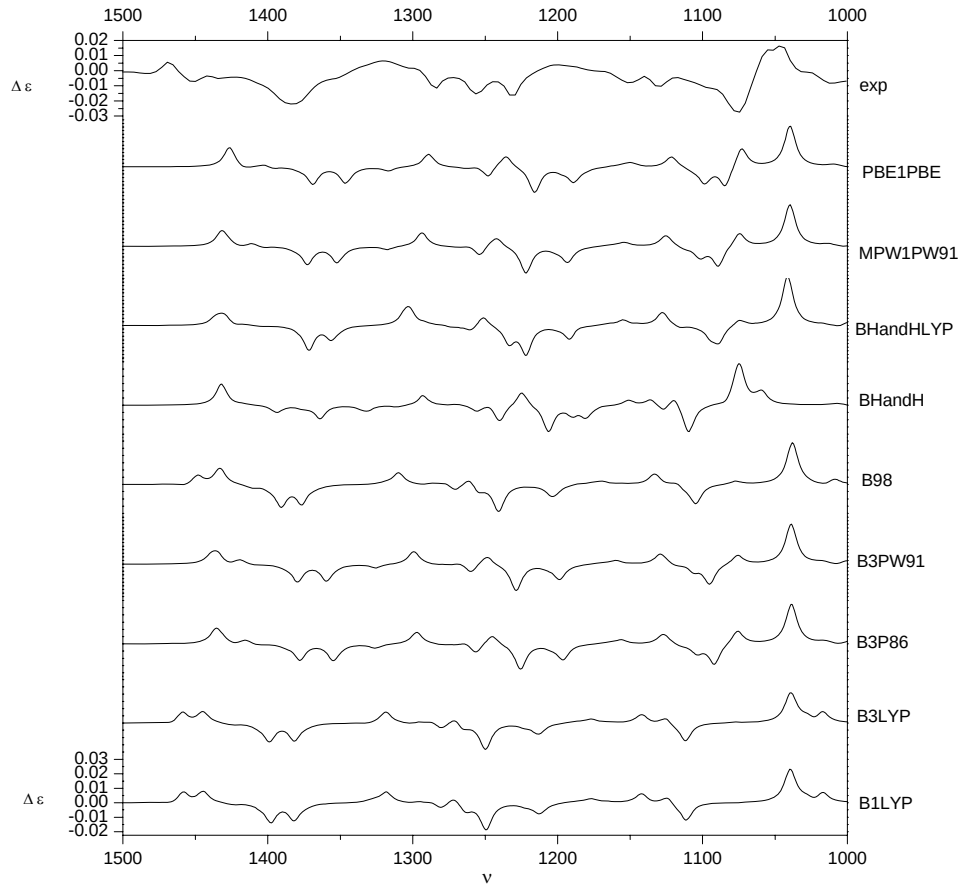

Figure S6.3 Simulated (1*S*,8*S*)-**1** VCD DFT/6-31G* for different functionals and experimental spectra. Intensities are in molar absorptivity units, frequencies in cm^{-1}. Frequencies are scaled with functional dependent scaling factors (see Table S6.7).

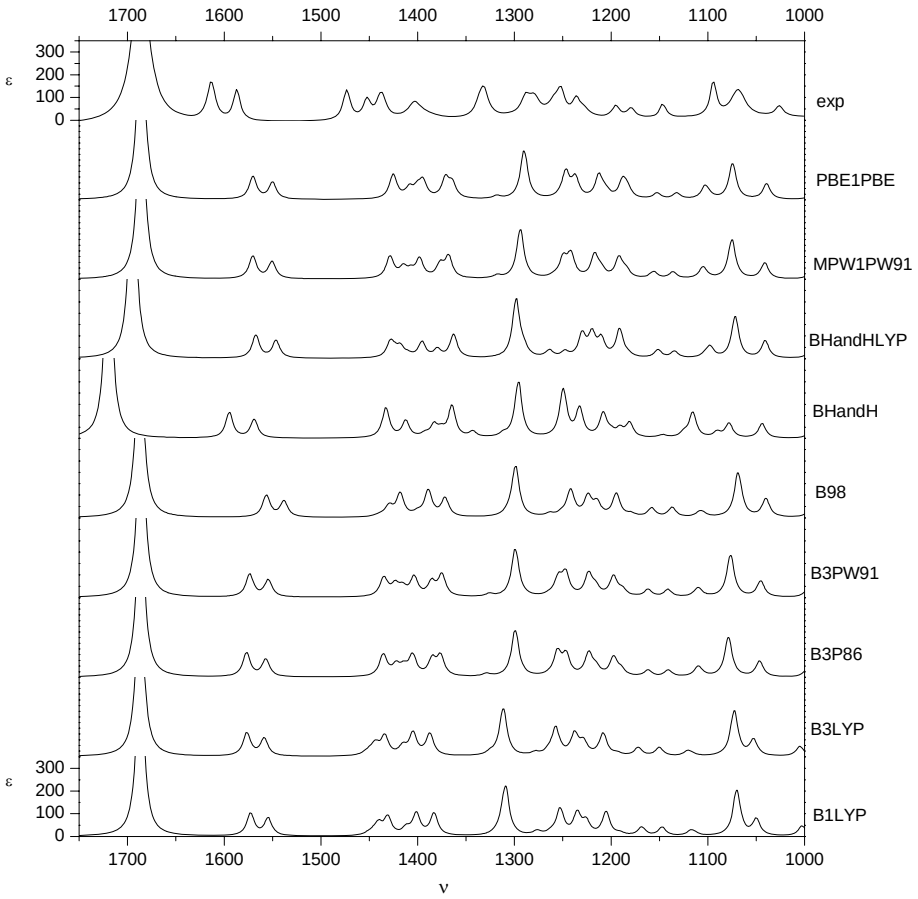

Figure S6.4 Simulated (*S*)-**2** IR DFT/6-31G* for different functionals and experimental spectra. Intensities are in molar absorptivity units, frequencies in cm^{-1}. Frequencies are scaled with functional dependent scaling factors (see Table S6.7).

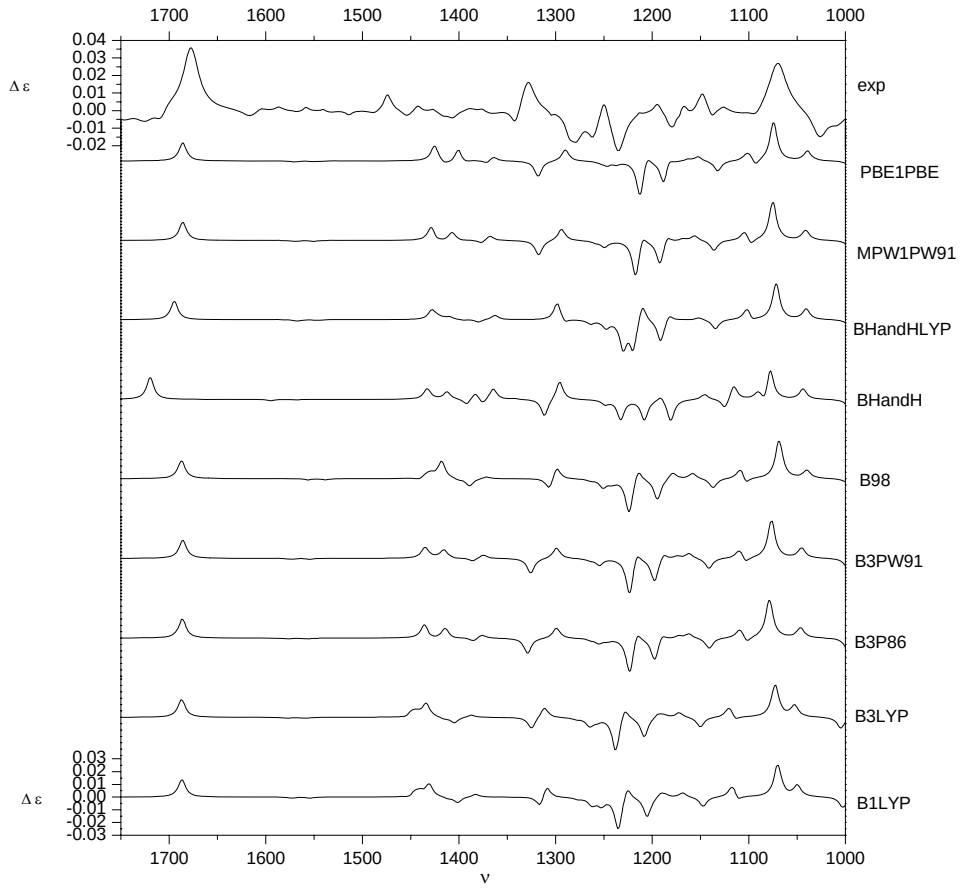

Figure S6.5 Simulated (*S*)-**2** VCD DFT/6-31G* for different functionals and experimental spectra. Intensities are in molar absorptivity units, frequencies in cm^{-1}. Frequencies are scaled with functional dependent scaling factors (see Table S6.7).

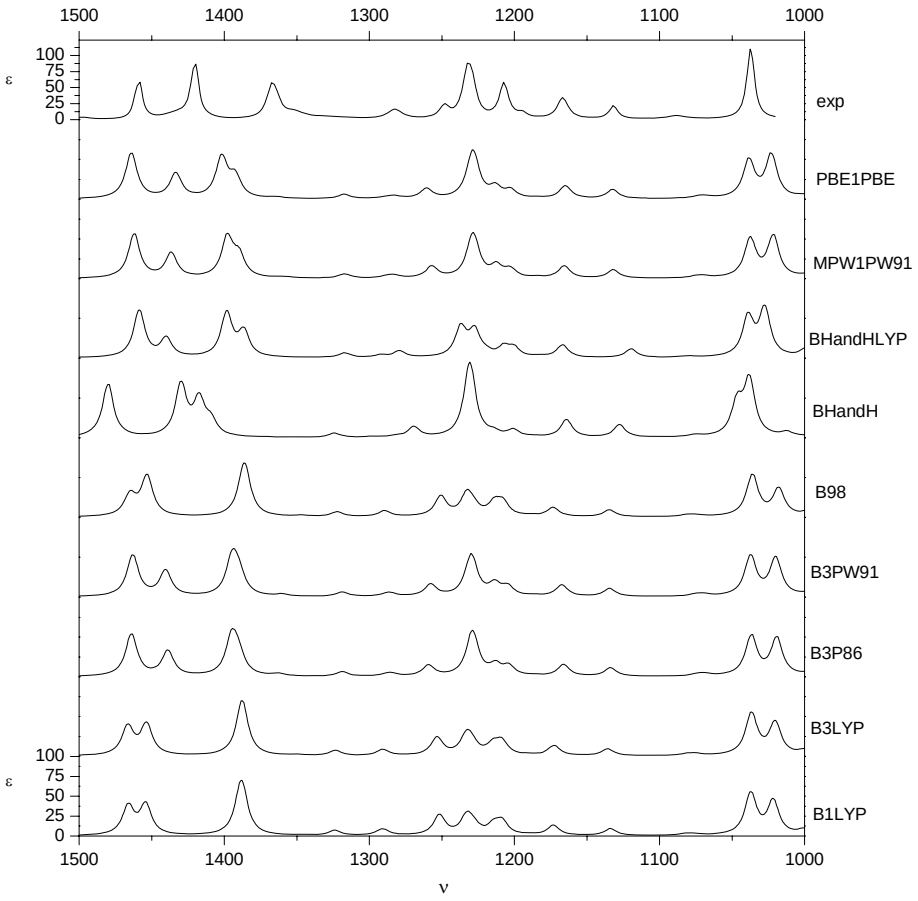

Figure S6.6 Simulated (1*R*,2*S*,7*S*,8*R*)-**3** IR DFT/6-31G* for different functionals and experimental spectra. Intensities are in molar absorptivity units, frequencies in cm^{-1}. Frequencies are scaled with functional dependent scaling factors (see Table S6.7).

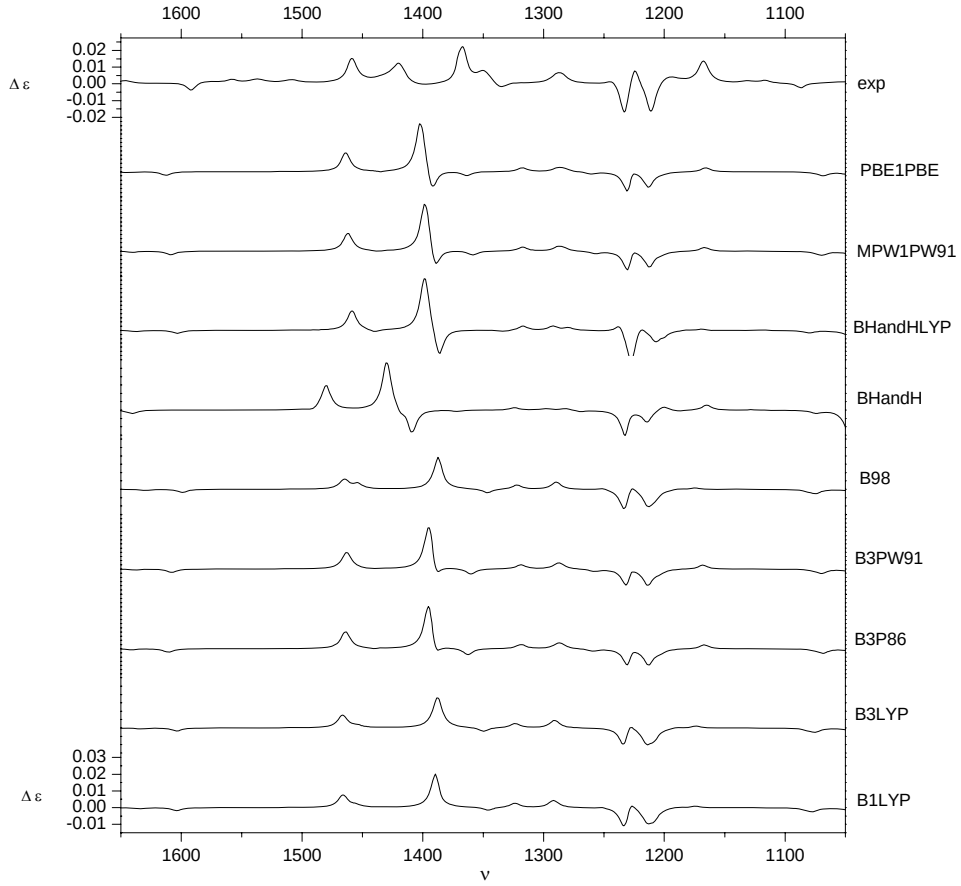

Figure S6.7 Simulated (1*R*,2*S*,7*S*,8*R*)-**3** IR DFT/6-31G* for different functionals and experimental spectra. Intensities are in molar absorptivity units, frequencies in cm^{-1}. Frequencies are scaled with functional dependent scaling factors (see Table S6.7).

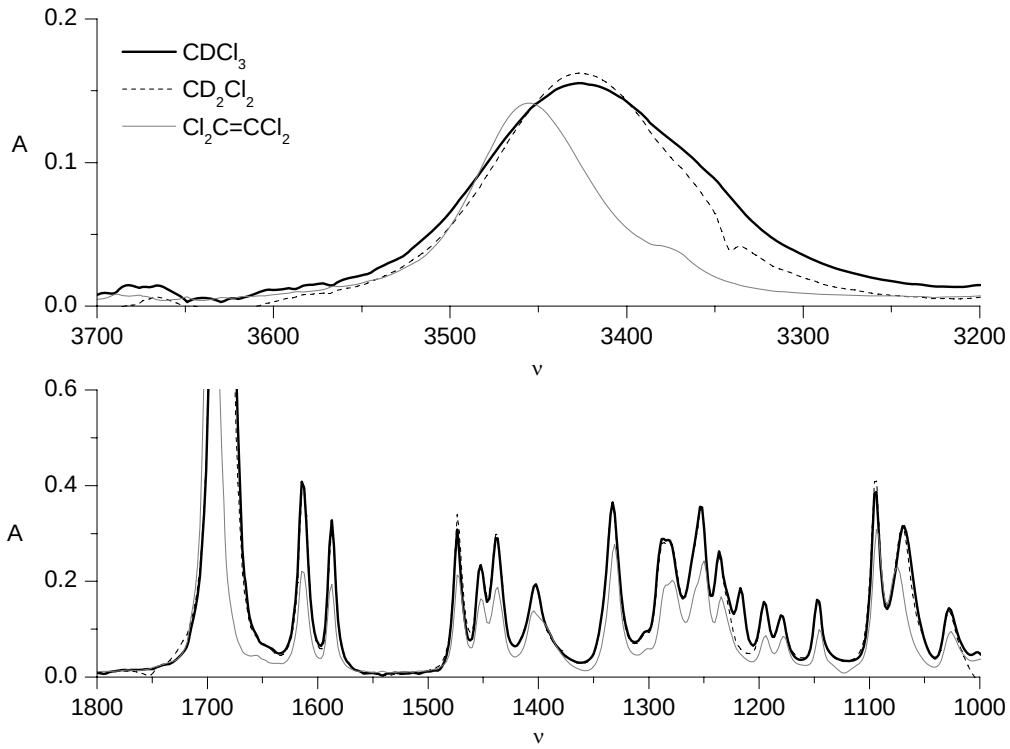

Figure S6.8 Mid IR and OH stretch region for (+)-**2** in three different solvents.

General experimental methods

All reactions were carried out under an argon atmosphere with magnetic stirring. All solvents were purified or dried according to standard procedures. m-CPBA was purified from a commercial 70−75% mixture using a known procedure (Bortolini, O. et al. *J. Org. Chem.* **1987**, *52*, 5093−5095). Column chromatographic separations were performed with silica gel. ^{1}H NMR spectra were recorded at 300 MHz or at 500 MHz. ^{13}C NMR spectra were recorded at 75 MHz. HRMS were recorded with a Q-Tof-2, equipped with a standard electrospray ionization interface.

Mixture of *meso*/(±)-1,2,3,6,7,8-Hexahydro-*as*-indacene-1,8-diol: *meso*/(±)-**1**

A suspension of diketone **4** (5.06 g, 27.2 mmol) was stirred in MeOH (150 mL) at 0 °C and $NaBH_4$ was added (1.03 g, 27.2 mmol) in several portions in such a way that the temperature did not exceed 10 °C. The mixture was then stirred at room temperature for 1h, after which it was poured into H_2O (350 mL) and EtOAc (400 mL). The aqueous layer was separated and again extracted with EtOAc (2 x 400 mL). The organic layer was washed with saturated aqueous NaCl and dried with Na_2SO_4. Filtration and removal of the solvent *in vacuo* resulted in 5.12 g (26.9 mmol, 99%) of a 3/1 mixture *meso*/(±)-**1** as a white solid.
R_f ((±)-**1**): 0.20 (toluene/*i*PrOH 95:5); R_f (*meso*): 0.29 (toluene/*i*PrOH 95:5).The ratio *meso*/(±)-**1** was determined by integration of the ^{1}H-aromatic signals *meso*: δ = 7.14 (2H, s) ppm; (±)-**1**: δ = 7.10 (2H, s) ppm and confirmed by reversed phase HPLC: Phenomenex Luna (2) C18 4,6 x 250mm 5µm, H_2O (5mM NH_4OAc)/CH_3CN 70/30: retention times **4** = 5.2 min, (±)-**1** = 7.3 min, (±)-**2** = 13.0 min, *meso*-**1**= 13.8 min

3,6-Dihydro-*as*-indacene (**5**)

The meso/(±)-**1** 3/1 mixture (5.12 g, 26.9 mmol) was dissolved in dry benzene (500 mL) and after heating to 80 °C, *p*-TSA·H_2O was added (51 mg, 0.268 mmol, 1 %). The mixture was subsequently refluxed in a Dean-Stark apparatus for 160 minutes, cooled to room temperature and poured into 5% aqueous $NaHCO_3$ (200 mL). The organic layer was dried with Na_2SO_4. The slightly yellow solid, obtained after filtration and removal of the volatiles, was dissolved in *n*-hexane/CH_2Cl_2 (2/1) and purified by chromatography on silica gel (150 mL, eluent: *n*-hexane) resulting in 3.68 g **5** (23.9 mmol, 89 %) as a white solid.
Rf: 0.55 (n-hexaan/Et_2O 95:5); m.p. = 99−100 °C; ^{1}H NMR (300 MHz, $CDCl_3$): δ (ppm) = 3.45 (dd [app. t], J= 1.9, 1.9 Hz, 4H), 6.60 (dt, J= 5.7, 1.9 Hz, 2H), 7.10 (dt, J= 5.7, 1.9 Hz, 2H), 7.34 (s, 2H); ^{13}C NMR (75 MHz, $CDCl_3$): δ (ppm) = 39.0 (CH_2), 119.8 (CH), 130.0 (CH), 134.1 (CH), 137.5 (C), 142.0 (C); MS (m/z, %): 154 (71, M+), 153 (100), 152 (42), 76 (33); IR (KBr): 3054, 2898, 2882, 1624, 1430, 1394, 1384, 1313, 1118, 962, 916, 794, 704 cm^{-1} Elemental analysis. Calculated for $C_{12}H_{10}$: C, 93.46; H, 6.54 Found: C, 93.21; H, 6.72.

$(-)_{365}$-(1*R*,2*S*,7*S*,8*R*)-1,2,7,8-di-epoxy-3,6-dihydro-*as*-indacene (**3**)

4-Methylmorpholine *N*-oxide (381.5 mg, 3.26 mmol, 5 eq) and Mn-(*R*,*R*)-Salen (20.7 mg, 0.033 mmol, 5%) were dissolved in CH_2Cl_2 (7.5 mL) after which the mixture was cooled to −78 °C. Diene **5** (100.6 mg, 0.65 mmol) was added at −78 °C and after dissolution, *m*-CPBA (~90% purity, 378 mg, 2.0 mmol, 3 eq) was added in one portion. After 110 minutes, 1N aqueous NaOH (2 mL) was added and the mixture was then poured into 1N aqueous NaOH (8 mL) and CH_2Cl_2 (10 mL). The organic layer was washed with saturated aqueous $NaHCO_3$ (10 mL) followed by saturated aqueous NaCl (20 mL). The combined H_2O layers were extracted with CH_2Cl_2 (2 x 20mL). The combined organic layers were dried on Na_2SO_4, filtered, concentrated and filtered over silica gel (2 mL, pre-treated with a CH_2Cl_2/1% NEt_3 mixture). This resulted in 128 mg of a pale yellow solid. The product was recrystallized from toluene to obtain 93 mg of a white solid **3** (0.50 mmol, 77%, >98% ee, >98% de). The product can be sublimated at 150 °C/0.2−0.3 mmHg.

Sublimation >200 °C, α_D^{25} = −0.8, α_{365}^{25} = −128.6 (c=0.99, $CHCl_3$). ^{1}H NMR (500 MHz, $CDCl_3$): δ (ppm) = 2.99 (dd, J= 17.5, 2.7 Hz, 2H), 3.20 (d, J= 17.5 Hz, 2H) 4.18 (dd [app. t], J= 2.7, 2.7 Hz, 2H), 4.47 (dd, J= 2.7, 0.9 Hz, 2H), 7.12 (2H, s) ppm; ^{13}C NMR (75 MHz, $CDCl_3$): δ (ppm) = 34.3 (CH_2), 57.2 (CH), 58.2 (CH), 125.9 (CH), 137.9 (C), 141.9 (C); MS (m/z, %): 186 (100), 158 (50), 130 (72), 129 (60), 128 (68), 115 (58) Analysis on Chiralcel OD−H column, see supporting information: IR ($CDCl_3$) : 3050, 2914, 2252, 1459, 1420, 1367, 1231, 1207, 1037, 1005, 983, 910, 831, 808, 753, 714, 622 cm^{-1}; HRMS found: [M+H]+: 187.0761; calculated for $C_{12}H_{11}O_2$: 187.0758. Elemental analysis. Calculated for $C_{12}H_{10}O_2$: C, 77.40; H, 5.41 Found: C, 77.31; H, 5.50.

(1*S*,8*S*)-1,2,3,6,7,8-Hexahydro-*as*-indacene-1,8-diol **1** and (8*S*)-8-hydroxy-3,6,7,8-tetrahydro-*2H*-*as*-indacen-1-one **2**:

A mixture of $[RuCl_2(\eta^6\text{-cymene})]_2$, (226 mg, 0.369 mmol), (*S*,*S*)-Ts-DPEN (282 mg, 0.770 mmol) and NEt_3 (145 μl, 1.04 mmol) was dissolved in degassed DMF (70 mL) and stirred for 1 h at 80 °C in a closed vessel under argon. At room temperature, this solution was added to **4** (4.71 g, 0.0253 mol) in a flask equipped with an argon balloon. After addition of HCOOH:NEt_3 (5:2 azeotrope; 35 mL) the mixture was stirred for 96 h. The solution was poured into H_2O (500 mL) and extracted with toluene (8 x 500 mL). After drying with Na_2SO_4, filtration and evaporation of the volatiles, the crude material (5.72 g) was purified by chromatography on silica gel with gradient elution (iPrOH/toluene, 1−5 %) resulting in three fractions: 0.43 g of an apolar fraction containing (8*S*)-**2**, 0.134 g *meso*-**1** (0.704 mmol, ~ 2 %) and 4.2 g of a more polar fraction containing (1*S*,8*S*)-**1** (>99 % ee). The polar fraction was further purified by crystallization from *n*hexane/benzene 50/50 resulting in 3.905 g (1*S*,8*S*)-**1** (20.53 mmol, 81 %, >99 % ee). The apolar fraction was further purified by chromatography on silica gel (pentane/acetone, 90/10) resulting in 247 mg (8*S*)-**2** (1.312 mmol, 5 %, 98 % ee)

Data for (1*S*,8*S*)-**1** from ref 14 (Chapter 6): For analytical purposes the product was crystallized twice from CH_2Cl_2. R_f : 0.20 (tolueen/*i*PrOH 95:5), mp = 155.5−156.5 °C; α_D^{20} = +70.5 (c 1.09, $CHCl_3$); ^{1}H NMR (500 MHz, $CDCl_3$): δ (ppm) = 1.91 (2H, dddd [app. dq], J= 8.4, 9.3, 9.3, 12.5), 2.56 (2H, dddd,

J = 2.0, 7.1, 7.5, 12.5), 2.77 (2H, ddd, J = 7.5, 9.3, 15.0), 2.94 (2H, ddd, J = 2.0, 9.3, 15.0), 5.47 (2H, dd [app. t], J = 7.1, 8.4), 7.10 (2H, s); ^{13}C NMR (125 MHz, $CDCl_3$): δ (ppm) = 29.7 (CH_2), 35.9 (CH_2), 75.6 (CH), 124.5 (CH), 140.6 (C), 141.1 (C) ppm; MS (m/z, %): 115 (40), 128 (67), 129 (100), 144 (74), 153 (48), 154 (34), 171 (28), 172 (64), 190 (M^+, 8); ES−MS: 129.0 (16), 155.0 (29) [M-2xH_2O+H]$^+$, 173.0 (100) [M-H_20+H]$^+$, 213.0 (6) [M+Na]$^+$, IR ($CDCl_3$) 2360, 2340, 2254, 1794, 1643, 1561, 1469, 1383, 1329, 1230, 1166, 1095, 1075, 918, 909, 902, 736, 651, 625, 543 cm^{-1}. Elemental analysis. Calculated for $C_{12}H_{14}O_2$: C, 75.76; H, 7.42 Found: C, 75.68; H, 7.51

HPLC: Chiralcel OD−H column, solvent: n-hexane/EtOH (97:3), flow rate = 1 mL/min, T= 35 °C, retention times: (1*S*,8*S)*-**1** = 14.2 min, (1*R*,8*R)*-**1** = 16.1min.

Data for (8*S*)-**2** from ref 14 (Chapter 6): For analytical purposes the product was crystallized twice from diisopropyl ether. R_f : 0.16 (CH_2Cl_2/EtOAc 98:2), mp = 108−110 °C; α_D^{25} = +98.2 (c 1.04, $CHCl_3$, >99 % ee); ^{1}H NMR (500 MHz; $CDCl_3$): δ (ppm) = 2.03 (1H, dddd [app. dq], J= 8.2, 9.5, 9.5, 13.0 Hz), 2.61 (dddd, 1H, J=1.8, 7.8, 8.0, 13.0), 2.69−2.80 (2H, m), 2.87 (1H, ddd, J= 8.0, 9.5, 15.9), 3.04 (1H, ddd, J= 1.8, 9.5, 15.9 Hz), 3.14−3.23 (2H, m), 5.58 (1H, dd, J= 7.8, 8.2 Hz), 7.34 (1H, d, J= 7.8 Hz), 7.44 (1H, d, J= 7.8 Hz); ^{13}C NMR (125 MHz, $CDCl_3$): δ (ppm) = 26.6 (CH_2), 30.3 (CH_2), 33.9 (CH_2), 36.5 (CH_2), 75.2 (CH), 126.0 (CH), 131.7 (CH), 133.5 (C), 142.2 (C), 144.8 (C), 154.8 (C), 210.2 (C); MS (m/z, %):188 (M^+, 52), 187 (25), 160 (100), 159 (59), 132 (28), 128 (27), 115 (31), 103 (9), 91 (14), 77 (17), 63 (14), 51 (18); ES−MS: 129.0 (10), 171.0 (100) [M-H_20+H]$^+$, 211.0 (4) [M+Na]$^+$; IR ($CDCl_3$) 2937, 2248, 1687, 1614, 1587, 1473, 1452, 1438, 1403, 1333, 1287, 1282, 1253, 1236, 1094, 1069, 920, 909, 904, 899, 839, 752, 740, 731, 647, 590 cm^{-1}. Elemental analysis. Calculated for $C_{12}H_{12}O_2$: C, 76.57; H, 6.43 Found: C, 76.46; H, 6.57.
HPLC: Chiralcel OD−H column, solvent: n-hexane/EtOH (98:2), flow rate = 1 mL/min, T= 35 °C, retention times= (8*S)*-**2** = 11.5 min , (8*R)*-**2**= 12.8 min.

Data for meso-diol see ref 14 (Chapter 6).

Chapter 7

Table S7.1 For compound **3**: Experimental Lorentzian fitted and B3LYP/cc-pVTZ vibrational frequencies, dipole strengths and rotational strengths taking into account the fundamentals of the 10 lowest energy minima (a−j).
Table S7.2 For compound **5**: Experimental Lorentzian fitted and B3LYP/cc-pVTZ IR frequencies, dipole strengths and rotational strengths taken into account the fundamentals of the 13 lowest energy minima (a−m).

Figure S7.1 Pictorial representation of the most contributing B3LYP/cc-pVTZ PES minima for (*R*)-**3**.
Figure S7.2 representation of most contributing B3LYP/cc-pVTZ PES minima for (*S*)-**5**

Table S7.1 For compound **3**: Experimental Lorentzian fitted and B3LYP/cc-pVTZ vibrational frequencies (ν, in cm^{-1}), dipole strengths (D, in 10^{-40} esu^2cm^2) and rotational strengths (R, in 10^{-44} esu^2cm^2) taking into account the fundamentals of the 10 lowest energy minima (a–j). B3LYP/cc-pVTZ vibrational frequencies are scaled with a factor 0.98.

	B3LYP/cc-pVTZ			experiment					
Fund	ν	*D*	*R*	ν	*D*	assign	ν	*R*	assign
27b	958.38	1.23	−1.14	969.92	29.81	27b+d	973.22	−2.58	27b+d
27f	958.83	0.12	−0.12	978.31	67.55	27a+c/28a+b			
27d	959.77	0.08	−0.10						
28b	969.46	42.60	−1.47				981.54	3.29	28a+b/27a+c
27c	969.68	0.04	−0.01						
27a	970.28	38.52	5.82						
28a	971.64	1.23	0.38						
27e	972.35	2.59	0.24						
28e	974.08	2.75	0.33						
28f	975.09	6.54	−0.51						
28d	1010.98	21.70	1.09	1014.15	73.00	28c+d	1020.41	6.91	28c+d
28c	1011.77	22.54	4.29						
29c	1019.93	2.85	−0.37	1031.30	105.69	29	1030.27	−6.94	29
29a	1023.43	36.85	−0.03	1044.81	40.24	30	1046.54	−22.22	30/29
29d	1024.06	4.31	−0.51						
29b	1024.50	48.40	−8.64						
29e	1025.10	7.45	0.15						
29f	1025.56	5.70	0.49						
30d	1025.87	4.30	1.53						
30c	1026.48	10.92	−1.46						
30b	1027.22	14.79	2.92						
30a	1027.30	47.48	−10.20						
30f	1033.37	2.01	−1.05						
30e	1033.75	2.59	−1.50						
30i	1033.90	1.89	0.34				1065.66	1.82	30i+g+h
30g	1035.52	2.85	0.65						
30h	1036.18	3.51	0.53						
30j	1039.99	2.05	−0.91				1082.45	−8.73	31g+h/30j
31h	1057.57	0.27	−0.38	non vis					
31g	1059.76	0.32	−0.43						
31a	1072.55	26.41	3.15	1084.61	43.44	31	1096.68	21.05	31
31b	1074.57	14.28	4.72				1105.69	10.94	32
31d	1078.46	0.93	0.56						
31c	1078.77	5.55	0.02						
31f	1086.87	5.19	1.96						
32d	1088.33	5.94	−1.36						
31e	1088.39	4.47	1.70						
32c	1088.62	2.70	−0.79						
32b	1100.76	21.70	7.97	1100.34	49.88	32a+f+g+e			
32a	1105.88	15.22	8.78						

32f	1107.80	2.18	−0.19						
32g	1107.94	2.02	−0.18						
32e	1113.23	2.01	−0.17						
33d	1119.55	9.04	−0.56	1132.22	65.31	33	1131.37	−10.43	33
33b	1120.27	23.48	−1.97						
33a	1121.71	41.77	−1.45						
33c	1121.98	11.52	−0.31						
33f	1122.28	6.60	−0.70						
33e	1122.69	8.94	0.22						
34a	1140.96	0.00	−0.01	1142.57	32.03	34	1158.96	2.22	34
34e	1143.03	1.10	0.18						
34d	1143.05	1.27	0.36						
34c	1144.02	0.08	0.08						
34b	1144.04	4.69	1.55						
34f	1148.79	1.45	0.09						
35e	1165.79	22.78	−3.16	1186.36	22.53	35	1188.29	7.09	35f
35f	1168.48	9.33	3.15	1196.02	45.66	35	1198.46	14.49	35
35i	1175.35	2.93	1.75	1207.46	47.86	35			
35d	1185.80	4.17	1.44						
35j	1185.90	3.30	0.99						
35b	1186.37	15.21	3.01						
35c	1189.70	2.52	1.94						
35a	1190.11	14.92	7.15						
36f	1209.32	2.65	−0.84	1218.88	26.91	36e+f+g	1225.62	−27.60	36
36e	1213.70	0.94	1.66	1231.12	37.56	36			
36g	1219.96	3.20	−1.71						
36h	1222.05	4.30	−1.45						
36a	1231.19	31.57	−1.85						
36b	1231.86	17.72	−2.49						
36d	1233.69	4.64	−0.42						
36c	1233.75	7.56	−0.85						
37b	1250.21	8.94	−2.62	1247.72	9.06	37/38c+d	1248.71	−5.09	37b+d
37d	1252.46	3.55	−1.54	1261.07	26.75	38c+d			
37f	1256.79	0.83	1.44				1266.90	5.03	38d+a/37a+c
37c	1258.14	5.03	0.74						
37a	1260.42	4.65	−1.15						
37e	1260.50	1.01	−1.34						
38c	1262.30	0.54	−0.65						
38d	1263.08	1.50	1.62						
38f	1267.04	0.79	−1.24	1279.31	15.60	38/39c+d	1282.73	−0.35	38a+b
38e	1267.75	0.31	0.30				1286.56	−1.44	38a+b
38a	1268.88	5.98	−0.40						
38b	1274.58	8.63	−1.59						
39d	1281.53	1.06	0.31				1295.85	2.57	39
39c	1282.11	0.37	0.47						
39e	1288.73	1.35	−1.24	1299.34	23.14	39/40			
39f	1290.17	1.44	−1.21						
39b	1297.61	16.62	11.26						

39a	1298.78	29.36	13.22						
40e	1303.56	1.36	1.05				1302.87	−1.48	40a+b+e+f
40b	1303.60	6.65	−5.73						
40a	1304.91	12.63	−7.58						
40f	1306.43	1.87	0.00						
40d	1324.22	2.91	1.12	1315.95	8.10	40d+c	1315.13	6.36	40d+c
40c	1324.55	3.26	1.37						
40h	1333.59	2.34	−0.41	1343.28	39.69	41/40h+g	1343.87	20.83	41
40g	1334.91	1.88	−0.20						
41c	1342.65	9.13	−1.38						
41a	1344.70	5.06	3.60						
41b	1344.72	4.66	4.46						
41d	1346.09	6.99	0.03						
41e	1346.86	0.87	1.80						
41f	1347.85	0.62	1.18						
42d	1369.36	2.05	−3.32	1384.81	104.44	42/43	1369.39	−17.13	42
42c	1370.44	2.35	−3.77						
42b	1373.03	6.26	−8.69						
42a	1373.90	7.73	−10.50						
42e	1378.12	5.47	0.58						
42f	1380.96	5.14	−0.02						
43a	1385.94	3.27	−3.05				1385.27	−5.37	43/44
43b	1387.50	2.32	−1.74				1397.21	−50.56	43/44
43e	1387.85	1.33	−0.41						
43f	1389.49	3.84	−0.84						
43d	1391.96	1.23	−0.52						
43c	1393.15	1.49	−0.53						
44a	1399.83	24.06	−9.27	1402.56	60.50	44			
44b	1399.96	15.77	−6.55						
44f	1402.49	1.48	0.70						
44c	1403.93	7.57	−2.65						
44d	1405.23	4.92	−1.79						
44e	1405.43	3.51	1.23						
45e	1450.00	0.38	0.40	1461.03	43.83	47/47/46/45	1436.67	3.51	45a+b+e+f
45a	1450.87	1.41	0.89	1468.77	128.65	48/47/46			
45b	1450.91	0.90	−0.74						
45f	1451.12	0.34	−0.15						
45d	1462.49	1.49	−0.89				1446.92	−4.74	47/46/45d+c
45c	1462.63	0.75	−0.52				1457.68	−7.44	47/46/45d+c
46a	1466.77	4.96	0.53						
46b	1468.85	4.08	0.62						
46e	1469.19	1.14	−0.12						
46f	1469.47	1.23	−0.34						
46d	1470.24	8.92	0.22						
47b	1470.77	38.44	−0.10						
46c	1472.26	1.04	−0.26						
47a	1472.65	49.46	−0.57						
47d	1472.89	0.63	−0.37						

47c	1474.17	10.39	0.08						
47f	1474.71	9.25	0.30						
47e	1475.63	10.73	−0.70						
48a	1479.78	5.11	1.11				1468.83	6.25	48
48d	1480.05	1.47	−0.33						
48e	1480.08	1.53	0.23						
48b	1480.12	3.92	0.76						
48c	1480.69	2.26	−0.05						
48f	1482.66	1.05	0.01						

Table S7.2 For compound **5**: Experimental Lorentzian fitted and B3LYP/cc-pVTZ IR frequencies (ν, in cm^{-1}), dipole strengths (*D*, in 10^{-40} esu^2cm^2) and rotational strengths (*R*, in 10^{-44} esu^2cm^2) taken into account the fundamentals of the 13 lowest energy minima (a−m). B3LYP/cc-pVTZ frequencies are scaled with a factor 0.98.

	B3LYP/cc-pVTZ			Experiment					
Fund	ν	*D*	*R*	ν	*D*	assign	ν	*R*	assign
29d	1014.25	1.58	0.02	1029.22	97.97	31/30/29d	1027.08	−12.03	31/30/29d
29e	1014.44	1.33	−1.02	1044.73	5.52	31			
30c	1022.91	3.24	−4.60						
30f	1023.56	1.70	−1.88						
30h	1023.58	3.39	−0.05						
31c	1023.99	9.44	2.10						
30g	1024.12	5.31	−0.03						
31f	1024.16	7.93	0.88						
30b	1024.16	16.22	−1.17						
30e	1024.32	13.13	−0.47						
30a	1024.47	24.55	0.43						
30d	1024.86	13.57	−0.45						
31a	1027.92	1.26	1.04				1044.31	8.56	31
31d	1028.36	1.32	−0.67						
31b	1028.44	1.05	1.48						
31g	1028.94	0.28	0.01						
31h	1029.91	1.10	0.24						
31e	1030.53	1.42	−0.16						
32c	1047.32	7.58	0.02	1056.28	7.84	32	1058.06	1.84	32
32f	1048.46	3.59	−2.10	1072.63	7.56	32	1069.71	−3.31	32
32h	1054.66	2.01	−0.03				1079.42	−3.07	32
32g	1058.97	1.53	−1.50						
32e	1070.20	2.69	−1.75						
32b	1070.83	4.85	4.27						
32d	1071.41	1.12	−1.21						
32a	1074.09	2.18	−0.22						
33e	1091.45	2.41	2.22	1093.60	10.40	33d+e	1089.42	3.29	33e
33d	1091.68	2.73	0.91				1094.95	4.70	33d
33h	1101.54	0.77	−0.44	1105.71	14.29	33a+g+h	1106.33	−4.92	33
33g	1102.20	1.22	0.12						

33a	1102.58	13.17	−3.77						
33b	1110.52	3.22	−1.60	1131.34	78.38	34/33b+f+c			
33f	1112.83	5.47	−0.04						
33c	1116.57	2.40	−0.92				1121.67	4.15	34/33c
34d	1118.32	12.63	1.38				1128.72	5.78	34/33c
34a	1119.30	17.25	0.67						
34g	1121.18	7.18	0.63						
34b	1121.87	19.35	1.15						
34e	1122.25	15.99	1.11						
34c	1123.11	19.03	0.60						
34h	1123.31	7.13	0.08						
34f	1123.90	10.93	0.09						
35b	1138.95	0.12	−0.11	1142.15	28.37	35	1140.08	−5.96	35
35g	1140.03	2.29	−0.76						
35e	1141.67	0.02	−0.05						
35f	1142.29	3.27	−0.80						
35d	1142.46	3.08	−0.95						
35a	1144.34	4.48	−1.06						
35c	1148.18	2.36	0.02						
35h	1148.31	0.50	0.05						
36i	1161.95	0.96	−1.33	not vis			not vis		
36j	1160.98	0.98	−0.25						
36d	1176.69	6.23	−5.68	1184.90	27.23	36	1182.17	−15.89	36
36a	1176.74	10.99	−8.27				1190.99	−5.08	36
36e	1177.84	4.37	−1.08						
36b	1178.21	5.25	−1.37						
36f	1179.03	3.55	−1.31						
36g	1181.89	1.91	−1.37						
36c	1183.98	8.64	−2.22						
36h	1184.48	2.59	−1.14						
37m	1196.75	1.02	0.41	1207.97	12.77	37k+l+m	not vis		
37l	1198.35	1.06	−0.12						
37k	1201.16	0.86	0.34						
37h	1211.89	0.44	0.56	1218.68	10.17	37	1209.91	10.54	37c+h+g+f
37c	1212.71	2.29	1.38						
37g	1213.31	1.17	1.41						
37f	1214.76	2.12	2.67						
37a	1218.61	0.76	0.23				1220.39	−1.89	37a+b
37b	1219.79	2.99	−2.75						
37d	1224.00	0.18	1.20				1228.71	2.75	37d+e
37e	1225.13	1.25	0.08						
38h	1246.17	0.12	0.24	1247.86	4.31	38	1246.23	−1.18	38
38g	1246.78	0.62	−0.09				1249.31	8.50	38
38f	1249.88	2.62	0.47				1255.82	11.88	38/39
38c	1251.31	1.29	0.68						
38a	1251.67	4.80	−1.14						
38d	1253.72	1.88	−0.56						
38e	1260.59	0.57	2.09	1258.61	8.36	38e+b/39			

38b	1261.05	1.45	1.31						
39g	1261.08	0.42	0.56						
39c	1261.57	1.66	0.77						
39d	1262.23	0.62	2.29						
39h	1262.38	0.57	0.72						
39e	1263.28	0.69	−0.39						
39f	1266.82	2.47	0.85						
39a	1274.79	0.77	2.45	1276.45	7.39	40/39a+b			
39b	1275.62	0.33	1.06						
40e	1280.81	0.45	−0.73						
40d	1281.48	1.25	−0.55						
40b	1283.82	0.92	1.39						
40a	1283.92	5.52	6.01						
40g	1283.95	0.92	−0.19				1276.65	−2.81	40g+h
40h	1285.56	0.17	−0.06						
40f	1300.76	0.52	0.98	1301.97	1.51	41/40c+f	1288.58	4.96	41/40f+c
40c	1300.78	1.94	1.49				1301.71	7.33	41/40f+c
41c	1306.77	0.16	−1.69						
41f	1307.06	0.23	−1.61						
41d	1309.61	1.80	2.07						
41e	1309.69	1.47	1.74						
41a	1310.65	2.01	2.57						
41b	1312.05	2.48	0.83						
41h	1326.88	2.60	1.40	1319.07	2.00	41hg			
41g	1329.15	2.72	0.95						
42g	1338.27	0.10	0.48	1338.42	11.38	42	1343.57	−36.50	42
42h	1339.70	0.04	0.28	1345.05	13.85	42			
42c	1345.91	0.79	0.62						
42a	1347.05	9.19	−9.70						
42b	1347.35	7.27	−5.77						
42f	1347.54	0.64	−0.13						
42d	1352.05	1.75	−4.43						
42e	1352.86	2.25	−4.70						
43e	1359.93	7.06	1.90	1356.26	10.95	43	1357.01	5.27	43
43d	1364.28	9.05	1.53	1362.91	17.92	43			
43a	1365.88	5.54	1.19						
43b	1365.90	2.02	0.10						
43f	1366.43	0.74	−1.48				1373.47	−6.24	43
43g	1366.47	0.29	−1.03						
43c	1366.97	1.04	−1.69						
43h	1368.69	0.17	−0.67						
43l	1373.33	0.46	−0.57						
43k	1374.34	0.97	−0.34						
43m	1374.50	0.60	−0.58						
44f	1385.01	0.33	0.37	1381.79	20.21	44	1383.72	3.92	44
44a	1385.10	0.37	0.19						
44c	1386.04	0.55	0.62						
44b	1386.55	0.31	0.20						

44d	1389.73	3.42	0.29						
44g	1391.59	0.76	0.19						
44e	1391.60	2.78	0.11						
44h	1393.05	0.60	0.13						
45a	1402.76	14.00	4.24	1397.58	52.24	45	1395.96	5.05	45
45b	1403.78	11.49	3.18	1404.76	37.56	45	1401.30	14.91	45
45c	1404.12	8.44	3.21						
45h	1404.20	2.93	0.64						
45f	1406.25	5.89	2.62						
45g	1407.93	3.02	0.70						
45e	1408.99	8.70	1.91						
45d	1409.30	6.39	1.61						
46a	1452.61	0.62	0.61	1448.49	1.37	46a+b	1438.10	−2.30	46a+b
46b	1452.98	0.56	−0.52						
46f	1458.75	0.16	0.10	1458.79	15.05	49/48/47/46	1448.25	2.30	46d+c
46c	1458.82	0.29	−0.22	1467.59	186.74	49/48/47/46			
46d	1459.61	2.03	1.33	1485.27	2.98	49/48/47/46			
46e	1459.88	0.78	0.67						
46g	1462.59	0.40	0.47						
46h	1464.49	0.18	0.29						
47f	1464.79	1.60	−0.51						
47c	1465.17	2.36	−0.83						
47b	1469.80	1.64	0.26				1463.52	2.02	48/47
47d	1469.99	16.52	−0.46						
47a	1470.36	36.21	−0.75						
47g	1470.53	7.44	0.19						
48a	1470.80	2.64	0.76						
47e	1471.17	1.23	0.18						
48d	1471.77	1.05	0.47						
48f	1471.95	14.61	0.25						
47h	1472.01	0.60	0.09						
48g	1472.44	0.74	0.11						
48b	1472.99	23.95	−0.26						
48c	1473.64	20.45	0.64						
48h	1474.20	6.46	0.02						
48e	1474.35	15.83	−0.18						
49d	1478.65	2.44	0.48				1468.95	−4.21	49
49a	1478.82	4.02	−0.83				1482.76	−2.05	49
49g	1479.11	0.83	0.25						
49h	1479.51	0.96	0.06						
49e	1479.61	3.09	−0.07						
49f	1480.84	1.54	−0.37						
49c	1481.08	2.07	−0.38						
49b	1481.89	2.56	−0.43						

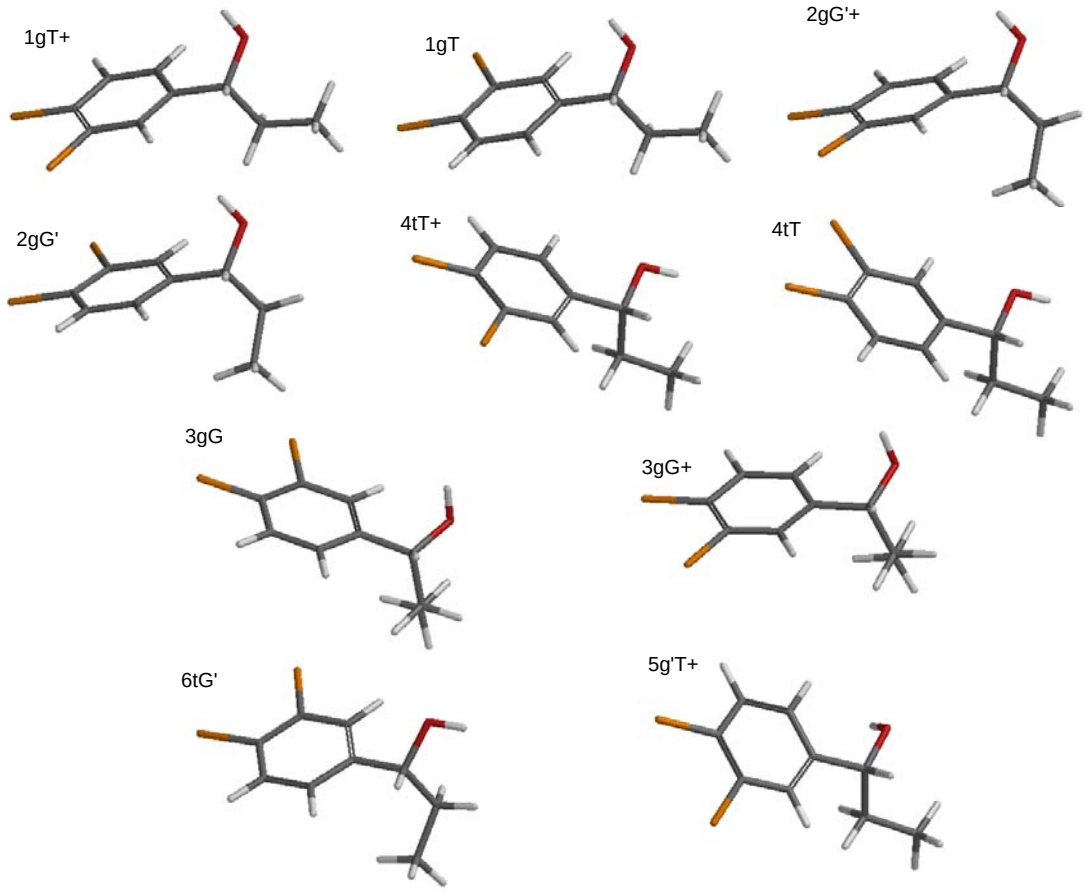

Figure S7.1 Pictorial representation of the most contributing B3LYP/cc-pVTZ PES minima for (*R*)-**3**.

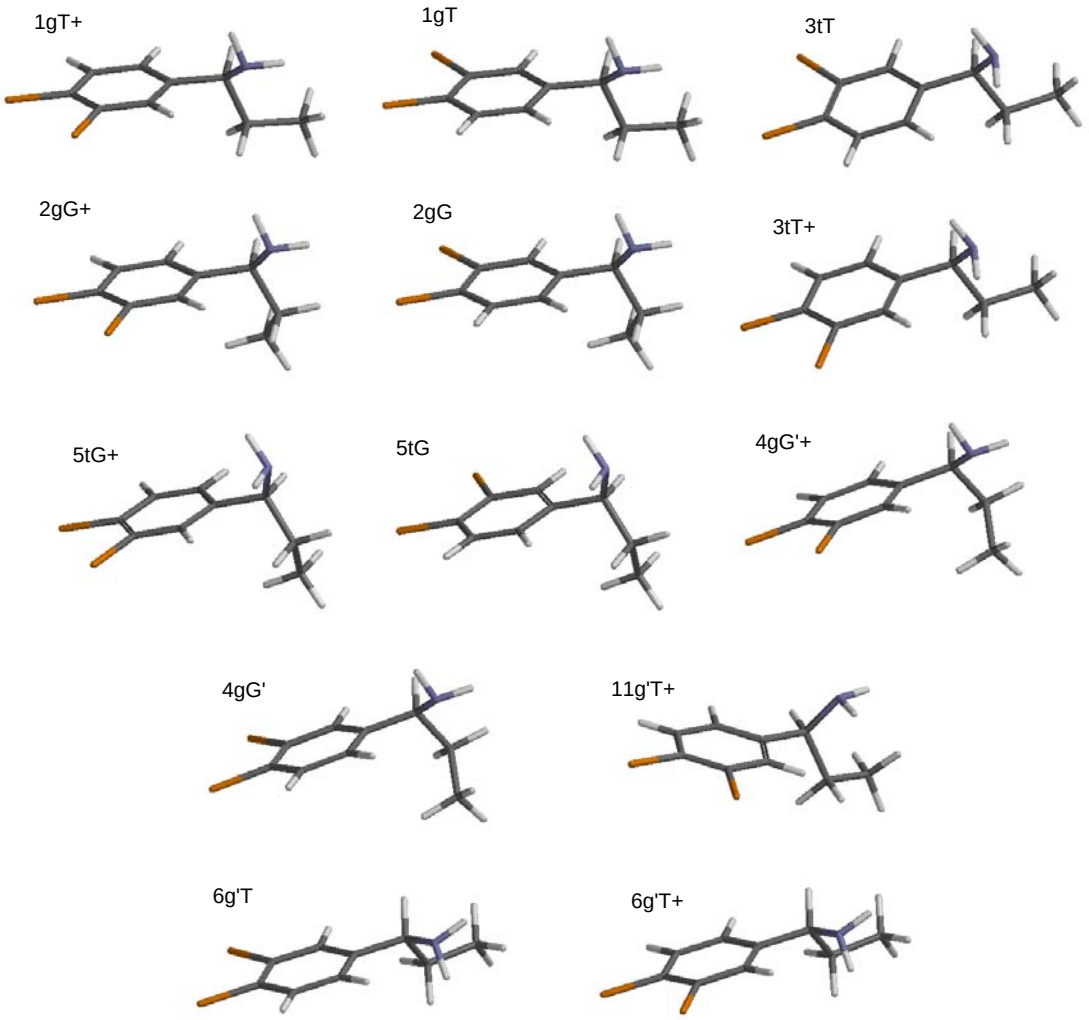

Figure S7.2 Pictorial representation of most contributing B3LYP/cc-pVTZ PES minima for (*S*)-**5**

Chapter 8

8.2 Intermolecular association of tetrahydrofuran-2-carboxylic acid in solution: A vibrational circular dichroism study

Table S8.1 B3LYP/6-31++G** conformational description monomer **1**
Table S8.2 B3LYP/ cc-pVTZ conformational description monomer **1**
Table S8.3 B3LYP/ 6-31++G** conformational description dimer **1**
Table S8.4 B3LYP/aug-cc-pVTZ monomer normal modes
Table S8.5 B3LYP/aug-cc-pVTZ dimer normal modes

Figure S8.1 The OH and CO stretching regions for solutions of (*R*)-(+)-**1** in CS_2
Figure S8.2 $CDCl_3$ and CS_2 simulated and experimental spectra
Figure S8.3 Simulated IR DFT/6-31++G** spectra for different functionals
Figure S8.4 Simulated VCD DFT/6-31++G** spectra for different functionals

8.4 A DFT conformational analysis and VCD study on methyl tetrahydrofuran-2-carboxylate

Table S8.6 DFT/6-31G* conformational description **3**
Table S8.7 DFT/cc-pVTZ fundamental assignment tables
Figure S8.5 Simulated (*S*)-(+)-**1** IR DFT/cc-pVTZ spectra for different functionals and experimental spectrum.
Figure S8.6 Simulated (*S*)-(+)-**1** VCD DFT/cc-pVTZ spectra for different functionals and experimental spectrum.

Table S8.1 B3LYP/6-31++G** label, pseudo-rotational coordinates (q in Å and φ in degrees), key dihedral angles (τ_1 and τ_2 in degrees), relative free energies (ΔG^0 in kcal/mol) and Boltzmann populations (% P, 298.15 K) for the unique monomer minima of **1**. Minimum G and H are not reported.

label	q	φ	τ_1 $O^8C^6C^2O^1$	τ_2 $O^7C^6O^8H^9$	ΔG^0	% P
A	0.37	260	−3	182	0.00	38.79
B	0.36	77	5	180	0.09	33.25
C	0.35	108	152	−1	0.94	7.96
E	0.34	98	−30	−1	0.99	7.32
F	0.37	239	−39	−1	1.07	6.35
D	0.36	227	153	−1	1.07	6.32

Table S8.2 B3LYP/cc-pVTZ label, pseudo-rotational coordinates (q in Å and φ in degrees), key dihedral angles (τ_1 and τ_2 in degrees), relative free energies (ΔG^0 in kcal/mol) and Boltzmann populations (%P, 298.15K) for the unique monomer minima of **1**

label	q	φ	τ_1 $O^8C^6C^2O^1$	τ_2 $O^7C^6O^8H^9$	ΔG^0	%P
A	0.36	256	5	180	0.00	35.8
B	0.36	78	−1	181	0.05	32.8
C	0.34	113	155	−1	0.73	10.7
D	0.36	226	157	−1	0.92	7.6
F	0.36	239	−36	0	0.96	7.1
E	0.34	99	−24	0	0.99	6.7
G	0.35	108	155	177	5.98	0.0
H	0.36	225	156	177	6.24	0.0

Table S8.3 B3LYP/6-31++G** label, symmetry, pseudo-rotational coordinates (q in Å and φ in degrees), key dihedral angles (T in degrees), relative enthalpies (ΔH^0 in kcal/mol), relative free energies (ΔG^0 in kcal/mol) and Boltzmann populations (% P, 298.15K) for the unique dimer minima of **1**.

Label		q_1	φ_1	T_1 $O^8C^6C^2O^1$	q_2	φ_2	$T_{1'}$ $O^{8'}C^{6'}C^{2'}O^{1'}$	ΔH^0	ΔG^0	% P
EC	C_1	0.34	101	−32	0.34	107	154	0.22	0.00	17.8
CC	C_2	0.34	105	153	0.34	105	153	0.14	0.14	14.0
FE	C_1	0.36	238	−38	0.34	105	−30	0.49	0.16	13.6
FD	C_1	0.36	235	−36	0.36	230	154	0.00	0.28	11.2
DC	C_1	0.36	232	152	0.35	103	153	0.12	0.30	10.8
FC	C_1	0.37	236	−38	0.34	108	153	0.07	0.30	10.7
ED	C_1	0.34	97	−33	0.36	231	152	0.20	0.51	7.5
DD	C_2	0.36	231	152	0.36	231	152	0.07	0.73	5.2
FF	C_2	0.36	236	−40	0.36	236	−40	0.26	0.77	4.9
EE	C_2	0.34	103	−29	0.34	103	−29	0.68	0.83	4.4

Table S8.4 B3LYP/aug-cc-pVTZ vibrational frequencies (ν, in cm^{-1}), dipole strengths (*D*, in 10^{-40} esu^2cm^2) and rotational strengths (*R*, in 10^{-44} esu^2cm^2) for different (*S*)-monomer conformations.

	A			D			E			C			B			F		
	ν	*D*	*R*	ν	*D*	*R*	ν	*D*	*R*	ν	*D*	*R*	ν	*D*	*R*	ν	*D*	*R*
1	42	218	−13	46	204	−7	30	293	−14	42	156	−21	57	249	−16	37	154	−11
2	87	48	7	50	107	5	48	156	16	55	272	15	88	36	7	47	125	16
3	197	129	−1	191	8	3	158	5	3	152	16	5	198	100	3	195	11	2
4	239	151	−4	248	33	8	249	77	−13	241	7	0	285	210	−16	255	10	−2
5	317	177	29	300	11	5	288	11	−4	298	5	6	327	125	24	282	76	−4
6	443	21	0	410	78	−8	435	20	8	407	76	−6	474	20	3	425	17	5
7	561	30	−22	591	348	−18	578	149	−9	572	212	37	565	73	−57	583	322	31
8	612	53	−38	603	134	24	585	444	57	606	360	−111	589	6	6	597	195	10
9	678	28	4	640	253	−26	641	208	−13	641	145	47	678	41	1	628	392	−33
10	731	115	67	703	120	5	736	254	−33	738	218	13	752	350	0	691	63	18
11	743	308	−23	751	152	0	755	98	47	757	95	12	756	98	25	757	211	20
12	839	83	−49	812	31	3	819	4	−3	827	11	−5	822	7	5	818	34	−18
13	881	63	46	874	39	20	869	40	8	869	16	2	882	79	−32	880	39	32
14	906	29	−21	918	14	−14	900	43	4	906	12	12	907	60	10	911	44	−28
15	934	9	9	930	17	4	924	45	−14	925	38	−6	929	31	−13	933	8	−1
16	940	87	−3	950	58	41	939	98	−27	939	88	−25	938	68	−45	943	84	73
17	967	89	53	969	63	3	964	2	3	963	9	−8	968	29	−2	956	77	−13
18	1039	94	6	1033	15	−13	1042	33	19	1040	17	7	1053	88	38	1029	40	1
19	1079	429	−21	1100	1148	−50	1101	310	−65	1101	1118	28	1074	438	75	1088	277	51
20	1134	13	10	1112	318	−5	1108	353	79	1122	272	−22	1116	21	0	1123	288	−33
21	1188	41	50	1151	121	2	1172	439	20	1141	244	−33	1180	106	−11	1182	566	−17
22	1204	30	−32	1208	13	20	1197	57	20	1195	23	5	1193	16	−13	1205	26	24
23	1214	6	−23	1213	24	27	1203	95	−45	1204	21	−1	1221	10	−35	1209	6	−9
24	1261	11	−7	1257	8	−4	1257	17	21	1255	8	9	1263	15	13	1261	12	−2
25	1304	21	7	1291	3	13	1287	6	16	1284	20	35	1292	6	6	1306	1	−2
26	1329	8	2	1315	17	−21	1324	3	5	1304	22	10	1329	5	−2	1336	3	−12

27	1341	16	1	1330	14	19	1344	1	2	1325	3	3	1340	31	28	1338	4	3
28	1354	218	−85	1336	16	−16	1360	45	5	1347	4	2	1349	185	−70	1361	24	3
29	1375	621	65	1379	22	−5	1368	104	16	1389	22	−18	1375	581	122	1365	123	−24
30	1394	314	4	1401	45	−6	1393	9	−4	1405	26	1	1397	336	−5	1387	10	−2
31	1493	12	−1	1492	8	−2	1496	15	−2	1495	11	−1	1495	13	−4	1492	7	−1
32	1503	12	−2	1506	11	−5	1505	18	−3	1504	16	−7	1505	21	−3	1503	14	−1
33	1529	1	3	1528	5	1	1531	1	−2	1530	2	2	1530	3	−6	1526	2	1
34	1836	727	−83	1820	607	17	1798	701	−58	1817	578	43	1835	687	−76	1800	745	−49
35	3013	69	−7	3010	56	2	3021	86	5	3026	85	3	3016	73	7	3000	69	−4
36	3034	17	8	3052	29	−5	3054	20	6	3054	20	5	3047	20	5	3050	26	−10
37	3047	16	−15	3060	22	10	3058	11	−14	3061	16	−16	3050	10	18	3056	21	17
38	3056	24	3	3065	18	−6	3073	65	41	3075	59	45	3064	35	−14	3067	19	−12
39	3090	39	−30	3096	22	−32	3076	4	0	3078	3	8	3093	30	25	3093	35	−40
40	3104	30	26	3102	37	44	3102	24	−38	3101	14	−46	3105	34	−24	3101	31	49
41	3125	16	−3	3117	36	−13	3115	31	23	3113	41	27	3127	8	7	3118	30	−14
42	3614	173	−30	3734	71	4	3731	69	−4	3734	68	2	3605	181	−32	3737	74	−2

Table S8.5 B3LYP/aug-cc-pVTZ vibrational frequencies (*ν*, in cm^{-1}), dipole strengths (*D*, in 10^{-40} esu^2cm^2) and rotational strengths (*R*, in 10^{-44} esu^2cm^2) for different (*SS*)-dimer conformations.

	CC			FD			DD			EC			EE			DC			FF			ED			FC			FE		
	ν	*D*	*R*	ν	*D*	*R*	ν	*D*	*R*	ν	*D*	*R*	ν	*D*	*R*	ν	*D*	*R*	ν	*D*	*R*	ν	*D*	*R*	ν	*D*	*R*	ν	*D*	*R*
1	18	7	−1	23	354	−3	24	112	−1	18	506	1	21	30	−2	10	31	2	15	67	−4	20	432	−2	19	443	1	18	20	−1
2	30	154	7	30	280	−2	34	215	7	29	299	1	34	119	−28	25	181	6	23	145	7	27	354	−11	27	81	2	27	149	8
3	37	237	−15	32	138	−5	34	18	5	39	45	3	35	107	7	41	145	−12	32	369	22	37	17	1	30	393	−17	37	57	−13
4	41	6	−1	46	185	20	40	91	0	44	190	−34	43	384	24	46	49	−4	39	88	−20	43	76	−3	42	249	−2	46	342	8
5	48	55	5	52	59	−11	47	57	−15	53	195	23	45	11	−2	50	62	4	40	17	−3	55	252	12	48	45	16	52	48	−1
6	71	110	−3	72	7	−2	72	112	1	71	4	1	73	40	6	73	108	−3	74	23	6	73	8	−1	73	6	−1	74	18	4
7	84	14	−1	85	25	0	85	9	0	86	25	−1	82	53	2	85	14	0	81	53	1	84	23	0	85	28	−1	82	52	2
8	110	858	−14	112	249	4	113	680	−4	112	260	0	117	26	7	112	745	−11	115	80	4	113	203	5	108	281	−3	117	29	5
9	120	2	4	134	98	4	125	0	2	136	106	−5	119	3	−2	125	3	3	122	0	0	135	112	2	137	98	3	122	16	0
10	144	1	1	142	2	−2	140	1	1	140	14	7	154	2	−3	142	17	1	152	1	−3	144	2	−1	140	7	3	153	2	−3
11	167	5	−6	211	4	3	211	5	2	164	71	−2	171	2	2	173	57	2	206	3	3	177	4	2	163	106	−3	169	3	2
12	168	127	11	223	106	8	222	139	4	178	6	1	171	3	3	217	73	4	217	34	14	218	63	5	216	19	6	218	18	9
13	260	5	1	258	31	4	265	75	8	261	42	0	265	4	3	262	54	4	266	30	−1	263	88	2	265	3	3	269	26	0
14	274	18	−1	273	1	−2	268	0	0	278	130	−3	277	235	−9	273	10	1	267	0	1	276	118	−10	271	14	−1	271	104	−2
15	333	1	−4	307	183	−14	330	1	−3	302	97	−13	312	2	8	332	8	−1	303	0	2	303	96	−10	307	178	−16	309	26	5
16	336	248	41	362	495	13	350	276	35	353	360	12	323	665	−38	345	245	34	328	855	−31	359	403	10	355	435	17	326	759	−34
17	434	0	0	428	27	−3	436	0	−2	432	25	−6	460	0	−6	436	4	−1	455	0	−1	428	23	−4	431	29	−5	457	47	−7
18	462	455	5	473	402	3	450	452	7	480	497	12	480	684	−6	457	440	6	464	602	−22	477	473	12	474	448	4	474	589	−12
19	596	0	0	595	5	4	597	4	−4	596	12	0	596	0	1	597	20	−5	591	5	0	594	10	−1	596	7	9	593	11	8
20	597	11	−9	598	23	1	598	29	−3	597	4	−4	597	22	1	598	2	−3	593	13	20	598	20	−2	601	6	−6	597	11	3
21	652	7	−19	674	30	13	676	1	10	652	14	22	645	8	5	654	109	−18	668	0	0	652	57	25	657	135	−9	649	43	20
22	660	351	−21	686	262	−26	690	478	−67	658	255	−24	656	165	49	683	319	−29	689	143	−9	684	285	−35	681	137	−13	681	118	6
23	729	85	−5	700	73	8	697	70	−11	730	83	−12	728	80	−5	701	39	−5	697	59	11	702	38	−6	700	96	15	697	108	23
24	733	30	−25	702	109	−16	701	37	5	736	17	−1	733	9	3	728	60	−18	701	184	36	732	47	−3	734	58	−13	731	49	0
25	772	11	8	748	34	−3	745	12	−6	772	1	7	771	6	1	748	6	2	748	29	0	749	10	5	752	14	−3	752	12	−1
26	782	123	52	752	5	3	753	24	13	779	109	27	781	76	−8	778	81	30	755	10	−4	773	44	2	777	73	34	777	55	−9

27	838	29	38	835	16	17	835	9	−23	837	12	−2	837	18	31	835	7	12	836	18	−34	835	24	−1	838	32	−4	837	1	5
28	843	26	−7	841	32	−15	841	26	24	844	47	35	843	47	19	843	38	7	842	33	28	841	33	28	844	24	13	843	56	18
29	870	14	15	877	47	33	879	63	70	869	21	27	870	20	23	873	23	−6	879	14	−1	872	29	−7	867	12	−6	868	17	−12
30	870	27	−29	880	40	31	879	27	−4	869	18	−44	870	25	−45	876	47	31	879	64	64	876	46	31	880	40	31	881	40	33
31	908	0	0	916	22	−10	917	8	3	906	10	8	906	4	−2	909	15	15	915	1	1	907	12	7	909	15	16	906	8	8
32	909	29	31	919	18	−11	918	28	−26	909	15	15	907	15	16	919	17	−9	915	47	−21	918	18	−11	916	22	−11	916	25	−11
33	929	25	−33	932	15	2	933	8	25	928	40	−12	927	40	−41	930	34	−10	933	1	8	928	37	−11	929	40	−5	926	44	−11
34	929	37	18	934	10	1	933	21	−19	929	34	−7	927	45	19	932	16	2	933	25	−9	932	17	1	934	14	0	935	12	−1
35	944	13	−23	949	70	39	952	88	3	942	88	−38	943	23	−42	944	91	−29	948	131	37	945	92	−39	942	89	−26	941	96	−37
36	944	174	−34	953	50	43	953	19	78	943	99	−25	943	163	−31	953	54	41	948	8	47	952	51	41	948	67	40	948	69	42
37	965	4	−6	971	68	−9	976	4	−24	964	11	3	966	0	−1	965	11	3	969	38	−61	965	10	4	965	14	3	964	10	5
38	965	22	11	977	48	−12	979	140	25	966	11	5	966	22	11	977	63	1	970	65	34	977	71	0	971	51	−19	972	51	−13
39	983	5	−30	987	16	−13	990	5	−28	987	3	11	992	1	10	989	12	−19	980	1	6	989	3	−15	986	3	0	992	12	15
40	1019	490	10	1019	482	65	1022	386	78	1021	491	−14	1029	428	10	1021	459	28	1018	514	49	1024	437	52	1020	505	21	1027	403	40
41	1042	5	14	1031	47	−14	1033	11	15	1041	33	10	1042	12	21	1035	64	−38	1030	13	22	1035	84	−42	1032	52	−23	1032	95	−32
42	1043	83	0	1035	79	−49	1035	182	−104	1043	65	4	1044	136	−6	1042	55	1	1031	84	−62	1043	67	6	1042	47	6	1042	83	4
43	1111	18	97	1097	384	88	1104	673	−48	1107	404	168	1108	870	24	1105	384	−4	1093	745	18	1104	389	278	1096	374	47	1095	453	−2
44	1111	746	−23	1105	287	−27	1106	11	63	1111	384	−34	1109	13	88	1110	332	50	1096	0	−9	1106	400	−164	1111	346	32	1108	348	53
45	1125	460	−18	1128	227	93	1129	602	−73	1120	163	−25	1120	321	−32	1127	440	−52	1127	380	12	1119	153	−28	1126	207	14	1121	203	−25
46	1127	0	−10	1129	288	−91	1129	14	78	1126	224	−25	1122	3	−28	1128	105	37	1128	0	−2	1127	288	−10	1128	199	−25	1129	159	7
47	1194	170	−3	1206	15	−1	1206	7	19	1192	93	−7	1193	152	−10	1193	82	2	1204	32	−14	1192	68	−11	1195	93	7	1192	83	−4
48	1194	4	11	1207	20	1	1206	29	−22	1194	81	8	1193	7	−1	1201	32	−8	1204	2	13	1200	25	−4	1203	21	−13	1201	17	−9
49	1202	19	8	1208	23	32	1209	30	43	1201	21	−9	1201	11	34	1206	17	−4	1207	27	53	1207	18	−3	1206	19	4	1206	17	2
50	1203	34	−29	1211	24	30	1209	20	17	1202	19	−12	1201	29	−48	1211	22	33	1207	21	13	1211	24	31	1208	20	28	1208	24	31
51	1256	2	−1	1257	67	−1	1257	4	29	1253	17	−4	1254	3	−1	1257	42	13	1260	0	−3	1255	12	−3	1255	5	0	1252	24	−7
52	1256	17	9	1260	16	−12	1258	108	−33	1255	5	2	1254	48	−12	1257	9	1	1260	33	−22	1257	81	−5	1260	12	−6	1261	16	−13
53	1264	11	81	1271	314	76	1266	4	24	1271	493	69	1288	41	46	1265	21	46	1304	11	32	1271	329	76	1271	469	76	1286	21	27
54	1277	1139	112	1306	6	12	1277	797	155	1287	24	44	1288	4	7	1276	957	135	1305	1	−4	1290	33	30	1285	19	−6	1306	6	13
55	1287	0	3	1307	31	−41	1308	0	1	1288	20	−10	1315	1	−18	1287	35	−11	1319	13	−65	1308	32	−45	1306	6	12	1316	50	−2
56	1288	95	−44	1327	439	−20	1310	206	−134	1318	227	45	1319	299	75	1308	115	−76	1329	570	29	1318	224	33	1326	40	23	1326	266	−1
57	1326	0	4	1332	41	34	1334	11	32	1325	7	2	1335	3	−15	1325	7	2	1337	1	1	1333	7	19	1327	406	−27	1337	183	−1
58	1326	15	1	1336	37	−33	1334	0	3	1338	226	−29	1339	373	−55	1332	20	24	1337	9	17	1335	10	−2	1336	8	10	1339	10	−15

59	1345	7	−1	1337	1	1	1337	12	−17	1347	3	0	1348	3	6	1338	30	−26	1339	1	−2	1338	288	−51	1341	179	−9	1342	219	−23
60	1345	1	4	1341	170	−8	1338	71	−21	1349	99	33	1349	189	57	1347	4	1	1341	388	−27	1350	69	30	1346	12	−3	1348	217	40
61	1377	104	−69	1360	58	8	1373	128	−11	1360	81	42	1360	163	85	1373	85	−12	1358	120	17	1360	84	41	1360	62	9	1359	131	49
62	1379	2	10	1374	72	−10	1375	0	−2	1379	58	−37	1361	0	0	1379	39	−25	1359	2	−8	1374	66	−10	1379	65	−38	1360	7	2
63	1396	1	0	1387	15	1	1390	25	−25	1393	13	−6	1394	26	−8	1390	19	−9	1386	18	6	1391	20	−12	1388	13	0	1388	13	0
64	1397	7	0	1390	23	−15	1392	14	7	1396	5	−2	1394	3	−4	1397	4	0	1386	8	−6	1394	12	−7	1396	5	−2	1393	15	−6
65	1462	160	−44	1467	206	−18	1463	208	−44	1467	151	−17	1468	159	−9	1463	173	−43	1467	215	−24	1465	186	−17	1467	172	−20	1469	176	−18
66	1486	3	59	1491	10	22	1489	4	71	1490	4	34	1494	1	43	1488	4	69	1490	0	12	1491	10	43	1491	8	16	1491	3	11
67	1495	27	−4	1492	5	−1	1492	21	−5	1495	23	−6	1496	34	−10	1492	12	−2	1491	4	−2	1492	11	22	1493	1	1	1494	11	8
68	1496	0	−2	1494	3	14	1492	0	9	1496	9	5	1496	0	3	1498	12	−4	1494	0	5	1496	10	−9	1497	12	1	1496	7	13
69	1503	2	0	1505	10	9	1504	5	11	1503	19	6	1506	10	24	1504	10	−16	1503	8	25	1505	6	4	1504	19	7	1503	13	−2
70	1503	34	1	1505	15	−43	1504	14	−46	1506	23	−33	1507	33	−89	1506	17	1	1503	23	−71	1506	29	−59	1505	15	−16	1505	24	−59
71	1530	5	6	1526	8	−1	1527	12	−1	1530	3	3	1531	7	−5	1527	7	0	1525	5	−6	1528	7	1	1527	3	−5	1528	3	−4
72	1530	0	0	1526	2	−3	1527	1	0	1532	4	−5	1531	1	−4	1531	2	2	1525	2	−4	1532	3	−5	1529	3	3	1531	5	−5
73	1705	2	−60	1695	76	20	1707	3	−87	1693	58	−5	1683	8	150	1706	3	−75	1687	4	104	1693	66	14	1693	61	0	1685	6	126
74	1759	1412	77	1753	1614	−55	1761	1504	45	1751	1537	−9	1740	1756	−185	1760	1464	67	1743	1885	−146	1752	1576	−50	1751	1577	−13	1741	1818	−166
75	3022	250	4	3005	52	78	3005	13	243	3012	0	10	2997	0	3	3006	57	21	3004	2	126	3007	14	129	3006	56	75	3002	19	92
76	3022	2	−6	3007	64	39	3006	104	−199	3021	136	−1	3022	271	3	3021	129	−1	3004	124	−78	3009	41	−136	3010	7	−43	3005	56	−58
77	3030	0	−52	3012	2	−106	3021	0	−75	3024	122	6	3022	6	−8	3024	0	−63	3011	0	13	3016	136	5	3028	128	−2	3026	134	−5
78	3054	45	77	3050	44	−7	3050	70	36	3055	39	2	3055	54	86	3051	40	−3	3050	70	41	3051	44	−5	3050	42	−5	3049	40	−5
79	3054	13	−77	3051	40	−4	3050	10	−46	3055	26	13	3055	14	−60	3055	30	1	3050	11	−50	3054	30	7	3055	35	9	3055	35	13
80	3059	2	−35	3057	20	23	3056	38	73	3060	13	−19	3059	3	−41	3056	21	25	3057	25	59	3057	20	18	3059	18	12	3056	18	17
81	3059	24	−5	3057	18	14	3056	5	−23	3061	14	−18	3059	22	6	3060	13	−18	3057	12	−34	3061	15	−16	3061	16	−21	3060	12	−20
82	3073	103	−70	3064	19	−33	3063	19	−52	3074	57	38	3074	94	−43	3064	20	−41	3068	29	−52	3065	20	−25	3069	19	−25	3066	20	−24
83	3073	12	113	3067	19	−23	3063	18	−25	3074	62	44	3074	25	120	3073	50	14	3068	8	9	3075	60	31	3074	49	48	3073	50	40
84	3076	9	−25	3093	149	−83	3094	176	−181	3076	1	9	3077	19	11	3076	12	19	3093	257	−181	3078	14	18	3077	6	3	3079	11	4
85	3076	2	48	3095	87	−61	3094	6	29	3077	5	5	3078	0	−3	3095	78	−68	3093	0	−1	3095	140	−69	3094	131	−80	3093	173	−106
86	3101	40	42	3101	26	62	3101	32	20	3102	90	−70	3101	428	126	3101	44	44	3100	3	−43	3101	45	46	3101	28	64	3101	25	69
87	3101	18	−109	3101	46	46	3101	43	90	3102	5	14	3101	19	−114	3101	31	−24	3100	49	171	3102	50	−25	3102	47	−30	3102	111	−14
88	3113	268	107	3117	1158	391	3117	240	72	3113	875	172	3108	4687	66	3113	179	67	3116	1532	378	3113	1601	242	3113	811	147	3112	3784	259
89	3113	1	7	3118	112	−103	3117	4	41	3114	16	−7	3114	2	10	3117	89	38	3117	0	18	3116	1973	130	3117	1018	137	3116	981	7
90	3137	4926	63	3121	4119	−101	3128	5115	17	3122	4366	−19	3115	278	−144	3131	4997	34	3121	3906	−409	3118	1726	−195	3120	3505	−143	3118	514	−278

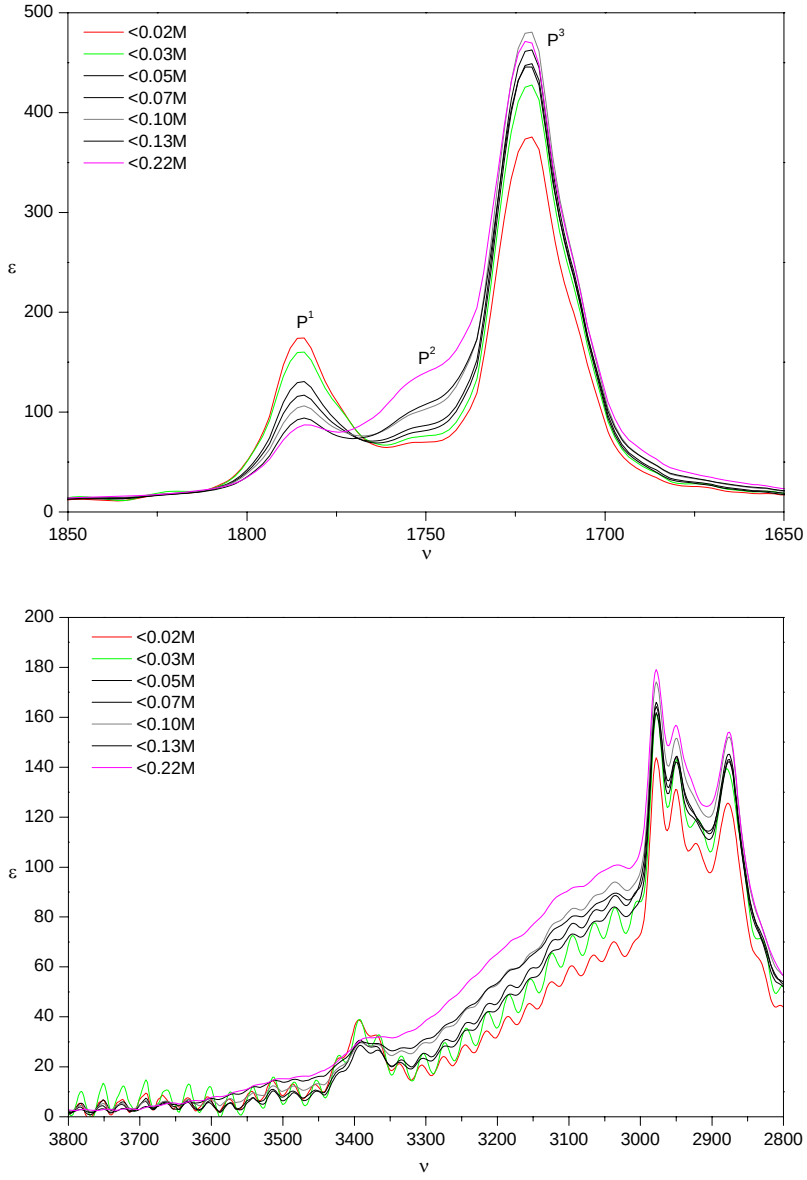

Figure S8.1 The carbonyl and hydroxyl stretching infrared regions (molar absorbtivity units) for solutions of (*R*)-(+)-**1** in CS_2. The concentrations are not exact due to bad solubility in CS_2 (oversaturated solutions) and vary within the ranges of 0.01 M and 0.22 M. Frequencies in cm^{-1}.

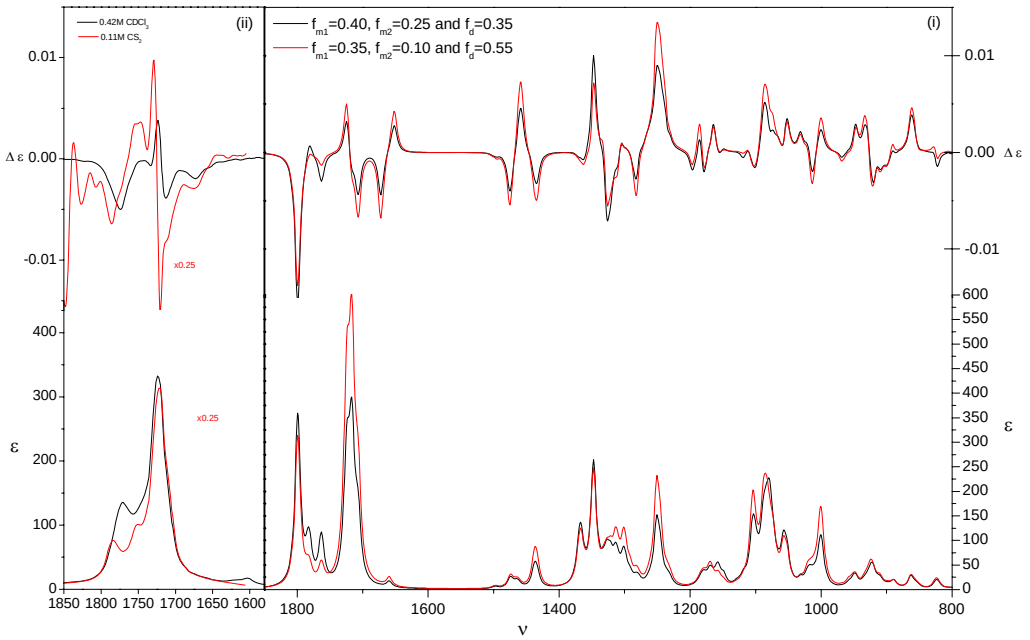

Figure S8.2 (i) B3LYP/aug-cc-pVTZ simulated spectra for different fraction of monomer and dimer; black spectra: f_{m_1} = 0.40, f_{m_2} = 0.25 and f_d = 0.35, and f_{m_1} = 0.35, f_{m_2} = 0.10, f_d = 0.55 based on an "educated guess" for CS_2 equilibrium fractions (there are indications for monomer solvent-solute stabilization in $CDCl_3$; the fraction of dimer in CS_2 is larger, the fraction of monomer **1** (A/B) only slightly lower, due to the extra stabilization of the intra-molecular hydrogen bond, and for monomer 2 (C/D/E/F) the fraction is low).
(ii) Experimental spectra for (*S*)-(−)-1 in $CDCl_3$ (0.42M) and CS_2 (0.11M) scaled down (factor 0.25). Intensities in molar absorptivity units, frequencies is cm^{-1}

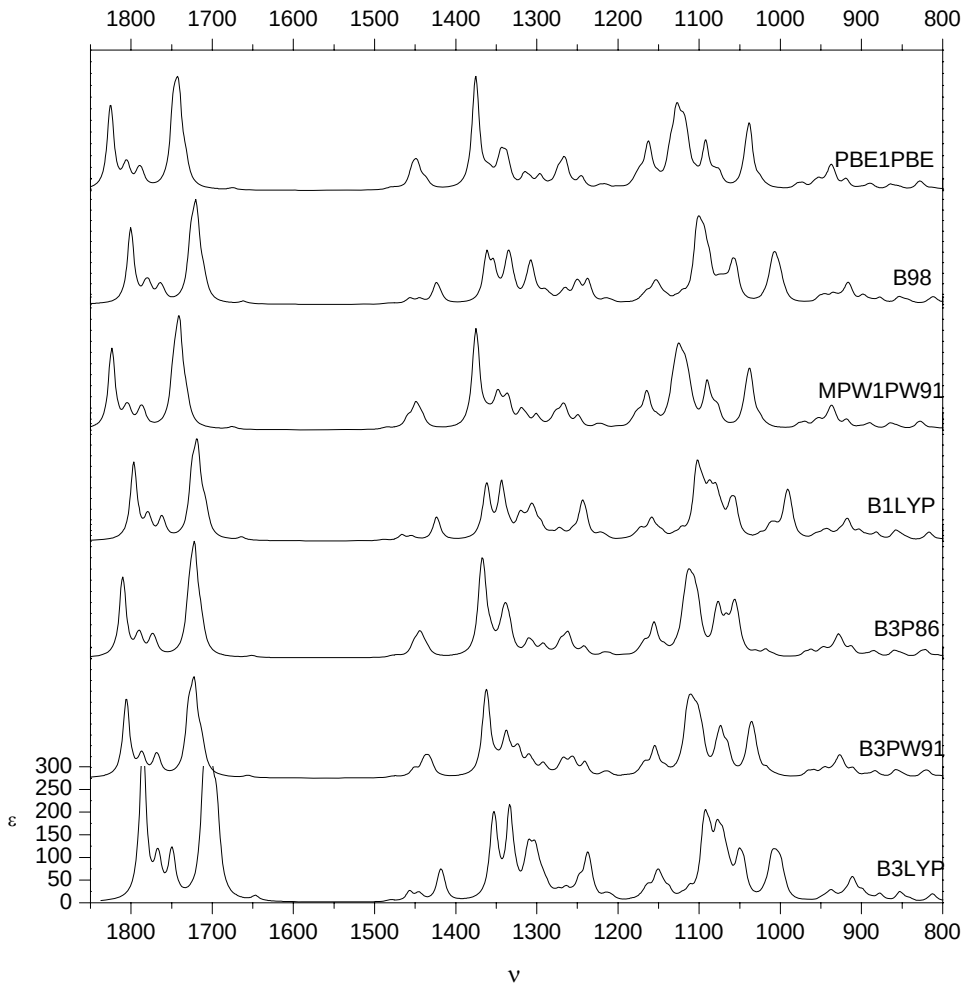

Figure S8.3 Simulated IR DFT/6-31++G** spectra for different functionals. Intensities are in molar absorptivity units, frequencies in cm^{-1}

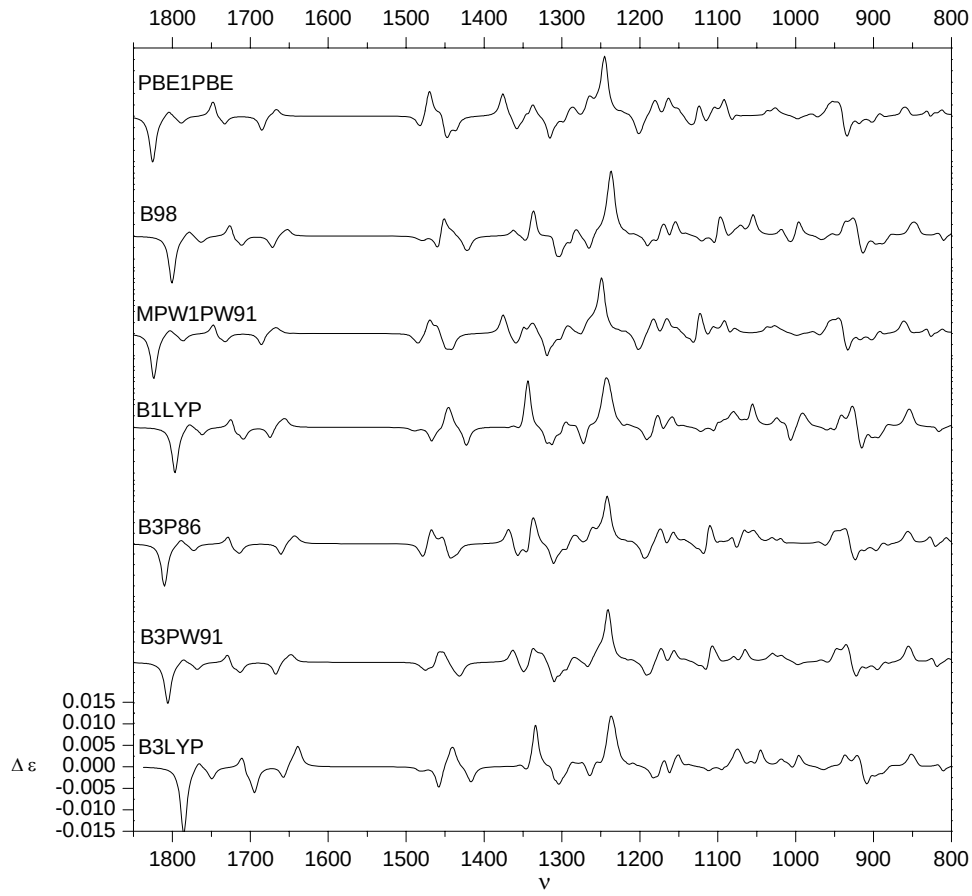

Figure S8.4 Simulated VCD DFT/6-31++G** spectra for different functionals. Intensities are in molar absorptivity units, frequencies in cm^{-1}

Table S8.6 DFT (B1LYP, B3LYP, B3P86, B3PW91, B98, BHandH, BHandHLYP, MPW1PW91 and PBE1PBE)/6-31G* label, pseudo-rotational coordinates (q in Å and φ in degrees), key dihedral angle (τ_1 in degrees), relative Gibbs energies (ΔG^0 in kcal/mol) and Boltzmann populations (% P, 298.15 K) for located conformations of **3**.

functional	conf	τ_1 $O^8C^6C^2O^1$	q	φ	ΔG^0	% P
B1LYP	U	147	0.37	226	0.00	28.24
	Y	111	0.37	228	0.01	27.69
	T	153	0.36	113	0.14	22.46
	X	−25	0.35	103	0.51	11.96
	V	−44	0.37	237	0.64	9.64
B3LYP	T	152	0.36	112	0.00	34.43
	Y	109	0.38	228	0.03	32.71
	X	−24	0.35	103	0.38	18.23
	V	−43	0.37	237	0.51	14.63
B3P86	T	154	0.36	113	0.00	27.28
	U	151	0.38	224	0.04	25.69
	Y	107	0.38	227	0.17	20.54
	X	−19	0.36	105	0.34	15.37
	V	−40	0.37	237	0.53	11.12
B3PW91	Y	112	0.38	229	0.00	38.30
	U	150	0.37	226	0.36	20.98
	T	154	0.36	112	0.38	20.33
	X	−19	0.36	103	0.72	11.44
	V	−40	0.37	238	0.86	8.96
B98	T	155	0.36	116	0.00	34.03
	U	152	0.37	222	0.03	32.27
	X	−21	0.36	108	0.36	18.40
	V	−42	0.37	235	0.47	15.31
BHandH	T	159	0.37	117	0.00	36.93
	X	−18	0.37	111	0.30	22.35
	U	164	0.38	215	0.62	12.87
	V	−39	0.38	233	0.79	9.82
	Y	104	0.39	224	0.81	9.40
	W	73	0.38	84	0.86	8.64
BHandHLYP	T	156	0.35	113	0.00	33.55
	U	157	0.36	223	0.29	20.61
	X	−25	0.35	104	0.33	19.13
	V	−42	0.37	238	0.53	13.65
	W	83	0.36	83	0.56	13.06
MPW1PW91	T	155	0.36	114	0.00	35.86
	U	154	0.37	224	0.15	28.07
	X	−19	0.36	105	0.31	21.26
	V	−40	0.37	237	0.52	14.81
PBE1PBE	Y	111	0.38	227	0.00	34.05
	T	156	0.36	114	0.20	24.15

U	155	0.38	222	0.38	17.79
X	−18	0.37	107	0.51	14.36
V	−39	0.38	236	0.75	9.66

Table S8.7 Lorentzian fitted experimental and broadened DFT (B3LYP, B3LYP, B3P86, B3PW91, B98, BHandHLYP, MPW1PW91 and PBE1PBE)/cc-pVTZ IR/VCD frequencies (υ, in cm^{-1}) and dipole/rotational strengths (D in 10^{-40} esu^2cm^2 and R in 10^{-44} esu^2cm^2) accounting for the significant minima i.e. T, U, X, V and W. Harmonic frequencies are scaled with factor 0.98.

	B3LYP/cc-pVTZ			experiment					
Fund	v	*D*	*R*	v	*D*	fund	v	*R*	fund
21U	1015.4	5.3	−2.3	1039.0	65.1	21			
21T	1020.5	4.8	3.0				1035.4	9.4	21TXV
21X	1024.3	12.3	3.4				1045.0	3.8	
21V	1026.3	39.4	0.0				1054.4	0.4	
21W	1045.5	6.1	2.2	1074.0	81.1	21W/22/23	1067.8	2.9	21W/22/23X
22W	1057.5	81.4	8.9	1086.6	266.4		1075.4	7.7	
22V	1069.7	72.3	9.8	1097.3	193.5		1081.1	7.3	
22U	1083.1	111.6	10.0	1108.9	18.0		1085.9	14.0	
22X	1085.3	70.4	9.7						
22T	1088.2	106.7	11.9						
23X	1093.4	35.4	−5.2						
23W	1098.5	2.9	−2.4				1098.4	2.2	23
23T	1102.4	103.9	1.3				1101.1	2.6	
23U	1103.5	125.5	0.9						
23V	1107.6	20.0	−2.6						
24W	1151.5	0.9	0.5	1176.1	135.5	24/25/26WXT	1163.9	−3.8	24/25/26WXT
24T	1151.9	1.2	−0.8				1177.2	−19.7	
24U	1152.0	1.5	−1.1						
24X	1152.1	0.7	0.0						
24V	1152.3	0.6	0.1						
25X	1163.6	23.5	−0.9						
25T	1164.5	152.8	6.9						
25W	1168.1	23.6	−2.2						
25U	1171.3	120.5	−4.7						
26W	1172.2	35.2	−3.7						
26X	1173.1	3.1	−0.9						
26T	1174.6	9.2	−2.8						
25V	1180.7	7.8	3.7	1213.6	498.2	25V/26VU/27/28/29	1191.1	2.9	25V/26VU/27/28TUW
26V	1181.0	1.7	2.7	1255.5	77.0		1210.9	31.4	
27T	1183.4	7.4	0.6				1218.5	6.8	
26U	1184.2	4.4	2.4						
27W	1185.7	1.8	−0.3						
27X	1186.2	7.8	0.3						
27V	1187.1	4.4	1.0						
27U	1187.2	21.3	10.5						
28T	1192.5	168.1	4.0						
28U	1196.9	119.8	14.1						
28W	1204.5	108.1	4.9						
28X	1223.1	24.6	−6.4				1238.7	1.3	28XV/29/30TX
29T	1228.8	4.2	3.3				1245.6	−1.1	
29U	1233.1	0.3	−1.3				1259.1	−1.6	
28V	1235.5	4.8	−3.7				1261.2	2.4	
29W	1237.2	6.2	3.5						

29V	1259.4	127.4	−8.1	1281.2	111.4	29VX/30			
29X	1261.5	14.1	4.6						
30T	1263.5	2.0	2.5						
30X	1265.8	76.8	3.7						
30V	1280.8	0.9	−2.2				1275.8	−12.7	30VUW
30U	1281.9	8.0	−10.8						
30W	1289.2	0.2	−0.7						
31T	1298.0	1.0	0.4	1293.3	63.0	31/32	1283.9	−20.1	31/32UV
31X	1301.2	4.8	−2.8	1305.0	13.6		1293.8	−6.4	
31U	1303.1	5.5	3.3				1302.7	−1.8	
31W	1305.7	0.9	0.4						
32U	1310.1	3.8	−4.1						
31V	1311.7	3.2	−0.7						
32V	1312.2	0.2	1.1						
32X	1318.8	3.0	2.4				1314.3	6.7	32XTW
32T	1319.3	1.3	0.0				1322.6	3.4	
32W	1321.6	0.5	−1.0						
33V	1331.4	5.0	0.1	1338.2	3.8	33VX	1335.2	7.8	33VX
33X	1331.8	5.9	4.6						
33U	1347.4	12.5	−2.5	1351.8	40.3	33UT	1346.6	−4.3	33UTW/34
33T	1354.1	13.6	−7.5	1369.8	20.1		1352.3	−14.3	
33W	1359.1	0.9	1.2	1377.5	2.2	33W/34	1368.6	−6.4	
34V	1360.2	1.2	−0.3						
34U	1365.2	10.5	−1.5						
34X	1366.2	1.0	−0.5						
34T	1370.4	3.9	1.2						
34W	1371.3	11.4	0.6						
35T	1442.9	6.6	−0.8	1438.4	58.6	35	1436.7	−5.2	35
35U	1443.1	7.2	−0.7						
35X	1443.5	4.0	−0.4						
35W	1443.8	4.3	−0.1						
35V	1444.3	4.7	−0.3						
36U	1455.5	5.9	0.2	1449.9	34.7	36/37/38/39	1437.6	−5.9	36/37/38/39
36W	1455.7	3.1	0.0	1461.3	38.1		1442.9	−1.8	
36T	1455.7	6.2	0.3				1452.2	−1.9	
36X	1455.8	3.7	−0.1				1461.8	−2.5	
36V	1455.8	3.6	−0.1				1465.4	−0.3	
37W	1456.5	1.9	−0.5						
37U	1461.0	1.9	−0.4						
37V	1461.3	0.7	−0.1						
37T	1464.3	3.4	−0.4						
37X	1465.2	1.9	−0.5						
38W	1468.4	6.7	−1.3						
39W	1469.3	0.4	0.6						
38X	1469.7	4.1	0.4						
38V	1470.2	3.6	0.4						
38T	1470.5	6.7	−0.7						
38U	1470.6	6.7	−0.6						
39V	1473.3	2.1	0.1						

39T	1473.7	4.9	−1.9						
39U	1474.4	2.6	−1.2						
39X	1474.7	3.3	−0.1						
40U	1496.0	1.3	0.0	1487.2	5.5	40			40
40V	1497.1	0.3	0.0						
40W	1499.6	0.1	−0.3						
40T	1500.2	0.4	0.3						
40X	1501.9	0.2	−0.4						
41X	1751.3	82.3	−5.8	1733.9	214.1	41	1729.0	−1.5	41XVW
41V	1755.2	86.7	−4.7	1747.9	405.8				
41W	1757.1	54.4	3.4						
41T	1767.8	117.5	8.8				1746.0	3.1	41TU
41U	1771.4	114.7	1.1				1750.2	20.1	

	B1LYP/cc-pVTZ						experiment		
Fund	v	*D*	*R*	v	*D*	Fund	v	*R*	Fund
21U	1021.1	6.1	−2.3	1039.0	65.1	21			
21T	1025.5	5.1	3.1				1035.4	9.4	21TXV
21X	1029.9	13.5	3.6				1045.0	3.8	
21V	1033.3	41.1	0.1				1054.4	0.4	
21W	1052.1	7.7	2.1	1074.0	81.1	21W/22/23	1067.8	2.9	21W/22/23X
22W	1066.9	81.9	9.0	1086.6	266.4		1075.4	7.7	
22V	1078.8	71.6	10.2	1097.3	193.5		1081.1	7.3	
22U	1091.7	96.8	9.7	1108.9	18.0		1085.9	14.0	
22X	1094.8	66.4	7.6						
22T	1096.6	89.1	9.6						
23X	1101.1	40.2	−3.2						
23W	1105.8	2.8	−2.3				1098.4	2.2	23
23T	1110.9	123.0	3.4				1101.1	2.6	
23U	1112.4	143.8	1.8						
23V	1116.1	21.5	−2.7						
24W	1159.8	0.9	0.5	1176.1	135.5	24/25/26WXT	1163.9	−3.8	24/25/26WXT
24T	1160.2	1.2	−0.6				1177.2	−19.7	
24U	1160.3	1.5	−1.0						
24X	1160.3	0.7	0.0						
24V	1160.5	0.7	0.1						
25X	1171.6	23.2	−1.0						
25T	1173.2	139.6	7.3						
25W	1176.4	14.4	−1.7						
25U	1180.9	105.4	−6.0						
26W	1180.9	39.6	−4.4						
26X	1181.5	3.3	−0.7						
26T	1183.1	10.8	−3.1						
25V	1188.1	7.4	3.1	1213.6	498.2	25V/26VU/27/28/29	1191.1	2.9	25V/26VU/27/28TUW
26V	1189.2	1.9	3.3	1255.5	77.0		1210.9	31.4	
26U	1191.9	5.5	5.2				1218.5	6.8	
27T	1192.0	7.1	0.5						
27W	1194.0	1.4	−0.1						
27X	1195.0	7.2	0.3						

27V	1195.7	4.1	1.0						
27U	1195.7	17.4	8.6						
28T	1203.0	185.6	4.8						
28U	1206.6	139.9	14.9						
28W	1215.3	115.6	4.8						
28X	1231.7	22.2	−6.1				1238.7	1.3	28XV/29/30TX
29T	1236.7	4.1	3.3				1245.6	−1.1	
29U	1240.9	0.3	−1.3				1259.1	−1.6	
28V	1243.7	3.9	−3.3				1261.2	2.4	
29W	1245.2	6.4	3.6						
29V	1270.7	131.2	−8.5	1281.2	111.4	29VX/30			
29X	1271.5	7.8	3.9						
30T	1272.7	1.9	2.3						
30X	1276.5	88.2	3.8						
30V	1290.1	1.2	−2.4				1275.8	−12.7	30VUW
30U	1290.9	8.4	−11.0						
30W	1298.2	0.2	−0.7						
31T	1307.2	1.0	0.4	1293.3	63.0	31/32	1283.9	−20.1	31/32UV
31X	1310.5	5.5	−2.9	1305.0	13.6		1293.8	−6.4	
31U	1311.9	5.9	2.7				1302.7	−1.8	
31W	1315.1	0.9	0.5						
32U	1319.2	3.5	−3.7						
31V	1320.5	3.4	−0.9						
32V	1322.2	0.4	1.3						
32X	1327.9	3.2	2.5				1314.3	6.7	32XTW
32T	1328.1	1.3	0.1				1322.6	3.4	
32W	1330.4	0.5	−1.0						
33V	1341.2	5.1	0.2	1338.2	3.8	33VX	1335.2	7.8	33VX
33X	1341.3	6.2	4.7						
33U	1357.3	12.6	−2.8	1351.8	40.3	33UT	1346.6	−4.3	33UTW/34
33T	1364.2	14.1	−7.9				1352.3	−14.3	
33W	1369.1	0.8	1.2	1369.8	20.1	33W/34	1368.6	−6.4	
34V	1370.2	1.3	−0.3	1377.5	2.2				
34U	1376.0	11.1	−1.7						
34X	1376.2	1.1	−0.5						
34T	1380.9	4.6	1.1						
34W	1382.3	12.1	0.7						
35T	1453.6	6.5	−0.8	1438.4	58.6	35	1436.7	−5.2	35
35U	1453.8	7.1	−0.7						
35X	1454.1	3.9	−0.4						
35W	1454.7	4.3	−0.1						
35V	1454.9	4.6	−0.3						
36U	1465.4	5.7	0.2	1449.9	34.7	36/37/38/39	1437.6	−5.9	36/37/38/39
36T	1465.6	6.0	0.3	1461.3	38.1		1442.9	−1.8	
36W	1465.6	3.0	0.0				1452.2	−1.9	
36X	1465.7	3.6	−0.1				1461.8	−2.5	
36V	1465.7	3.5	−0.1				1465.4	−0.3	
37W	1466.2	1.8	−0.5						
37U	1470.6	1.8	−0.4						
37V	1470.9	0.7	−0.1						

37T	1473.9	3.3	−0.4							
37X	1474.8	1.8	−0.5							
38W	1478.2	6.6	−1.1							
39W	1479.1	0.3	0.4							
38X	1479.4	4.1	0.4							
38V	1479.9	3.6	0.4							
38T	1480.1	6.6	−0.6							
38U	1480.3	6.6	−0.6							
39V	1483.0	2.0	0.0							
39T	1483.5	4.7	−1.8							
39U	1484.3	2.5	−1.2							
39X	1484.5	3.2	−0.1							
40U	1506.2	1.2	0.0	1487.2	5.5	40				40
40V	1507.1	0.3	0.0							
40W	1509.5	0.1	−0.3							
40T	1510.2	0.4	0.3							
40X	1511.8	0.2	−0.4							
41X	1762.8	83.9	−5.8	1733.9	214.1	41	1729.0	−1.5		41XVW
41V	1766.9	88.1	−4.7	1747.9	405.8					
41W	1768.5	55.4	3.3							
41T	1779.4	119.6	9.0				1746.0	3.1		41TU
41U	1783.1	117.0	1.3				1750.2	20.1		

	B3P86/cc-pVTZ						experiment			
Fund	v	*D*	*R*	v	*D*	Fund	v	*R*	Fund	
21U	1030.0	11.1	−5.1	1039.0	65.1	21				
21T	1031.8	5.4	3.6							
21X	1039.6	16.0	3.1				1035.4	9.4		21XVW
21V	1049.8	33.4	−0.6				1045.0	3.8		
21W	1057.0	6.1	1.1				1054.4	0.4		
22W	1082.6	58.7	5.7	1074.0	81.1	22/23	1067.8	2.9		22/23W
22U	1086.5	14.9	4.5	1086.6	266.4		1075.4	7.7		
22V	1086.5	47.8	8.5	1097.3	193.5		1081.1	7.3		
22T	1091.7	8.1	−3.0	1108.9	18.0		1085.9	14.0		
22X	1093.5	23.1	−10.7							
23W	1095.8	5.1	−0.9							
23X	1112.5	84.6	14.8				1098.4	2.2		23XVTU
23V	1118.7	45.4	0.2				1101.1	2.6		
23T	1121.8	180.3	8.9							
23U	1124.7	192.5	5.6							
24W	1150.9	0.6	0.4	1176.1	135.5	24/25XWTU/26XWT	1163.9	−3.8		24
24T	1151.4	0.8	−0.4							
24U	1151.5	0.9	−0.6							
24X	1151.6	0.6	0.0							
24V	1151.7	0.5	0.1							
25X	1164.8	24.3	0.8				1177.2	−19.7		25XWTU/26XWT
25W	1168.5	1.2	−0.4							
25T	1168.6	98.4	9.1							
26X	1173.3	4.9	−1.2							

26W	1175.2	19.4	−2.8						
26T	1175.6	4.9	−4.0						
25U	1176.6	28.0	−6.2						
25V	1180.0	4.3	0.4	1213.6	498.2	25V/26VU/27/28/29TUW	1191.1	2.9	25V/26VU/27/28TUW
26V	1181.9	2.1	3.2	1255.5	77.0		1210.9	31.4	
26U	1183.5	5.2	−2.1				1218.5	6.8	
27T	1184.4	4.7	1.9						
27X	1185.5	11.1	0.3						
27V	1187.7	6.7	3.2						
27W	1187.9	6.5	−1.7						
27U	1189.9	23.0	14.2						
28T	1206.5	248.2	11.0						
28U	1208.8	168.0	21.3						
28W	1219.8	95.6	3.0						
28X	1226.0	14.1	−4.5				1238.7	1.3	28XV/29TUWX/30T
29T	1228.6	8.6	5.5				1245.6	−1.1	
29U	1232.2	1.4	−0.9				1259.1	−1.6	
28V	1235.8	2.1	−1.9				1261.2	2.4	
29W	1238.0	10.8	4.3						
29X	1259.2	1.3	3.3	1281.2	111.4	29XV/30/31/32			
30T	1262.9	2.6	1.1	1293.3	63.0				
29V	1271.2	17.1	5.7	1305.0	13.6		1275.8	−12.7	29V/30UXVW/31/32UV
30U	1276.6	12.5	−13.7				1283.9	−20.1	
30X	1280.5	77.3	6.7				1293.8	−6.4	
30V	1284.4	107.5	−18.0				1302.7	−1.8	
30W	1286.2	0.5	−1.5						
31T	1289.5	1.5	0.4						
31X	1296.2	35.9	−10.5						
31U	1297.3	5.2	4.9						
31W	1301.1	1.1	0.7						
32U	1305.2	7.5	−6.3						
31V	1306.0	1.6	−0.8						
32V	1308.9	9.6	1.6						
32X	1315.6	6.1	3.2				1314.3	6.7	32XTW
32T	1316.8	1.8	0.4				1322.6	3.4	
32W	1317.8	0.5	−0.8						
33V	1327.1	3.3	−0.1	1338.2	3.8	33VX	1335.2	7.8	33VX
33X	1328.1	9.5	7.9						
33U	1345.5	16.0	−1.9	1351.8	40.3	33UTW/34V	1346.6	−4.3	33UTW/34
33T	1353.2	21.2	−9.9				1352.3	−14.3	
33W	1356.7	0.3	0.6				1368.6	−6.4	
34V	1357.7	1.4	−0.2						
34X	1364.8	1.5	−0.3	1369.8	20.1	34XUZW			
34U	1365.8	15.1	−3.0	1377.5	2.2				
34T	1371.6	7.4	0.4						
34W	1374.2	13.5	1.2						
35T	1438.2	12.5	−1.6	1438.4	58.6	35	1436.7	−5.2	35
35U	1438.4	12.0	−1.1						
35X	1438.6	7.8	−0.6						
35V	1439.5	8.5	−0.6						

35W	1440.2	7.0	−0.1						
36W	1444.5	1.8	−0.5	1449.9	34.7	36/37/38/39	1437.6	−5.9	36/37/38/39
36U	1448.3	6.2	0.1	1461.3	38.1		1442.9	−1.8	
36X	1448.5	4.6	0.0				1452.2	−1.9	
36T	1448.5	7.4	0.4				1461.8	−2.5	
36V	1448.6	4.1	−0.1				1465.4	−0.3	
37W	1448.6	3.0	0.0						
37V	1450.8	0.8	−0.1						
37U	1450.8	2.6	−0.4						
37T	1453.4	4.8	−0.5						
37X	1454.4	2.8	−0.9						
38W	1458.6	3.8	−1.1						
39W	1462.7	2.3	0.4						
38X	1463.4	4.5	0.7						
38T	1463.7	6.8	−3.0						
38V	1463.8	1.9	−1.4						
39V	1464.0	4.6	2.0						
39T	1464.3	7.4	−0.1						
38U	1464.5	6.9	−0.2						
39X	1465.0	4.6	−0.1						
39U	1465.8	3.1	−1.9						
40U	1487.9	1.5	−0.1	1487.2	5.5	40			40
40V	1489.3	0.4	0.0						
40W	1492.6	0.0	−0.2						
40T	1493.1	0.7	0.5						
40X	1495.0	0.4	−0.4						
41X	1773.0	88.5	−6.7	1733.9	214.1	41	1729.0	−1.5	41XVW
41V	1777.2	86.7	−5.0	1747.9	405.8				
41W	1778.5	44.8	2.4						
41T	1789.5	125.5	10.0				1746.0	3.1	41TU
41U	1793.1	109.3	1.3				1750.2	20.1	

	B3PW91/cc-pVTZ			experiment					
Fund	v	*D*	*R*	v	*D*	Fund	v	*R*	Fund
21X	1037.7	14.5	3.0	1039.0	65.1	21XVW	1035.4	9.4	21XVW
21V	1046.3	36.6	0.0				1045.0	3.8	
21W	1055.9	5.9	1.2				1054.4	0.4	
22W	1080.0	60.9	5.8	1074.0	81.1	22/23W	1067.8	2.9	22/23W
22V	1084.4	51.6	8.2				1075.4	7.7	
22U	1085.8	23.2	5.2				1081.1	7.3	
22T	1090.6	8.3	−2.5				1085.9	14.0	
22X	1091.9	20.6	−9.8						
23W	1093.9	3.6	−1.1						
23X	1108.8	81.7	14.4	1086.6	266.4	23XVTU	1098.4	2.2	23XVTU
23V	1116.1	43.5	0.0	1097.3	193.5		1101.1	2.6	
23T	1118.3	180.5	9.7	1108.9	18.0				
23U	1120.8	220.5	6.3						
24W	1149.4	0.6	0.4	1176.1	135.5	24/25/26/27	1163.9	−3.8	24

24T	1149.9	0.7	−0.4						
24U	1150.0	1.0	−0.7						
24X	1150.0	0.5	0.0						
24V	1150.2	0.5	0.1						
25X	1163.8	22.4	−0.1				1177.2	−19.7	25XTWU/26XWT
25T	1166.9	101.9	8.3						
25W	1167.5	2.0	−0.6						
26X	1171.5	4.8	−0.6						
26W	1173.6	22.2	−2.8						
26T	1173.7	6.4	−3.8						
25U	1174.4	45.9	−7.9						
25V	1178.3	3.6	0.4				1191.1	2.9	25V/26VU/27
26V	1180.3	3.1	3.9						
26U	1182.1	5.5	−1.4						
27T	1183.1	4.0	1.7						
27X	1184.3	10.4	0.2						
27V	1186.0	7.3	2.8						
27W	1186.4	6.1	−1.7						
27U	1187.6	28.8	15.0						
28T	1201.7	222.4	8.9	1213.6	498.2	28/29TUW	1210.9	31.4	28TUW
28U	1204.4	177.7	22.2	1255.5	77.0		1218.5	6.8	
28W	1214.9	96.6	3.6						
28X	1225.1	14.8	−4.1				1238.7	1.3	28XV/29/30T
29T	1228.0	6.9	5.0				1245.6	−1.1	
29U	1232.3	0.9	−0.9				1259.1	−1.6	
28V	1234.9	2.3	−2.2				1261.2	2.4	
29W	1236.8	8.0	3.7						
29X	1258.7	1.2	3.0	1281.2	111.4	29XV/30/31/32			
30T	1262.1	2.2	1.4	1293.3	63.0				
29V	1269.8	29.5	7.1	1305.0	13.6				
30U	1275.3	14.2	−14.4				1275.8	−12.7	30UXVW/31/32UV
30X	1277.1	80.9	5.5				1283.9	−20.1	
30V	1279.6	104.2	−19.9				1293.8	−6.4	
30W	1285.5	0.4	−1.4				1302.7	−1.8	
31T	1288.6	1.4	0.2						
31X	1294.1	25.3	−8.4						
31U	1299.3	3.6	5.7						
31W	1299.5	1.0	0.7						
32U	1304.1	8.6	−7.6						
31V	1305.1	2.2	−1.2						
32V	1309.1	5.5	1.8						
32X	1314.5	5.2	3.2				1314.3	6.7	32XTW
32T	1315.6	1.4	0.6				1322.6	3.4	
32W	1316.3	0.4	−0.7						
33V	1326.7	3.6	−0.1	1338.2	3.8	33VX	1335.2	7.8	33XV
33X	1327.0	7.1	6.5						
33U	1344.9	17.0	−2.2	1351.8	40.3	33UTW/34	1346.6	−4.3	33UTW/34
33T	1351.6	18.5	−9.1	1369.8	20.1		1352.3	−14.3	
33W	1355.9	0.3	0.7	1377.5	2.2		1368.6	−6.4	
34V	1357.0	1.4	−0.2						

34X	1364.0	1.3	−0.3						
34U	1364.2	15.8	−2.9						
34T	1370.0	5.6	0.8						
34W	1371.5	12.5	1.1						
35T	1437.1	10.2	−1.3	1438.4	58.6	35	1436.7	−5.2	35
35U	1437.4	12.0	−1.1						
35X	1437.6	6.5	−0.5						
35V	1438.5	7.8	−0.6						
35W	1438.8	5.9	−0.1	1449.9	34.7	36/37/38/39			
36W	1444.4	1.7	−0.5	1461.3	38.1		1437.6	−5.9	36/37/38/39
36U	1448.0	6.8	0.1				1442.9	−1.8	
36X	1448.1	4.1	0.0				1452.2	−1.9	
36T	1448.2	6.7	0.4				1461.8	−2.5	
36V	1448.2	4.1	−0.1				1465.4	−0.3	
37W	1448.2	2.8	0.0						
37U	1450.1	2.9	−0.4						
37V	1450.3	0.9	−0.1						
37T	1453.0	4.2	−0.5						
37X	1454.0	2.4	−0.8						
38W	1458.1	3.8	−1.1						
39W	1461.9	2.2	0.4						
38X	1462.5	4.1	0.5						
38V	1463.0	3.0	−1.0						
39V	1463.1	3.5	1.5						
38T	1463.3	6.1	−2.9						
39T	1463.4	6.8	0.1						
38U	1463.6	7.6	−0.3						
39U	1464.4	3.3	−2.0						
39X	1464.6	4.1	0.0						
40U	1487.9	1.6	0.0	1487.2	5.5	40			40
40V	1489.2	0.3	0.0						
40W	1491.6	0.0	−0.2						
40T	1492.9	0.4	0.4						
40X	1494.5	0.3	−0.4						
41X	1768.7	81.7	−6.2	1733.9	214.1	41	1729.0	−1.5	41XVW
41V	1772.8	88.7	−5.1	1747.9	405.8				
41W	1775.4	44.6	2.5						
41T	1786.8	118.2	8.9				1746.0	3.1	41TU
41U	1790.0	123.3	0.9				1750.2	20.1	

	B98/cc-pVTZ			experiment					
Fund	v	*D*	*R*	v	*D*	Fund	v	*R*	Fund
21U	1016.4	8.2	−3.8	1039.0	65.1	21			
21T	1018.3	5.7	3.6						
21X	1024.7	14.4	3.2				1035.4	9.4	21XVW
21V	1032.3	30.8	−0.7				1045.0	3.8	
21W	1044.5	11.2	3.0				1054.4	0.4	
22W	1069.8	120.7	12.1	1074.0	81.1	22/23	1067.8	2.9	22/23W
22V	1077.4	53.4	10.5	1086.6	266.4		1075.4	7.7	

22U	1083.7	25.9	5.9	1097.3	193.5		1081.1	7.3	
22T	1089.6	15.5	−0.7	1108.9	18.0		1085.9	14.0	
22X	1090.7	19.4	−9.4						
23W	1094.5	3.8	−3.2						
23X	1100.5	72.7	12.9				1098.4	2.2	23XTVU
23T	1109.8	179.0	10.0				1101.1	2.6	
23V	1110.2	31.5	−1.7						
23U	1111.6	174.1	5.5						
24W	1154.0	1.2	0.7	1176.1	135.5	24/25/26/27	1163.9	−3.8	24
24T	1154.4	0.8	−0.1						
24U	1154.6	1.1	−0.7						
24X	1154.6	0.6	0.0						
24V	1154.8	0.6	0.1						
25X	1163.5	22.6	0.9				1177.2	−19.7	25/26XWT
25T	1167.1	113.3	8.7						
25W	1168.4	15.2	−2.8						
26X	1172.3	3.3	−1.9						
26W	1173.3	49.0	−6.6						
26T	1175.4	1.9	−3.2						
25U	1175.7	60.7	−7.8						
25V	1178.1	6.4	4.4						
26V	1181.6	2.0	0.9				1191.1	2.9	26VU/27/28TUW
26U	1182.8	10.0	9.5				1210.9	31.4	
27T	1184.0	10.9	0.4				1218.5	6.8	
27W	1185.2	2.6	1.6						
27U	1187.8	5.6	3.2						
27X	1188.4	5.3	0.2						
27V	1188.8	2.4	0.5						
28T	1200.4	210.6	6.5	1213.6	498.2	28/29TUW			
28U	1203.3	147.8	16.5	1255.5	77.0				
28W	1211.6	179.6	6.2						
28X	1223.3	15.5	−5.1				1238.7	1.3	28X/29
29T	1227.2	3.8	2.9				1245.6	−1.1	
29U	1230.7	0.3	−1.3				1259.1	−1.6	
28V	1234.0	2.9	−2.6				1261.2	2.4	
29W	1235.8	12.8	6.2						
29X	1257.7	2.9	3.5	1281.2	111.4	29XV/30TXVU			
30T	1259.3	2.6	1.8						
29V	1266.8	107.5	−2.8				1275.8	−12.7	29V/30XVUW/31
30X	1269.1	85.2	4.1				1283.9	−20.1	
30V	1274.8	10.5	−6.3				1293.8	−6.4	
30U	1277.2	10.3	−11.5				1302.7	−1.8	
30W	1288.3	0.6	−2.1	1293.3	63.0	30W/31/32			
31T	1290.8	1.0	−0.5	1305.0	13.6				
31U	1294.0	4.2	3.1						
31X	1294.7	10.2	−3.9						
31W	1298.1	1.3	0.9						
32U	1303.3	4.9	−4.5						
31V	1305.0	1.4	−0.6						
32V	1307.0	4.0	1.1						

32T	1312.0	1.4	0.2				1314.3	6.7	32TXW
32X	1313.3	5.8	2.6				1322.6	3.4	
32W	1317.1	0.7	−1.2						
33V	1327.8	4.3	−0.3	1338.2	3.8	33VX	1335.2	7.8	33VX
33X	1328.0	4.9	4.0						
33U	1344.8	13.4	−2.1	1351.8	40.3	33UTW/34	1346.6	−4.3	33UTW/34
33T	1351.3	17.7	−8.3	1369.8	20.1		1352.3	−14.3	
33W	1358.6	0.6	1.2	1377.5	2.2		1368.6	−6.4	
34V	1359.5	1.4	−0.2						
34U	1365.2	9.1	−1.2						
34X	1366.0	1.3	−0.4						
34W	1368.9	21.5	1.3						
34T	1371.0	3.8	1.0						
35T	1444.0	7.7	−0.9	1438.4	58.6	35	1436.7	−5.2	35
35U	1444.4	7.4	−0.6						
35X	1444.4	4.4	−0.4						
35W	1445.0	7.8	−0.1						
35V	1445.2	5.1	−0.4						
36W	1452.2	2.6	−0.5	1449.9	34.7	36/37/38/39	1437.6	−5.9	36/37/38/39
37W	1455.3	4.9	−0.1	1461.3	38.1		1442.9	−1.8	
36U	1455.3	5.1	0.1				1452.2	−1.9	
36V	1455.3	3.3	−0.1				1461.8	−2.5	
36X	1455.3	3.4	0.0				1465.4	−0.3	
36T	1455.4	6.1	0.4						
37U	1457.2	1.6	−0.2						
37V	1457.2	0.6	−0.1						
37T	1460.5	3.3	−0.3						
37X	1461.4	2.0	−0.6						
38W	1464.6	6.4	−2.0						
39W	1468.7	4.1	0.7						
38X	1469.5	3.5	0.4						
38V	1469.8	1.2	−2.0						
39V	1470.0	4.0	2.5						
38T	1470.2	6.7	−0.6						
38U	1470.4	6.0	−0.3						
39T	1471.0	4.8	−1.8						
39U	1471.8	2.2	−1.4						
39X	1471.8	3.0	0.0						
40U	1493.8	1.2	−0.1	1487.2	5.5	40			40
40V	1494.6	0.3	0.0						
40W	1497.9	0.1	−0.4						
40T	1498.0	0.6	0.3						
40X	1500.2	0.2	−0.3						
41X	1766.1	75.6	−5.5	1733.9	214.1	41	1729.0	−1.5	41XVW
41V	1769.8	78.0	−4.5	1747.9	405.8				
41W	1771.5	82.2	4.9						
41T	1781.8	118.4	9.4				1746.0	3.1	41TU
41U	1785.3	102.1	1.8				1750.2	20.1	

	BHandHLYP/cc-pVTZ						experiment		
Fund	v	*D*	*R*	v	*D*	Fund	v	*R*	Fund
21X	1078.0	23.2	4.3				1035.4	9.4	21XVW
21V	1093.2	41.1	−1.2	1039.0	65.1	21VW	1045.0	3.8	
21W	1097.6	8.6	0.8				1054.4	0.4	
22U	1135.9	10.3	3.7	1074.0	81.1	22	1067.8	2.9	22/23W
22W	1137.0	29.0	1.6				1075.4	7.7	
22V	1139.0	47.0	9.7				1081.1	7.3	
22T	1140.4	7.4	−4.9				1085.9	14.0	
22X	1143.4	29.2	−12.1						
23W	1149.7	26.7	2.8						
23X	1171.5	88.8	13.9	1086.6	266.4	23/24	1098.4	2.2	23XVTU
23V	1176.7	62.3	2.2	1097.3	193.5		1101.1	2.6	
23T	1180.0	188.3	7.9	1108.9	18.0				
23U	1185.5	195.2	7.7						
24W	1204.5	0.7	0.2				1163.9	−3.8	24/25/26/27
24T	1204.9	1.4	−0.1				1177.2	−19.7	
24X	1204.9	1.1	0.0						
24V	1205.0	1.0	0.0						
24U	1205.0	1.3	−0.5						
25X	1216.3	29.1	1.8	1176.1	135.5	25/26/27			
25W	1220.1	1.2	0.0						
25T	1221.8	112.0	15.4						
26X	1227.5	5.5	−1.0						
25V	1229.8	6.3	0.6						
26T	1230.0	6.7	−4.8						
26W	1230.1	14.6	−3.4						
25U	1230.9	7.4	−5.8						
26V	1234.6	2.7	4.9						
26U	1235.9	9.0	4.7						
27T	1239.1	2.4	1.1						
27W	1240.6	1.4	−0.7						
27X	1241.7	7.6	0.7						
27V	1242.2	4.0	1.8						
27U	1242.9	9.5	7.7						
28T	1273.6	285.4	12.2	1213.6	498.2	28/29TUW	1191.1	2.9	28/29TUW
28U	1273.6	179.8	17.9				1210.9	31.4	
28X	1278.3	10.0	−3.9				1218.5	6.8	
29T	1280.0	19.0	10.3						
29U	1285.2	10.2	2.6						
28W	1285.6	45.6	−1.4						
28V	1288.0	3.0	−2.3						
29W	1290.4	54.1	7.1						
29X	1321.1	1.6	3.5	1255.5	77.0	29XV/30/31/32	1238.7	1.3	29X/30T
30T	1322.0	4.0	−0.8	1281.2	111.4		1245.6	−1.1	
				1293.3	63.0		1259.1	−1.6	
				1305.0	13.6		1261.2	2.4	
29V	1332.5	7.8	4.7				1275.8	−12.7	29V/30UWXV/31/32U
30U	1336.6	15.6	−14.2				1283.9	−20.1	

30W	1344.8	0.5	−1.4				1293.8	−6.4	
30X	1345.9	66.4	6.7				1302.7	−1.8	
30V	1350.9	126.4	−17.6						
31T	1351.5	1.6	−0.2						
31U	1357.1	8.6	1.4						
31X	1361.0	64.9	−13.9						
31W	1362.1	1.1	0.6						
32U	1365.7	3.7	−2.8						
31V	1366.9	23.7	−5.3						
32V	1372.5	9.0	3.7				1314.3	6.7	32VTXW
32T	1374.2	1.7	1.2				1322.6	3.4	
32X	1375.0	12.8	4.6						
32W	1376.0	0.3	−0.4						
33X	1390.8	16.3	9.0	1338.2	3.8	33XV	1335.2	7.8	33XV
33V	1392.0	6.0	0.7						
33U	1409.8	15.0	−2.5	1351.8	40.3	33UTW/34	1346.6	−4.3	33UTW/34
33T	1417.8	24.4	−11.5	1369.8	20.1		1352.3	−14.3	
33W	1420.4	0.2	0.5	1377.5	2.2		1368.6	−6.4	
34V	1421.8	1.8	−0.1						
34X	1428.6	2.2	−0.4						
34U	1434.8	17.7	−4.2						
34T	1439.2	14.3	−1.2						
34W	1443.4	13.9	1.3						
35T	1506.4	13.4	−2.2	1438.4	58.6	35/36/37/38/39	1436.7	−5.2	35
35U	1506.6	10.4	−1.3	1449.9	34.7				
35X	1506.7	8.3	−0.7	1461.3	38.1				
35V	1507.3	9.5	−0.9						
35W	1508.1	3.0	−0.6						
36W	1509.6	4.8	−0.1				1437.6	−5.9	36/37/38/39
36U	1510.9	5.2	0.0				1442.9	−1.8	
36T	1511.1	7.0	0.3				1452.2	−1.9	
36X	1511.1	4.3	0.0				1461.8	−2.5	
36V	1511.2	4.1	−0.1				1465.4	−0.3	
37W	1511.4	2.2	0.1						
37V	1513.1	0.4	0.1						
37U	1513.3	2.6	−0.2						
37T	1516.7	4.6	−0.4						
37X	1517.0	2.1	−0.7						
38W	1523.1	2.8	−0.9						
39W	1524.2	1.0	0.4						
38X	1524.7	4.5	0.6						
38V	1525.2	3.8	0.7						
38T	1525.6	7.3	−0.6						
38U	1525.8	5.6	−0.2						
39V	1526.7	2.4	−0.1						
39T	1527.7	5.6	−2.0						
39X	1528.5	4.2	0.1						
39U	1529.3	2.5	−1.6						
40U	1553.4	1.1	0.1	1487.2	5.5	40			40
40V	1554.2	0.3	0.0						

40W	1556.5	0.0	−0.2						
40T	1557.2	0.4	0.4						
40X	1558.5	0.4	−0.5						
41X	1846.4	105.1	−7.4	1733.9	214.1	41	1729.0	−1.5	41XWT
41W	1851.2	40.6	1.6	1747.9	405.8				
41V	1851.3	105.4	−5.5						
41T	1863.3	147.0	11.5				1746.0	3.1	41TU
41U	1867.4	112.4	2.1				1750.2	20.1	

	MPW1PW91/cc-pVTZ						experiment		
Fund	v	*D*	*R*	v	*D*	Fund	v	*R*	Fund
21X	1048.2	16.6	3.0	1039.0	65.1	21XVW	1035.4	9.4	21XVW
21V	1060.2	33.8	−0.6				1045.0	3.8	
21W	1065.2	5.9	0.8				1054.4	0.4	
22U	1092.7	11.6	4.0	1074.0	81.1	22/23/24	1067.8	2.9	22/23W
22W	1094.5	36.4	2.5	1086.6	266.4		1075.4	7.7	
22V	1095.6	42.9	7.6	1097.3	193.5		1081.1	7.3	
22T	1097.6	6.4	−4.1	1108.9	18.0		1085.9	14.0	
22X	1100.0	23.7	−10.6						
23W	1103.3	20.3	1.7						
23X	1126.0	83.5	14.1				1098.4	2.2	23XVTU/24
23V	1130.3	54.9	1.7				1101.1	2.6	
23T	1134.6	175.7	7.5						
23U	1138.2	205.4	6.7						
24W	1157.8	0.5	0.3						
24T	1158.4	0.7	−0.3						
24X	1158.4	0.6	0.0						
24U	1158.5	0.8	−0.6						
24V	1158.6	0.5	0.1						
25X	1172.0	26.0	1.4	1176.1	135.5	25/26/27	1163.9	−3.8	25/26XTW
25W	1175.2	1.0	−0.2				1177.2	−19.7	
25T	1176.2	102.7	11.1						
26X	1180.6	5.5	−1.1						
26T	1182.7	5.3	−4.3						
26W	1183.1	15.1	−2.5						
25U	1184.0	21.9	−7.0						
25V	1186.4	4.8	0.0						
26V	1188.5	1.9	3.8				1191.1	2.9	26VU/27/28TUW
26U	1190.1	4.2	−0.2				1210.9	31.4	
27T	1192.0	6.2	2.2				1218.5	6.8	
27X	1193.3	11.3	0.3						
27V	1195.1	7.0	3.1						
27W	1195.3	5.2	−1.6						
27U	1197.0	22.3	13.0						
28T	1217.4	250.4	11.9	1213.6	498.2	28/29TUW			
28U	1219.0	176.1	22.5	1255.5	77.0				
28W	1230.9	84.7	2.2						
28X	1233.4	12.4	−4.0				1238.7	1.3	28XV/29TUWX
29T	1235.6	10.1	6.4				1245.6	−1.1	

29U	1239.8	2.7	−0.3				1259.1	−1.6	
28V	1242.9	2.3	−1.8				1261.2	2.4	
29W	1245.2	11.8	4.2						
29X	1267.0	1.7	3.6	1281.2	111.4	29XV/30/31/32			
30T	1270.7	2.8	0.4	1293.3	63.0				
29V	1277.8	10.0	5.0	1305.0	13.6		1275.8	−12.7	29V/30/31/32UV
30U	1283.1	15.6	−14.7				1283.9	−20.1	
30X	1289.9	60.0	7.2				1293.8	−6.4	
30W	1293.0	0.6	−1.6				1302.7	−1.8	
31T	1295.7	1.6	0.1						
30V	1295.8	118.3	−18.0						
31X	1304.2	55.5	−13.1						
31U	1305.6	4.5	5.0						
31W	1307.9	1.1	0.8						
32U	1311.8	8.7	−7.0						
31V	1312.8	5.2	−2.2						
32V	1317.6	11.2	2.4						
32X	1322.4	7.6	3.5				1314.3	6.7	32XTW
32T	1323.3	1.7	0.8				1322.6	3.4	
32W	1324.1	0.4	−0.6						
33V	1335.2	3.6	0.1	1338.2	3.8	33VX	1335.2	7.8	33VX
33X	1335.8	12.0	8.5						
33U	1354.0	17.0	−2.1	1351.8	40.3	33UTW/34V	1346.6	−4.3	33UTW/34
33T	1361.4	22.7	−10.5				1352.3	−14.3	
33W	1365.1	0.2	0.5				1368.6	−6.4	
34V	1366.2	1.5	−0.2						
34X	1373.5	1.8	−0.3	1369.8	20.1	34XUTW			
34U	1375.3	16.8	−3.4	1377.5	2.2				
34T	1381.1	8.2	0.2						
34W	1383.4	12.8	1.3						
35T	1446.8	12.9	−1.8	1438.4	58.6	35/36W	1436.7	−5.2	35/36W
35U	1447.1	12.7	−1.2						
35X	1447.1	8.3	−0.7						
35V	1448.0	9.4	−0.8						
35W	1449.0	6.9	−0.1						
36W	1450.9	1.3	−0.5						
36U	1455.8	6.2	−0.2	1449.9	34.7	36UXVT/37/38/39	1437.6	−5.9	36UXVT/37/38/39
36X	1455.9	4.5	0.0	1461.3	38.1		1442.9	−1.8	
36V	1456.0	4.2	−0.1	1487.2	5.5		1452.2	−1.9	
36T	1456.0	7.3	0.4				1461.8	−2.5	
37W	1456.1	2.6	0.0				1465.4	−0.3	
37V	1456.8	0.8	0.0						
37U	1456.9	3.0	−0.1						
37T	1459.7	4.9	−0.5						
37X	1460.6	2.7	−0.9						
38W	1465.4	3.0	−0.9						
39W	1469.9	2.1	0.4						
38V	1470.1	2.7	0.0						
38T	1470.4	6.5	−2.5						
38X	1470.5	4.5	0.6						

39V	1471.1	4.0	0.6						
39T	1471.5	7.5	−0.5						
39X	1471.6	4.7	0.0						
38U	1471.6	7.4	0.6						
39U	1472.2	2.7	−2.8						
40U	1495.5	1.5	0.0	1487.2	5.5	40			40
40V	1496.8	0.4	0.0						
40W	1499.5	0.0	−0.2						
40T	1500.6	0.6	0.5						
40X	1502.3	0.4	−0.4						
41X	1787.2	89.9	−6.9	1733.9	214.1	41	1729.0	−1.5	41XVW
41V	1791.7	91.0	−5.2	1747.9	405.8				
41W	1793.1	40.2	2.0						
41T	1804.6	127.8	10.1				1746.0	3.1	41TU
41U	1808.1	114.3	1.4				1750.2	20.1	

	PBE1PBE1/cc-pVTZ					experiment			
Fund	v	*D*	*R*	v	*D*	Fund	v	*R*	Fund
21X	1049.0	16.6	2.7				1035.4	9.4	21XVW
21V	1062.6	29.5	−1.0	1039.0	65.1	21VW	1045.0	3.8	
21W	1064.6	5.5	0.5				1054.4	0.4	
22U	1089.0	7.9	3.4	1074.0	81.1	22/23W	1067.8	2.9	22/23W
22W	1093.1	18.2	0.3				1075.4	7.7	
22T	1094.1	6.5	−4.9				1081.1	7.3	
22V	1094.2	37.6	6.8				1085.9	14.0	
22X	1097.6	25.4	−10.9						
23W	1103.9	35.4	3.5						
23X	1128.5	81.2	13.2	1086.6	266.4	23XVTU/24	1098.4	2.2	23XVTU/24
23V	1131.8	58.5	2.7	1097.3	193.5		1101.1	2.6	
23T	1136.6	165.3	4.5	1108.9	18.0				
23U	1141.0	189.3	5.8						
24W	1154.1	0.4	0.3						
24T	1154.6	0.7	−0.2						
24U	1154.7	0.7	−0.5						
24X	1154.7	0.6	0.0						
24V	1154.9	0.5	0.1						
25X	1168.6	29.0	3.2	1176.1	135.5	25/26/27	1163.9	−3.8	25/26/27
25W	1171.3	1.0	0.0				1177.2	−19.7	
25T	1173.5	111.0	13.5						
26X	1177.8	6.2	−1.6						
26T	1179.7	3.3	−4.6						
26W	1179.9	11.9	−2.2						
25U	1181.0	12.8	−5.6						
25V	1183.0	5.1	0.1						
26V	1185.2	1.3	2.9						
26U	1186.4	4.1	−0.9						
27T	1188.8	10.3	2.8						
27X	1189.7	12.7	0.5						
27V	1192.2	7.1	3.7						
27W	1192.5	5.8	−1.7						
27U	1194.3	21.2	13.0						
28T	1217.5	259.9	13.4	1213.6	498.2	28/29TUW	1191.1	2.9	28/29TUWX

28U	1218.5	161.1	22.4	1255.5	77.0		1210.9	31.4	
28X	1229.3	11.6	−4.2				1218.5	6.8	
28W	1230.7	74.6	1.3						
29T	1231.3	14.9	7.9						
29U	1235.4	5.5	0.1						
28V	1238.7	2.3	−1.4						
29W	1241.7	17.3	4.8						
29X	1262.0	2.0	4.0	1281.2	111.4	29XV/30/31/32	1238.7	1.3	29X/30T
30T	1266.4	3.5	−0.3	1293.3	63.0		1245.6	−1.1	
							1259.1	−1.6	
							1261.2	2.4	
29V	1272.1	6.8	4.0				1275.8	−12.7	29V/30UXWV/31/32UV
30U	1278.0	16.1	−14.7				1283.9	−20.1	
30X	1286.4	40.3	7.8				1293.8	−6.4	
30W	1287.6	0.8	−1.8				1302.7	−1.8	
31T	1289.6	1.9	0.2						
30V	1295.6	103.8	−15.9						
31U	1299.1	4.7	4.9						
31X	1301.0	73.2	−15.3						
31W	1303.3	1.2	0.8						
32U	1306.6	9.4	−6.9						
31V	1307.3	6.2	−2.6						
32V	1312.5	21.4	1.9						
32X	1317.3	8.9	3.5				1314.3	6.7	32XTW
32T	1318.3	2.0	0.9				1322.6	3.4	
32W	1319.2	0.3	−0.5						
33V	1330.2	4.4	0.0	1338.2	3.8	33VX	1335.2	7.8	33XV
33X	1331.5	17.6	9.9						
33U	1348.9	16.9	−1.8	1351.8	40.3	33UTW/34	1346.6	−4.3	33UTW/34
33T	1356.8	25.5	−11.2	1369.8	20.1		1352.3	−14.3	
33W	1359.9	0.2	0.4	1377.5	2.2		1368.6	−6.4	
34V	1361.2	1.5	−0.1						
34X	1368.8	2.1	−0.1						
34U	1371.5	17.0	−3.7						
34T	1377.4	10.0	−0.3						
34W	1380.2	13.0	1.3						
35T	1441.1	15.8	−2.2	1438.4	58.6	35/36/37/38/39	1436.7	−5.2	35
35X	1441.4	10.0	−0.8	1449.9	34.7				
35U	1441.4	13.7	−1.3	1461.3	38.1				
35V	1442.3	10.7	−1.0						
35W	1442.7	3.7	−0.5						
36W	1444.0	5.7	−0.1						
36U	1448.6	5.9	−0.4				1437.6	−5.9	36UXVT/37/38/39
36X	1448.8	4.9	0.1				1442.9	−1.8	
36V	1448.9	4.2	−0.1				1452.2	−1.9	
36T	1448.9	7.9	0.3				1461.8	−2.5	
37W	1449.0	2.6	0.1				1465.4	−0.3	
37V	1449.1	0.8	0.0						
37U	1449.4	3.4	0.1						
37T	1452.2	5.9	−0.5						
37X	1453.0	3.1	−1.1						
38W	1458.1	2.8	−0.9						
38V	1462.8	2.8	−0.1						
38T	1463.0	7.3	−2.7						
39W	1463.3	2.1	0.4						

38X	1463.9	5.0	1.2						
39X	1464.3	4.8	−0.4						
39V	1464.6	3.9	0.7						
39T	1464.9	7.9	−0.5						
38U	1465.0	7.3	1.8						
39U	1465.4	2.5	−3.9						
40U	1488.3	1.5	−0.1	1487.2	5.5	40			40
40V	1489.4	0.4	0.0						
40W	1492.4	0.0	−0.2						
40T	1493.3	0.8	0.5						
40X	1495.2	0.5	−0.4						
41X	1789.0	92.2	−7.2	1733.9	214.1	41	1729.0	−1.5	41XVW
41V	1793.5	87.7	−5.1	1747.9	405.8				
41W	1794.2	38.2	1.8						
41T	1805.3	132.8	11.1				1746.0	3.1	41TU
41U	1809.1	106.1	1.7				1750.2	20.1	

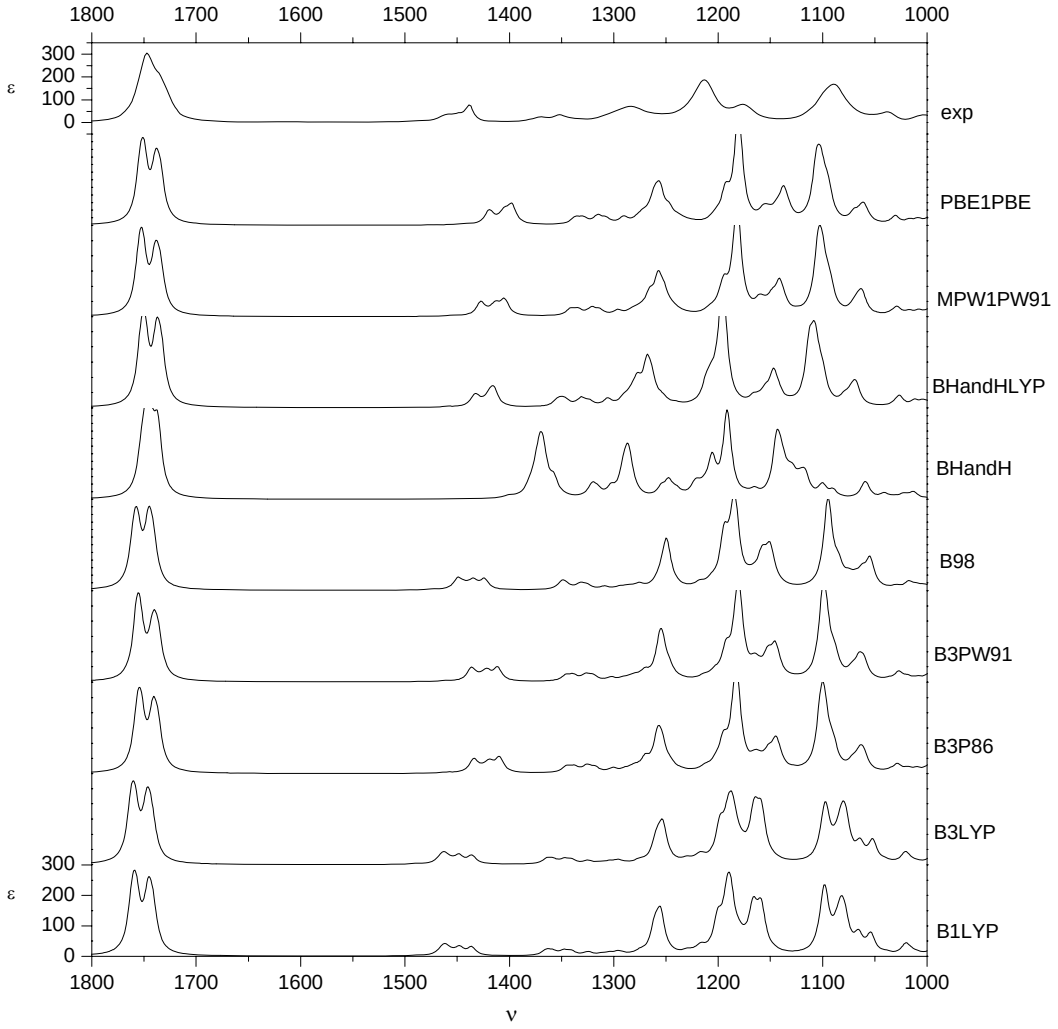

Figure S8.5 Simulated (*S*)-(+)-**3** IR DFT/cc-pVTZ for different functionals and experimental spectrum. Intensities are in molar absorptivity units, frequencies in cm^{-1}. Frequencies are scaled with functional dependent scaling factors (see Table 8.10).

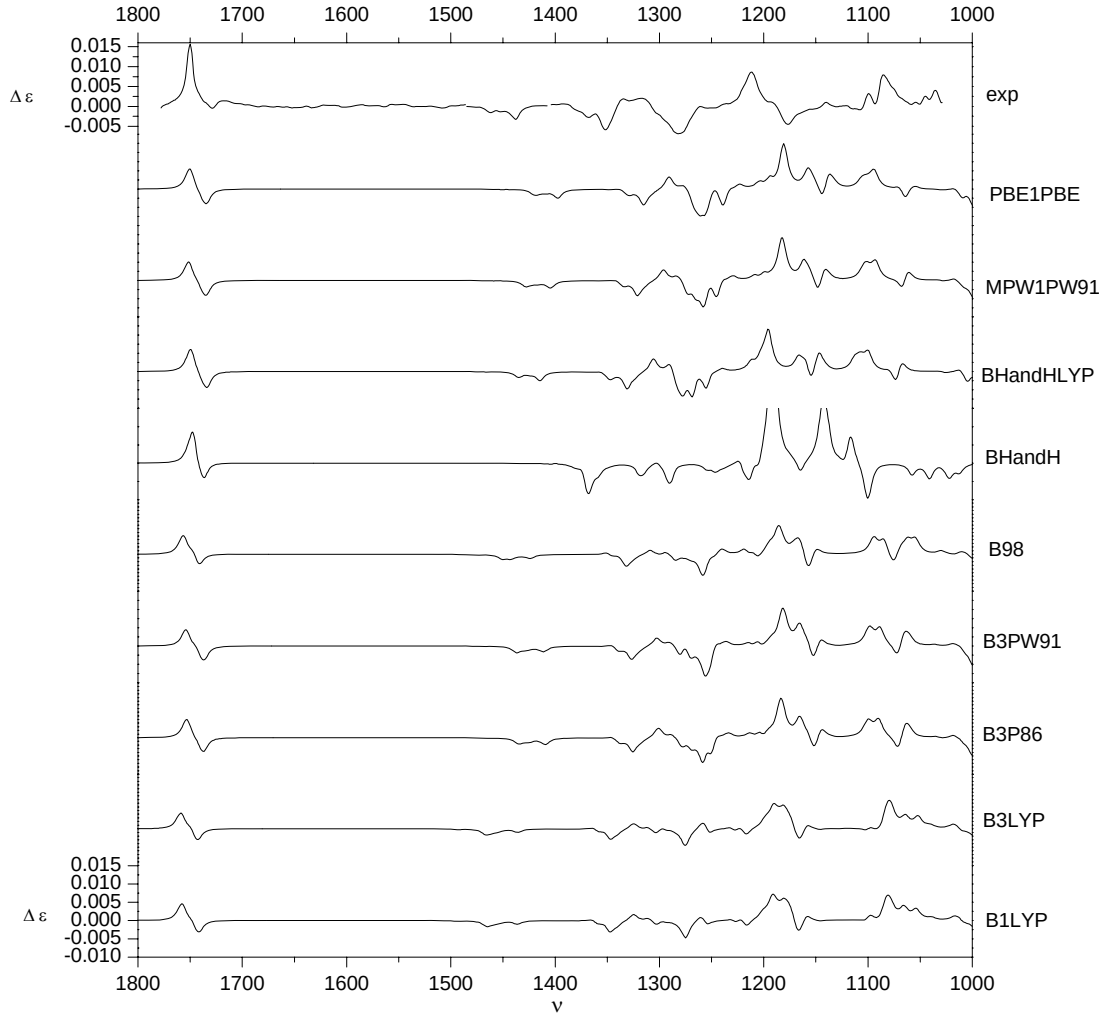

Figure S8.6 Simulated (*S*)-(+)-**3** VCD DFT/cc-pVTZ for different functionals and experimental spectrum. Intensities are in molar absorptivity units, frequencies in cm^{-1}. Frequencies are scaled with functional dependent scaling factors (see Table 8.10).